NOVEL ACTUATION MECHANISMS FOR MEMS MIRRORS

KOH KAH HOW

NATIONAL UNIVERSITY OF SINGAPORE

2013

NOVEL ACTUATION MECHANISMS

FOR MEMS MIRRORS

KOH KAH HOW

(B. Eng.(Hons.)), National University of Singapore

A THESIS SUBMITTED

FOR THE DEGREE OF DOCTOR OF PHILOSOPHY

DEPARTMENT OF

ELECTRICAL AND COMPUTER ENGINEERING

NATIONAL UNIVERSITY OF SINGAPORE

2013

Declaration

I hereby declare that the thesis is my original work and it has been written by me in its entirety.
I have duly acknowledged all the sources of information which have been used in the thesis.

This thesis has also not been submitted for any degree in any university previously.

Koh Kah How
14th January 2013

Acknowledgements

First and foremost, I would like to take this opportunity to express my sincere gratitude to my graduate advisor, Associate Professor Vincent Lee Chengkuo for his invaluable guidance and encouragement throughout my Ph.D. study. Without his help, I would not be able to overcome all the difficulties alone and be here at this final stage of my candidature. I will never forget the time he sacrificed on me and the personal advice he gave me. I would also like to thank Dr. Takeshi Kobayashi, Soon Bo Woon, Wang Nan and Qian You for their support and advice rendered regarding the fabrication of my devices. Without their help, my designs can never be realized successfully.

I would also like to express my deepest appreciation to Dr. Lap Chan, Dr. Ng Chee Mang and Leong Kam Chew for their support and knowledge sharing during the weekly presentation session at GlobalFoundries, Sinagpore. Without this EDB-Globalfoundries scholarship opportunity, I would not have gained this much of knowledge, both technical and non-technical, from the interaction with them and the rest of the Special Group (SP) students. And not forgetting my fellow group of batch-mates from SP13, whom I have spent fun and memorable times with during our postgraduate studies over the past years.

To the past and current colleagues that I've met in CICFAR, Dr. Hsiao Fu-Li, Dr. Lin Yu-sheng, Dr. Liu Huicong, Dr. Lou Liang, Li Bo, Zhang Songsong, Pitchappa Prakash, Ho Chong Pei and many others, I'm grateful that our paths have crossed. Without the presence of these colleagues, my

research life would be much tougher without their help, discussion and laughter. In addition, I would also like to extend my appreciation to Mrs Ho Chiow Mooi for her administrative help and logistics support for the purchase and loan of equipment over the past years.

Finally yet importantly, I would like to express my deepest gratitude to my parents, brother and fiancée, Katherine Kor, for being with me and supporting me all these while. Their unconditional love is the most precious gift in my life.

Table of Content

Declaration i
Acknowledgements ii
Table of Content iv
Summary vii
List of Tables ix
List of Figures x
List of Symbols xix

Chapter 1 Introduction

1.1 Optical MEMS 1
1.2 Applications of MEMS mirror 2
1.2.1 Projection Display 2
1.2.2 Variable Optical Attenuator 4
1.3 Actuation Schemes 6
1.3.1 Electrothermal actuation 7
1.3.2 Electrostatic actuation 9
1.3.3 Piezoelectric actuation 11
1.3.4 Electromagnetic actuation 13
1.4 Actuation Mechanisms 14
1.4.1 MEMS Scanners 15
1.4.2 MEMS Variable Optical Attenuators 19
1.5 Objectives of Thesis 22
1.6 Thesis organization 23

Chapter 2 MEMS Scanners Driven by 1×10 PZT Beam Actuators

2.1 Introduction 25
2.2 Design and Modeling 26
2.3 Device Microfabrication 30
2.4 Experimental Setup 33
2.5 Results and Discussion 35

2.5.1 Bending mode operation 35
2.5.2 Torsional mode operation 38
2.5.3 Mixed mode operation 42
2.6 Summary 48

Chapter 3 A PZT Driven MEMS VOA Using Attenuation Mechanism With Combination of Rotational and Translational Effects

3.1 Introduction 49
3.2 Design and Modeling 51
3.3 Device Microfabrication 57
3.4 Experimental Setup 58
3.5 Results and Discussion 61
3.5.1 Bending mode operation 61
3.5.2 Torsional mode operation 63
3.5.3 Mixed mode operation 67
3.6 Summary 69

Chapter 4 A MEMS Scanner Based on Dynamic Mixed Mode Excitation of a S-shaped PZT Actuator

4.1 Introduction 71
4.2 Design & Modeling 72
4.3 Device Microfabrication 76
4.4 Results and Discussion 79
4.4.1 DC Response 79
4.4.2 AC Response 80
4.5 Performance comparison of current designs with existing piezoelectric MEMS scanners 89
4.6 Summary 92

Chapter 5 A MEMS Scanner Using Hybrid Actuation Mechanisms With Low Operating Voltage

5.1 Introduction 94
5.2 Design & Modeling 95
5.2.1 Electrothermal Actuation 96

5.2.2 Electromagnetic Actuation 102
5.2.3 Modal Analysis 104
5.3 Device Microfabrication 105
5.4 Results & Discussion 110
5.4.1 Static characterization 111
5.4.2 Dynamic characterization 114
5.5 Performance comparison of current design with existing EM MEMS scanners 119
5.6 Summary 121

Chapter 6 Study of a MEMS VOA Driven By Hybrid Electromagnetic and Electrothermal Actuation Mechanisms

6.1 Introduction 123
6.2 Design and modeling 124
6.2.1 EM actuation and attenuation principle 125
6.2.2 ET actuation and attenuation principle 128
6.3 Experimental setup 129
6.4 Results and Discussion 134
6.4.1 Optomechanical performance for EM attenuation mechanism 135
6.4.2 Optomechanical performance for ET attenuation mechanism 139
6.4.3 Optomechanical performance for hybrid attenuation mechanism.. 144
6.5 Performance comparison of current designs with existing MEMS VOAs 145
6.6 Summary 148

Chapter 7 Conclusion and Future Work

7.1 Conclusion 150
7.2 Future Work 154
REFERENCES 157
APPENDIX 167
A. List of Awards 167
B. List of Publications 167

Summary

Recent developments in the rapidly emerging discipline of micro-electro-mechanical systems (MEMS) have shown special promise in sensors, actuators, and micro-optical systems. In fact, optics is an ideal application domain for MEMS technology as photons have no mass and are easier to be actuated compared with other microscale objects. In conjunction with properly designed mirrors, lenses and gratings, various micro-optical systems driven by microactuators can be made to perform many different functions of light manipulations such as reflection, beam steering, filtering, and collimating, etc.

In this thesis, various MEMS mirror designs for two-dimensional (2-D) scanning and variable optical attenuator (VOA) applications are explored. Four unique designs based on piezoelectric and hybrid actuation mechanisms have been conceptualized. With the focus on the development of novel actuation mechanisms to drive the MEMS mirrors, characterization of these designs have been made from the perspective of the aforementioned applications.

Two designs of piezoelectric driven MEMS scanners using mechanical supporting beam integrated with 1×10 PZT actuators are designed, fabricated and characterized. Through this design variation, the performances of these PZT MEMS scanners are investigated by using different actuation mechanisms to produce 2-D scanning patterns for both the devices. In the case of VOA application, an attenuation range of 40 dB was achieved at $1V_{dc}$, which is among the lowest operating voltage to be reported in the literature so far for MEMS-based VOA.

To further improve the scanning performance and reduce the number of PZT actuators, a S-shaped actuator design was investigated. For the same ac driving voltage, the optical deflection angle achieved by this S-shaped actuator design is demonstrated to be larger than that of the 1×10 PZT actuator design. 2-D scanning images were also successfully demonstrated by superimposing two ac signals into one signal to be used to excite the PZT actuator and drive MEMS mirror.

Besides piezoelectric driven MEMS mirror, hybrid driven CMOS compatible MEMS mirror based on electrothermal and electromagnetic actuation mechanisms are also examined for 2-D scanning and VOA applications. Various Lissajous scanning patterns were demonstrated at low power condition, making the proposed hybrid actuation design approach suitable for mobile 2-D raster scanning applications powered by batteries with limited capacity. For the case of VOA application, three types of attenuation mechanisms based on electromagnetic, electrothermal and hybrid actuations were explored and studied. This unique design of using both electrothermal and electromagnetic actuators simultaneously to achieve attenuation is the first demonstration of such hybrid driven CMOS compatible MEMS VOA device.

List of Tables

Table 1-1. Piezoelectric coefficient of selected piezoelectric materials [64]. 13
Table 2-1. Dimensions of the MEMS scanners for both designs. 28
Table 2-2 Comparison of designs A and B 47
Table 4-1. Dimensions of MEMS scanner driven by S-shaped PZT actuator. 74
Table 4-2. Comparison of FOM for different PZT MEMS scanner designs. 90
Table 5-1. Thermo-mechanical properties of materials used for ET actuator simulation and modal analysis in ANSYS. 101
Table 5-2. Structural parameters of the fabricated MEMS scanner shown in Fig. 5-10 109
Table 5-3. Comparison of FOM for different EM scanner designs. 120
Table 6-1. Detailed dimension of the microstructures for the hybrid MEMS VOA device...130
Table 6-2. Comparison of the optomechanical performance for EM and ET attenuation 143
Table 6-3. Comparison of FOM for different MEMS VOA designs 146

List of Figures

Fig. 1-1. Schematic illustration of the (a) DMD, consisting of micromirrors, springs, hinges, yokes and CMOS substrate [21, 22], and (b) GLV, where the color of each pixel is determined by the relative position of the three movable and fixed ribbons [23, 24]. 4

Fig. 1-2. (a) A SHOWWX+ laser picoprojector developed by Microvision Inc. in 2010, projecting a presentation from a media player onto a wall [26]. (b) A DLP-based picoprojector being integrated into a commercial smartphone, Samsung Galaxy Beam GT-I8530. [25]. 4

Fig. 1-3. Schematic diagram illustrating the various optical components in a DWDM-based optical communication network............................6

Fig. 1-4. Schematic diagram of (a) out-of-plane bimorph actuator showing its displacement in response to Joule heating when biased [34], (b) in-plane U-shaped actuator design, which deploys hot-cold arms of different widths [37], and (c) in-plane V-shaped chevron beam actuator which buckles in the direction of tip when a current flows through it [42]..8

Fig. 1-5. Schematic diagram illustrating the various types of electrostatic actuators commonly adopted in literature. They are (a) out-of-plane parallel plate actuator [45], (b) in-plane rotary combs [49], (c) out-of-plane staggered vertical combs [59], and (d) out-of-plane angular vertical combs [59]. 10

Fig. 1-6. Schematic diagram illustrating the change in perovskite crystal structure (a) before, and (b) after voltage is applied across it. 11

Fig. 1-7. (a) A SEM photo showing the electroplated gold electromagnetic coils on the mirror plate and actuated by ac current at resonance in the presence of permanent magnet [76]. (b) A schematic diagram illustrating a permanent magnetic film integrated on the mirror plate and actuated by the surrounding ac magnetic field [79]......14

Fig. 1-8. SEM photos of MEMS scanners based on gimbaled, two frame designs driven by (a) electromagnetic [81], (b) staggered vertical electrostatic comb actuators [55], (c)-(e) piezoelectric PZT actuators [69, 89, 96], and (f)-(g) gimbal-less designs driven by folded dual S-shaped electrothermal bimorph [92] and piezoelectric unimorph actuator [95], respectively. (h) Optical microscope photo of a piezoelectric MEMS scanner for high resolution 1-D scanning [71]. 17

Fig. 1-9. Photos of simple 2-D MEMS mirror designs driven by (a) a L-shaped thermal bimorph cantilever actuator [97], and (b) external coil exciting a mirror plate electroplated with permalloy [98].....18

Fig. 1-10. Schematic diagrams illustrating the attenuation principle for various types of MEMS VOAs designs such as (a) shutter type [101], (b) planar reflective type [102], and (c) 3-D reflective type [103]. 19
Fig. 2-1. Schematic diagram of the MEMS scanners driven by 1×10 PZT beam actuators for (a) design A, and (b) design B, respectively. In design A, the electrical connections of the PZT beam actuators are connected in series, i.e., the top electrode of one PZT actuator is electrically connected to the bottom electrode of the adjacent actuator. In design B, the electrical connections of the ten PZT actuators are separated. The inset shows an illustration of torsional mode, where the mirror twists about the y-axis. 27
Fig. 2-2. Equivalent circuit of the 1×10 PZT beam actuators labelled 1-10, and their corresponding bond pads for (a) design A, and (b) design B, respectively. 27
Fig. 2-3. Modal analysis of the MEMS scanner using finite element software ABAQUS. (a) 1st bending mode at 6Hz. (b) 2nd bending mode at 33Hz. (c) 1st torsional mode at 121Hz. (d) 2nd torsional mode at 204Hz. 30
Fig. 2-4. Microfabrication process flow for making the devices. 31
Fig. 2-5. Magnified photos showing the packaged MEMS scanners for (a) design A, and (b) design B, respectively. 31
Fig. 2-6. Optical microscopes photos of (a) PZT actuators connected in series for design A, where the top electrode of a PZT actuator is connected to the bottom electrode of the adjacent actuator, (b) bond pads connected to the bottom electrodes of their respective actuators for design A, (c) PZT actuators that are electrically isolated from one another for design B, (d) bond pads connected to either the top or bottom electrode of the actuators for design B, (e) PZT actuators fabricated in parallel on top of a Si cantilever, and (f) Si mirror surface. 33
Fig. 2-7. Schematic drawing of the experimental setup for measuring the mirror deflection angle when the MEMS scanners are driven under ac actuation voltages. 34
Fig. 2-8. Biasing configuration during bending mode operation for (a) design A, where an ac voltage of, for example, $10V_{pp}$, was applied to the ten serially connected PZT actuators, and (b) design B, where an ac voltage of, for example, $10V_{pp}$, was applied to the ten PZT actuators individually. 35
Fig. 2-9. Frequency response during bending mode operation for (a) Design A, where $10V_{pp}$ was applied to the ten serially connected PZT actuators, and (b) Design B, where $5V_{pp}$ was applied simultaneously to all the ten actuators individually. The inset

shows an example of a horizontal scanning trajectory obtained for design A. 36
Fig. 2-10. AC response during bending mode operation for designs A and B. In design A, ac voltages at 34 Hz were applied to the ten PZT actuators, while in design B, ac voltages at 30 Hz were applied to the ten PZT actuators individually. 36
Fig. 2-11. Biasing configuration during torsional mode operation for (a) design A, where an ac voltage of, for example, $10V_{pp}$, was applied to the ten serially connected PZT actuators, and (b) design B, where an ac voltage of, for example, $10V_{pp}$, was applied to PZT actuators 1 and 10, while the rest of the actuators were biased at gradually lower V_{pp} values. For actuators 1-5, the biases were applied to the bottom electrodes, while the top electrodes were grounded. In the case of actuators 6-10, the biases were applied to the top electrodes, while the bottom electrodes were grounded. (c) Schematic diagram showing the implementation of the potential divider circuit for design B, where the ac output of the function generator is split into five equal electric potentials. 39
Fig. 2-12. Frequency response during torsional mode operation for (a) Design A, where $10V_{pp}$ was applied to the ten serially connected PZT actuators, and (b) Design B, where $5V_{pp}$ was applied to the first and tenth actuator. The inset shows an example of a vertical scanning trajectory obtained for design A obtained. 41
Fig. 2-13. AC response during torsional mode operation for designs A and B. In design A, ac voltages at 198 Hz were applied to the ten PZT actuators, while in design B, ac voltages of different values at 89 Hz were applied to the PZT actuators. 41
Fig. 2-14. Biasing configuration during mixed mode operation for (a) design A, where an ac voltage of, for example, $3V_{pp}$, at 34 Hz was applied to the PZT actuators 1-5 for bending mode, while $3V_{pp}$, at 198 Hz, was applied to the PZT actuators 6-10 for torsional mode, and (b) design B, where an ac voltage of, for example, $3V_{pp}$, at 89 Hz was applied to PZT actuators 1-3 and 8-10 for torsional mode, while $3V_{pp}$, at 30 Hz was applied to the PZT actuators 4-7 for bending mode. For actuators 1-3, the biases were applied to the bottom electrodes, while the top electrodes were grounded. In the case of actuators 8-10, the biases were applied to the top electrodes, while the bottom electrodes were grounded. (c) Schematic diagram showing the external electrical circuit required for mixed mode operation for design B. 43
Fig. 2-15. AC response during mixed mode operation for (a) design A and, (b) design B. 45
Fig. 2-16. Lissajous scan patterns obtained during mixed mode operation for (a) design A and, (b) design B 46

Fig. 3-1. Schematic drawing of the piezoelectric MEMS VOA with dual core collimator arranged in a 3-D configuration such that the light beam focuses on the far edge center of the mirror plate. Bending mode occurs when all the ten actuators are biased simultaneously at same voltage. Torsional mode occurs where a set of five actuators bends in one direction while the other set of five actuators bends in the opposite direction. 51
Fig. 3-2. Schematic diagram illustrating the side profile of the dc-biased PZT actuator during bend mode operation, with experimental vertical displacement of $\delta_{actuator}$, mechanical rotation angle of $\theta_{B,mirror}$ and radius of curvature, r...52
Fig. 3-3 Schematic diagrams showing the attenuation mechanism for bending mode: (a) configuration refers to the initial state of insertion loss. All of the laser beam from the input fiber is coupled back into output fiber when the actuators are not biased, i.e., mirror surface remains normal to laser beam; (b) a portion of the laser beam from input fiber deviates from the optimized reflection light path when the actuators are biased, i.e., mirror undergoes rotational and translational motion (c) mirror is rotated by an angle, θ_B,mirror, and the laser beam is displaced by a distance, $\delta_{B,laser}$...54
Fig. 3-4. Schematic diagrams showing attenuation mechanism for torsional mode: (a) all of the light beam from the input fiber is coupled back into output fiber when the actuators are not biased. It is the initial state of insertion loss; (b) configuration refers to the attenuation state where a portion of the laser beam from input fiber is not coupled back to the output fiber due to that actuators 1-5 and actuators 6-10 being oppositely biased, i.e. mirror undergoes rotational motion (c) mirror is rotated by an angle, $\theta_{T,mirror}$, and the laser beam is displaced by a distance, $\delta_{T,laser}$. 54
Fig. 3-5. Close-up photo showing the packaged PZT MEMS VOA with a gold-coated surface...57
Fig. 3-6. Measured average displacement of fixed-free actuator tips versus dc driving voltage applied to the top electrodes of all ten actuators. 58
Fig. 3-7. Schematic drawing of the measurement setup for 3-D MEMS VOA characterization carried out on an anti-vibration optical bench. The stage is capable of moving in X-Y-Z directions and tilting along X-Y(θz) and Y-Z(θx) planes as well.......................60
Fig. 3-8. Experimental data for bending mode. (a) Measured attenuation curve versus dc voltage applied simultaneously to the top electrodes of the ten actuators while the bottom electrodes are grounded. (b) Bottom right (red) curve shows measured average displacement of actuator tip, $\delta_{actuator}$, versus dc voltage applied

simultaneously to the top electrodes of ten actuators. Top left (blue) curve shows the displacement of laser beam, $\delta_{B,laser}$, versus dc voltage. The displacement of laser beam, $\delta_{B,laser}$, is calculated using equations (3.5)-(3.7) and the values of $\delta_{actuator}$ obtained from the red curve. 62
Fig. 3-9. Schematic drawing illustrating the electrical connections of the top and bottom electrodes of each actuator to the dc power supply in (a) bias case A, and (b) bias case B. (c) A look-up table showing the individual dc bias driving each actuator under bias case A and B for a given dc power supply voltage. 64
Fig. 3-10. Experimental data for torsional mode. (a) Measured attenuation curves versus dc driving voltage of the power supply for both bias cases A and B. (b) Top left (red) curve shows measured average displacement of mirror edges, δ_{mirror}, versus dc driving voltage of power supply. Bottom right (blue) curve shows the displacement of laser beam, $\delta_{T,laser}$, versus dc voltage of power supply. Both curves were obtained using bias case A. The displacement of laser beam, $\delta_{T,laser}$, is calculated using equations (3.8)-(3.10) and the values of δ_{mirror} obtained from the red curve. 66
Fig. 3-11. Measured attenuation value as a function of dc bias applied to the 2 sets of actuators 1-5 and 6-10. 68
Fig. 4-1. (a) Schematic drawing of the MEMS scanner actuated by single S-shaped PZT actuator. Bending and torsional modes occur when the device is excited at the respective resonant frequencies. (b) Top view of the MEMS scanner and the respective dimensions of the structures. 73
Fig. 4-2. Finite element modal analysis for the two different mirror designs using finite element simulation software ABAQUS. The 1st design being simulated is a micromirror driven by a S-shaped actuator design during (a) bending mode operation, where eigenfrequency at 34.9 Hz and a maximum normalized Z-displacement of 1 was obtained, and (b) torsional mode operation, where eigenfrequency of 72.1 Hz and a maximum normalized Z-displacement of 0.9 was obtained. The 2nd design being simulated is a micromirror driven by straight cantilever actuator design during (c) bending mode operation, where eigenfrequency of 35.3 Hz and a maximum normalized Z-displacement of 1 was obtained, and (d) torsional mode operation, where eigenfrequency of 128 Hz and a maximum normalized Z-displacement of 0.36 was obtained. 74
Fig. 4-3. Microfabrication process flow for making the S-shaped PZT actuator and the micromirror. 77
Fig. 4-4. Close-up photo showing the packaged MEMS mirror on a dual in-line package (DIP). The bond wires connect the bond pads on the device to the external pins of the DIP. 78

Fig. 4-5. Optical microscope images of (a) S-shaped PZT actuator with a portion of the mirror plate, and (b) two bond pads and their respective bond wires to the DIP. 79
Fig. 4-6. Measured ODA versus DC voltage applied to S-shaped PZT actuator. 80
Fig. 4-7. Frequency response showing a semi-log plot of measured ODA versus excitation frequency at 0.5 V_{pp} for both bending and torsional modes. 81
Fig. 4-8. AC response for bending and torsional modes where the MEMS scanner was excited independently with ac signals of 27 Hz and 70 Hz, respectively. 81
Fig. 4-9. Schematic diagram illustrating the biasing circuit required to produce 2-D scanning pattern. Two sinusoidal waveforms of different frequencies were inputted into a summing amplifier. V_B and V_T denote the peak-to-peak voltage for the ac excitation signals with frequencies 27 Hz and 70 Hz, respectively. 83
Fig. 4-10. Waveform obtained from different voltage output. (a) Dotted (red) and solid (blue) curves show the respective output of the 2 function generators when both V_B and V_T were at 0.5 V_{pp}. (b) Dotted (red) curve shows the resultant output from the summing amplifier V_{out} when V_B and V_T are 0.5V_{pp}. 84
Fig. 4-11. Screenshot capture of the waveforms obtained from a oscilloscope connected to the V_{out} terminal, with various voltage bias combinations such as (a) V_B = 1V_{pp}, V_T = 0V_{pp}, (b) V_B = 0.8V_{pp}, V_T = 0.3V_{pp}, (c) V_B = 0.5V_{pp}, V_T = 0.5V_{pp}, and (d) V_B = 0.3V_{pp}, V_T = 1V_{pp}. 87
Fig. 4-12. 2-D Lissajous scanning patterns obtained when various combinations of sinusoidal V_B and V_T were supplied by the two function generators and superimposed by the summing amplifier, where (a) V_B = 3V_{pp}, V_T = 0V_{pp}, (b) V_B = 1V_{pp}, V_T = 0V_{pp}, (c)V_B = 0.8V_{pp}, V_T = 0.3V_{pp} , (d) V_B = 0.5V_{pp}, V_T = 0.5V_{pp}, and (e) V_B = 0.3V_{pp}, V_T = 1V_{pp}. The experimental setup of the scanning line obtained in (a) were slightly different from those obtained in (b)-(e) so that the entire scanning line can be accommodated onto the ruler scale. 88
Fig. 5-1. Schematic diagram of the proposed MEMS scanner incorporated with hybrid actuation mechanisms. The vertical and horizontal scanning motions are driven by ET and EM actuation mechanisms, respectively. 96
Fig. 5-2. Schematic diagram illustrating the (a) proposed ET bimorph actuator made of Al and Si, with the inset showing the winding design of the Al metal layer and thin thermal insulating SiO_2 deposited around the windings; (b) working principle of ET actuation and rotation about the vertical scanning axis i.e. x-axis

when ET actuators 1 & 2 are biased serially to give a mechanical torque. 97
Fig. 5-3. Simulated plot illustrating the change in the tip displacement of a single clamped ETl actuator for a unit temperature change. The thickness of the Al metal layer is varied from 0.1µm to 6µm for different Si device layer thickness of a SOI wafer. 99
Fig. 5-4. Plots of mechanical rotation angle and maximum temperature of device versus total dc voltage applied to actuators 1 and 2. Results are obtained from FEM simulation using ANSYS. 100
Fig. 5-5. Simulation result by ANSYS when ET actuators 3 and 4 are biased with a total DC voltage of 10V. (a) Y-displacement profile of the device where the mirror rotates about the x-axis. (b) Temperature distribution profile of the device. 101
Fig. 5-6. Schematic drawing illustrating the working principle of EM actuation and rotation about the horizontal scanning axis i.e. z-axis when a mechanical torque, in the presence of external magnetic field, is generated due to the current flow in the coil embedded in the frame. (b) Top viewing drawing illustrating the dimensions of the coils. Two turns of the EM coil are shown for simplicity. 102
Fig. 5-7. Various mode shapes of the device derived from ANSYS simulation. (a) 2nd eigenmode at 87.5 Hz for vertical scanning. (b) 3rd eigenmode at 160.3 Hz for horizontal scanning. (c) 6th eigenmode at 3014 Hz for horizontal scanning. 104
Fig. 5-8. Microfabrication process flow of the device 106
Fig. 5-9. Photos showing (a) an unpackaged 2-D MEMS scanner placed beside a Singapore five-cent coin, (b) the device packaged in a dual inline package, and (c) a close-up view showing the bond pads connected to the pins of the package via gold bond wires. 108
Fig. 5-10. Optical micrographs showing the (a) C-shaped hinge connecting the ETactuators to the frame, (b) T-shaped torsion bar, (c) Al EM coils embedded in the frame, and (d) Al windings of the ET actuator. 108
Fig. 5-11. Experimental setup for the optical characterization of device. Inset shows the packaged device placed in between the magnets, with red laser light impinging on the mirror surface 110
Fig. 5-12. I-V curves obtained for the EM coil, ET actuators 1 and 2 connected in series and ET actuators 3 and 4 connected in series. Inset shows a detailed sweep of the coil within the $1V_{dc}$ range, obeying a linear fit of I(mA) = 1.8V (V). 111
Fig. 5-13. DC response for (a) ET actuation, and (b) EM actuation. 113
Fig. 5-14. Bode plots illustrating the frequency response for (a) ET actuation where actuators 1 and 2 are biased in series, and (b) EM actuation. 114

Fig. 5-15. AC response for (a) ET actuation at 74Hz for two different cases of biasing configurations; (b) EM actuation at 202Hz, with inset showing an example of a horizontal scanning trajectory line produced during EM actuation. 116
Fig. 5-16. Various Lissajous patterns generated from different combinations of ET and EM biasing configurations. ET actuators 1 and 2 at 2 V_{dc} and 2 V_{ac}, 74 Hz are responsible for the horizontal scanning in all 3 patterns while the biasing conditions for the vertical scanning are (a) 0.1 V_{ac} or 0.126 mA, 202 Hz; (b) 0.2 V_{ac} or 0.252 mA , 202Hz; (c) 2 V_{ac} or 2.5 mA, 2926 Hz respectively.................... 118
Fig. 5-17. Performance comparison of the various EM MEMS scanners reported in literature. 120
Fig. 6-1. Schematic diagram of the hybrid actuated MEMS VOA with dual-fiber collimator arranged in 3-D free space configuration such that the light beam focuses on the center of the aluminum mirror surface. Insets A and B show the top view drawings illustrating the dimensions and layout of the EM coils and ET windings, respectively. The number of EM coils and ET windings have been reduced for simplicity purposes. 125
Fig. 6-2. Schematic diagrams showing the (a) EM actuation mechanism in the presence of an external permanent magnetic field and current flowing in the coils embedded in the frame, and (b) EM attenuation principle, where the laser beam is rotated and displaced by an angle θ_{EM} and distance $\delta_{EM,laser}$, respectively.... 125
Fig. 6-3. Schematic diagram showing the (a) ET actuation mechanism where ET actuators 1 and 2 are biased and heated up, and (b) ET attenuation principle, where the laser beam is rotated and displaced by an angle θ_{ET} and distance $\delta_{ET,laser}$, respectively. 128
Fig. 6-4. A magnified photo showing the packaged MEMS VOA device. Insets A and B show the optical micrographs of the ET windings and EM coils respectively. Inset C shows a SEM micrograph of the ET actuator, C-shaped joint, frame, T-shaped torsion bar and mirror. 130
Fig. 6-5. (a) Schematic diagram of the measurement setup carried out on an anti-vibration optical bench. The stages are capable of moving in X-Y-Z directions and tilting along X-Y (θz) and Y-Z (θx) planes as well. (b) Photo illustrating the actual measurement setup which includes the tunable laser, power meter, two dc power supplies and stages. (c) A magnified photo at the DUT region, where the DUT is mounted upright in the presence of an external permanent magnetic field. The dual fiber collimator is adjusted to a working distance of 1mm away from the mirror surface. 131
Fig. 6-6. White light interferometer measurement of the surface roughness for the aluminium coated mirror. 131

Fig. 6-7. Measured I-V curves for the EM coils and ET actuators, respectively..134
Fig. 6-8. (a) Experimental optical deflection angle and analytically calculated laser spot displacement versus dc voltage applied to the EM coil. The inset shows a schematic diagram of the EM attenuation mechanism, where the laser spot no longer couples perfectly from the input fiber into the output fiber after EM actuation. (b) Measured attenuation-bias curves for difference current direction in the EM coils. 136
Fig. 6-9. Measured wavelength dependent loss at various attenuation states for EM attenuation..138
Fig. 6-10. Comparison of mechanical rotation angle (θ) obtained from simulation software ANSYS and optical rotation angle (2θ) obtained from He/Ne red laser experiment. Inset shows the simulated y-profile of the device obtained from ANSYS when ET actuators 1 and 2 were biased serially at $3V_{dc}$...........................139
Fig. 6-11. Analytically calculated and experimental data obtained for ET attenuation mechanism. (a) Derived IR laser spot displacement versus dc driving voltage applied serially to ET actuators 1 and 2. The inset shows a schematic diagram of the ET attenuation mechanism, where the laser spot no longer couples perfectly from the input fiber into the output fiber after ET actuation. (b) Measured attenuation-bias curves for different sets of ET actuators...140
Fig. 6-12. Measured wavelength dependent loss at various attenuation states for ET attenuation..142
Fig. 6-13. Measured attenuation value as a function of dc driving voltages applied to EM and ET actuators during hybrid actuation. 144
Fig. 6-14. Performance comparison of various MEMS VOAs reported in literature...147
Fig. 7-1. Proposed system architecture to integrate proposed MEMS scanner for display applications. 154

List of Symbols

Symbol	Description	Unit
r	Radius of curvature	µm
D	Working distance of dual core collimator	mm
$\theta_{B,mirror}$	Mechanical rotation angle of the mirror during bending mode	°
$\theta_{T,mirror}$	Mechanical rotation angle of the mirror during torsional mode	°
L_{mirror}	Length of mirror plate	mm
$L_{actuator}$	Length of actuator	mm
$\delta_{actuator}$	Vertical displacement of actuator	µm
$\delta_{B,laser}$	Displacement of laser beam during bending mode	µm
$\delta_{T,laser}$	Displacement of laser beam during torsional mode	µm
$R_{dot\ size}$	Radius of laser spot	µm
d_{31}	Piezoelectric constant	pm/V
S_{Si}	Compliance of silicon	GPa^{-1}
S_{PZT}	Compliance of PZT	GPa^{-1}
t_{Si}	Thickness of silicon	µm
t_{PZT}	Thickness of PZT	µm
E_{Si}	Young's Modulus of silicon	GPa
E_{PZT}	Young's Modulus of PZT	GPa
α_{Si}	Coefficient of thermal expansion of silicon	K^{-1}
α_{PZT}	Coefficient of thermal expansion of PZT	K^{-1}
w_{Si}	Width of silicon	µm
wPZT	Width of PZT	µm
ΔT	Difference in temperature	K

Chapter 1
Introduction

1.1 Optical MEMS

Micro-electro-mechanical systems (MEMS) technology has demonstrated great promise in opening new frontiers in the applications of sensors and actuators. Mechanical sensing and actuation mechanisms are now integrated with electronics on a silicon substrate through the various micro-fabrication technologies available today. This has brought forth rapid progress in various industries such as telecommunication, biomedical and military defense. Components fabricated with the emerging technologies of MEMS are being incorporated rapidly into numerous applications. These MEMS applications include inertial MEMS such as accelerometers and gyroscopes in automobile and consumer electronics, thermoelectric and vibration-based energy harvesters in implantable biomedical devices and wireless sensor nodes, respectively.

In the optical MEMS regime, microstructures such as micromirrors, microlens and gratings are driven to move or deform by actuators so that unique functions such as light manipulation can be achieved. Cornerstones for the success of optical MEMS technology include actuator technology, optics design and development of movable or tunable micromechanical elements such as rigid reflective mirror [1], deformable reflective mirror [2, 3], shutters [4, 5], gratings [6], waveguides [7], and microlens [8, 9] . MEMS and optics make a perfect match as MEMS devices have dimensions and actuation

distances comparable to the wavelength of light. In addition, optical MEMS have long been a goal of forward-thinking electronics innovators, with big companies such as IBM and Intel having reported significant successes in using the traditional CMOS toolkit to micromachine optical interconnects and structures [10, 11]. As these companies and other research laboratories around the world pursue on a "computing with light" paradigm, the look for optical MEMS to serve as connection between arithmetic-logic units on the same chip will ensue in the near future.

1.2 Applications of MEMS mirror

With a number of advantage, including small size, light weight and fast speed compared to conventional bulky scanners, optical MEMS mirrors have been drawing attention for a wide range of applications such as displays [12, 13], optical communications [14-16], microspectroscopy [17] and optical coherence tomography [18-20].

1.2.1 Projection Display

In the field of projection display application, the most successful MEMS-based commercial product is probably the Digital Micromirror Device (DMD), which utilize the Digital Light Processing (DLP) technology developed proprietary by Texas Instrument in the early 1990s [21, 22]. As shown in Fig. 1-1(a), the DMD consists of a semiconductor-based array of fast, effective micron-meter size mechanical mirrors to redirect light from LEDs or lasers into raster patterns that create visible displays. Each micromirror corresponds to an image pixel and the pixel brightness can be

controlled by switching between two tilt states. First generation DMD device with pixel pitch of 17µm, 0.7µm gap and ±10° rotation has given way to 10.8µm pitch, 0.7µm gap and ±12° rotation in their current latest 1080p resolution product. Greater rotation can accommodate higher numerical aperture, while smaller pixel pitch shrinks the chip area, offering cost benefit to microdisplay and optical systems.

Besides using MEMS mirror which are reflective-type devices, diffractive-type devices in the form of gratings have also been reported for scanning purposes. In 1994, Solgaard *et al.* from Stanford University developed the grating light valve (GLV), providing an alternative MEMS-based technology for implementation in commercial projectors [23, 24]. The key idea behind GLV technology is the use of movable ribbons to modulate the phase of light so that it can be regarded as a MEMS tunable phase grating. As shown in Fig. 1-1(b), each pixel consists of three movable and three fixed ribbon strips, with each pair of movable and fixed ribbons being responsible for the intensity of red, green or blue color. As such, the color of a pixel on the screen is determined by the amount of red, blue and green light being diffracted and incident collectively on the pixel as 1st order light.

In recent years, optical MEMS devices have also formed a circle of growing interest, with the development of handheld picoprojectors based on scanning mirror technology becoming an intriguing killer applications in consumable electronics, IT and amusement business [12, 13]. Traditional high-resolution mirror array approach developed for digital projector remains too large to be adapted into a portable device. In order to display a much

bigger multimedia in the forms of images, movies or presentations on an ordinary surface e.g. a wall or a table, MEMS-based scanner technology can be incorporated into these portable gadgets that allow people to share these multimedia much more easily and spontaneously [25, 26].

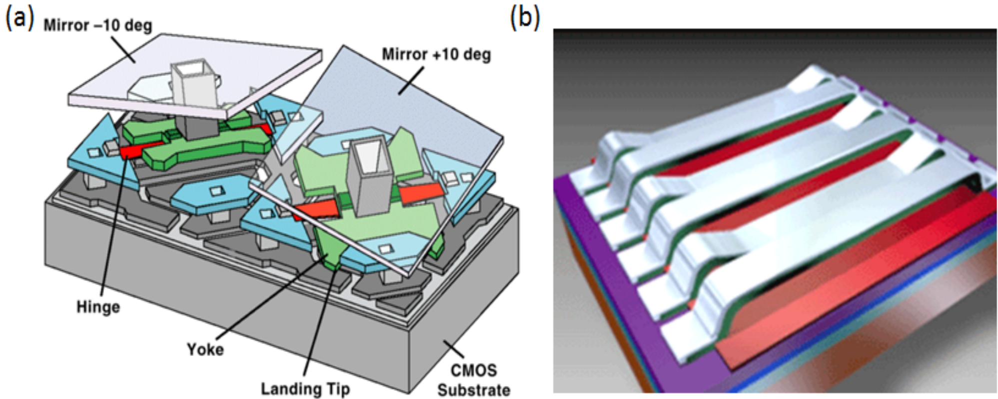

Fig. 1-1. Schematic illustration of the (a) DMD, consisting of micromirrors, springs, hinges, yokes and CMOS substrate [21, 22], and (b) GLV, where the color of each pixel is determined by the relative position of the three movable and fixed ribbons [23, 24].

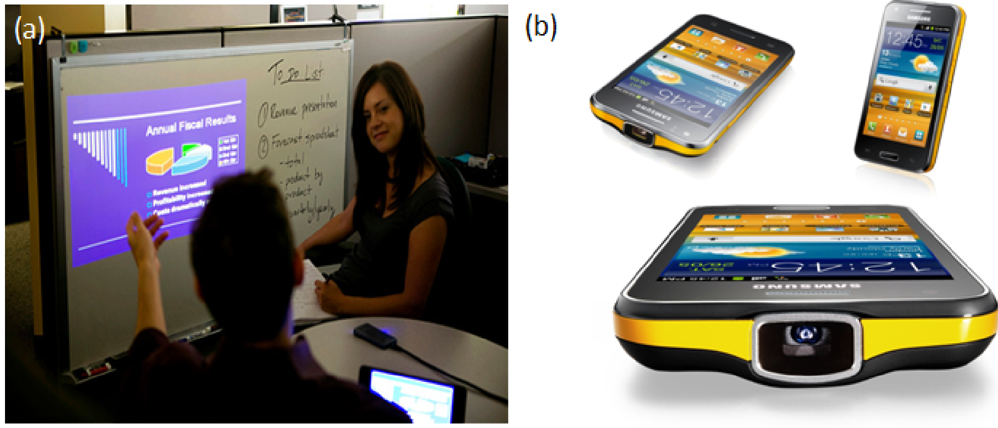

Fig. 1-2. (a) A SHOWWX+ laser picoprojector developed by Microvision Inc. in 2010, projecting a presentation from a media player onto a wall [26]. (b) A DLP-based picoprojector being integrated into a commercial smartphone, Samsung Galaxy Beam GT-I8530. [25].

1.2.2 Variable Optical Attenuator

Besides projection display applications, optical MEMS have also been an enabling tool for numerous cutting-edge devices in optical communications. With the increasing demand for higher bandwidth and speed

in telecommunications, better fiber optics network is required for smooth and high transmission rates in the range of tens to hundreds gigabit per second (Gbps). As shown in Fig. 1-3, the development of dense wavelength division multiplexing (DWDM) technology has allowed multiple multiplexed optical signals to be transmitted on a single optical fiber through the use of different laser light wavelengths to carry different signals. With DWDM technology, telecommunications companies are now able to expand the capacity of the network without laying more optical fibers. In the late 90s and early 2000, significant progress in the optical MEMS technology, alongside with the development of DWDM systems, has been made in the telecommunication industry. Enormous investments have been made on optical MEMS technology as it has been recognized to be an indispensable technology meant to fulfill the missing link that can help connect other existing technologies to form an all-optical communication network. Many crucial MEMS-based components such as variable optical attenuator (VOA) [27], optical switch [28-30] and tunable laser [31] for telecommunication applications have been demonstrated and commercialized.

Among these optical communication applications, VOA and its array are crucial components for enabling the advanced optical network. Currently, VOAs are adopted to groom power levels across the DWDM spectrum, which help minimize crosstalk and maintain the desired signal noise ratio. In the case of MEMS technology, such MEMS VOA devices offer physical features like transparency (bit rate and protocol independent), tunability, scalability, low electrical operation power consumption, and small form factor. In addition, these MEMS VOAs deploy the free space light attenuation configuration and

demonstrate their prevalence advantages over other solutions in terms of device features, wavelength independence, transparency etc. This allows them to reduce incoming light intensity in an analog control manner regardless of the difference in wavelength and protocol.

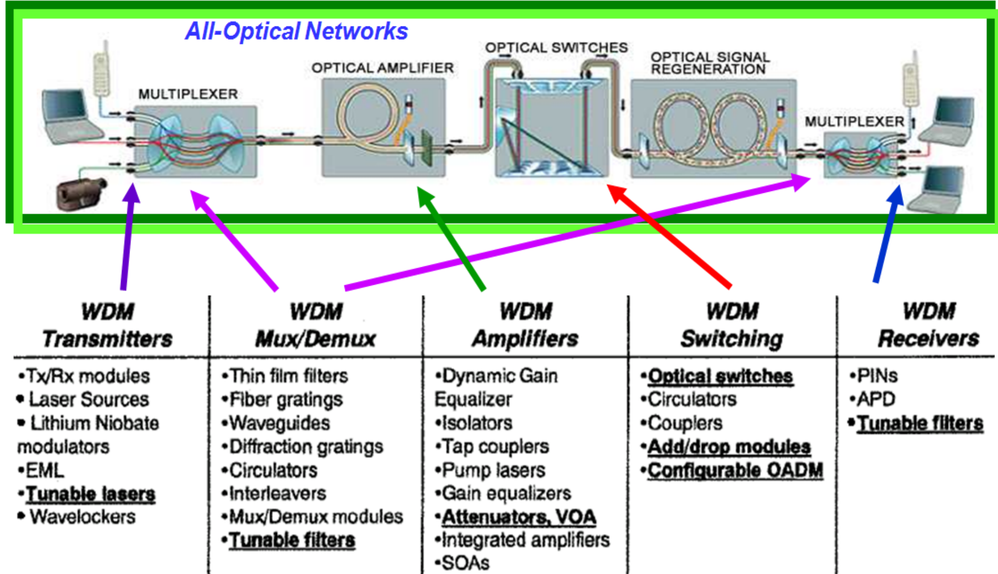

WDM Transmitters	WDM Mux/Demux	WDM Amplifiers	WDM Switching	WDM Receivers
•Tx/Rx modules • Laser Sources • Lithium Niobate modulators •EML •**Tunable lasers** • Wavelockers	•Thin film filters •Fiber gratings •Waveguides •Diffraction gratings •Circulators •Interleavers •Mux/Demux modules •**Tunable filters**	•Dynamic Gain Equalizer •Isolators •Tap couplers •Pump lasers •Gain equalizers •**Attenuators, VOA** •Integrated amplifiers •SOAs	•**Optical switches** •Circulators •Couplers •**Add/drop modules** •**Configurable OADM**	•PINs •APD •**Tunable filters**

Fig. 1-3. Schematic diagram illustrating the various optical components in a DWDM-based optical communication network.

1.3 Actuation Schemes

Recent developments in the rapidly emerging discipline of MEMS have shown immense promise in actuators and micro-optical systems [32]. In conjunction with properly designed mirrors, lenses and gratings, various micro-optical systems driven by microactuators can provide many unique functions in light manipulations such as reflection, beam steering, filtering, focusing, collimating, and diffracting, etc. In the next few sections, the four major actuation schemes, i.e. electrothermal, electrostatic, piezoelectric and electromagnetic, for in-plane or out-of-plane movement are introduced. Each

actuation schemes have their inherent advantages and disadvanatages, while their design feasibilities are often limited to the fabrication method used.

1.3.1 Electrothermal actuation

Electrothermal actuation makes use of the difference in thermal expansion of materials to achieve mechanical actuation. The thermal expansion of a solid material is characterized by the coefficient of thermal expansion (CTE), $\alpha_{T,}$ and it has a unit of strain per change in temperature (K^{-1}). With a small temperature change of ΔT, the introduced mechanical strain is defined as the product, $\alpha_T \bullet \Delta T$. One of the basic actuator structures for thermal actuation, as shown in Fig. 1-4(a), is a electrothermal bimorph which consists of a cantilever with two different material layers [33-36]. The actuation relies on the difference in linear expansion coefficients of two materials, with one layer expanding by a larger amount compared to the other. This results in stress at the interface of these two layers, leading to bending of the cantilever. The elevated temperature can be created by heating up the cantilever when a bias current flows through an embedded resistor in the cantilever, i.e. Joule heating effect.

In addition to out-of-plane actuation, there are also other applications that demand in-plane displacement which will involve designs that are different from the above-mentioned bimorph actuator. For example, in-plane actuation is made possible by designing a single material, U-shaped electrothermal actuator consisting of two arms of uneven widths [37]. As shown in Fig. 1-4(b), when an electrical current is applied from one anchor to the other, the arm with the larger electrical resistance heats up more. This

results in higher temperature and larger volume expansion in the thinner arm, i.e. so called hot arm. The other thicker arm is relatively cold and is referred as cold arm. Eventually, the U-shaped thermal actuator will deflect laterally towards the cold arm side due to asymmetrical thermal expansion when the actuator is dc biased. Other variations of the classical single hot-cold arms design have also surfaced, with some research groups focusing on two hot arms and one cold arm design [38-40], and one group having integrated a piezoresistive lateral displacement sensor embedded into the actuator [41]. Other designs for in-plane electrothermal actuators, such as V-shaped chevron beam actuators illustrated in Fig. 1-4(c), have also been reported [42-44].

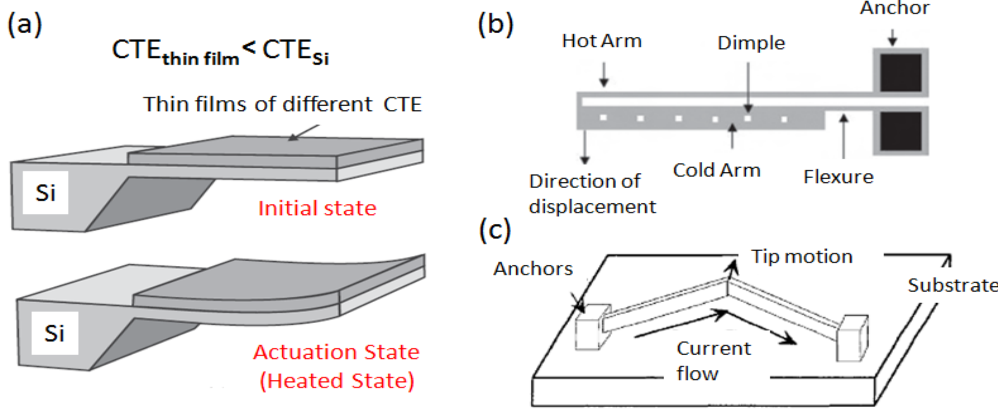

Fig. 1-4. Schematic diagram of (a) out-of-plane bimorph actuator showing its displacement in response to Joule heating when biased [34], (b) in-plane U-shaped actuator design, which deploys hot-cold arms of different widths [37], and (c) in-plane V-shaped chevron beam actuator which buckles in the direction of tip when a current flows through it [42].

Compared to other actuation schemes, electrothermal actuator can achieve large forces (~100µN) and static displacement (~100µm) at relatively low voltages (~5V) [32]. However, it requires a large amount of thermal energy for their energy and therefore consumes substantial electrical energy (~1W). In addition, it has a slower response and ac operation of thermal actuator is generally limited to frequency response of less than 1 kHz. This is due to the time constant associated with heat transfer. High temperature and

complicated thermal management are further drawbacks of thermal actuation. For example, the upper practical limit for temperature in polysilicon and single-crystal-silicon based electrothermal actuator is approximately 600°C and 800°C respectively, above which material property changes such as localized plastic yielding and material grain growth become an issue.

1.3.2 Electrostatic actuation

In electrostatic actuation, a typical configuration usually consists of a movable electrode connected to suspended mechanical springs while a fixed electrode is anchored onto the substrate. When a voltage is applied to the capacitive electrodes, the electrostatic attractive force actuates the movable electrode to the stationary electrode, causing the area of overlap and the capacitance between the two electrodes to increase. As a result, the spring suspending the movable electrode is deformed. Thus, the force balance between the spring restoring force and the electrostatic force determines the displacement of the movable electrode.

There are two major types of electrodes that are commonly used for electrostatic actuation: parallel plate [45, 46] and interdigitated combs, as illustrated in Fig. 1-5. In the lateral and vertical comb actuation setups, the force is independent on the displacement, unlike the parallel plate actuator setup. In addition, the force is inversely proportional to the gap distance, hence making the force generated to be much smaller than that of parallel plate actuator. This can be compensated by having more fingers and applying a higher voltage. There are currently four categories of comb drive designs: lateral combs [4, 47], rotary combs [6, 48, 49], staggered vertical combs

(SVC) [50-55], and angular vertical combs (AVC) [56-61]. In a SVC actuator shown in Fig. 1-5(c), it requires a vertical offset between the moving combs and the fixed combs for out-of-plane rotation. In order to create the vertical offset between the two sets of combs, various fabrication techniques such as wafer bonding [50-52], integration of polysilicon and surface micromachining [53], double-side alignment lithography on a SOI wafer [54, 55] have been used. In the case of AVC illustrated in Fig. 1-5(d), the movable combs are often fabricated in the same layer as the fixed fingers and then tilted upward by various post-fabrication methods such as plastic deformation [56, 57], residual stress [58], reflow of PR [59], and manual assembly [60, 61].

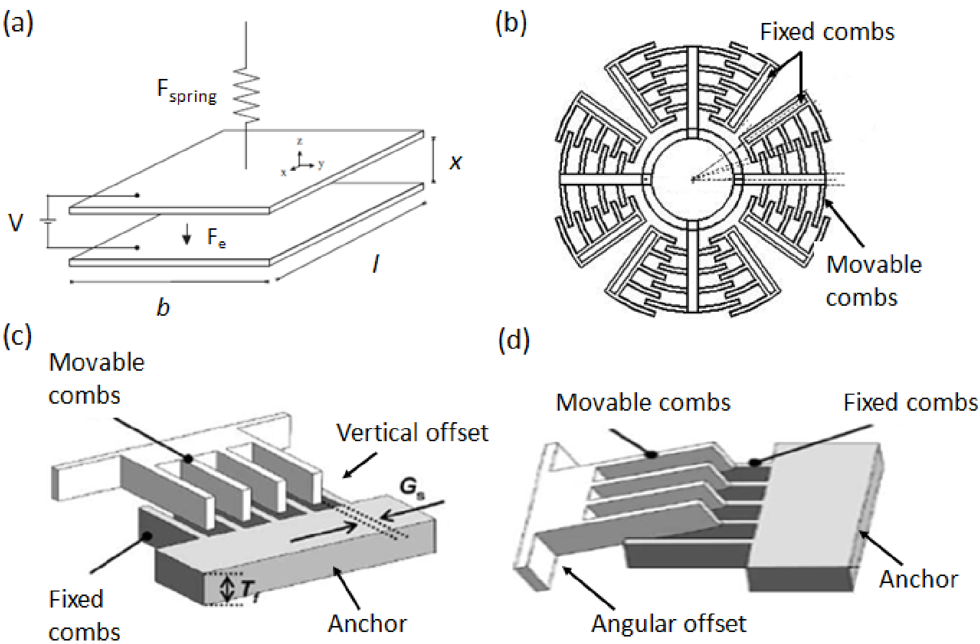

Fig. 1-5. Schematic diagram illustrating the various types of electrostatic actuators commonly adopted in literature. They are (a) out-of-plane parallel plate actuator [45], (b) in-plane rotary combs [49], (c) out-of-plane staggered vertical combs [59], and (d) out-of-plane angular vertical combs [59].

In general, parallel plate and comb actuators are the available designs that may be used in bulk micromachined optical MEMS devices, while polysilicon-based comb actuators are often used in surface micromachined

structures. Briefing speaking, parallel plate actuation can provide large force (~50µN) with small displacement (~5µm), but the force is highly nonlinear and instable within the displacement range. On the other hand, interdigitated comb actuation provides a moderate level of force (~10µN) with resonable displacement (~30µm). Compared with other forms of actuation mechanisms, electrostatic actuation offers fast response time (~1ms) with negligible power consumption and can be easily integrated with electronic control. However, it faces many challenging issues such as low mechanical stability due to pull-in, non-linearity, and a very high actuation voltage (~50V).

1.3.3 Piezoelectric actuation

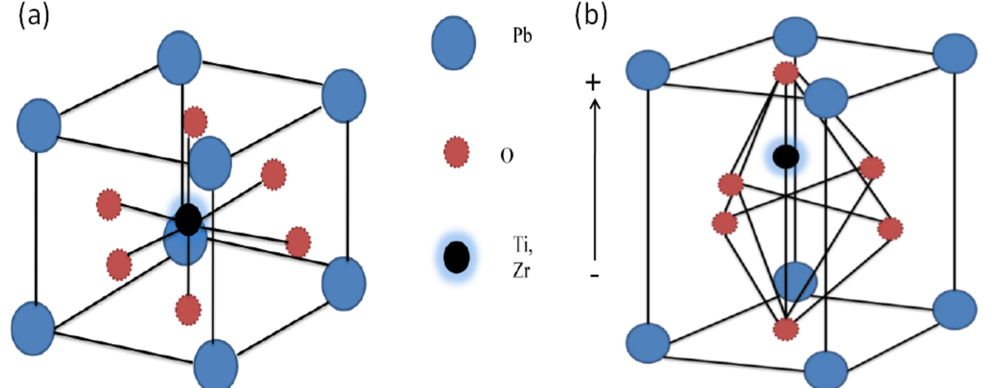

Fig. 1-6. Schematic diagram illustrating the change in perovskite crystal structure (a) before, and (b) after voltage is applied across it.

Piezoelectric effect is understood as the linear electromechanical interaction between the mechanical and the electrical state in a crystalline material. An applied dc voltage across the electrodes of a piezoelectric material will result in a net strain that is proportional to the magnitude of the electric field. A lack of center of symmetry in piezoelectric crystal means that a net movement of positive and negative ions with respect to each other as a result of stress will produce an electric dipole as shown in Fig. 1-6. Adding up

these individual dipoles over the entire crystal gives a net polarization and an effective field within the material. Conversely, a mechanical defomation of the crystal is produced when an electric field is applied, which make this phenomenon extremely useful in driving optical MEMS devices [62, 63].

In general, piezoelectric effect is often described in terms of piezoelectric charge coefficient, d_{ij}, which relates the static voltage or electric field in the *i* direction to displacement of applied force in the *j* direction. When a piezoelectric material is deposited on top of a microstructure, e.g. a Si cantilever, the axes 1 and 3 are defined as longitudinal and normal direction of the cantilever, respectively. The piezoelectric charge coefficients are given as d_{33} when both voltage and force are along the vertical axis (axis 3), while d_{31} when voltage is along the vertical axis but the force generated is along the longitudinal axis (axis 1). The piezoelectric charge coefficient, which is the proportionality constant between strain and electric field, indicates that a higher value of it would be highly desirable for actuation purposes.

Most of the piezoelectric materials have perovskite crystal structure and they include quartz (SiO_2), lithium niobate ($LiNbO_3$), aluminium nitride (AlN), zinc oxide (ZnO) and lead zirconate titanate (PZT), while the most well known polymer based piezoelectric material is polyvinylidene fluoride (PVDF). Among these materials, PZT has the largest piezoelectric charge coefficients (d_{31} and d_{33}) as shown in Table 1-1 [64]. Due to its excellent piezoelectric properties, PZT has often been used in numerous optical MEMS applications such as adaptive optics [65, 66], optical communication [67, 68],

and beam scanning [69-71]. However, unlike AlN, PZT is not CMOS compatible, hence making mass production by CMOS foundries impossible.

Table 1-1. Piezoelectric coefficient of selected piezoelectric materials [64].

Material	Piezoelectric coefficients
Barium titanate	d_{33} = 85.6 pm/V; d_{31} = 34.5 pm/V
Aluminum nitride	d_{33} = 4.5 pm/V
Zinc oxide	d_{33} = 12.4 pm/V
Lead zirconate titanate	d_{33} = 360 pm/V; d_{31} = 180 pm/V
Polyvinylidene fluoride	d_{31} = 20 pm/V; d_{33} = 30 pm/V

1.3.4 Electromagnetic actuation

Lorentz force is generated when a current-carrying element is placed within a magnetic field and it occurs in a direction equivalent to the cross product of the current and magnetic field. Although Lorentz force actuation may be applied to MEMS devices in a number of ways, the prevailing approach is to have metal coils integrated on a micromirror and actuated by an ac current at resonance when the mirror is placed near a permanent magnet [72-77]. Fig. 1-7(a) shows a three-axis actuated micromirrror developed by Cho *et al.*, where actuation coils made of gold are electroplated on the mirror plate and cantilever actuators [76]. Another approach, as shown in Fig. 1.7(b), is to integrate a permanent magnet (hard ferromagnet) or a permalloy layer (soft ferromagnet) on a movable mirror while a Lorentz force is introduced through the interaction between magnetic layer and surrounding ac magnetic field of an external solenoid [78-82]. The availability of permanent magnetic materials that are compatible with MEMS processing is limited and this brings

necessary process development effort. Thus, it is common for the magnetic field to be generated externally, while the discrete and movable electromagnetic actuators often comprise metal coils.

Similar to electrostatic actuation, electromagnetic actuation provides moderate switching speed (~10ms) and low power consumption (~100mW) but the assembly of permanent external magnets and coils make it extremely challenging. Fabricating ferroelectric materials can also be challenging, as these thin films may not be compatible with the standard CMOS processes.

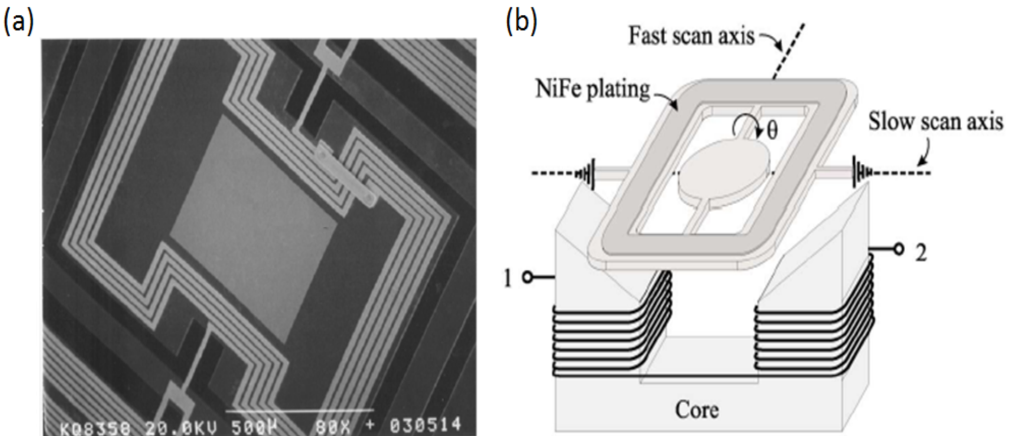

Fig. 1-7. (a) A SEM photo showing the electroplated gold electromagnetic coils on the mirror plate and actuated by ac current at resonance in the presence of permanent magnet [76]. (b) A schematic diagram illustrating a permanent magnetic film integrated on the mirror plate and actuated by the surrounding ac magnetic field [79].

1.4 Actuation Mechanisms

Actuation mechanisms, compared to actuation schemes, often encompass a wider field of considerations such as mechanical structure design, placement of optics, biasing configurations etc. Details of the various types of actuation mechanisms, in relation to 2-D scanning and VOA applications, will be discussed in this section.

1.4.1 MEMS Scanners

A wide variety of actuation mechanisms for MEMS scanners have been reported in literature, with many of them deploying the two frames design for 2-D actuation [55, 74, 81, 83-89]. For example, in the work reported by Jain *et al.,* bi-directional 2-D scanning was performed by fabricating two sets of large vertical displacement thermal actuators on separate frames [83]. The orthogonal orientation of the two sets of actuators results in two perpendicular axes of rotation for the mirror. By biasing both sets of electrothermal actuators with ac voltages simultaneously, Lissajous figures were obtained. Yalcinkaya *et al.* also reported a state-of-the-art MEMS scanner for high resolution displays driven by electromagnetic coils, with full optical deflection angles of 65° and 53° achieved for slow (60 Hz, sawtooth) and fast (21.3 kHz, sinusoid) scanning, respectively [74]. A similar gimbaled MEMS scanner electroplated with ferromagnetic film, as shown in Fig. 1-8(a), was later demonstrated by Tang *et al*. in 2010. This feat was later replicated by Chu *et al.*, where their electrostatic driven MEMS scanner in Fig. 1-8(b) was able to achieve slow and fast scanning at 162 Hz, 14° and 40 kHz, 11.5° respectively in vacuum condition [55].

In the regime of piezoelectric driven MEMS scanners, the research group of Prof. Toshiyoshi from University of Tokyo first demonstrated, in 2005, a double-gimbal MEMS scanner design which composed of two orthogonal pairs of unimorph PZT actuators as shown in Fig. 1.8(c) [69]. The scanner performed large optical deflection angles of 23° (4.3 kHz for X-scan) and 52° (90.3 Hz for Y-scan) at driving voltages of 10-20 V_{ac} with a 5V dc

offset. This effort was followed up in 2007 with a newly developed PZT-meandering actuator that allows angular displacement in a cascaded meandering actuator to be accumulated, as shown in Fig. 1.8(d) [88]. The scanner delivered large static mechanical angle of ±5.6° and ±8.6° for the inner and outer axes, respectively. In the same year, they also demonstrated another MEMS scanner design, as shown in Fig. 1.8(e), obtaining wide range 2-D scan by combining resonant motion for the fast horizontal axis (11.2 kHz, 39° optical deflection angle) and quasi-static operation for the vertical axis (DC ~60 Hz, 29° optical deflection angle). operating at 40 V_{pp} [89].

Apart from the above-mentioned MEMS scanners that deploy gimbaled designs to allow physical decoupling of the two scanning axes, gimbal-less MEMS scanners are also common designs that have been reported in literature [90-95]. Such gimbal-less MEMS mirror designs have 3 degree-of-freedom actuations, including rotations around two axes in the mirror plane, and out-of-plane piston actuation. To overcome mirror plate shift and rotation shift problems, Jia *et al.* designed folded dual S-shaped bimorph actuators as shown in Fig. 1-8(f) to drive the mirror [92]. This MEMS scanner was recently implemented into a miniature optical coherence tomography probe where high resolution 3-D tissue images were obtained [93]. Such tip-tilt-piston MEMS scanner was also demonstrated by Zhu *et al.* on a folded, three-segment piezoelectric actuator design as shown in Fig. 1.8 (g) [95].

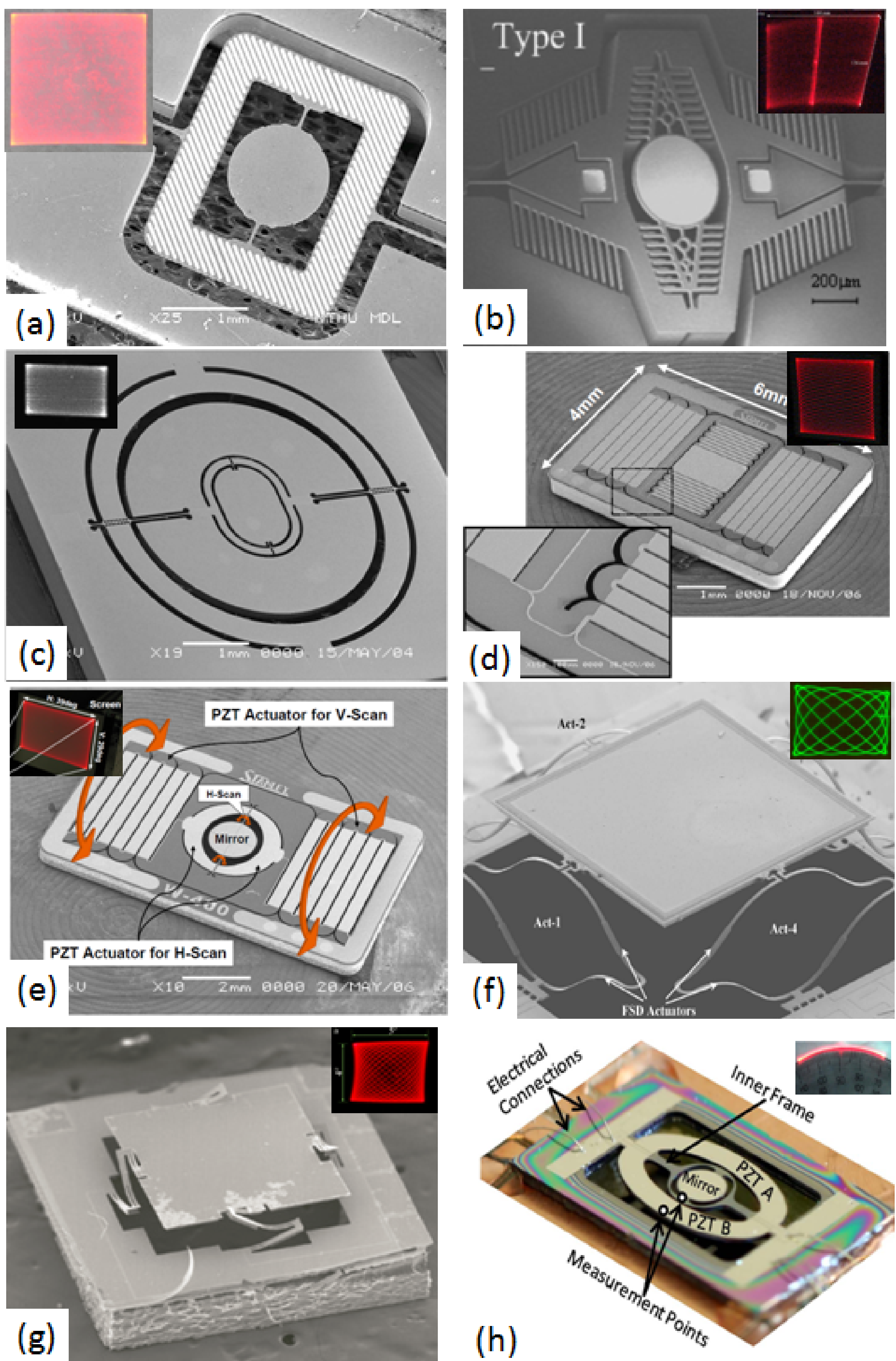

Fig. 1-8. SEM photos of MEMS scanners based on gimbaled, two frame designs driven by (a) electromagnetic [81], (b) staggered vertical electrostatic comb actuators [55], (c)-(e) piezoelectric PZT actuators [69, 89, 96], and (f)-(g) gimbal-less designs driven by folded dual S-shaped electrothermal bimorph [92] and piezoelectric unimorph actuator [95], respectively. (h) Optical microscope photo of a piezoelectric MEMS scanner for high resolution 1-D scanning [71].

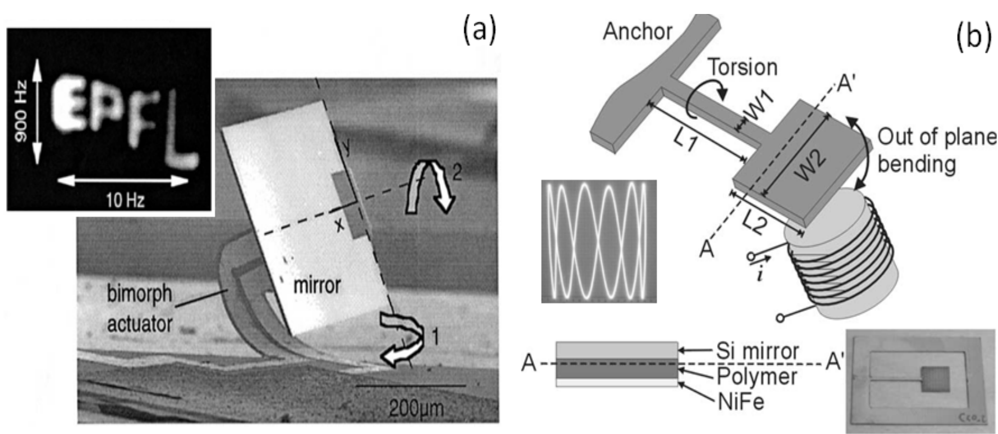

Fig. 1-9. Photos of simple 2-D MEMS mirror designs driven by (a) a L-shaped thermal bimorph cantilever actuator [97], and (b) external coil exciting a mirror plate electroplated with permalloy [98].

Besides gimbaled and gimbal-less MEMS mirror designs, straightforward and compact MEMS mirror designs have also been reported. For example, Schweizer *et al.* developed a L-shaped thermal bimorph cantilever actuated mirror as shown in Fig. 1-9(a), allowing orthogonal angular motion and 2-D scanning to be made possible through a single cantilever actuator [97]. Another similar mirror design illustrated in Fig. 1-9(b) was made by Isikman *et al.*, where magnetic permalloy NiFe was electrodeposited on a mirror plate supported by a straight, narrow cantilever beam [98]. This actuation configuration allows for 2-D scanning by using a single external actuation coil.

The approach of using two single-axis MEMS mirrors to achieve 2-D scanning has also gathered popularity in recent years as the design of the actuation mechanism for the fast and slow scanning axis can now be decoupled, hence allowing the fast scanning MEMS mirror to achieve much better performance in terms of scan rate and optical deflection angle. For example, Arslan *et al.* have successfully demonstrated a torsional comb-driven 1-D MEMS scanner that is able to achieve a 76° total optical deflection angle

at 21.8 kHz, 196 V_{pp} [99]. Similarly, Isamoto *et al.* have also reported an electrostatic 1-D MEMS mirror scanning at 69.7 kHz, with optical deflection angle of 6.5° [100]. More recently, as shown in Fig. 1.8(h), Baran *et al.* developed a resonant 1-D piezoelectric MEMS scanner that operates at 40 kHz, 24 V peak voltage, giving an optical deflection angle of 38.5° [71]. These above-mentioned works demonstrate the feasibility of utilizing mechanical mode amplification to achieve enhanced performance. However, without proper design consideration, these fast scanning devices will suffer from high dynamic mirror deformation.

1.4.2 MEMS Variable Optical Attenuators

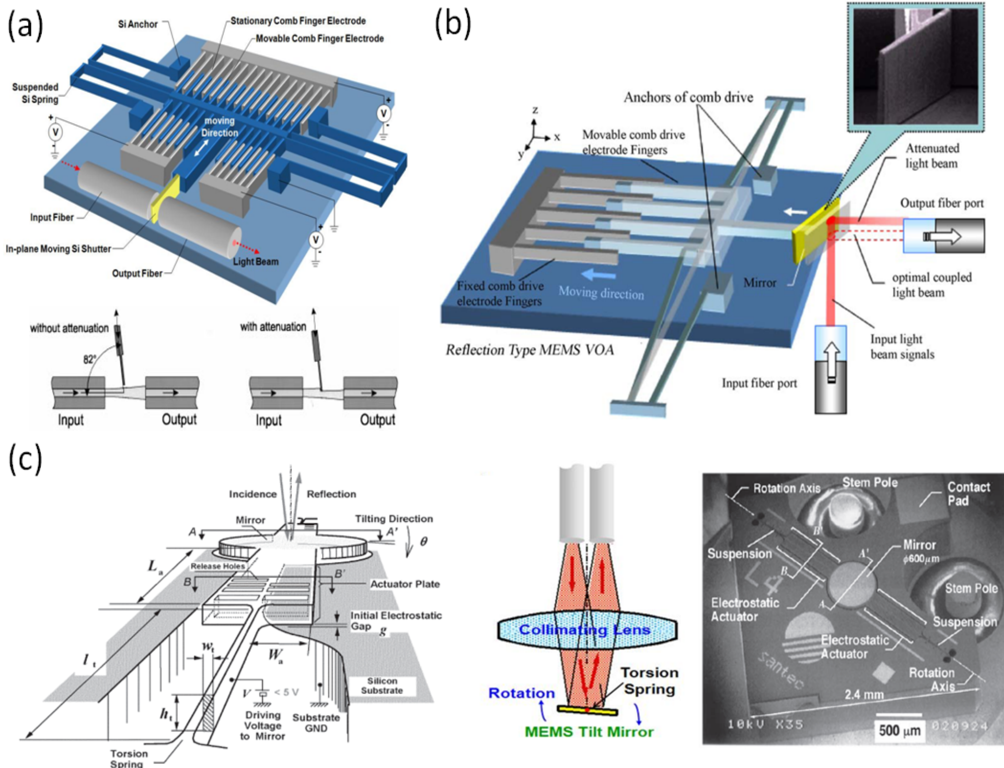

Fig. 1-10. Schematic diagrams illustrating the attenuation principle for various types of MEMS VOAs designs such as (a) shutter type [101], (b) planar reflective type [102], and (c) 3-D reflective type [103].

The first MEMS-based VOAs were demonstrated by two different groups from Lucent Technology. In 1998, Ford and Walker developed a

MEMS VOA using a surface-micromachined silicon nitride suspended membrane with λ/4 optical thickness above a silicon substrate with a fixed 3λ/4 spacing. Voltage applied to electrodes on top of the membrane creates an electrostatic force and pulls the membrane closer to the substrate such that the intensity of reflective light is controlled accordingly [104]. Later in 1999, Barber *et al*. developed a MEMS VOA using a surface-micromachined poly-Si micromirror arranged between ends of two fibers and aligned along the same axis [101]. As illustrated in Fig. 1-10(a), the micromirror functions as a shutter and can move in out-of-plane direction with a given bias due to electrostatic force. The attenuation of this MEMS VOA is determined as a function of the position of micromirror, i.e., the percentage of blocked light.

In addition to the shutter type MEMS VOAs [4, 101, 105-107], there are two more categories of reflective-type MEMS VOAs: planar reflective type and 3-D reflective type. In planar reflective type MEMS VOA shown in Fig. 1-10(b), attenuation is achieved due to the change in coupling efficiency between the input and output fiber when the mirror is actuated. The two commonly adopted designs in these planar type MEMS VOA include using single reflective [49, 102, 108-110] and retro-reflective mirrors [48, 111-113]. With proper design of actuators, a well-optimized DRIE process and appropriate selection of lens fibers, single-reflective-type VOAs performance are superior to that of shutter-type VOAs. General speaking, attenuation scheme based on microshutter design offers the benefits of low insertion loss (IL) and large attenuation range due to the close proximity between the input and output optical fibers. However, it also results in a large polarization dependent loss (PDL) and a strong back reflection due to diffraction and the

coaxial assembly, respectively. On the other hand, the planar reflective type attenuation mechanism offers low PDL and low wavelength dependent loss (WDL), but suffers from high IL due to a certain amount of separation needed for fiber assembly. Combining optics and a reflective mirror to be assembled in a 3-D configuration, as depicted in Fig. 1-10(c), is also a key approach of making MEMS VOA devices [68, 103, 114, 115]. In conjunction with large micro-optics such as dual-core collimators, such 3-D reflective type VOA device can also gain excellent data of return loss, PDL and WDL under reasonable driving voltage.

Besides having two fixed optical fibers optically coupled using MEMS actuators as exemplified by shutter and reflective type MEMS VOAs, research on MEMS VOAs where the optical coupling between a fixed and an initially aligned movable fiber is changed through the use of a microactuator to push the movable fiber are also made [116-118]. Such optical attenuation method requires no additional microoptical elements in the optical path, hence does not introduce PDL and WDL. Unamuno *et al.* first demonstrated an alignment and fixing method for optical fiber based on electrothermal chevron MEMS actuator and curing of adhesive, respectively [117]. This fiber alignment method was further improved by them a year later with a vernier latching mechanism, which allows the VOA device to retain the desired attenuation state without provision of electrical power [118]. Optical power coupled between the two single mode fibers varied from 3.72 dBm to -44dBm, during which the VOA latched in 30 stable positions.

1.5 Objectives of Thesis

This thesis aims to explore various kinds of interesting MEMS mirror designs for 2-D scanning and VOA applications. A wide variety of MEMS scanners based on various actuation schemes have been reported in literature and summarized in section 1.4.1, with most of them deploying either the two frames or/and multi-actuators designs for 2-D actuation. One of the aims in this thesis, therefore, is to explore other kinds of actuation mechanisms that have not been reported previously and integrate them with silicon micromirrors for 2-D scanning illustration. In the case of VOA applications, limited research efforts have been made in 3-D reflective type MEMS VOAs in contrast to the research activities devices that have been widely reported in planar shutter and reflective type MEMS VOA. Thus, in this thesis, new 3-D reflective type MEMS VOAs assembled with optics in a free space configuration and driven by novel actuation mechanisms will also be explored.

With these objectives in mind, four MEMS mirror designs, which are capable of moving in six degree of freedom, have been conceptualized, and fabricated successfully. With the focus on the development of unique actuation mechanisms to drive the MEMS mirror, characterization of the aforementioned designs are made from the application perspective. To reach these goals, the following research tasks are endeavored.

1. To demonstrate novel MEMS scanners designs based on either piezoelectric or hybrid actuation scheme. The fabricated MEMS mirrors seek to exhibit Lissajous scanning patterns, hence illustrating their capabilities for proof-of-concept 2-D scanning applications.

2. To develop low voltage driven 3-D reflective type MEMS VOAs based on either piezoelectric or hybrid actuation schemes and incorporate novel actuation mechanism that involves combination of rotational and translational effects to achieve optical attenuation. These new MEMS VOA designs aim to follow up and strengthen our group's previous successful work in early 2009 where data of a 1-V PZT-driven MEMS VOA were reported for the first time in literature [68].

1.6 Thesis organization

This thesis summarizes the various works on MEMS mirrors for VOA and 2-D scanning applications that were undertaken during the course of my candidature. The content of each chapter in the thesis is as follows:

Chapter 2 presents two MEMS scanner designs, i.e. designs A and B, driven by 1×10 array of piezoelectric PZT beam actuators for 2-D scanning applications. In design A, there are ten PZT beam actuators that are electrically connected in series, with a mirror plate at the end of the actuators. In design B, the dimensions of the device remain the same while the ten PZT beam actuators are electrically isolated instead. Lissajous scanning patterns were obtained by, for example, exciting half of the 1x10 actuators at bending mode while exciting the remaining actuators at torsional mode for design A. In the case of design B, the actuation mechanism to elicit 2-D scanning is different from that of design A.

Chapter 3 discusses on the experimental data obtained for VOA application based on design B in Chapter 2. A dual core fiber collimator was aligned perpendicularly to the mirror in a three-dimensional light attenuation

arrangement. The attenuation curves under DC bias for different operation modes were also investigated.

Chapter 4 provides the third MEMS scanner design i.e., design C, which offers better scanning performance at lower actuation voltage. Instead of using a 1×10 array of PZT actuators to drive the mirror, a single S-shaped PZT actuator is deployed. Various Lissajous scanning patterns were demonstrated by superimposing two ac sinusoidal electrical signals of different frequencies into one signal to be used to actuate the mirror.

Chapter 5 presents a novel hybrid CMOS compatible MEMS scanner based on hybrid actuation mechanism. Both electrothermal and electromagnetic actuations have been integrated in the same device for slow and fast scanning, respectively. Many Lissajous patterns were demonstrated at low power condition, making our proposed actuation design approach suitable for mobile 2-D raster scanning applications powered by batteries with limited capacity.

Chapter 6 further investigates the use of the hybrid-driven MEMS mirrors for VOA application mentioned in Chapter 5. Three types of attenuation mechanisms based on electromagnetic, electhrothermal and hybrid actuations were explored and studied. Our unique design of using both electrothermal and electromagnetic actuators simultaneously to achieve attenuation is the first demonstration of such a hybrid driven CMOS compatible MEMS VOA device.

Finally, the main contributions of this thesis and suggestions for future work are summarized in Chapter 7.

Chapter 2
MEMS Scanners Driven by 1×10 PZT Beam Actuators

2.1 Introduction

MEMS scanners are fundamental components in many optoelectronics applications such as display, microspectroscopy and biomedical imaging. One of the key factors that has contributed to the remarkable MEMS commercial success is the development of Si-based micromachining technology and CMOS MEMS [119]. The integration of micromechanical parts and CMOS circuits has facilitated mass production of MEMS devices in CMOS foundries due to their high production yield and low fabrication cost. However, limited material selection in CMOS MEMS and CMOS compatible processes restrict the Si-based actuators to be mainly electrothermal, electrostatic or electromagnetic [58, 120, 121].

Actuators deploying piezoelectric PZT ($PbZr_XTi_{1-X}O_3$) films are also attractive alternatives to Si-based actuators because of its potential to offer higher output force at lower voltage compared to the other actuators [122-124]. In this chapter, two designs of piezoelectric driven MEMS scanners using mechanical supporting beam integrated with 1x10 PZT actuator array are explored and characterized. In the first design, i.e. design A, there are ten PZT beam actuators that are electrically connected in series, with a mirror plate at the end of the actuators. In the second design, i.e. design B, the dimensions of the device are identical with design A, except that the ten PZT beam actuators

are electrically isolated instead. Through this design variation, we aim to investigate the performance of the PZT MEMS scanners by using different actuation mechanisms to elicit 2-D scanning for both the devices. Although electrothermal bimorph beam actuators have been well characterized in terms of their capability to generate large deflection in bending mode [33, 83, 120], no design of torsional mirror driven by beam actuators has been reported for piezoelectric actuation mechanism yet. As such, our unique piezoelectric beam actuator design is the first demonstration of large torsion mirror using PZT beam actuators.

2.2 Design and Modeling

Schematic diagrams of the piezoelectric MEMS scanners demonstrated in this chapter are shown in Fig. 2-1. In both designs, there are ten patterned PZT thin film actuators arranged in parallel along the longitudinal direction of the scanners. A silicon cantilever beam, derived from the Si device layer of a silicon-on-insulator (SOI) wafer, remains beneath the ten PZT actuators so as to provide mechanical support. In design A shown in Fig. 2-1(a), the PZT actuators are electrically connected in series, with the bottom electrode of each actuator connected to the top electrode of the adjacent actuator. However, in design B shown in Fig. 2-1(b), the electrical connections of the ten PZT actuators are separated from one another.

The equivalent electrical circuits of the 1×10 PZT actuators for both designs A and B are shown in Fig. 2-2(a) and 2-2(b), respectively. Each actuator consists of one top and bottom electrode sandwiching a PZT thin film of 3 μm thickness, i.e. a capacitive structure. In design A, the 1×10 PZT

actuators are ten serial connected capacitors labelled 1-10, with their corresponding bond pads labelled a-k. On the other hand, in the case of design B, the electrical connections of the top and bottom electrodes for each actuator are separated from one another. The dimensions of the scanners for both designs are summarized in Table 2-1.

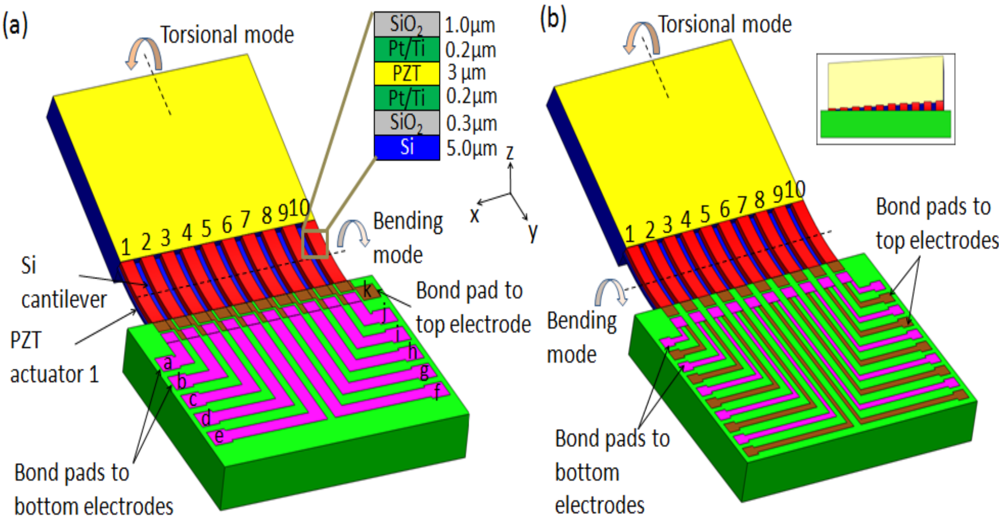

Fig. 2-1. Schematic diagram of the MEMS scanners driven by 1×10 PZT beam actuators for (a) design A, and (b) design B, respectively. In design A, the electrical connections of the PZT beam actuators are connected in series, i.e., the top electrode of one PZT actuator is electrically connected to the bottom electrode of the adjacent actuator. In design B, the electrical connections of the ten PZT actuators are separated. The inset shows an illustration of torsional mode, where the mirror twists about the y-axis.

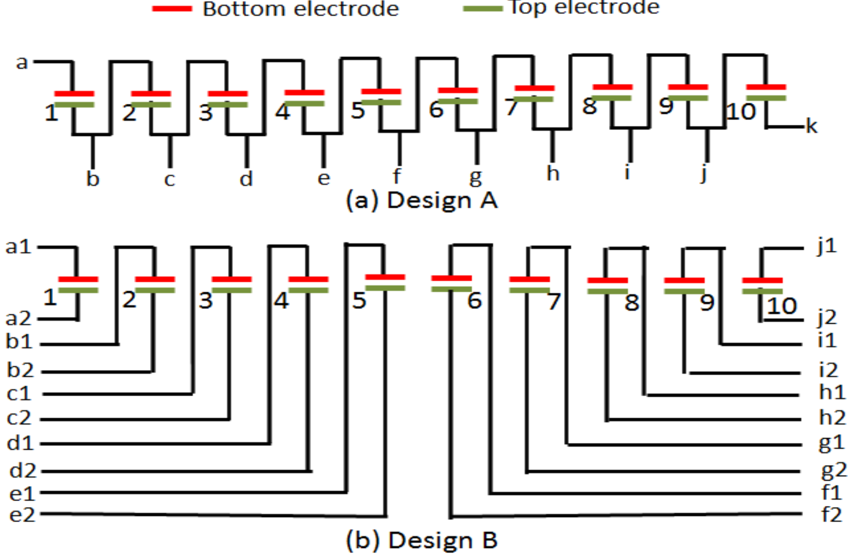

Fig. 2-2. Equivalent circuit of the 1×10 PZT beam actuators labelled 1-10, and their corresponding bond pads for (a) design A, and (b) design B, respectively.

Table 2-1. Dimensions of the MEMS scanners for both designs.

PZT actuators	Si cantilever	Si mirror plate
3 mm long × 0.24mm wide × 3 μm thick	3 mm long × 5 mm wide × 5 μm thick	5 mm long × 5 mm wide × 0.4 mm thick

In design A, the MEMS scanner is designed to drive in three modes: bending, torsional and mixed (or combinational). As shown in Fig. 2-1(a), bending mode occurs when an ac driving voltage corresponding to the resonant frequency for bending mode is applied to the actuators simultaneously. The displacement introduced by the bent actuators under bias causes the mirror to undergo translational and rotational movement about the x-axis, hence achieving horizontal scanning effect when a laser is shone on the mirror surface. In torsional mode, an ac driving voltage corresponding to the resonant frequency for torsional mode is applied to the actuators, causing the mirror to twist about the y-axis. To obtain a 2-D scan, i.e. mixed mode, the ten actuators can be biased such that both bending and torsional modes happen simultaneously, causing the mirror plate to rotate about the x- and y-axis at the same time. This can be done by biasing half of the PZT actuators at resonant frequency corresponding to bending mode, while the other half of them at resonant frequency corresponding to torsional mode.

In the case of design B, the MEMS scanner can also operate in the three modes mentioned previously. Similar to design A, bending mode occurs when an ac driving voltage is applied simultaneously to the actuators in design B. However, in torsional mode operation, design B with the separated electrical connections can, instead, achieve torsional scanning based on the difference in the ac biasing voltage applied individually to the ten PZT

actuators. For example, design B can achieve twisting about the y-axis by biasing actuators 1-5 in such a way that they bend downwards while actuators 6-10 are biased to bend upwards in the opposite direction at resonant condition. This difference in bending directions for the two sets of actuators causes the mirror to twist about the y-axis, achieving vertical scanning effect when ac voltages of varying amplitude are applied to the ten actuators. This actuation mechanism differs from that of design A in torsional mode. As such, besides depending on the resonance phenomenon for torsional scanning, the difference in the direction of actuator displacement due to 180° phase difference in the applied bias also helps to magnify the torsional scanning of the mirror. To obtain a 2-D scan with design B, the ten actuators are biased such that both bending and torsional modes happen simultaneously. Details of the biasing configuration and actuation mechanisms for both designs A and B will be described later in the chapter.

Modal analysis by finite element software, ABAQUS, was done to explore the different mode shapes of the MEMS scanners at different harmonic frequencies. A model based on the dimensions of the scanner was built in the software. The model was assumed to be made entirely of silicon as it has been calculated that silicon contributes 99.3% of the mass of the MEMS scanner, as compared with PZT which only contributes 0.6%. The input parameters and values in bracket for silicon is Poisson ratio (0.28), mass density (2330 kg/m^3) and Young's modulus (167 GPa) [125, 126]. A homogenous solid with isotropic elasticity was chosen. An encastre boundary condition was implemented on the fixed end of the silicon cantilever. Simulation results from Fig. 2-3 have demonstrated that our 1×10 actuator

array design is able to have multiple resonant modes with all six degrees of freedom in three-dimensional space. The 1st and 2nd bending modes were obtained at 6Hz and 33Hz, respectively, while the 1st and 2nd torsional modes were obtained at 121Hz and 204Hz, respectively.

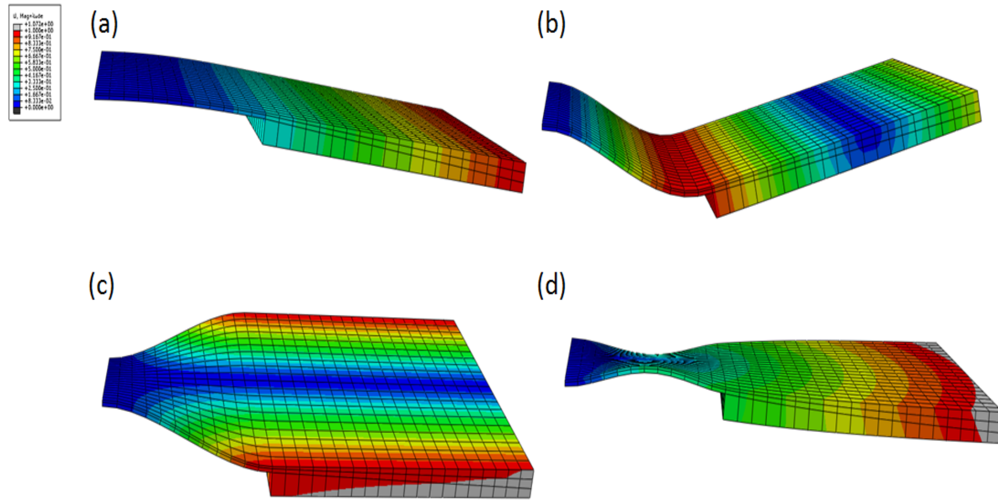

Fig. 2-3. Modal analysis of the MEMS scanner using finite element software ABAQUS. (a) 1st bending mode at 6Hz. (b) 2nd bending mode at 33Hz. (c) 1st torsional mode at 121Hz. (d) 2nd torsional mode at 204Hz.

2.3 Device Microfabrication

Fig. 2-4 shows the microfabrication process flow of the MEMS scanners. A SOI wafer with 5-μm thick Si device layer, 1-μm-thick buried oxide (BOX) and 725-μm-thick Si handle layer was used as the starting material for the device. A thermal oxide layer of 0.37 μm was formed from the Si device layer surface. Pt/Ti layers were deposited by sputtering to form the bottom electrodes, followed by deposition of 3 μm PZT thin film by sol-gel process. The PZT film deposited has a (100)-orientated columnar structure, which helps to maximize the dielectric constant and electrical properties of the PZT film [127]. Finally, the top electrode was formed from multilayered

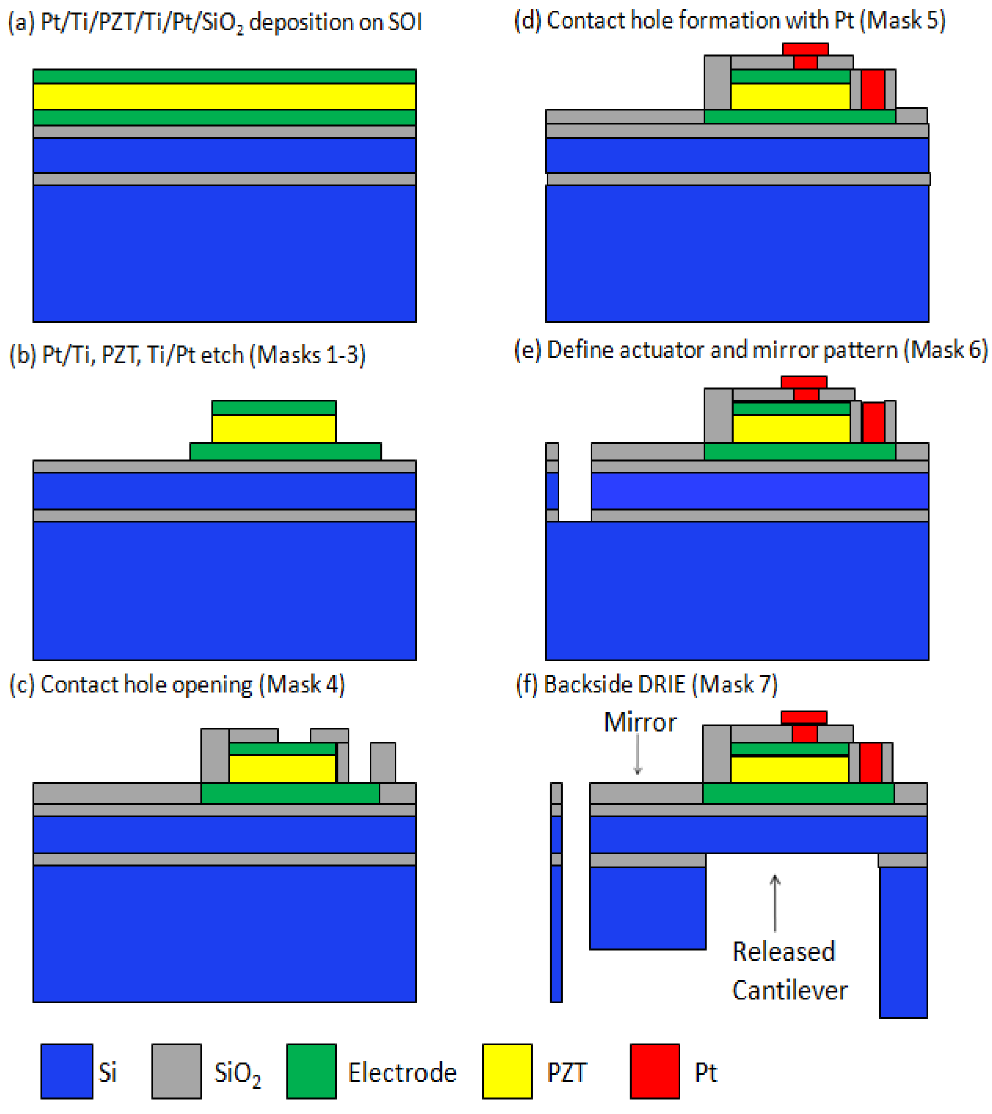

Fig. 2-4. Microfabrication process flow for making the devices.

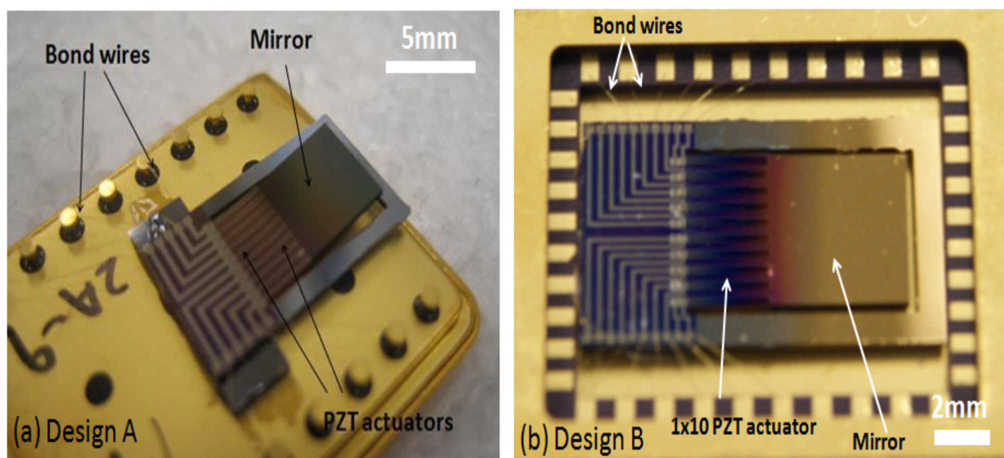

Fig. 2-5. Magnified photos showing the packaged MEMS scanners for (a) design A, and (b) design B, respectively.

deposition of Ti/Pt by sputtering. The deposited films were then pyrolyzed at 200-470°C for five minutes and crystallized by rapid thermal annealing at 700°C for two minutes. Pt was used due to its high stability in the processing temperature range. In Fig. 2-4(b), the top and bottom multilayered electrodes were etched away by Ar ion while the PZT thin film were wet-etched away using a mixture of HNO_3, HF and HCl. In Fig. 2-4(c), a 0.8-μm-thick oxide layer was deposited by RF-magnetron sputtering to serve as insulation. Contact holes etching were done by reactive ion etching (RIE) with CHF_3 gas. In Fig. 2-4(d), Pt wire of 1 μm with Ti adhesion was deposited by RF-magnetron sputtering and later etched by Ar ion. In Fig. 2-4(e), the thermal oxide, structural Si and BOX were etched by RIE using CHF_3 gas (SiO_2) and SF_6 gas (Si) to open the area of cantilever and mirror. Finally, in Fig. 3(f), the silicon substrate and BOX were etched from the backside to release the mirror and the cantilever. A thick Si plate of 400 μm remained beneath the mirror to maintain the rigidity and flatness of the mirror.

After the fabrication process, the MEMS scanners for both designs were bonded onto different metal packages and the bond pads were connected by gold wire to the metal pins of the packages as shown in Fig. 2-5(a) and 2-5(b), respectively. Fig. 2-6 shows the optical microscope photos for the various structures of both designs. Fig. 2-6(a) illustrates the serial connection of the PZT actuators in design A, where the top electrode of a PZT actuator is connected to the bottom electrode of the adjacent actuator, while Fig. 2-6(b) depicts the bond pads being connected to the bottom electrodes of their respective actuators. In Fig. 2-6(c), the PZT actuators are electrically isolated from one another for design B, while the bond pads are connected to either the

top or bottom electrode of the actuators as shown in Fig. 2-6(d). Fig. 2-6(e) and 2-6(f) show the 1×10 PZT actuators fabricated in parallel on top of a Si cantilever and the Si mirror surface, respectively.

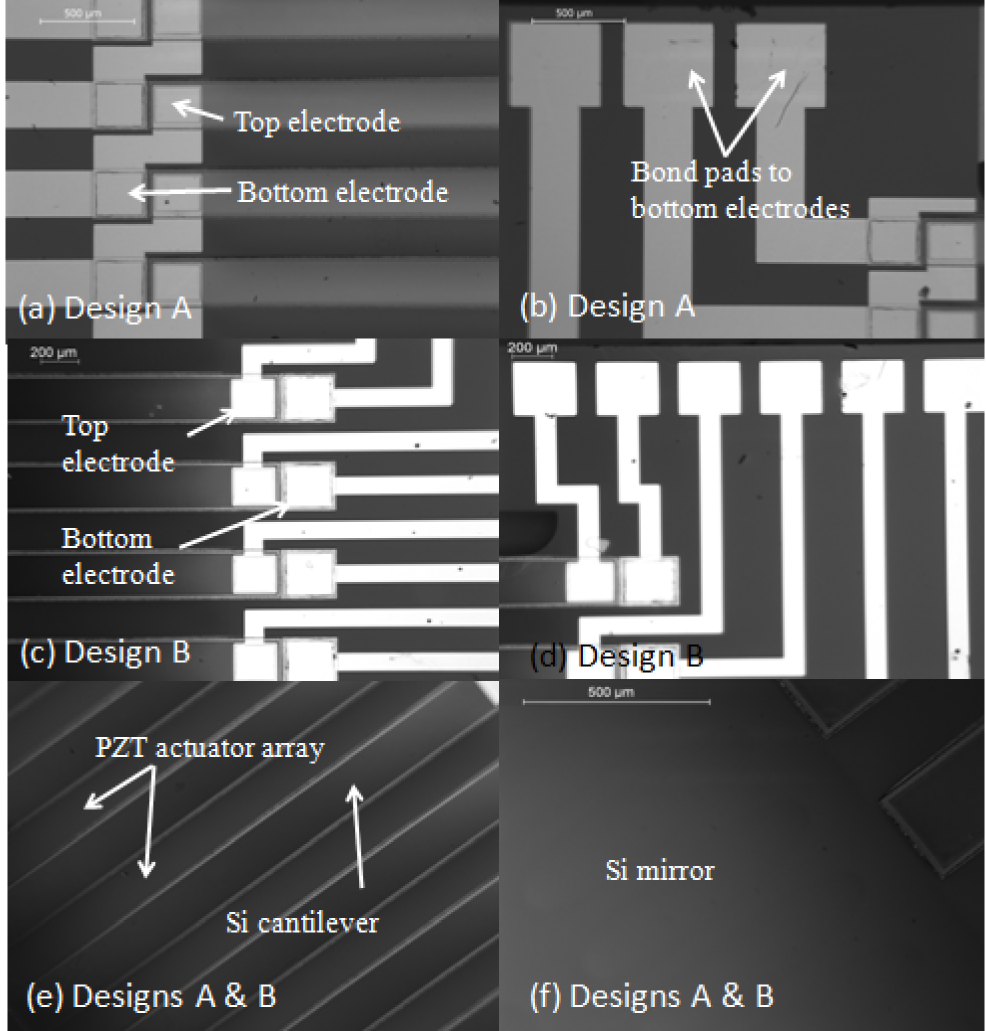

Fig. 2-6. Optical microscopes photos of (a) PZT actuators connected in series for design A, where the top electrode of a PZT actuator is connected to the bottom electrode of the adjacent actuator, (b) bond pads connected to the bottom electrodes of their respective actuators for design A, (c) PZT actuators that are electrically isolated from one another for design B, (d) bond pads connected to either the top or bottom electrode of the actuators for design B, (e) PZT actuators fabricated in parallel on top of a Si cantilever, and (f) Si mirror surface.

2.4 Experimental Setup

The schematic diagram of the experimental setup used to characterize the MEMS scanners is illustrated in Fig. 2-7. A He/Ne red laser source of wavelength 632.8nm is used. The incident light from the laser source located

at the left hand side of Fig. 2-7 is reflected by the mirror and propagates toward the screen on the right side with an optical deflection angle (ODA) of 2θ, where θ denotes the mechanical deflection angle. The screen is placed and fixed perpendicularly to the reflected light when the mirror is initially unbiased. When the actuators are driven in ac mode, a mechanical deflection angle of ±θ is introduced to the mirror. The resulted reflected light will be deviated from the original light path with an angle of ±2θ and the light spot on the screen will be shifted by a distance ±L. The value of θ can then be derived from the measured L and the known distance H, where H is the distance of the screen from the mirror. To enhance the piezoelectric characteristic of the actuators, poling treatment was done prior to the experiment at room temperature. A dc voltage of 25V, which is equivalent to a polarization electric field of 83kV/cm, was applied to each of the PZT actuators for 5 minutes, with the poling direction from the bottom electrode to top electrode. This allows the electric dipoles in the PZT film to be aligned in the same direction.

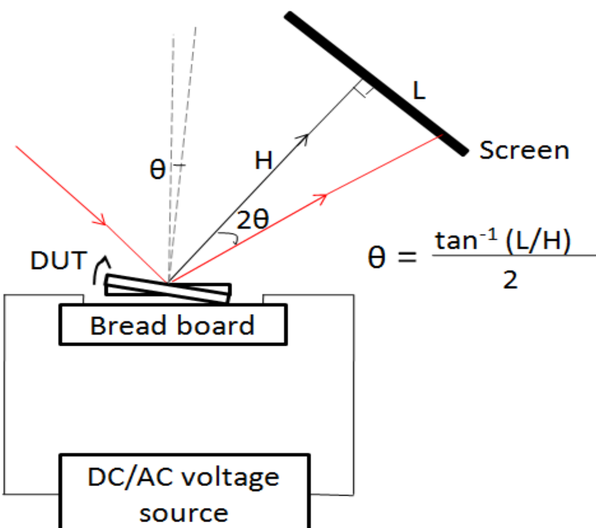

Fig. 2-7. Schematic drawing of the experimental setup for measuring the mirror deflection angle when the MEMS scanners are driven under ac actuation voltages.

2.5 Results and Discussion

2.5.1 Bending mode operation

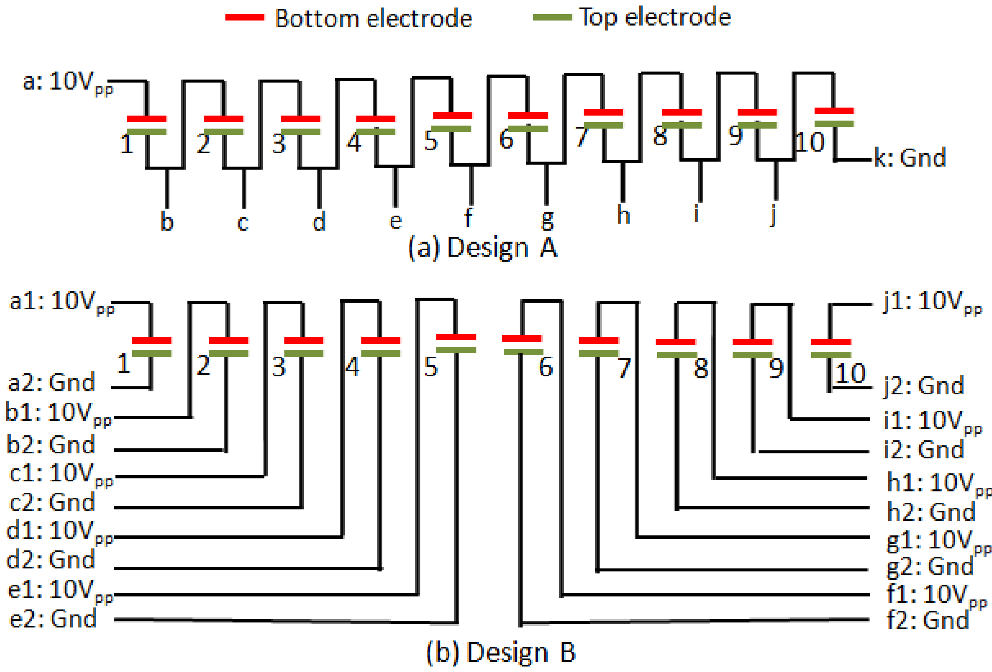

Fig. 2-8. Biasing configuration during bending mode operation for (a) design A, where an ac voltage of, for example, $10V_{pp}$, was applied to the ten serially connected PZT actuators, and (b) design B, where an ac voltage of, for example, $10V_{pp}$, was applied to the ten PZT actuators individually.

In the bending mode operation of the PZT MEMS scanners, sinusoidal ac voltages were applied according to the biasing configurations shown in Fig. 2-8(a) and 2-8(b) for designs A and B, respectively. In design A, an ac voltage was applied to bond pad "a" using a function generator (Agilent 33120A function waveform generator), while bond pad "k" was grounded. This results in the voltage applied by the function generator to be divided equally among the ten serially connected PZT actuators. In the case of design B, ac voltages were applied individually and simultaneously to all the bottom electrodes of the actuators, while the top electrodes were all grounded.

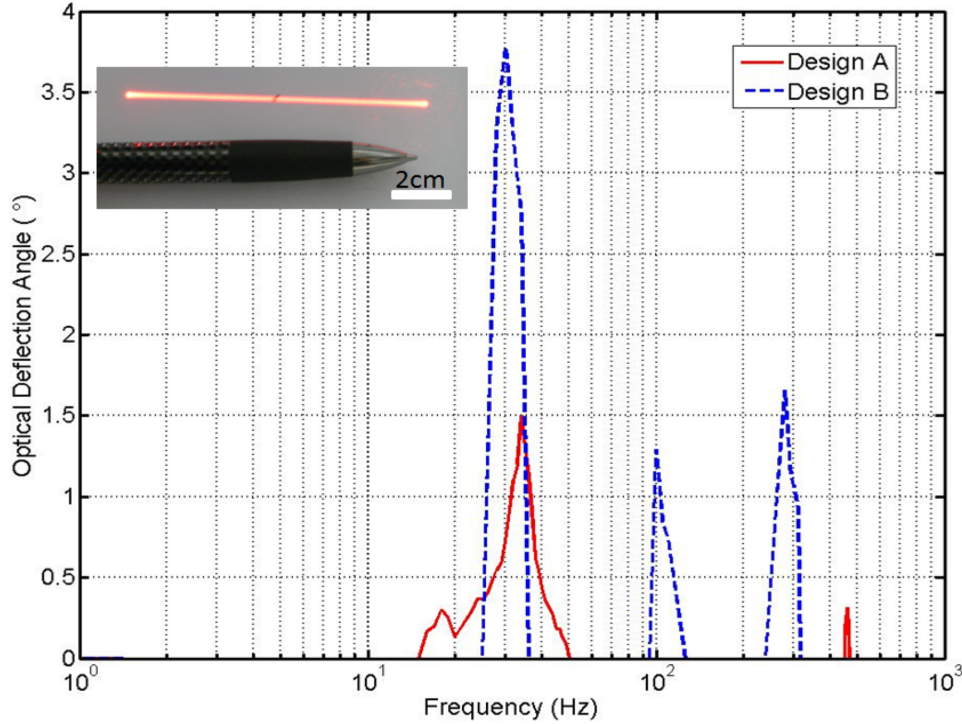

Fig. 2-9. Frequency response during bending mode operation for (a) Design A, where $10V_{pp}$ was applied to the ten serially connected PZT actuators, and (b) Design B, where $5V_{pp}$ was applied simultaneously to all the ten actuators individually. The inset shows an example of a horizontal scanning trajectory obtained for design A.

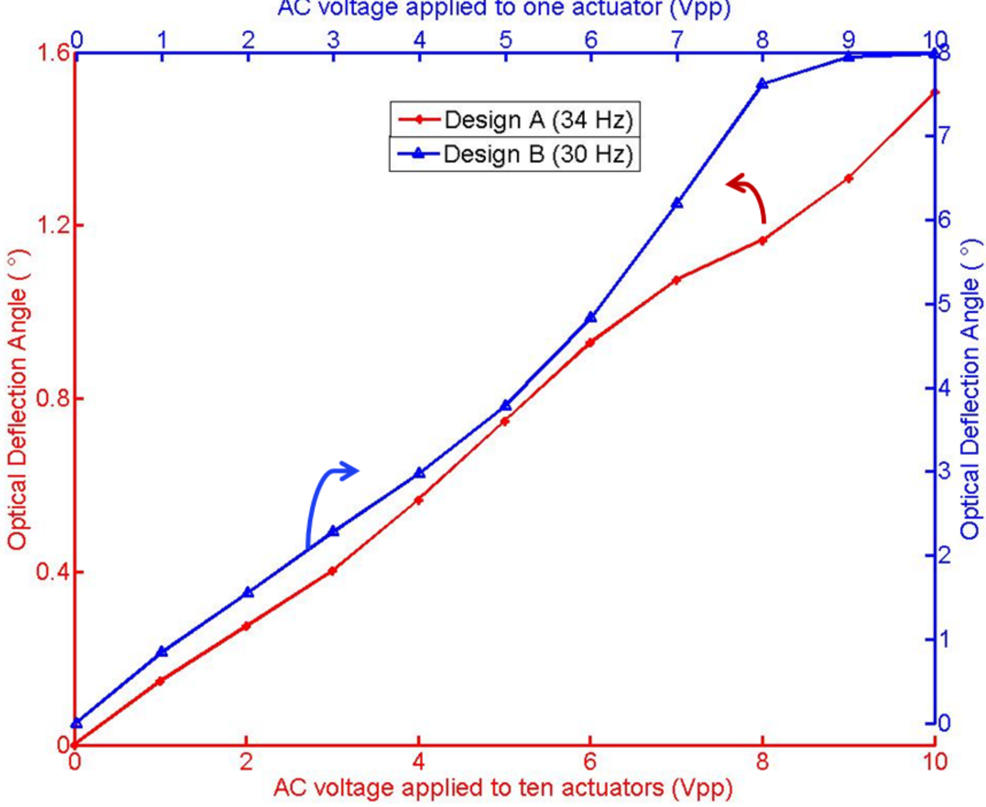

Fig. 2-10. AC response during bending mode operation for designs A and B. In design A, ac voltages at 34 Hz were applied to the ten PZT actuators, while in design B, ac voltages at 30 Hz were applied to the ten PZT actuators individually.

The frequency response spectra for both designs A and B are shown in Fig. 2-9. The voltages applied to both MEMS scanners were kept constant, while frequency sweeps from 1 Hz to 1 kHz were used to excite both of them. In design A, 10 V_{pp} was applied to the ten serially connected actuators, i.e. 1 V_{pp} across each actuator, while in design B, 5 V_{pp} was applied simultaneously to the ten individually connected actuators. A red He/Ne laser was shone on the mirror surface, forming a horizontal scan line trajectory on the screen, as illustrated in the inset of Fig. 2-9. ODAs at different frequencies of the ac signal were calculated using the horizontal scanned beam length and the distance between the micromirrors and the screen. Major ODA peaks of ±1.5° and ±3.8° were obtained at 34 Hz and 30 Hz for design A and B, respectively. These experimental resonant frequencies obtained correspond closely to the eigenfrequency of 33 Hz simulated by ABAQUS. In addition, the Q-factors for designs A and B were derived to be 6 and 5, respectively. The low Q-factors are mainly caused by the large mass inertia of the mirror plates in both designs.

Fig. 2-10 shows the ac response during bending mode for both designs. In design A, ac voltages from 1 V_{pp} to 10 V_{pp} at 34 Hz were applied to the ten PZT actuators, while in design B, ac voltages at 30 Hz were applied individually to all the ten PZT actuators. When the MEMS scanners were biased at their respective resonant frequency, the ODA increased rather linearly with increasing ac voltage, with the ODA for design B reaching saturation for voltages above 8 V_{pp}. ODAs of ±1.5° and ±8° were obtained when ac voltages of 10 V_{pp} were applied to design A and B, respectively. For the same applied voltage, a higher ODA was obtained for design B compared

to design A. This is due to the difference in the electrical connections of the two designs, where the ten actuators in design A shared the voltage applied by the function generator, while this same voltage applied by the function generator was uniform across all the ten actuators for design B. This resulted in a higher voltage applied across each of the PZT actuators in design B compared to design A, even though the voltage output from the function generator were the same for both designs. This gave rise to larger displacements for the ten electrically isolated PZT actuators and, hence larger ODA for design B.

2.5.2 Torsional mode operation

Fig. 2-11(a) and 2-11(b) illustrate the bias configurations needed for torsional mode operation in both designs A and B, respectively. The bias configurations for bending and torsional mode operations in design A are identical, while a more complex bias configuration for torsional mode is adopted in design B. As shown in Fig. 2-11(c), a potential divider was implemented to split the ac output of the function generator into five equal potential at the potential nodes between each resistors. The potential divider was realized using five equal resistors of resistance 20Ω connected in series with one another. For the set of actuators 1-5, the bottom electrodes for these actuators were connected to the various potential nodes while the top electrodes of these actuators are grounded. The reverse setup was made for the set of actuators 6-10, i.e. the bottom electrodes for these actuators were grounded while the top electrodes were connected to the various potential nodes. As a result, each actuator will have different ac bias amplitude, as

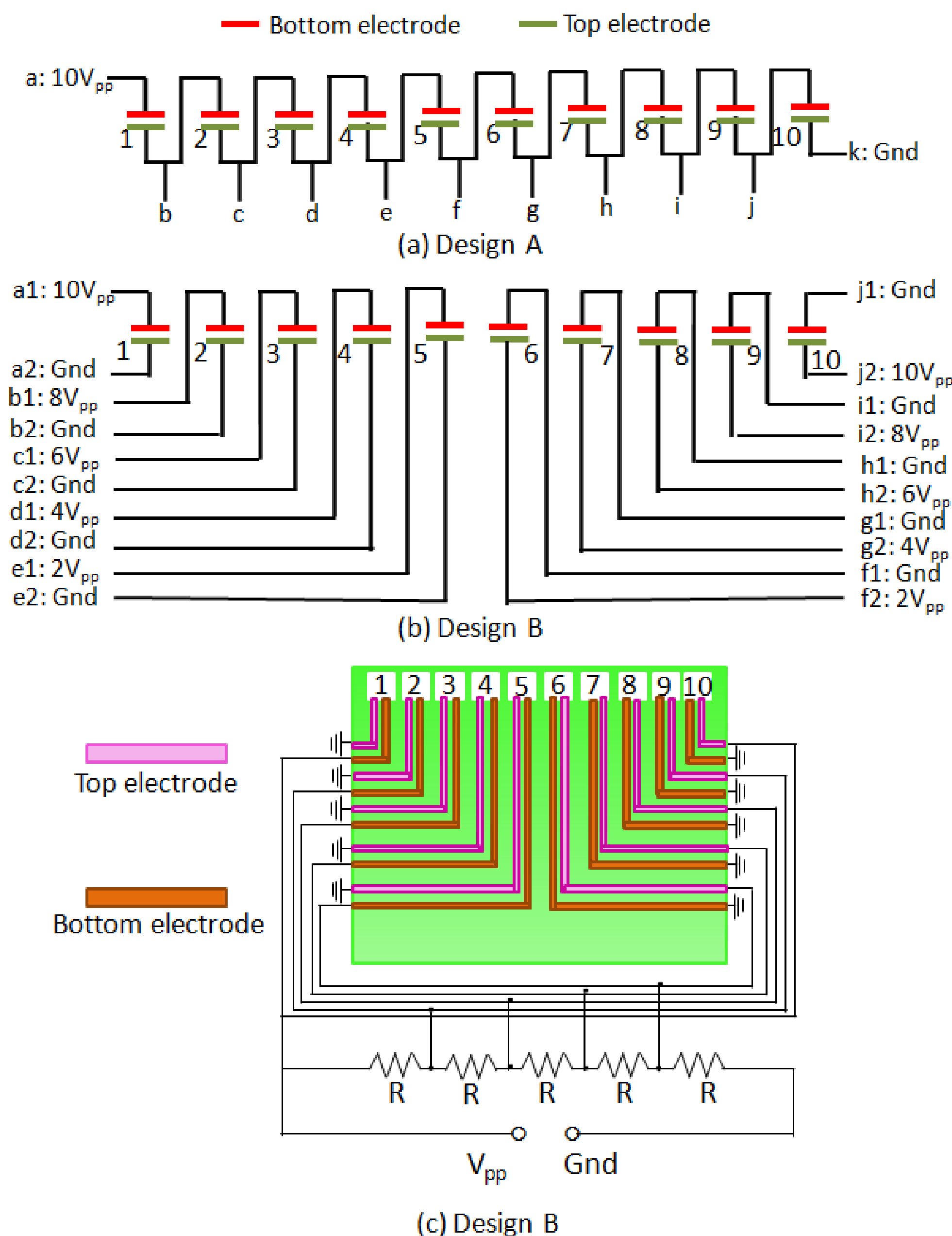

Fig. 2-11. Biasing configuration during torsional mode operation for (a) design A, where an ac voltage of, for example, $10V_{pp}$, was applied to the ten serially connected PZT actuators, and (b) design B, where an ac voltage of, for example, $10V_{pp}$, was applied to PZT actuators 1 and 10, while the rest of the actuators were biased at gradually lower V_{pp} values. For actuators 1-5, the biases were applied to the bottom electrodes, while the top electrodes were grounded. In the case of actuators 6-10, the biases were applied to the top electrodes, while the bottom electrodes were grounded. (c) Schematic diagram showing the implementation of the potential divider circuit for design B, where the ac output of the function generator is split into five equal electric potentials.

evident from Fig. 2-11(b). Such a biasing configuration for design B will cause the largest and the smallest actuator displacements to be introduced at the mirror edges and center, respectively. More importantly, the generated

displacements for these two sets of actuators are toward opposite directions, resulting in torsional movement of the mirror plate.

Fig. 2-12 shows the frequency response obtained for both designs A and B during torsional mode operation. The ac voltage output applied to both the MEMS scanners from the function generator were kept constant, while frequency sweeps from 1 Hz to 1 kHz were used to excite both of them. In design A, 10 V_{pp} was applied to the ten serially connected actuators, i.e. 1 V_{pp} across each actuator, while in design B, 5 V_{pp} was applied to the first and tenth actuators, with the rest of the actuators being biased at gradual decreasing values. A red He/Ne laser was shone on the mirror surface, forming a vertical scan line trajectory on the screen, as illustrated in the inset of Fig. 2-12. Major ODA peaks of ±0.5° and ±4.1° were obtained at 198 Hz and 89 Hz for designs A and B, respectively. These experimental resonant frequencies obtained correspond closely to the eigenfrequencies of 204 Hz and 121 Hz simulated by ABAQUS. In addition, the Q-factors for devices A and B were derived to be 66 and 8, respectively.

Fig. 2-13 shows the ac response during torsional mode operation for both designs. In design A, ac voltages from 1 V_{pp} to 10 V_{pp} at 198 Hz were applied, while in design B, ac voltages at 89 Hz were applied to the bias configurations described earlier in Fig. 2-11. When the MEMS scanners were biased at their respective resonant frequency, the ODA increased with increasing ac voltage, with the ODA for design B reaching saturation at 5 V_{pp}. ODAs of ±4.5° and ± 0.5° were obtained when ac voltages of 10 V_{pp} were applied to design A and B, respectively. For the same output voltage from the

function generator, a higher ODA was obtained for design B compared to design A. This is due to the difference in the electrical connections of the two designs, where the ten actuators in design A shared the voltage applied by the function generator, while this same voltage applied by the function generator

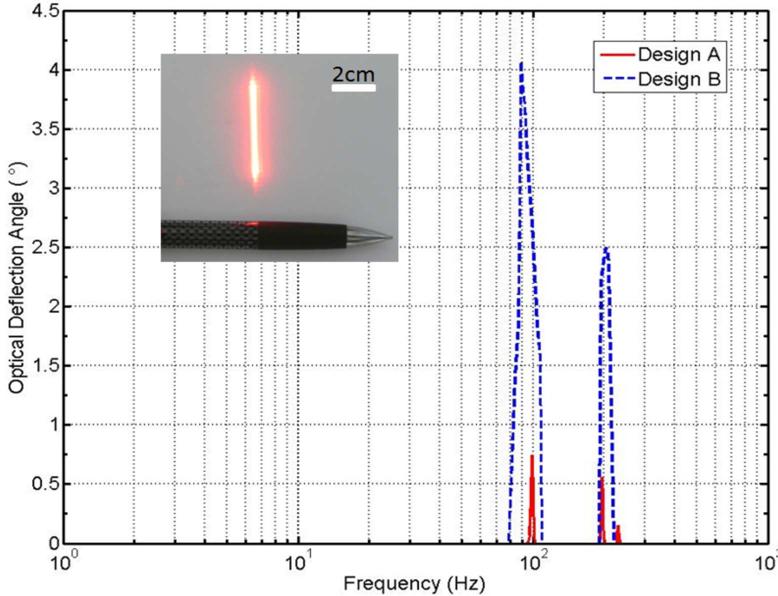

Fig. 2-12. Frequency response during torsional mode operation for (a) Design A, where $10V_{pp}$ was applied to the ten serially connected PZT actuators, and (b) Design B, where $5V_{pp}$ was applied to the first and tenth actuator. The inset shows an example of a vertical scanning trajectory obtained for design A obtained.

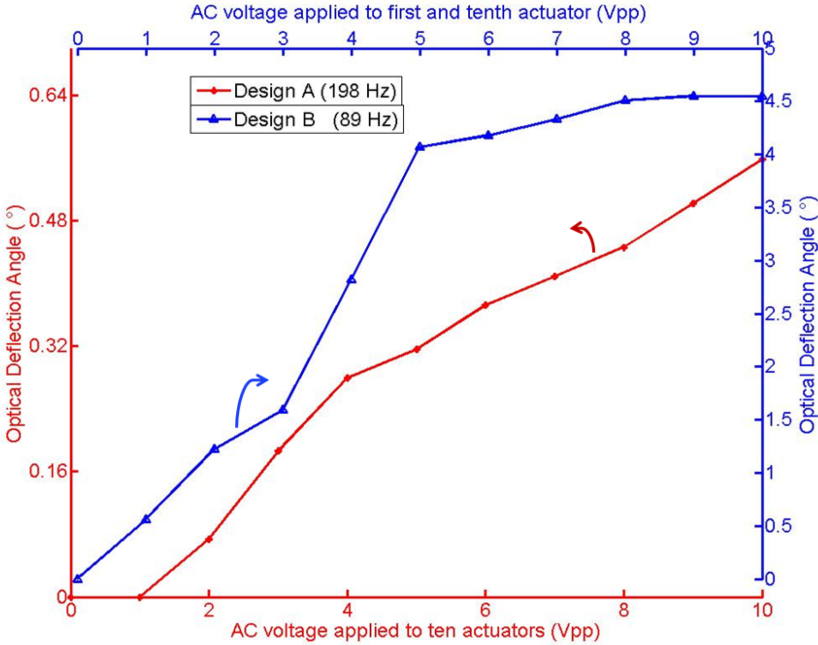

Fig. 2-13. AC response during torsional mode operation for designs A and B. In design A, ac voltages at 198 Hz were applied to the ten PZT actuators, while in design B, ac voltages of different values at 89 Hz were applied to the PZT actuators.

was gradually decreased using a potential divider in design B. This resulted in a higher voltage applied across each of the PZT actuators in design B compared to design A, even though the voltage output from the function generator were the same for both designs. More importantly, besides depending on the resonance phenomenon for torsional scanning (in the case of design A), the difference in the direction of actuator displacement due to the 180° phase difference in the applied bias also helps to magnify the torsional scanning of the mirror in design B.

2.5.3 Mixed mode operation

In mixed (or combinational) mode operation, bending and torsional actuations happen simultaneously to produce 2-D scanning pattern. Two function generators are needed to bias separately the two different sets of actuators responsible for bending and torsional mode, respectively. Fig. 2-14(a) and 2-14(b) illustrate the biasing configurations during mixed mode operation for designs A and B, respectively, while Fig. 2-14(c) shows the external electrical circuit required for mixed mode operation in design B. To elicit 2-D scanning in design A, actuators 1-5 were excited at resonant frequency corresponding to torsional mode (198 Hz), while actuators 6-10 were excited at resonant frequency corresponding to bending mode (34 Hz). In the case of design B, sinusoidal ac voltage of 30 Hz from the first function generator, V_B, was applied simultaneously to all the top electrodes of the actuators 4-7, while the bottom electrodes of these actuators were grounded. The ac output of 89 Hz from the second function generator, V_T, was split by a potential divider into three equal potential at the potential nodes between each resistor. For the set of actuators 1-3, the top electrodes for these actuators were

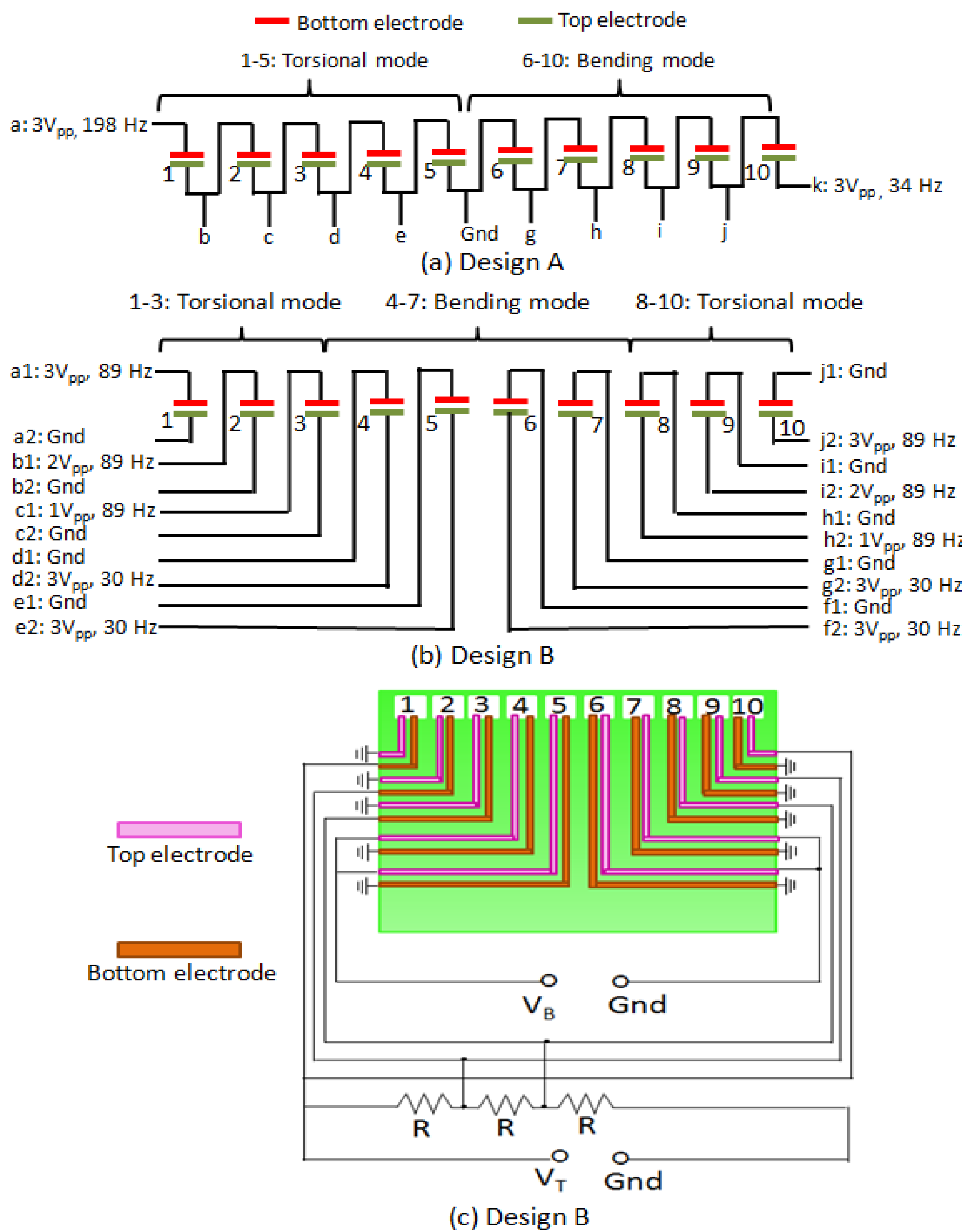

Fig. 2-14. Biasing configuration during mixed mode operation for (a) design A, where an ac voltage of, for example, 3V$_{pp}$, at 34 Hz was applied to the PZT actuators 1-5 for bending mode, while 3V$_{pp}$, at 198 Hz, was applied to the PZT actuators 6-10 for torsional mode, and (b) design B, where an ac voltage of, for example, 3V$_{pp}$, at 89 Hz was applied to PZT actuators 1-3 and 8-10 for torsional mode, while 3V$_{pp}$, at 30 Hz was applied to the PZT actuators 4-7 for bending mode. For actuators 1-3, the biases were applied to the bottom electrodes, while the top electrodes were grounded. In the case of actuators 8-10, the biases were applied to the top electrodes, while the bottom electrodes were grounded. (c) Schematic diagram showing the external electrical circuit required for mixed mode operation for design B.

connected to the various potential nodes while the bottom electrodes of these actuators were grounded. The reverse setup was made for the set of actuators 8-10. As a result, the generated displacement for the actuators 1-3 and 8-10

were toward opposite directions, resulting in torsional rotation of the mirror plate.

Fig. 2-15(a) and 2-15(b) show the ac responses for designs A and B, respectively. In design A, ODAs of approximately ±3° and ±0.5° were obtained when a 10 V_{pp} bias were applied to actuators 6-10 and 1-5 for bending mode and torsional mode actuations, respectively. For the same V_{pp}, the ODA derived from bending actuation during mixed mode operation was greater than that during bending mode operation. This is due to the voltage output from the function generator being shared among ten actuators during bending mode operation, while in mixed mode operation, the same voltage output was shared among five actuators only. This resulted in each actuator during mixed mode operation receiving a greater voltage bias compared to the actuators during bending mode operation, hence producing a larger deflection angle.

Fig. 2-15(b) shows the measured ODA obtained for design B during mixed mode operation under various ac voltages applied to the two sets of actuators 4-7 and 1-3, 8-10 operating in bending and torsional actuations, respectively. An ODA of ±2.2° was obtained when a 10 V_{pp} bias was applied to actuators 4-7 for bending mode actuation. This value obtained is much smaller when compared to that of ±8° obtained when all ten actuators were biased at 10 V_{pp}. This decrease in ODA is expected as the number of actuators involved in actuating the mirror is lowered from ten to four. In torsional actuation, an ODA of ±1.5° was obtained when 10 V_{pp} was applied by the second function generator.

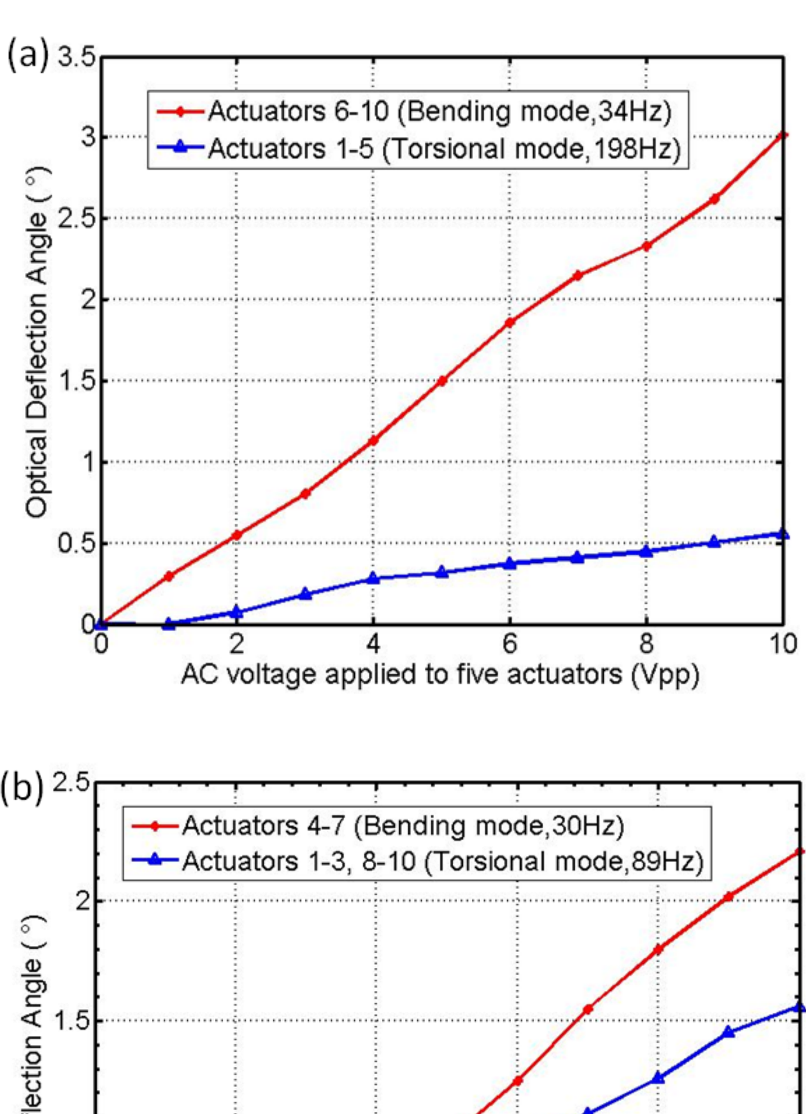

Fig. 2-15. AC response during mixed mode operation for (a) design A and, (b) design B.

Two-dimensional scanning patterns based on both designs were demonstrated during mixed mode operation by adopting the bias configuration shown in Fig. 2-14. Fig. 2-16(a) shows the Lissajous scanning pattern obtained from design A during resonance mixed mode operation, with actuators 6-10 biased at 6 V_{pp}, 34 Hz and actuators 1-5 biased at 10 V_{pp}, 198 Hz. Fig. 3-11(b)

shows another Lissajous pattern obtained from design B, with actuators 4-7 biased at 6 V_{pp}, 34 Hz and actuators 1-5 biased at 10 V_{pp}, 198 Hz.

(a) Actuators 6-10: 6V_{pp},34Hz (Bending mode)
Actuators 1-5: 10V_{pp}, 198Hz, (Torsional mode)

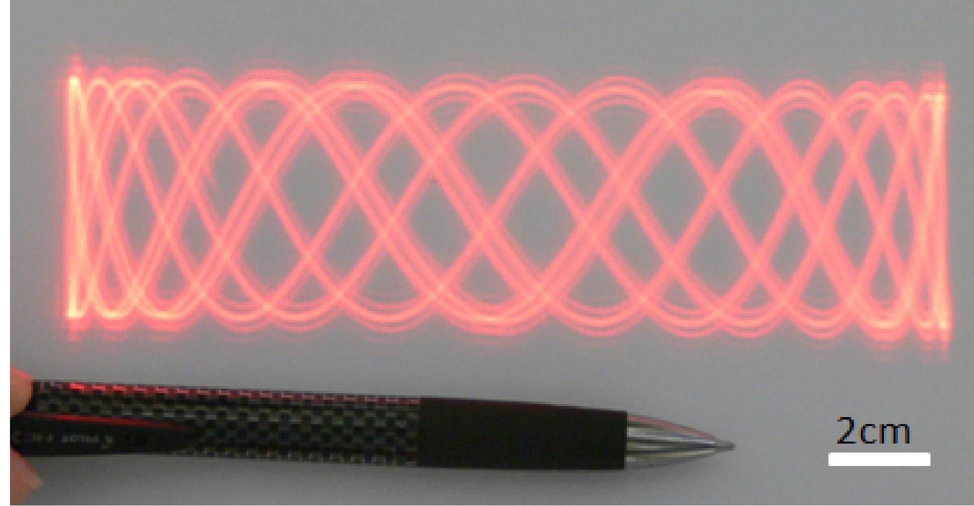

(b) Actuators 4-7: 10V_{pp}, 30Hz (Bending mode)
Actuators 1-3, 8-10: 5V_{pp}, 89Hz (Torsional mode)

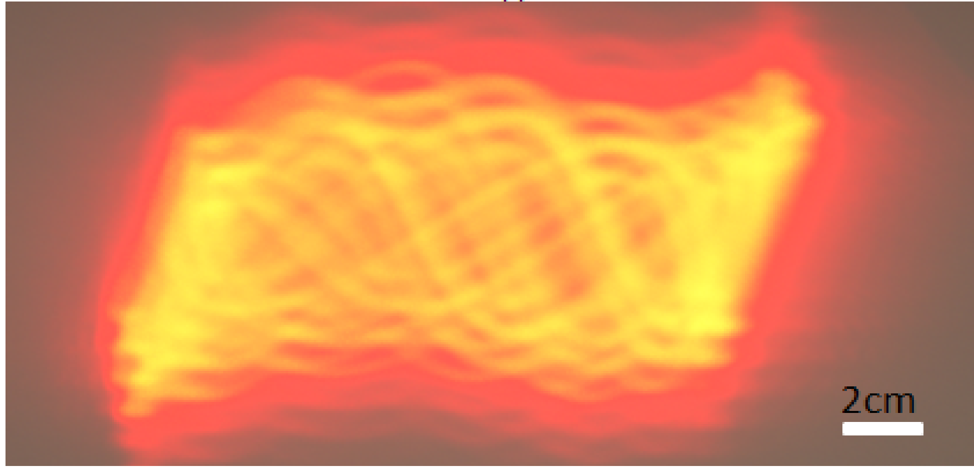

Fig. 2-16. Lissajous scan patterns obtained during mixed mode operation for (a) design A and, (b) design B

Table 2-2 Comparison of designs A and B

.		**Design A**	**Design B**
Design		Actuators are electrically connected in series	Actuators are not electrically connected.
Bending mode	Actuation Mechanism	Bias the actuators at 34Hz. The bias on each actuator is equal and is a fraction of the V_{pp} supplied by function generator as the actuators are electrically connected in series	Bias the actuators individually at 30Hz and V_{pp}. The bias on each actuator is V_{pp}.
	Performance	Actuators 1-10: ±1.5°, with 1V_{pp} bias on each actuator	Actuators 1-10: ±1°, with 1V_{pp} bias on each actuator
Torsional mode	Actuation Mechanism		
	Performance	Actuators 1-10: ±0.5°, with 1V_{pp} bias on each actuator	Actuators 1-10: ±0.5°, when 1V_{pp} is supplied by function generator
Mixed mode	Actuation Mechanism		

2.6 Summary

Two designs of piezoelectric driven MEMS scanners using mechanical supporting beam integrated with 1×10 individually biased PZT actuators have been successfully designed, fabricated and characterized. 3 modes of scanning operations have been investigated: bending, torsional and mixed. Table 3 summarizes and compares the bias configurations and performance during the three operation modes for both designs. In bending mode, the performance of both designs are similar to each other when the all the ten actuators are biased at the same voltage. In the case of torsional mode, the difference in the direction of actuator displacement due to the 180° phase difference in the applied bias for design B helps to magnify the torsional scanning of the mirror compared to design A. Finally, in mixed mode operation, clear Lissajous patterns were obtained successfully. As evident from the raster scanning patterns, crosstalk between the bending and torsional actuations was observed to be more significant in design B compared to design A. Nevertheless, these images demonstrate the potential of both MEMS scanners for low-frequency 2-D scanning applications.

Besides 2-D scanning application, the fabricated piezoelectric driven MEMS mirror (design B) will also be investigated further for VOA application. This shall be duly discussed in Chapter 3.

Chapter 3
A PZT Driven MEMS VOA Using Attenuation Mechanism With Combination of Rotational and Translational Effects

3.1 Introduction

MEMS technology has been an enabling tool for numerous telecommunication components in modern optical network systems based on dense-wavelength-division-multiplexing technology (DWDM). The phenomenal growth of the internet in the past decade has led to telecommunication companies making huge investments in these optical MEMS devices, which include variable optical attenuator (VOA), where it is commonly adopted to groom power levels across the DWDM spectrum.

Most of the designs of MEMS VOAs reported in the literature adopted attenuation mechanisms that can be generally classified into three categories: shutter-type [101, 105-107, 128, 129], planar reflective-type [102, 108-113] and three-dimensional (3-D) reflective-type [68, 103, 114, 115]. With the aim of reducing driving voltage, various Si-based electrothermal actuators have been developed for VOA applications. Driving voltage as low as 3 V_{dc} had been reported by using an array of electrothermal actuator driven surface micromachined pop-up mirror [129]. In recent years, a large vertical Si mirror (500 μm × 1200 μm) driven by a metal coil type electromagnetic actuator had

also been reported to achieve 40 dB dynamic range under 0.5 V_{dc} [128]. All these aforementioned research efforts adopted the planar light attenuation mechanism, i.e. the light path is parallel to the substrate surface.

From the literature review above, it can be seen that limited research effort has been made in 3-D reflective type MEMS VOAs in contrast to the reported activities in planar MEMS VOAs. Isamoto *et al.* demonstrated one of the few published 3-D MEMS VOA, in which an electrostatic parallel plate actuator was deployed to drive a tilting micromirror and the derived performance was outstanding as only 4.5 V_{dc} was needed to achieve 0.3° rotational angle and 40 dB attenuation range [103]. Achieving a low voltage driven micromirror in a 3-D light attenuation configuration is the main objective of our research attempt in the development of novel actuation mechanism for VOA application. Thus, in this chapter, we explore a MEMS VOA driven by a piezoelectric beam actuator integrated with 1×10 PZT actuator array. The device to be investigated for dc-operated VOA application in this chapter is the same as that of design B in chapter 2 where it has already been investigated for ac-operated 2-D scanning application. Design B is favoured over design A for VOA application as the electrical connections to each of the actuators are separated, hence allows for individual biasing condition. By addressing different bias voltages to the individual PZT actuator, we achieve translational mode and rotational mode simultaneously. The attenuation efficiency of these two modes is investigated, while mixed mode is reported as well.

3.2 Design and Modeling

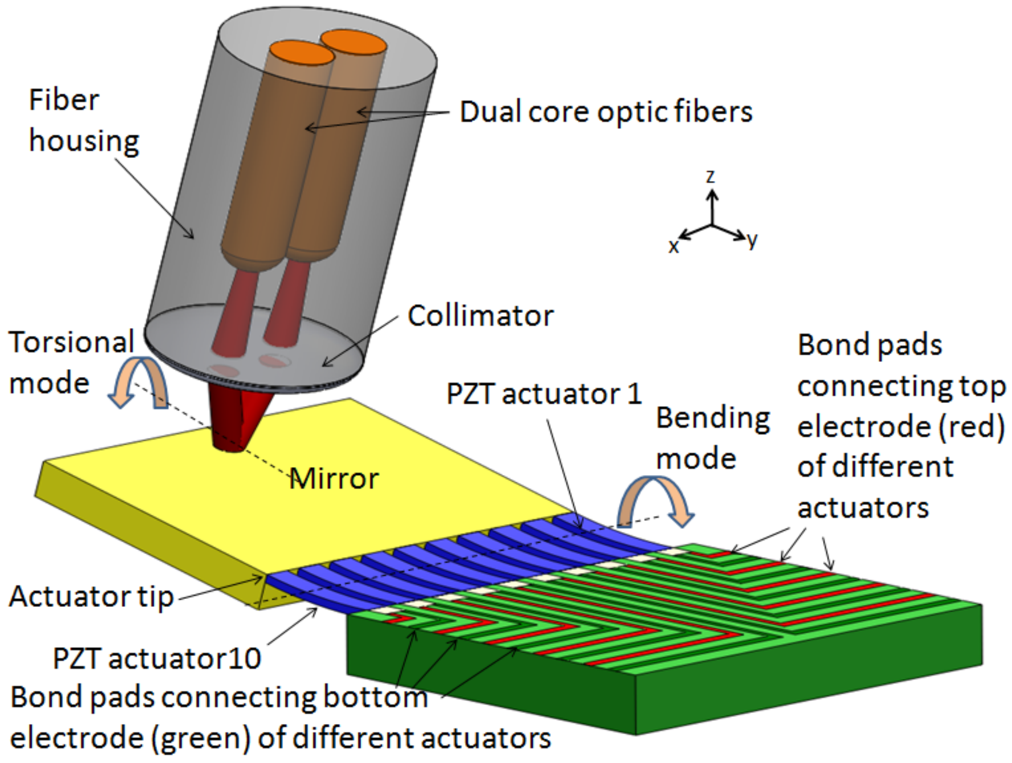

Fig. 3-1. Schematic drawing of the piezoelectric MEMS VOA with dual core collimator arranged in a 3-D configuration such that the light beam focuses on the far edge center of the mirror plate. Bending mode occurs when all the ten actuators are biased simultaneously at same voltage. Torsional mode occurs where a set of five actuators bends in one direction while the other set of five actuators bends in the opposite direction.

A schematic diagram of the piezoelectric PZT MEMS VOA demonstrated in this chapter is shown in Fig. 3-1. The dimensions of the device have been summarized in table 2-1 of chapter 2. Ten patterned PZT thin film actuators are arranged in parallel along one of the sides of the Si mirror, in other words, the longitudinal direction of the actuators. The electrical connections to the actuators are separated from one another, with individual bond pads connected to the top and bottom electrodes of the actuators. The novelty of our VOA design lies in the mirror capability to move with six degree of freedom for enabling 3-D attenuation scheme. Bending mode is elicited when all the actuators are biased simultaneously at the same

dc voltage. As a result, the mirror undergoes translational and rotational movement along the x-axis due to the displacement introduced by the bent actuators under bias. Torsional mode is induced when, for example, actuators 1-5 are biased in such a way that they bend up while actuators 6-10 are biased in an opposite way and bend in the opposite direction, i.e., bending downward. The difference in bending directions for the two sets of actuators causes the mirror to rotate along the y-axis.

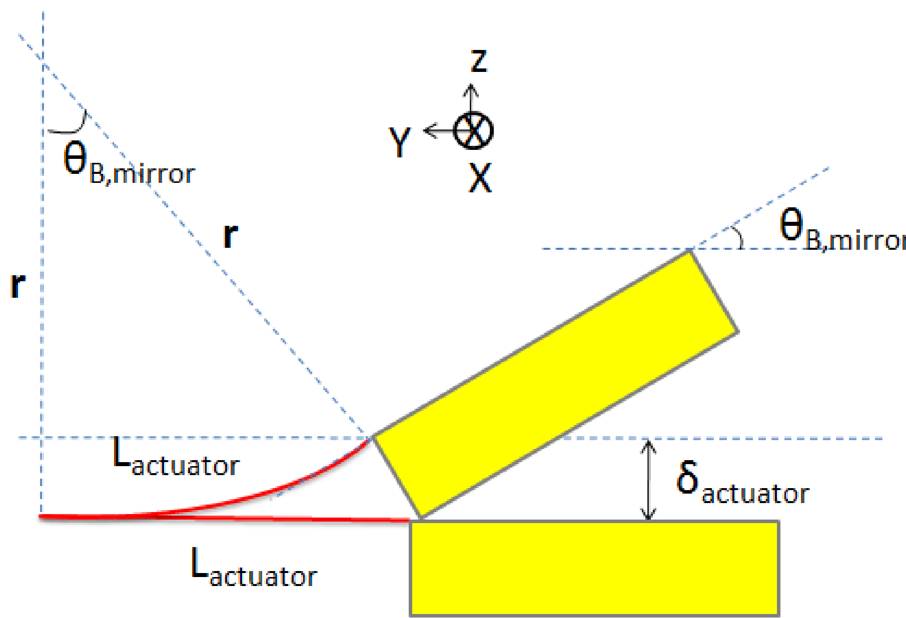

Fig. 3-2. Schematic diagram illustrating the side profile of the dc-biased PZT actuator during bend mode operation, with experimental vertical displacement of $\delta_{actuator}$, mechanical rotation angle of $\theta_{B,mirror}$ and radius of curvature, r.

Fig. 3-2 is used to derive the relationship between the experimental displacement of the dc-biased actuator and the mechanical rotation angle of the mirror plate, $\theta_{B,mirror}$. From Fig. 3-2, equation (3.1) can be derived as:

$$\delta_{actuator} = r - r\cos\theta_{B,mirror} \qquad (3.1)$$

where $\delta_{actuator}$ is the displacement of the dc-biased actuator tip, r is the radius of curvature and $\theta_{B,mirror}$ is the mechanical rotation angle of the mirror plate. Assuming $\theta_{B,mirror}$ is small, by small angle approximation,

$$\cos\theta_{B,mirror} = 1 - \frac{1}{2}\theta_{B,mirror}^2 \qquad (3.2)$$

$$r = \frac{L_{actuator}}{\theta_{B,mirror}} \qquad (3.3)$$

Substituting equations (3.2) and (3.3) into (3.1),

$$\delta_{actuator} = \frac{L_{actuator}\theta_{B,mirror}}{2} \qquad (3.4)$$

Making $\theta_{B,mirror}$ the subject, equation (3.4) becomes,

$$\theta_{B,mirror} = \frac{2\delta_{actuator}}{L_{actuator}} \qquad (3.5)$$

To further understand the attenuation mechanism better, schematic diagrams illustrated in Fig. 3-3 and Fig. 3-4 are used to illustrate the two modes of attenuation operation, i.e. bending and torsional modes. Fig. 3-3 shows the side profile of the mirror and the dual core collimator during bending mode operation. In Fig. 3-3(a), when the actuators are not biased, the normal of the mirror surface is aligned perfectly with the light beam, coupling all the light from the input fiber to the output fiber. When the mirror translates and rotates due to a dc voltage applied simultaneously to the ten actuators as shown in Fig. 3-3(b), a portion of the laser beam no longer couples into the output fiber, resulting in attenuation. In Fig. 3-3(c), both rotational and translational displacements are observed when the actuators are biased. Based on Fig. 3-3(c), an analytical model relating the displacement of the actuators

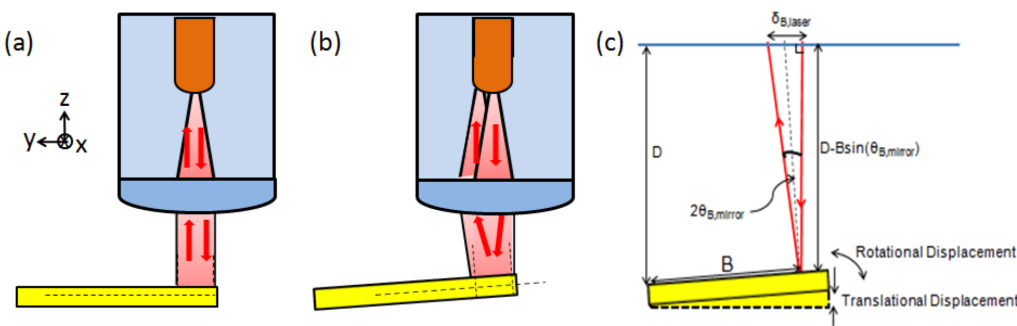

Fig. 3-3 Schematic diagrams showing the attenuation mechanism for bending mode: (a) configuration refers to the initial state of insertion loss. All of the laser beam from the input fiber is coupled back into output fiber when the actuators are not biased, i.e., mirror surface remains normal to laser beam; (b) a portion of the laser beam from input fiber deviates from the optimized reflection light path when the actuators are biased, i.e., mirror undergoes rotational and translational motion (c) mirror is rotated by an angle, θ_B,mirror, and the laser beam is displaced by a distance, $\delta_{B,laser}$.

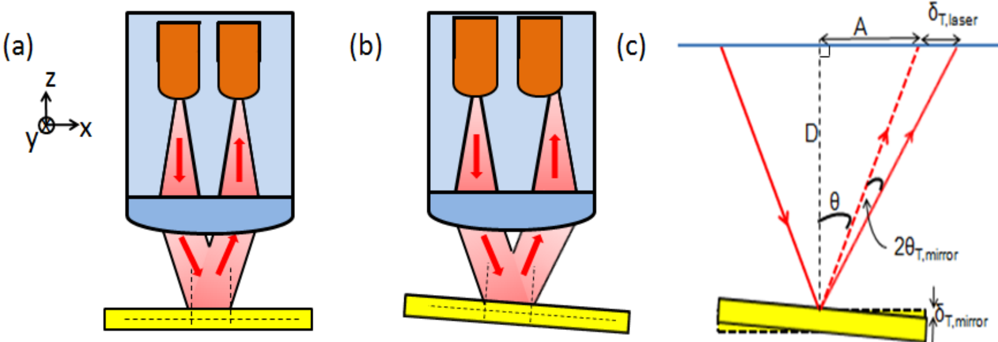

Fig. 3-4. Schematic diagrams showing attenuation mechanism for torsional mode: (a) all of the light beam from the input fiber is coupled back into output fiber when the actuators are not biased. It is the initial state of insertion loss; (b) configuration refers to the attenuation state where a portion of the laser beam from input fiber is not coupled back to the output fiber due to that actuators 1-5 and actuators 6-10 being oppositely biased, i.e. mirror undergoes rotational motion (c) mirror is rotated by an angle, $\theta_{T,mirror}$, and the laser beam is displaced by a distance, $\delta_{T,laser}$.

to the displacement of the laser beam from its original position can be built. The mechanical rotation angle of the mirror plate, $\theta_{B,mirror}$, is related to the displacement of the laser beam from its original position, $\delta_{B,mirror}$, by equations (3.5)-(3.7),

$$\theta_{B,mirror} = \frac{2\delta_{actuator}}{L_{actuator}} \tag{3.5}$$

$$B = L_{mirror} - R_{dot\ size}\cos(\theta_{B,mirror}) \tag{3.6}$$

$$\delta_{B,laser} = [D - B\sin(\theta_{B,mirror})]\tan(2\theta_{B,mirror}) \tag{3.7}$$

where $L_{actuator}$ is the length of the actuator (3 mm), $\delta_{actuator}$ is the displacement of the actuator tip, L_{mirror} is the length of the mirror plate (5 mm), $R_{dot\ size}$ is the radius of the circular laser beam spot (350 μm), D is the working distance of the dual core collimator (1 mm). With the above mentioned equations (3.5)-(3.7), we are able to calculate the theoretical displacement of the laser beam from its original position using the experimental data collected for the displacement of the dc-biased actuator tip measured under the optical microscope.

Similar analysis is done to investigate the attenuation mechanism during torsional mode operation. Fig. 3-4 shows the front profile of the mirror and the dual core fibers with collimator. In Fig. 3-4(a) where the actuators are initially unbiased, laser from the input fiber is coupled perfectly into the output fiber. However, in Fig. 3-4(b), the actuators 1-5 and 6-10 are oppositely biased, hence introducing opposite displacements for the two sets of actuators. As a result, the mirror undergoes torsional rotation, reflecting a portion of the laser beam away from its original position. Fig. 3-4(c) shows a simplified diagram of the laser beam being reflected by the rotated mirror. The torsional rotation angle of the mirror, $\theta_{T,mirror}$, is related to the displacement of the laser beam from its original position by equations (3.8)-(3.10):

$$\theta_{T,mirror} = \tan^{-1}\left(\frac{2\delta_{T,mirror}}{L_{mirror}}\right) \quad (3.8)$$

$$\theta = \tan^{-1}\left(\frac{A}{D}\right) \quad (3.9)$$

$$\delta_{T,laser} = D\tan(\theta + 2\theta_{T,miror}) - A \quad (3.10)$$

where $\delta_{T,mirror}$ is the displacement of the mirror edges observed under optical microscope, L_{mirror} is the length of the mirror plate (5mm), A is the half distance between the input and output fiber (125µm), D is the working distance of the dual core collimator (1mm). These equations (3.8)-(3.10) allow us to derive the displacement of the laser beam from its original position using the experimental $\delta_{T,mirror}$ obtained during torsional mode.

To evaluate the quality of the fabricated piezoelectric actuators, a model is necessary in order to compute the piezoelectric constant, d_{31}, of the PZT thin film. The following equations (3.11)-(3.14) are used to find the value of d_{31} [130]:

$$\delta_{\text{fixed-free actuator}} = \frac{3AB}{K} L_{\text{actuator}}^2 V\, d_{31} \qquad (3.11)$$

$$A = S_{si} S_{PZT} (S_{PZT} t_{Si} + S_{Si} t_{PZT}) \qquad (3.12)$$

$$B = \frac{t_{Si}(t_{Si} + t_{PZT})}{S_{PZT} t_{Si} + S_{Si} t_{PZT}} \qquad (3.13)$$

$$K = (S_{si})^2 (t_{PZT})^4 + 4 S_{si} S_{PZT} t_{Si} (t_{PZT})^3 + 6 S_{si} S_{PZT} (t_{Si})^2 (t_{PZT})^2 + 4 S_{Si} S_{PZT} (t_{Si})^3 (t_{PZT}) + (S_{PZT})^2 (t_{Si})^4 \qquad (3.14)$$

where $\delta_{\text{fixed-free actuator}}$ is the displacement of the fixed-free actuator tip observed under the optical microscope, $L_{actuator}$ is the length of the actuator (3mm), V is the applied voltage, S_{si} and S_{PZT} are the respective compliances of the strutural Si layer (6.0×10^{-12} Pa^{-1}) and PZT thin film (1.43×10^{-11} Pa^{-1}), t_{Si} and t_{PZT} are the respective thicknesses of the strutural silicon (5µm) and PZT film (3µm). From equation (3.11), it can be interpreted that the value of d_{31} can be derived from the gradient of a $\delta_{\text{fixed free actuator}}$-V plot.

3.3 Device Microfabrication

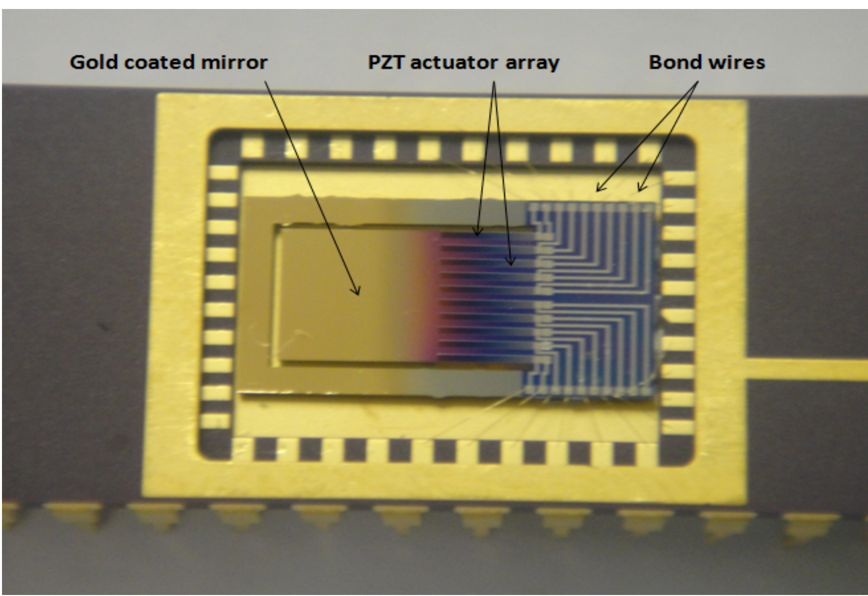

Fig. 3-5. Close-up photo showing the packaged PZT MEMS VOA with a gold-coated surface.

Fig. 3-5 shows the MEMS VOA device bonded onto a dual inline package (DIP) and the bond pads were connected to the metal pins of the DIP using gold bond wires. The fabrication process for the VOA device is identical to that described previously in Section 3 of Chapter 2. A thin film of gold was sputtered on the mirror surface using a shadow mask. This is necessary, as silicon is transparent to 1550nm radiation.

To enhance the piezoelectric characteristics, poling treatment was conducted on the PZT thin film actuators at 25 V_{dc} for 10 minutes at room temperature. In order to derive the value of transverse piezoelectric constant, d_{31}, the ten actuators were biased simultaneously at the same dc driving voltage while the displacement of the ten actuator tips are observed under the optical microscope. Prior to doing the experiment, the mirror plate of a spare VOA sample was broken off deliberately as the displacement of the actuator

tip in equation (3.11) is only valid for fixed-free piezoelectric actuator. The measured displacements of ten actuators were averaged. This was repeated for various dc voltages and the results were plotted in Fig. 3-6. A linear fit for the experimental data was also plotted, and as discussed in the previous section, the value of d_{31} can be derived from the gradient of the linear fit plotted. Using Fig. 3-6 and equation (3.11), the transverse piezoelectric constant d_{31} is estimated to be 136 pmV^{-1}.

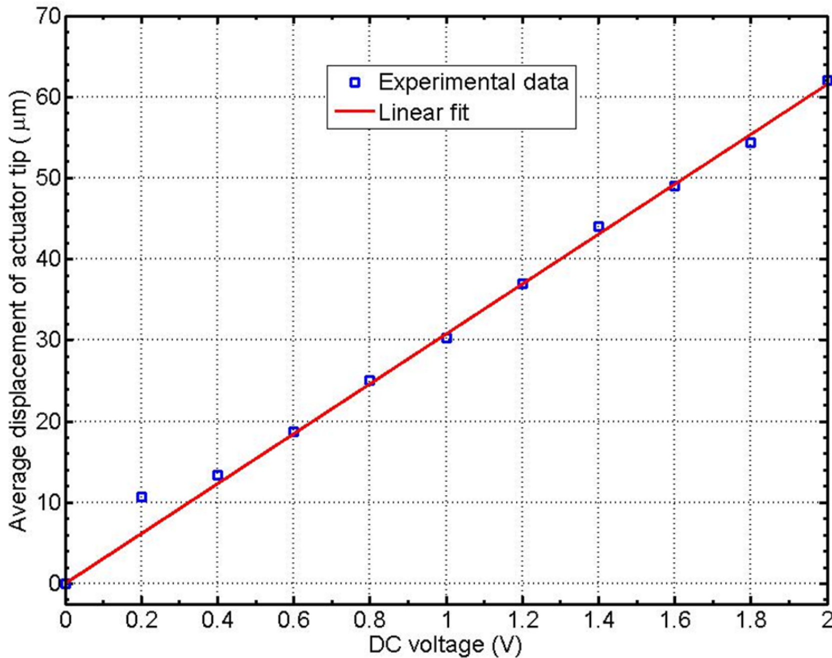

Fig. 3-6. Measured average displacement of fixed-free actuator tips versus dc driving voltage applied to the top electrodes of all ten actuators.

3.4 Experimental Setup

The schematic drawing of the measurement setup for MEMS VOA characterization is illustrated in Fig. 3-7. The dual fiber with collimator were made from standard 250µm Corning SMF-28 fibers with a core and total diameter (inclusive of core, cladding, coating) of 8.2 µm and 250 µm,

respectively. The fiber cores were separated by a distance of 250 μm, surrounded by glass and metal tubes, with a GRIN lens fitted in front of the fibers. The dual fiber with collimator was placed about 1mm (working distance) away from the mirror surface, while the device was mounted on a multi-axial x-y-z-θy-θz movable stage. Light from the 1550 nm laser source (Thorlabs Benchtop Laser Source S3FC1550) was launched via one fiber, i.e. input fiber through the collimator to the edge of the mirror furthest away from the actuator array, where the translational and rotational motion induced by the biased actuators were the biggest. This will allow for maximum attenuation at the lowest possible dc voltage. The reflected light was collected by the same collimator to the power meter (Newport dual-channel power meter 2832c) via the output fiber. Equations (5.11) and (5.12), along with the readings recorded on the power meter, were used to calculate the attenuation introduced by the biased device:

$$P_{reflected\ beam} = \frac{10^{\left(\frac{x}{10}\right)}}{1000} \qquad (3.15)$$

$$Attenuation = 10\log\left(\frac{P_{reflected\ beam}}{P_{light\ source}}\right) \qquad (3.16)$$

where x is the power meter reading in dBm, $P_{reflected\ beam}$ is the power of the reflected beam collected by the power meter, and $P_{light\ source}$ is the power of the laser source (2 mW). The collimated beam diameter had been characterized to be 700 μm ± 25 μm. The whole setup was established on an anti-vibration optical table to prevent disturbance from ambient vibration.

For the insertion loss measurement, the relative positions of the collimator and mirror were adjusted such that coupling loss is optimized or

minimized. In order to do so, red laser of 632.8 nm was first used as the light source. The red laser beam was shone through the collimator onto the far edge of the mirror plate. Subsequently, the x-y-z stage was adjusted to centralize the red laser spot onto the far edge of the mirror. The 1550 nm laser source was then fed into the input fiber after the coarse alignment step was confirmed. In the fine alignment adjustment, the position of the mirror relative to the collimator was fine-tuned by moving and tilting the x-y-z-θy-θz stages such that minimum loss is reached, i.e., insertion loss. The θy and θz adjustment knobs enable the tilting of the stage with respect to the y- and z-axis, respectively. The measured initial insertion loss in this setup is typically about 2~3 dB. This value is about 1~2 dB higher than commercially available VOA products. This is mainly attributable to the surface roughness and warpage of the mirror. Further optimization of the mirror fabrication and microstructures may reduce the insertion loss to be less than 1 dB.

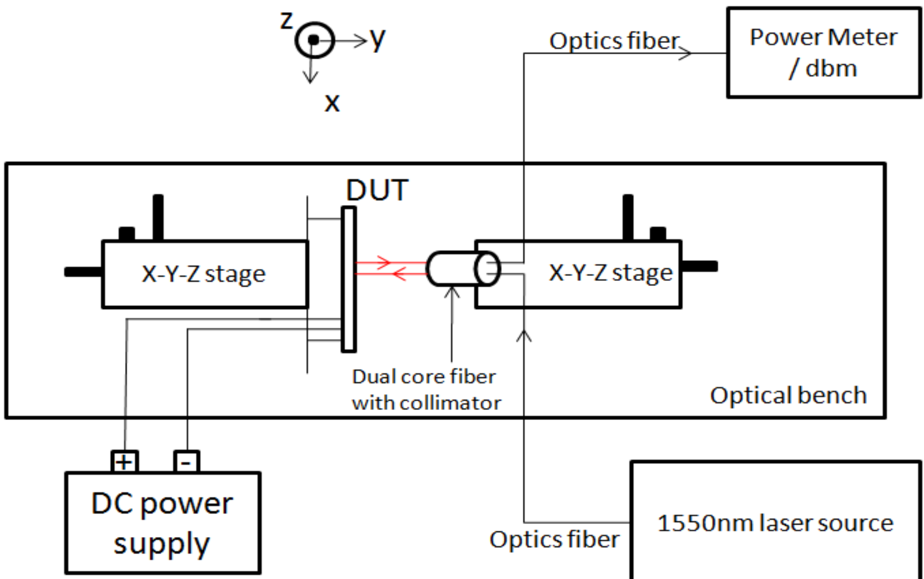

Fig. 3-7. Schematic drawing of the measurement setup for 3-D MEMS VOA characterization carried out on an anti-vibration optical bench. The stage is capable of moving in X-Y-Z directions and tilting along X-Y(θz) and Y-Z(θx) planes as well.

3.5 Results and Discussion

3.5.1 Bending mode operation

In the operation of the PZT MEMS VOA, various dc voltages are applied to the ten actuators to actuate the mirror. As a result, the reflected light deviates from the optimized light path corresponding to minimum insertion loss. The intensity of the reflected laser that is coupled back to the output fiber reduces, resulting in greater attenuation with increasing driving voltage. Based on the experimental setup in Fig. 3-7, the measured attenuation curve versus various dc voltages applied simultaneously to the ten actuators during bending mode operation is shown in Fig. 3-8(a). As discussed earlier, bending mode is elicited when all the top electrodes of the actuators are biased simultaneously at the same dc voltage while all the bottom electrodes are grounded. From Fig. 3-8(a), an attenuation range of 40 dB was achieved when 1 V_{dc} was applied to the ten actuators. A 40 dB dynamic range is sufficient with regards to most of the commercial applications. As such, this means that the PZT MEMS VOA developed in this study will require only a dc operating voltage of 1 V.

In Fig. 3-8(b), the displacement of the actuator tip (indicated previously in Fig. 3-1), $\delta_{actuator}$, were observed under the optical microscope, averaged and repeated for various dc voltages. The data obtained were plotted and shown in the bottom right (red) curve of Fig. 3-8(b). An average actuator tip displacement of 32 μm was obtained when the ten actuators were biased at 1 V_{dc}. This displacement, as accordance to equation (3.5), gave rise to a calculated mechanical rotation angle, $\theta_{B,mirror}$, of 1.2°. Electrothermal bimorph actuator has been known as a solution for large displacement under low drive

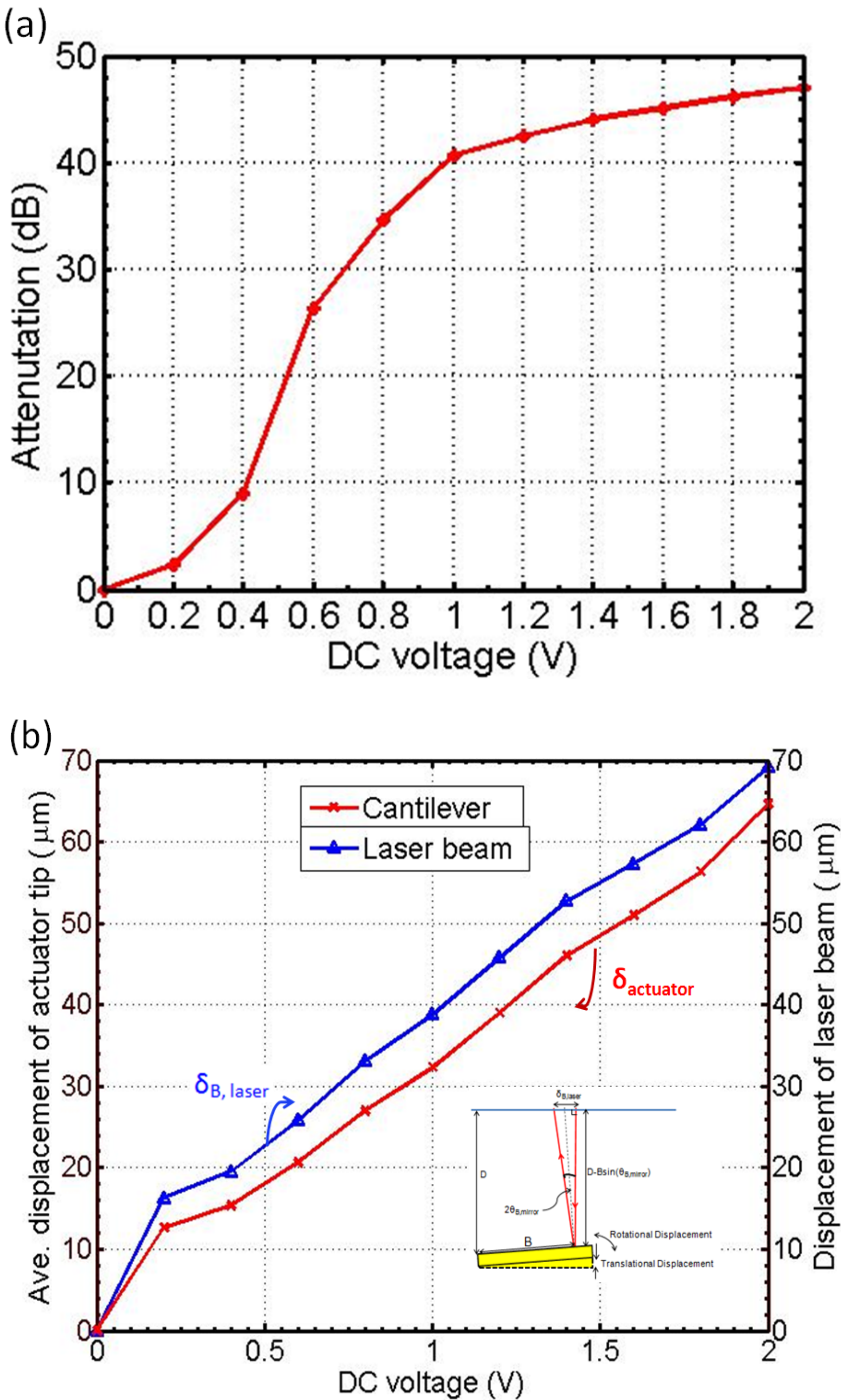

Fig. 3-8. Experimental data for bending mode. (a) Measured attenuation curve versus dc voltage applied simultaneously to the top electrodes of the ten actuators while the bottom electrodes are grounded. (b) Bottom right (red) curve shows measured average displacement of actuator tip, $\delta_{actuator}$, versus dc voltage applied simultaneously to the top electrodes of ten actuators. Top left (blue) curve shows the displacement of laser beam, $\delta_{B,laser}$, versus dc voltage. The displacement of laser beam, $\delta_{B,laser}$, is calculated using equations (3.5)-(3.7) and the values of $\delta_{actuator}$ obtained from the red curve.

voltage. This is exemplified by Jain *et al.* whose work have achieved 1° mirror rotation angle, when 1 V_{dc} was applied to the electrothermal beam actuator [33]. In comparison, our experimental data have demonstrated that piezoelectric actuator can perform as good as thermal bimorph actuator in applications based on dc operation.

The upper left (blue) curve in Fig. 3-8(b) shows the displacement of laser beam, $\delta_{B,laser}$ from its original position corresponding to minimum insertion loss. Values for the laser beam displacements were derived by substituting the values obtained for actuator tip displacements at various dc biases into equations (3.5)-(3.7). From the upper left curve in Fig. 3-8(b), it is observed that the displacement of the laser beam, $\delta_{B,laser}$, was approximately 35 μm at a driving voltage of 1 V_{dc}, i.e. a 35 μm laser beam displacement will result in an 40 dB attenuation of the laser beam.

3.5.2 Torsional mode operation

Fig. 3-9(a) and 3-9(b) show the two biasing configurations to induce torsional mode operation. A potential divider is implemented to split the dc power supply into four equal potential at the potential nodes between each resistors. For the set of actuators 1-5 in Fig. 3-9(a), the top electrodes for these actuators are connected to different potential nodes while the bottom electrodes are grounded. The reverse setup is made for the set of actuators 6-10, i.e., the top electrodes are grounded while the bottom electrodes of these actuators are connected to various potential nodes. On the other hand, for the set of actuators 1-5 in Fig. 3-9(b), the top electrodes for these actuators are grounded while the bottom electrodes are connected to different potential

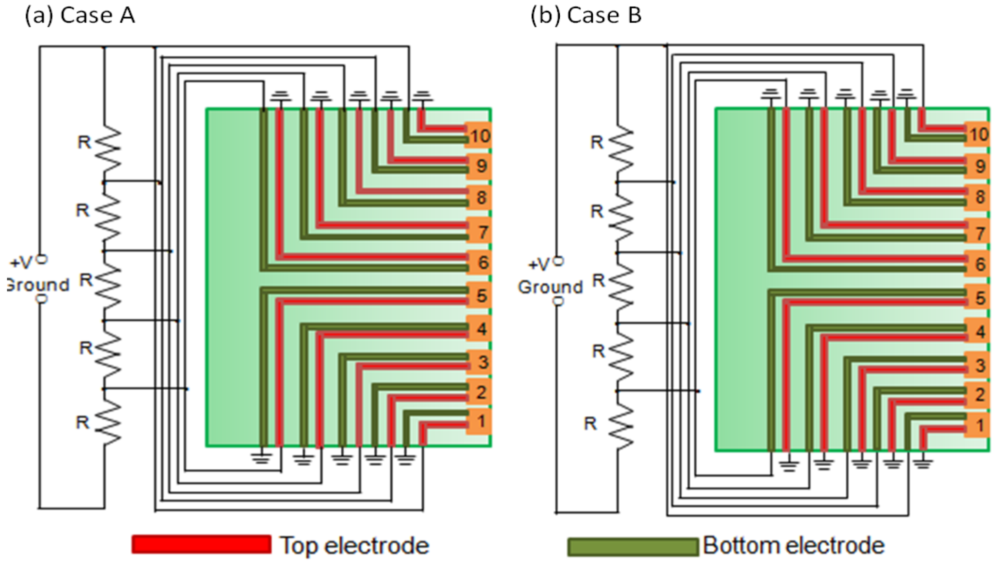

(c)

	Relative bias of top to bottom electrode /V					
Power Supply/V	1V		2V		3V	
Actuators	Case A	Case B	Case A	Case B	Case A	Case B
1	1.00	-1.00	2.00	-2.00	3.00	-3.00
2	0.80	-0.80	1.60	-1.60	2.40	-2.40
3	0.60	-0.60	1.20	-1.20	1.80	-1.80
4	0.40	-0.40	0.80	-0.80	1.20	-1.20
5	0.20	-0.20	0.40	-0.40	0.60	-0.60
6	-0.20	0.20	-0.40	0.40	-0.60	0.60
7	-0.40	0.40	-0.80	0.80	-1.20	1.20
8	-0.60	0.60	-1.20	1.20	-1.80	1.80
9	-0.80	0.80	-1.60	1.60	-2.40	2.40
10	-1.00	1.00	-2.00	2.00	-3.00	3.00

Fig. 3-9. Schematic drawing illustrating the electrical connections of the top and bottom electrodes of each actuator to the dc power supply in (a) bias case A, and (b) bias case B. (c) A look-up table showing the individual dc bias driving each actuator under bias case A and B for a given dc power supply voltage.

nodes. In the case of actuators 6-10, the top electrodes are connected to the various potential nodes while the bottom electrodes are grounded. As such, each of the actuators in both cases A and B will be biased at different values, as evident from the look-up table in Fig. 3-9(c). This results in largest and zero actuator displacement to be introduced at the mirror edges and center, respectively. More importantly, the generated displacements for the two sets

of actuators are towards opposite direction, resulting in torsional rotation of the mirror.

Fig. 3-10 shows the experimental data obtained during torsional mode operation. Fig. 3-10(a) shows the measured attenuation curve versus dc voltage of the power supply. Both bias cases A and B were investigated. An attenuation range of 40 dB was achieved at bias of 1.9 V_{dc} and 1.7 V_{dc} for cases A and B, respectively. Although the mirror and actuators are arranged in symmetric layout, there was still much difficulty in aligning the laser beam to be along the far edge center of the mirror. This accounts mainly for the discrepancy between these two measured curves for different bias cases. In addition, the dimensions of the ten actuators may not be exactly the same due to lithography inaccuracy and deviation in fabrication process. Thus, under the same dc voltages, the actuators in both bias cases may not perform the same displacement, hence partially contributing to the discrepancy between the 2 curves in Fig. 3-10(a).

In Fig. 3-10(b), the device was characterized based on biasing case A, while the absolute value for the displacements of the two opposite edges of the mirror, $\delta_{T,mirror}$, were measured, averaged, and repeated for different dc driving voltage of power supply. The results were tabulated and plotted as the upper-left (red) curve in Fig. 3-10(b). The bottom-right (blue) curve for laser beam displacement, $\delta_{T,Laser}$, was derived by substituting the mirror edge displacement, $\delta_{T,mirror}$, obtained under the optical microscope into equations (3.8)-(3.10). From the bottom-right curve in Fig. 3-10(b), it can be observed that at a power supply of 1.9 V_{dc}, an approximate laser beam displacement of

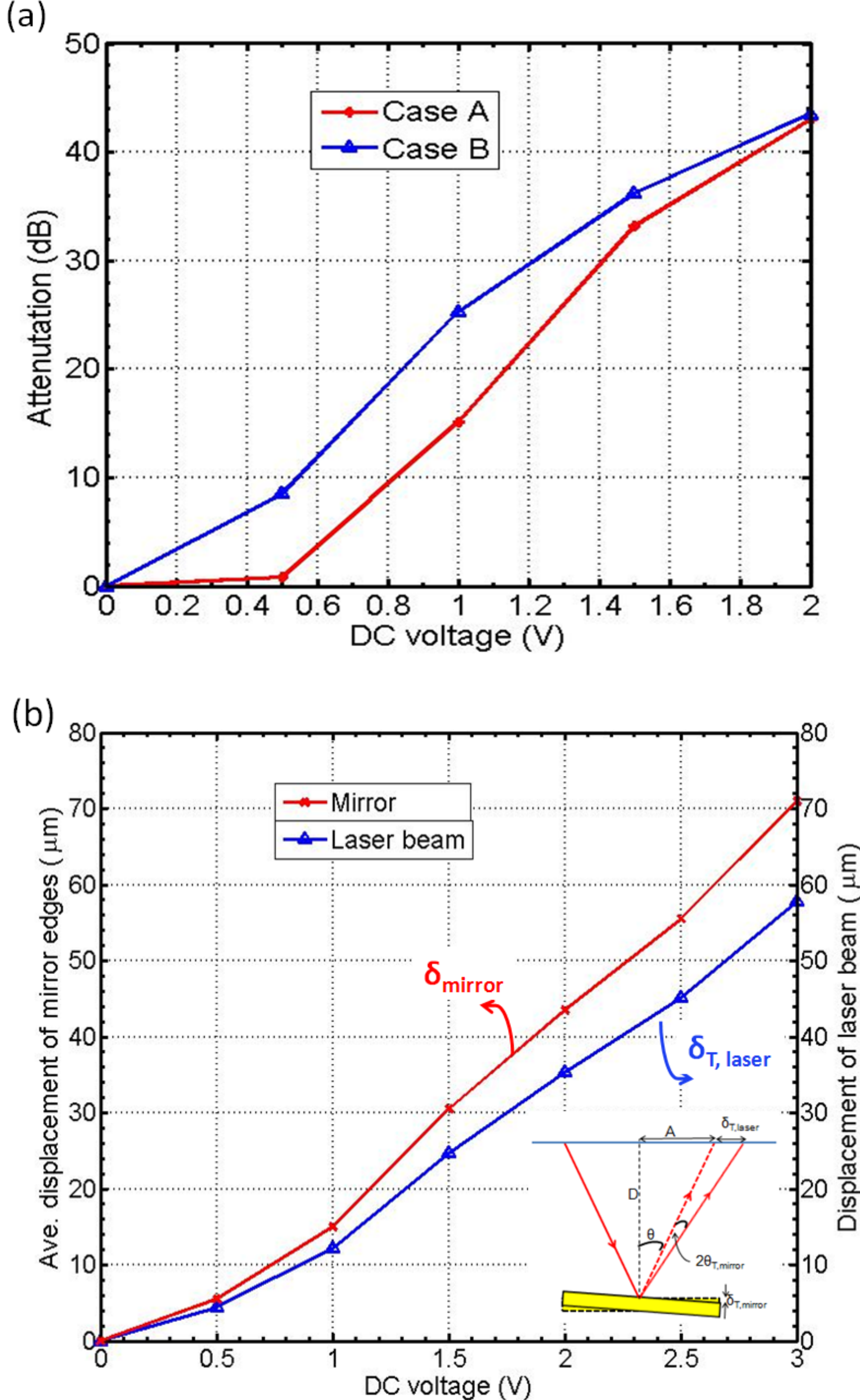

Fig. 3-10. Experimental data for torsional mode. (a) Measured attenuation curves versus dc driving voltage of the power supply for both bias cases A and B. (b) Top left (red) curve shows measured average displacement of mirror edges, δ_{mirror}, versus dc driving voltage of power supply. Bottom right (blue) curve shows the displacement of laser beam, $\delta_{T,laser}$, versus dc voltage of power supply. Both curves were obtained using bias case A. The displacement of laser beam, $\delta_{T,laser}$, is calculated using equations (3.8)-(3.10) and the values of δ_{mirror} obtained from the red curve.

33 µm from its original position was retrieved. This means that a 33 µm laser beam displacement is needed for 40 dB attenuation of laser beam in torsional mode. This value obtained during torsional mode operation (33 µm) is very close to that derived during bending mode operation (35 µm).

By comparing the two modes of attenuation operation, bending mode operation is deemed to be more effective in optical attenuation compared to torsional mode operation. This is evident from the experimental results as only 1 V_{dc} is required to obtain 40 dB attenuation range during bending mode whereas, in torsional mode operation, 1.8 V_{dc} is needed to achieve the same amount of attenuation. In additional to rotational movement, translational motion is also being introduced to the micromirror during the bending mode operation, which results in greater displacement of the reflection point on the micromirror. In the case of torsional mode operation, the torsional or twisting motion of the actuator array would not induce any displacement of the reflection point, hence requiring a higher driving voltage to achieve the same amount of attenuation range.

3.5.3 Mixed mode operation

In mixed mode operation, two dc power supplies are required to bias the 2 sets of cantilevers 1-5 and 6-10 separately. Both bending and torsional mode phenomenon are observed when the dc biases on both sets of cantilevers are not equivalent. Various voltage combinations were applied to the two sets of cantilevers and an attenuation characteristic topography was derived and shown in Fig. 3-11,. When a constant voltage of 1.2 V_{dc} was applied to actuators 1-5, the attenuation changed from 41dB to 47dB as the voltage

applied to actuators 6-10 increased from 0 V_{dc} to 2 V_{dc}. For the reverse case, i.e. a voltage of 1.2 V_{dc} was applied to actuators 6-10, the attenuation changes from 27dB to 50dB as the voltage applied to actuators 1-5 increased from 0 V_{dc} to 2 V_{dc}. This difference in attenuation characteristic between the two sets of actuators may be attributed to lithography inaccuracy and deviation in fabrication process.

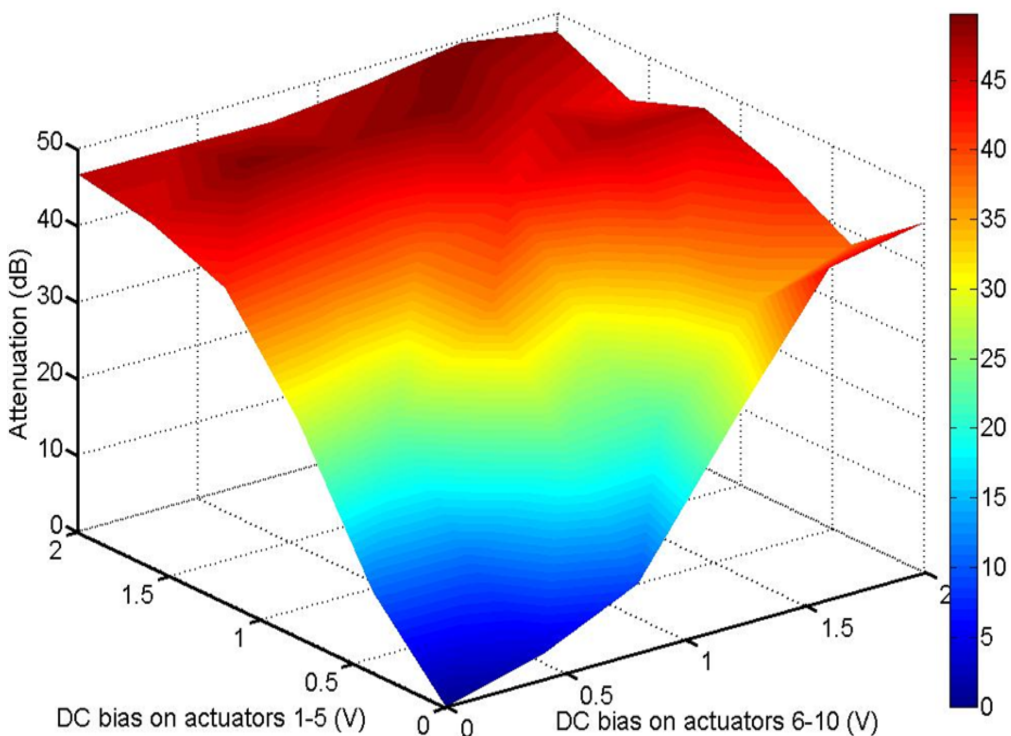

Fig. 3-11. Measured attenuation value as a function of dc bias applied to the 2 sets of actuators 1-5 and 6-10.

As such, with mixed mode operation, an additional degree of freedom in attenuation control can be attained. More specifically, any deviation of attenuation-DC bias characteristic among various PZT MEMS VOA devices due to fabrication process and assembly steps could be compensated by changing different driving voltages combination to the two sets of actuators.

3.6 Summary

In this chapter, a novel piezoelectric driven MEMS VOA using mechanical supporting cantilever beam integrated with multiple actuators was explored and characterized in a 3-D attenuation configuration using a dual core collimator. 3 modes of attenuation operation mode have been investigated: bending, torsional and mixed. Torsional attenuation based on the difference in the dc voltages applied to the piezoelectric actuators on a silicon cantilever beam was the first to be demonstrated in literature. This actuation mechanism differs greatly from those actuation mechanisms of mirror in torsional mode, i.e. the mirror rotation is generated against to torsion spring or torsion bar. Although thermal bimorph beam actuator has been well-characterized in terms of their capability to generate large deflection, i.e. in bending mode, no design in torsional mirror using beam actuator has been reported. Instead of using thermal bimorph beam actuator, our unique design of piezoelectric cantilever beam actuator is the first demonstration of large torsion mirror using beam actuator.

In addition, bending mode operation has been concluded to be more effective in optical attenuation compared to torsional mode operation. In the case of mixed mode operation, it offers greater flexibility in attenuation control, which helps to compensate for any difference in performance among the different MEMS VOAs that may arise due to fabrication process and assembly steps. Last but not least, the assimilation of PZT displacement sensing with PZT attenuation mechanism is a possible research direction that our device can head towards. This allows the detected signals received from

the displacement sensor to be used as feedback control reference. An instrument-level piezoelectric MEMS VOA with electronic feedback control circuits can hence be developed.

To improve the current 1×10 beam actuator design in terms of better scanning performance and reduced number of PZT actuators, a single S-shaped actuator design integrated with a silicon micromirror will be further proposed and investigated for 2-D MEMS scanner application in the next chapter.

Chapter 4
A MEMS Scanner Based on Dynamic Mixed Mode Excitation of a S-shaped PZT Actuator

4.1 Introduction

In the MEMS scanner regime, parameters such as large mirror size (~ 1 mm^2), large deflection angle and low driving voltage are in strong demand. Besides the difference in actuation schemes, a wide variety of actuation mechanisms for MEMS scanners have also been reported in literature, with most of them deploying either the two frames or/and multi-actuators design for 2-D actuation. Nevertheless, straightforward and compact MEMS scanner designs, such as the L-shaped thermal bimorph cantilever actuated mirror developed by Schweizer *et al.,* have also been reported [97].

In addition to the conventional straight or L-shaped cantilever actuator, electromagnetic and electrothermal driven MEMS scanners adopting meandering multi-actuators design have also been demonstrated [75, 131]. Actuator designed in meandering style offers several advantages over straight cantilever design. These advantages include a smaller footprint and a larger optical deflection angle due to its lower mechanical stiffness. Piezoelectric actuator made of a number of bars of PZT electrically connected in parallel and mechanically connected together in series in a meandering configuration was first conceptualized by Robbins *et al.* in 1991 [132-134]. Such

meandering PZT actuator design was not incorporated for MEMS scanner application till the works done by Tani *et al.* in 2005, where multiple meandering actuators were adopted in both the inner and outer scanning frames [88, 89]. However, there are still limited research effort being spend on a simple MEMS scanner design that makes use of only a single actuator to achieve 2-D scanning effect, as compared to those reported activities in two frames, multi-actuators driven mirror. Thus, in this chapter, the development work of a proof-of-concept MEMS scanner actuated by a S-shaped PZT actuator is reported. By addressing two excitation signals of different frequencies to the S-shaped PZT actuator, translational (bending mode) and rotational (torsional mode) motions operating at resonance condition can be obtained. 2-D scanning can thus be achieved by superimposing the two ac signals into one signal to be used to excite the PZT actuator and drive the micromirror. In contrast to our previous research attempts in chapter 2 where a 1×10 array of PZT actuators design is demonstrated for 2-D scanning applications, the S-shaped actuator design investigated in this chapter demonstrates improvement in terms of better scanning performance and reduced number of PZT actuators and bonding pads.

4.2 Design & Modeling

A schematic diagram of the MEMS scanner to be investigated in this chapter is shown in Fig. 4-1(a). The detailed dimensions of the device are given in Fig. 4-1(b) and summarized in Table 4-1. The mirror plate is driven by a S-shaped PZT actuator, which is capable of 6 degrees of freedom of movement. The main composition of the actuator consists of a top electrode

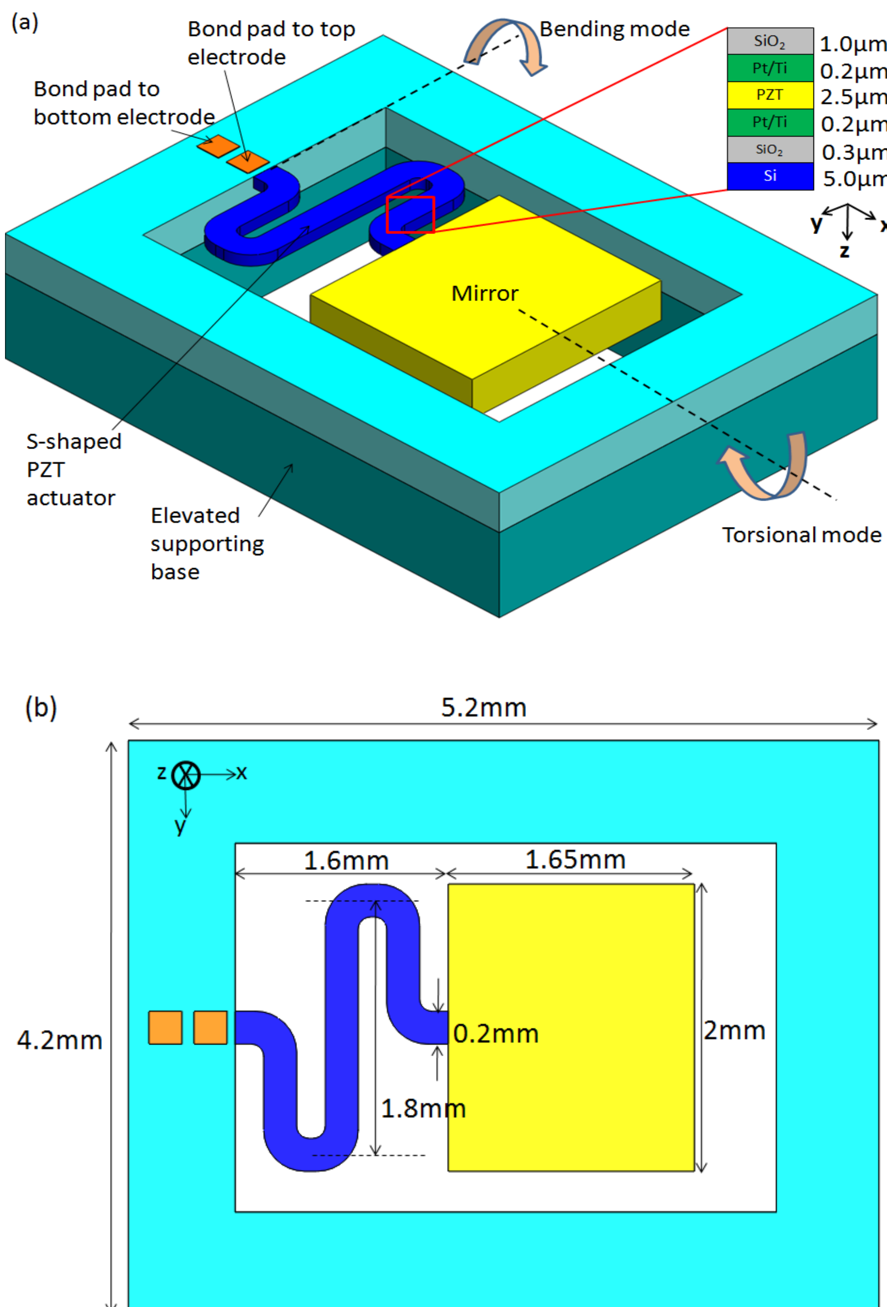

Fig. 4-1. (a) Schematic drawing of the MEMS scanner actuated by single S-shaped PZT actuator. Bending and torsional modes occur when the device is excited at the respective resonant frequencies. (b) Top view of the MEMS scanner and the respective dimensions of the structures.

layer (Pt/Ti), a piezoelectric PZT thin film and a bottom electrode layer (Pt/Ti). The top and bottom electrodes are individually connected to their bond pads. A proof mass is left beneath the mirror to maintain the rigidity and flatness of the reflecting surface during motion. Bending mode occurs in both

static and dynamic actuations. When an ac or dc bias is applied to the actuator, it bends and causes the mirror to undergo translational and rotational movement along the y-axis. Torsional mode is induced only during dynamic actuation, when ac resonant frequency corresponding to rotational motion along x-axis is used to excite the device.

Table 4-1. Dimensions of MEMS scanner driven by S-shaped PZT actuator.

Chip	Si mirror plate	S-shaped PZT actuator
5.2 mm x 4.2 mm	1.65 mm long x 2 mm wide x 0.4 mm thick	Longitudinal (x-direction): 1.6 mm Transverse (y-direction): 3.6 mm Thickness (z-direction): 9.2 μm Total length: 5.2 mm

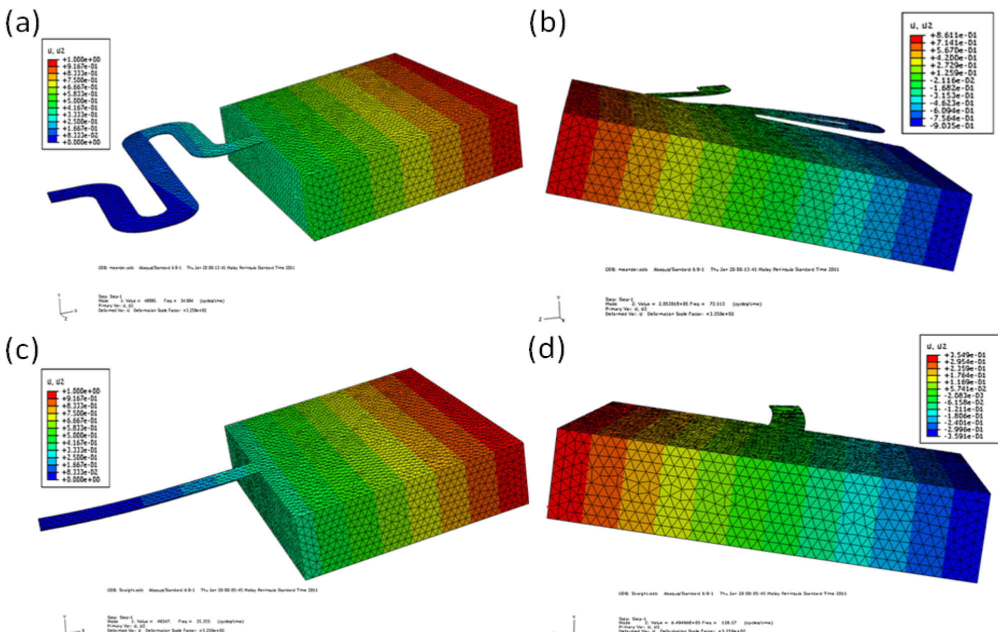

Fig. 4-2. Finite element modal analysis for the two different mirror designs using finite element simulation software ABAQUS. The 1st design being simulated is a micromirror driven by a S-shaped actuator design during (a) bending mode operation, where eigenfrequency at 34.9 Hz and a maximum normalized Z-displacement of 1 was obtained, and (b) torsional mode operation, where eigenfrequency of 72.1 Hz and a maximum normalized Z-displacement of 0.9 was obtained. The 2nd design being simulated is a micromirror driven by straight cantilever actuator design during (c) bending mode operation, where eigenfrequency of 35.3 Hz and a maximum normalized Z-displacement of 1 was obtained, and (d) torsional mode operation, where eigenfrequency of 128 Hz and a maximum normalized Z-displacement of 0.36 was obtained.

To better understand the operation modes, finite element analysis was done using the software ABAQUS. As shown in Fig. 4-2, two actuator designs were simulated: S-shaped and straight beam actuator design. In order to make a fair comparison between the two designs, the actuators simulated in both designs have the same thickness (9.2 μm), width (0.2mm), longitudinal length (1.6mm) and mirror plate dimensions. Fig. 4-2(a) and 4-2(b) show the S-shaped actuator design during bending and torsional mode, respectively, while Fig. 4-2(c) and 4-2(d) show the two operation modes for the straight beam actuator design. During bending mode operation simulated in Fig. 4-2(a) and 4-2(c), both designs show very similar results in terms of eigenfrequency and maximum Z-displacement. Eigenfrequencies of 34.9 Hz and 35.3 Hz were obtained for the S-shaped and straight actuator beam designs, respectively, while both designs also obtained the same maximum normalized out-of-plane Z-displacement of 1.

However, in the simulated torsional mode operation shown in Fig. 4-2(b) and 4-2(d), the results obtained for both designs were significantly different. Eigenfrequencies of 72.1 Hz and 128 Hz were obtained for S-shaped and straight actuator beam designs, respectively. In addition, the maximum normalized Z-displacement obtained in the S-shaped design was 0.9, which is larger compared to the straight beam design of 0.3. This may be explained by using the equation for torsional spring constant ($K_{\theta x}$) along x-axis for a serpentine or meandering spring, which is given by [135]:

$$K_{\theta x} = \left[\frac{2(N+2)}{EI} L_y + \frac{2(N+1)}{GJ} L_x\right]^{-1} \tag{4.1}$$

where N is the number of folds, E is the Young's modulus, I is the moment of inertia with respect to the x-axis, G is the shear modulus, J is the cross-section torsion factor of the spring element parallel to the x-axis, L_x is the length of the spring element parallel to x-axis, L_y is the length of the spring element parallel to y-axis. By analyzing equation (4.1), it can be recognized that the first term is contributed by the bending stiffness of the spring elements (of length L_y) parallel to the y-axis, while the second term is contributed by the torsional stiffness of the elements (of length L_x) parallel to the x-axis. Thus from equation (4.1), with additional spring elements parallel to the y-axis, the torsional spring constant for a S-shaped actuator is lowered compared to a straight beam actuator with no spring elements parallel to the y-axis. This causes the mechanical stiffness of the S-shaped actuator to be lower compared to the straight one, hence explaining why the simulated eigenfrequency to be lower (72.1Hz compared with 128Hz) and Z-displacement (0.9 compared with 0.3) to be larger for the S-shaped actuator design. As such, the simulation proves that in general, adopting a S-shaped actuator design is better than a straight one in terms of larger deflection angle due to the smaller torsional stiffness. However, the tradeoff is that the resonant frequency for a S-shaped actuator design during torsional mode will be lowered.

4.3 Device Microfabrication

The process flow, as shown in Fig. 4-3, and the fabrication steps needed to make the MEMS scanner is similar to that described previously in section 3 of chapter 2. A total of seven photo-lithography masks were used, while the device was assembled onto a dual inline package (DIP) after the

fabrication process. As shown in Fig. 4-4, a spacer chip of 1200 μm thickness was bonded between the device and DIP. The spacer chip helps to elevate the device from the base of the DIP, hence avoiding hindrance to the movement of the mirror plate during actuation. The bonds pads were connected by gold bond wires to the metal pins of the DIP. Fig. 4-5(a) and 4-5(b) show optical microscope images of the S-shaped PZT actuator and the two bond pads with their bond wires, respectively.

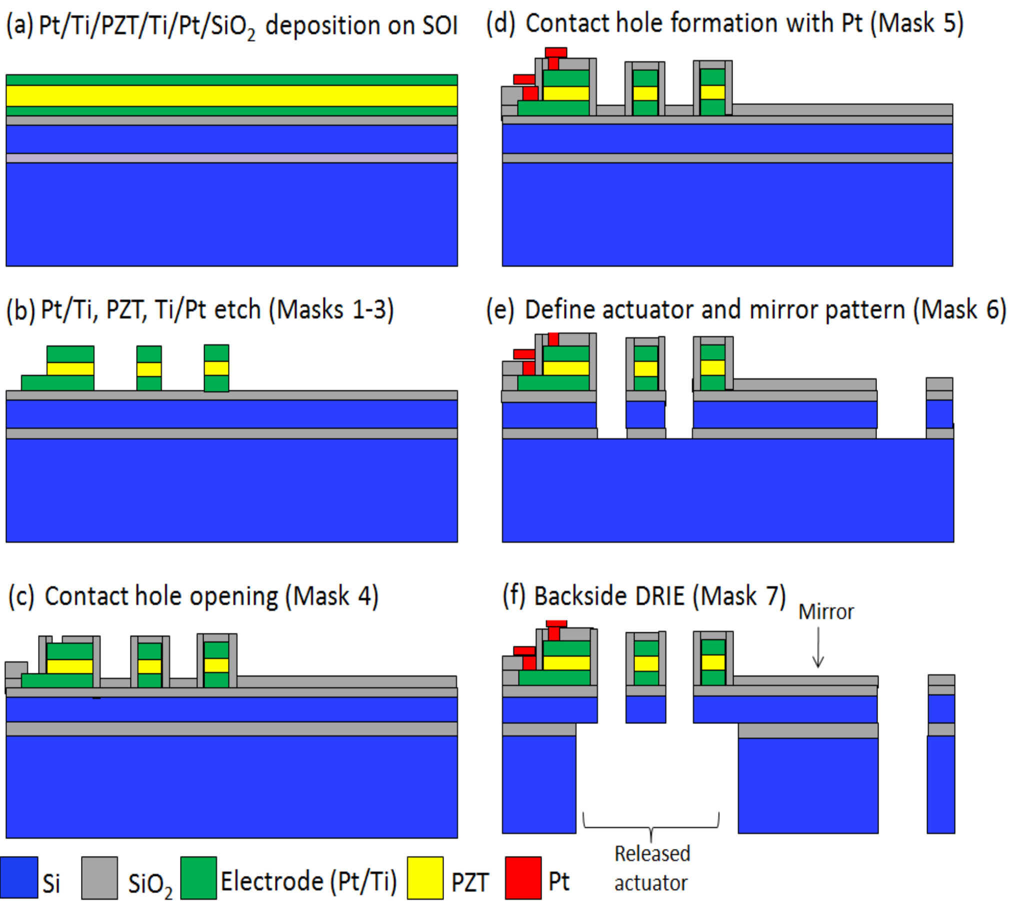

Fig. 4-3. Microfabrication process flow for making the S-shaped PZT actuator and the micromirror.

The process flow, as shown in Fig. 4-3, and the fabrication steps needed to make the MEMS scanner is similar to that described previously in section 3 of chapter 2. A total of seven photo-lithography masks were used,

while the device was assembled onto a dual inline package (DIP) after the fabrication process. As shown in Fig. 4-4, a spacer chip of 1200 μm thickness was bonded between the device and DIP. The spacer chip helps to elevate the device from the base of the DIP, hence avoiding hindrance to the movement of the mirror plate during actuation. The bonds pads were connected by gold bond wires to the metal pins of the DIP. Fig. 4-5(a) and 4-5(b) show optical microscope images of the S-shaped PZT actuator and the two bond pads with their bond wires, respectively.

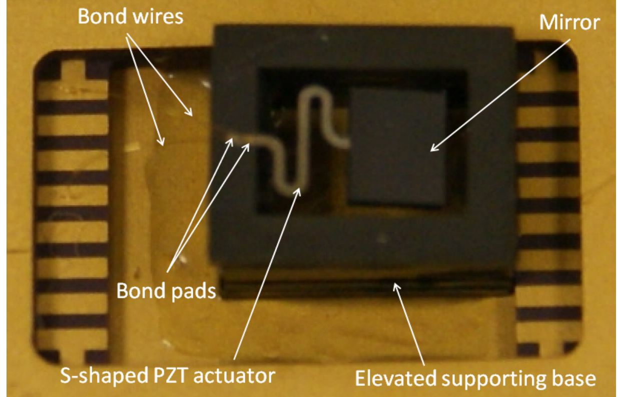

Fig. 4-4. Close-up photo showing the packaged MEMS mirror on a dual in-line package (DIP). The bond wires connect the bond pads on the device to the external pins of the DIP.

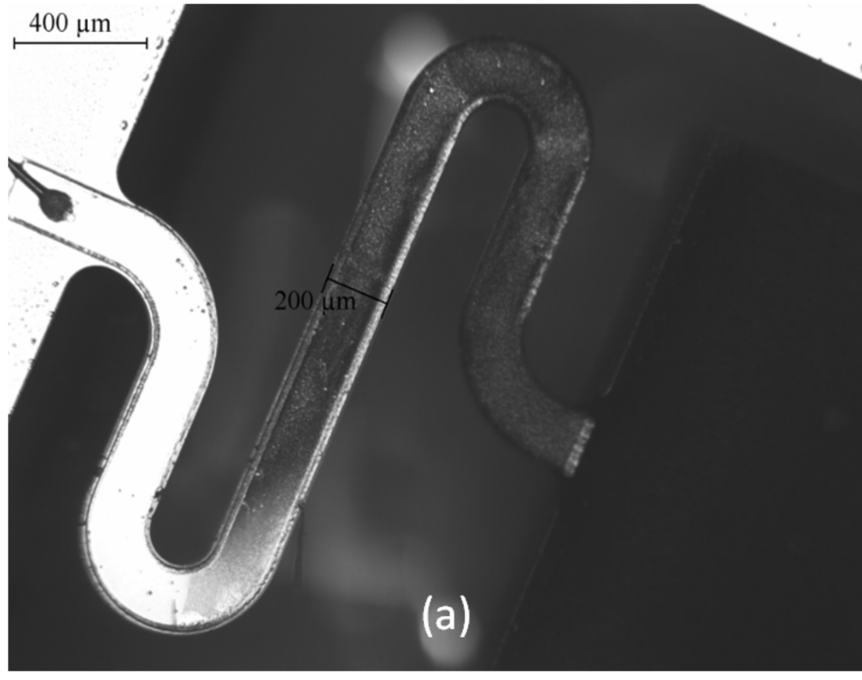

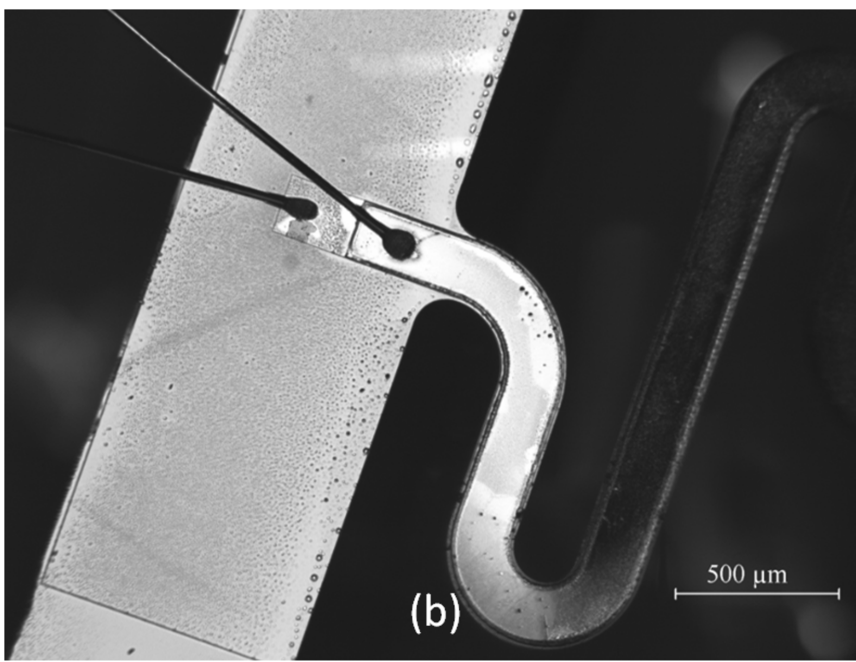

Fig. 4-5. Optical microscope images of (a) S-shaped PZT actuator with a portion of the mirror plate, and (b) two bond pads and their respective bond wires to the DIP.

4.4 Results and Discussion

Prior to characterization, poling treatment was conducted on the PZT actuator at room temperature to enhance the piezoelectric characteristics. A dc voltage of 20V, which is equivalent to a polarization electric field of 80kV/cm, was applied to the PZT actuator for 5 minutes, with the poling direction from the bottom electrode to top electrode. The experimental setup deployed is largely similar to that used previously to characterize the MEMS scanners in section 2.4 of chapter 2.

4.4.1 DC Response

When a dc bias is applied to the S-shaped PZT actuator, it bends as shown in Fig. 4-2(a), introducing a vertical displacement and causing the micromirror to translate. As such, the laser spot will be displaced by a distance

on the white screen. Fig. 4-6 shows the ODA (2θ) obtained when various biases, up to 10 V_{dc}, were applied to the actuator. The top and bottom electrodes were connected as the driving and ground biases, respectively. At 1 V_{dc} and 10 V_{dc}, an ODA of 0.22° and 3.35° were obtained, respectively.

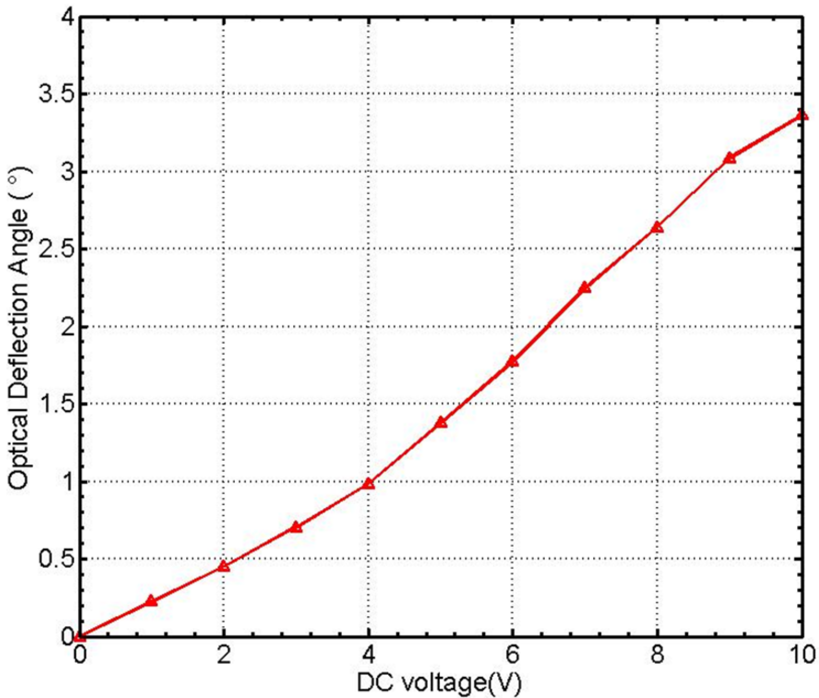

Fig. 4-6. Measured ODA versus DC voltage applied to S-shaped PZT actuator.

4.4.2 AC Response

Fig. 4-7 shows the semi-log plot of ODA with respect to ac excitation frequency varying from 1 Hz to 500 Hz, while peak-to-peak ac voltage of 0.5 V_{pp} was applied to the PZT actuator using a function generator. Two ODA peaks of ±3.1° and ±0.96° peaks at 27 Hz and 230 Hz, respectively, were observed during bending mode operation. For torsional mode operation, a single peak was observed at 70 Hz, with an ODA of ±0.84°. The resonant frequencies for bending (27 Hz) and torsional (70 Hz) modes coincide with the

eigenvalues, i.e., 35Hz and 72Hz, obtained from finite element modal analysis simulation. The measured quality factors for bending and torsional modes are 68 and 175, respectively.

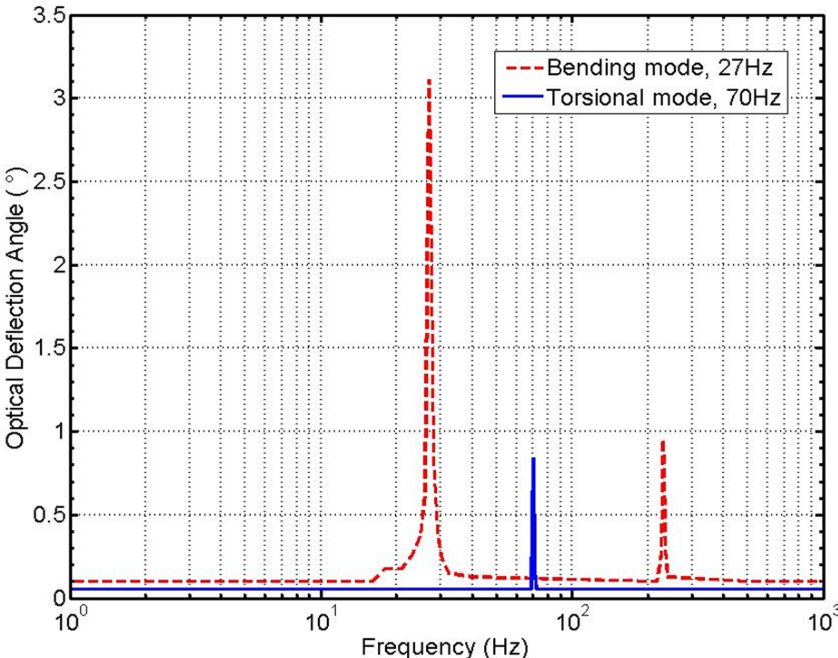

Fig. 4-7. Frequency response showing a semi-log plot of measured ODA versus excitation frequency at 0.5 V_{pp} for both bending and torsional modes.

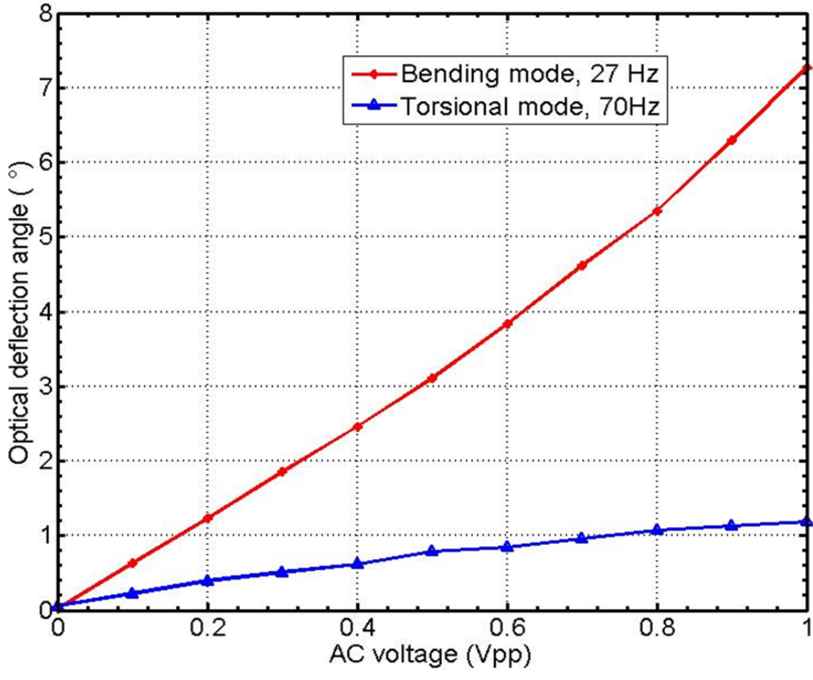

Fig. 4-8. AC response for bending and torsional modes where the MEMS scanner was excited independently with ac signals of 27 Hz and 70 Hz, respectively.

The dynamic ac response of the MEMS scanner under bending and torsional modes were investigated and presented in Fig. 4-8. In the biasing setup for bending mode operation, the actuator was excited with a 27 Hz signal and ac voltages up to 1 V_{pp} applied to it. The MEMS scanner achieved an ODA of ±7.26° at 1 V_{pp} during dynamic actuation, which is significantly larger when compared to the ODA of 0.22° obtained at 1 V_{dc} during static actuation. This phenomenon is due to the device attaining mechanical resonance, resulting in maximum energy transfer from the ac electrical excitation signal to the vibrating mechanical structures. For torsional mode operation, the biasing setup was similar to that in bending mode except that an ac signal with frequency of 70 Hz, instead of 27 Hz, was applied. An ODA of ±1.18° was observed at 1 V_{pp} during torsional mode operation. For the same peak-to-peak voltage, the ODA obtained during bending mode is much larger than that for torsional mode. This is because in bending mode, the mirror undergoes translational and rotational motion along the y-axis, whereas in torsional mode, the mirror only rotates along the x-axis (Fig. 4-1(a)). As such, rotational motion of the mirror plate during torsional mode would not induce displacement of the reflection point as bending mode do, hence making bending mode more efficient in beam steering.

In mixed mode operation, two ac electrical signals of 27 Hz and 70 Hz, corresponding to the resonant frequencies of bending and torsional modes, respectively, were applied simultaneously to the device so as to achieve 2-D scanning capability. The biasing circuit to realize mixed mode operation is illustrated in Fig. 4-9. Two function generators, each carrying sinusoidal

signals with frequencies of 27 Hz and 70 Hz, respectively, were inputted into a summing amplifier (Motorola MC1741C). Unlike our previous approach in chapter 2 where two ac signals of different frequencies can be applied separately to two different sets of actuators to achieve 2-D scanning effect, a summing amplifier is needed for our current MEMS scanner design as it has only one PZT actuator and two bond pads available for biasing. With the summing amplifier, two ac signals carrying resonant frequencies corresponding to bending and torsional modes can now be superimposed into one signal, which were used to excite and drive the PZT actuator to achieve 2-D scanning effect. The values of the resistors R_1, R_2 and R_f were chosen such that the summing amplifier has unity gain, i.e., the output voltage (V_{out}) of the summing amplifier is equivalent to the summation of the input voltages (V_B and V_T).

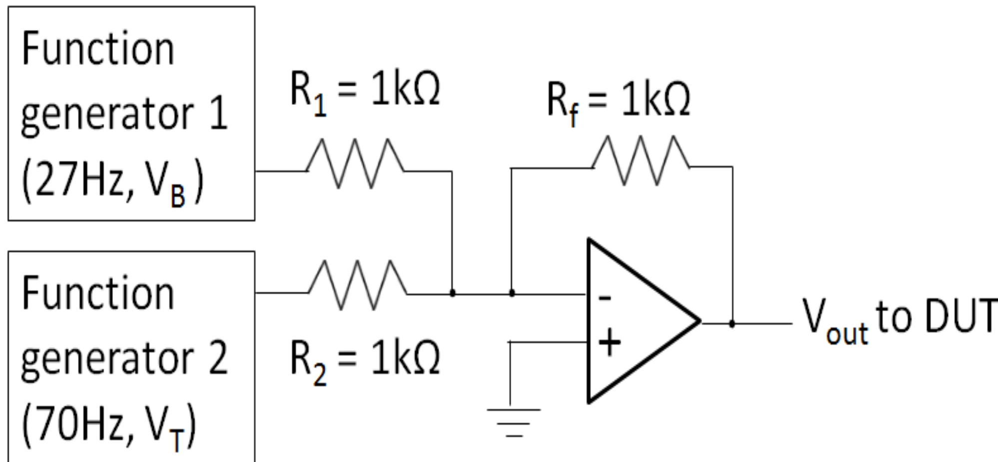

Fig. 4-9. Schematic diagram illustrating the biasing circuit required to produce 2-D scanning pattern. Two sinusoidal waveforms of different frequencies were inputted into a summing amplifier. V_B and V_T denote the peak-to-peak voltage for the ac excitation signals with frequencies 27 Hz and 70 Hz, respectively.

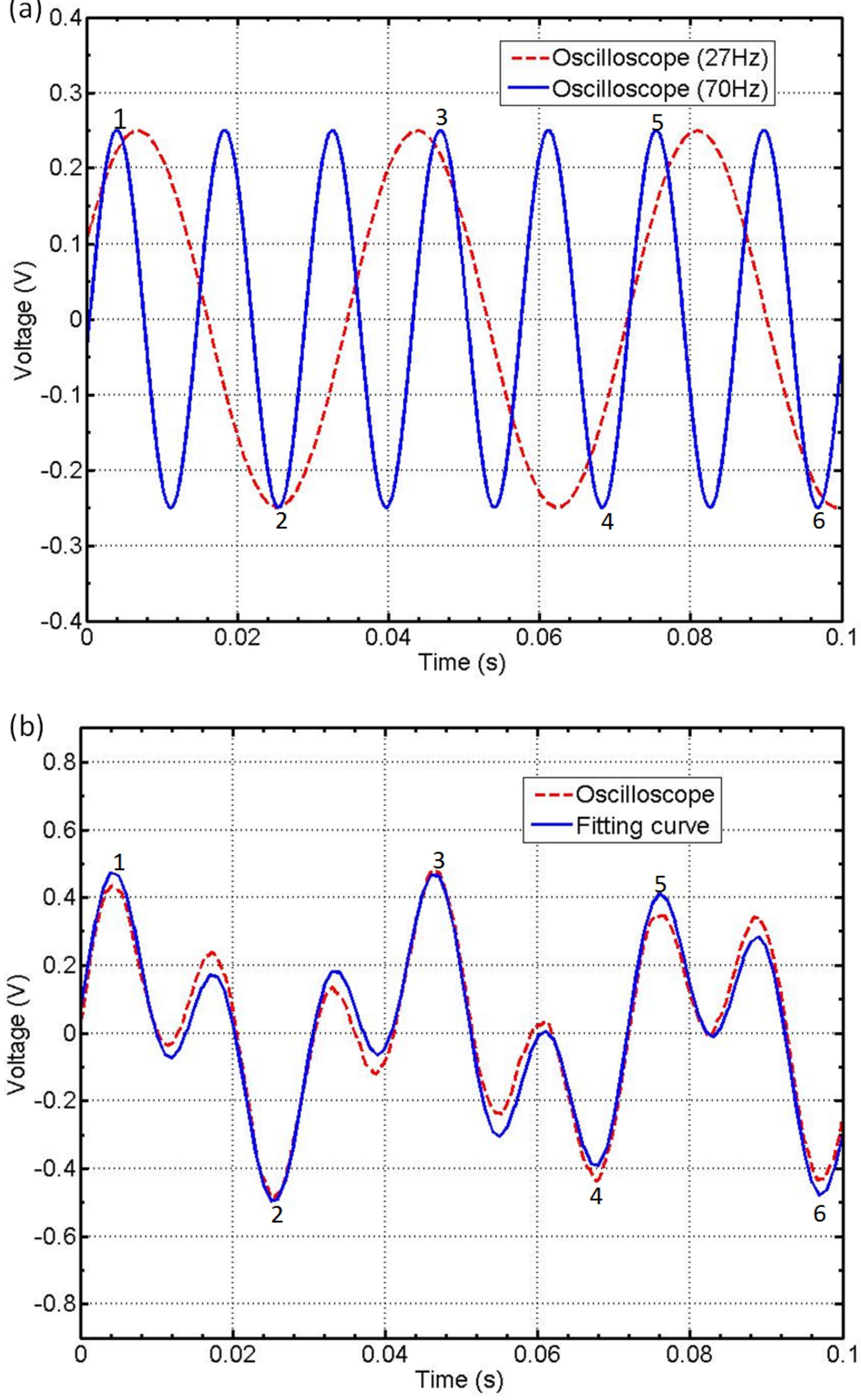

Fig. 4-10. Waveform obtained from different voltage output. (a) Dotted (red) and solid (blue) curves show the respective output of the 2 function generators when both V_B and V_T were at 0.5 V_{pp}. (b) Dotted (red) curve shows the resultant output from the summing amplifier V_{out} when V_B and V_T are 0.5V_{pp}.

To better understand and prove the effect of the summing amplifier on the two input ac signal, a HP/Agilent 54825A Infiniium Oscilloscope was used to read the output signals. Fig. 4-10(a) and 4-10(b) show the signals detected from the output of the function generators and summing amplifier, respectively, when both V_T and V_B were at 0.5 V_{pp}. The red dotted curve in Fig. 4-10(a) shows the trace given by V_B, i.e. the output of the first function generator with a 27 Hz and 0.5 V_{pp} sinusoidal waveform, while the blue solid curve shows the trace given by V_T, i.e. the output of the second function generator with a 70 Hz and 0.5 V_{pp} sinusoidal waveform. Both the red dotted and blue solid curves in Fig. 4-10(a) can be represented mathematically by equations (4.2) and (4.3) as:

$$V_B = -0.25sin[\omega_B(t+t_1)] \quad (4.2)$$

$$V_T = -0.25sin[\omega_T(t+t_1)] \quad (4.3)$$

$$V_{out} = -\left[0.25sin[\omega_B(t+t_1)] + 0.25sin[\omega_T(t+t_1)]\right] \quad (4.4)$$

where $\omega_B = 2\pi(27)$ Hz, $\omega_T = 2\pi(70)$ Hz and t_1 is the amount of time shift needed to match the mathematically derived sinusoidal curves with the oscilloscope traces.

In Fig. 4-10(b), the red dotted curve shows the trace detected on the oscilloscope from the output of the summing amplifier, i.e., $V_{out,}$ when two sinusoidal signals of 27Hz and 70Hz are inputted into the summing amplifier. On the other hand, the blue solid curve shows the fitting curve derived and plotted based on equation (4.4). The close fitting of the blue solid curve with the red dotted curve in Fig. 4-12(b) confirms that the output of the summing

amplifier is equivalent to the fitting curve. In other words, the summing amplifier superimposed the two sinusoidal signals of the function generators represented by equations (4.2) and (4.3), and produced the resulting waveform that obeys well with theoretical equation (4.4). Such experimental confirmation is important as it ensures that the output superimposed signal from the summing amplifier remains controllable through the adjustment of the various parameters such as frequencies, V_T, and V_B. More importantly, it proves that the output signal from the summing amplifier retains the ac characteristics of the input signals from the function generators. This permits us to bias the MEMS scanner with resonant frequencies corresponding to bending and torsional modes simultaneously, allowing it to achieve 2-D scanning effect with only one PZT actuator. The major peaks in Fig. 4-10(b) have also been numerically labelled and by matching these major peaks with the corresponding peaks in Fig. 4-10(a), we can infer that these major peaks are largely attributed by the peaks of the blue curve (70Hz) in Fig. 4-10(a).

Fig. 4-11 shows the different waveforms of V_{out} obtained from the oscilloscope when various combinations of V_B and V_T were used. Fig 4-11(a) illustrates a pure sinusoidal V_{out} of 1 V_{pp} and frequency of 27 Hz when $V_B = 1$ V_{pp}, $V_T = 0$ V_{pp}. As the value of V_B decreases and V_T increases as illustrated from Fig. 4-11(a) to Fig. 4-11(d), more peaks were observed in the resultant waveform V_{out}. This is due to the increased contribution from the 70 Hz signal from function generator 2, as a 70 Hz signal has more peaks per unit time when compared to the 27Hz signal from function generator 1.

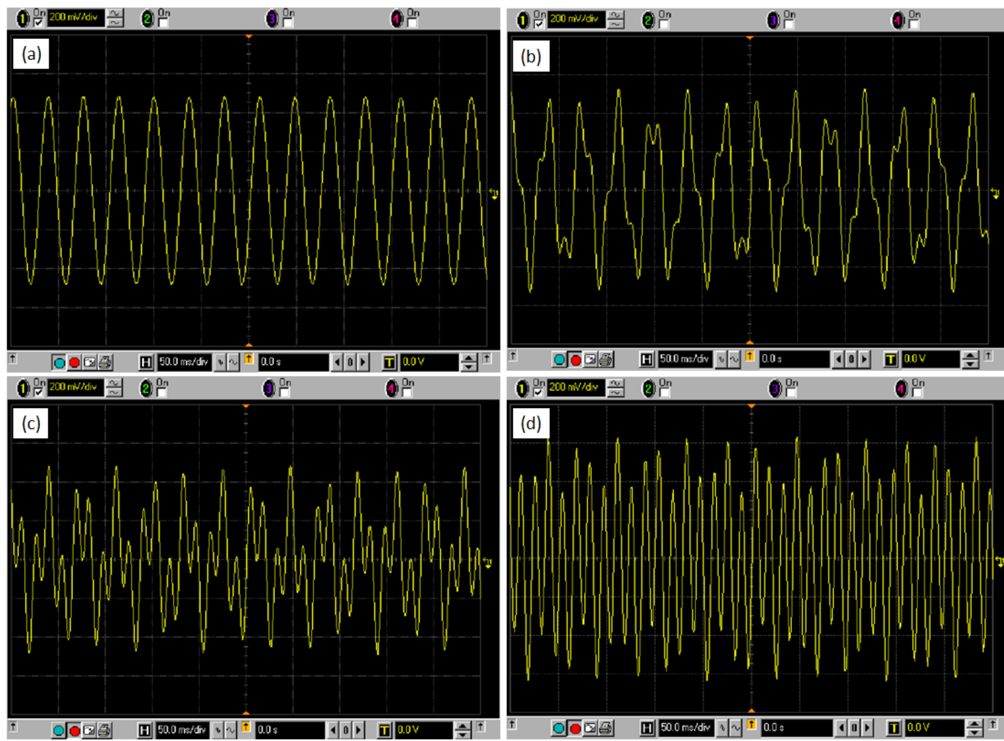

Fig. 4-11. Screenshot capture of the waveforms obtained from a oscilloscope connected to the V_{out} terminal, with various voltage bias combinations such as (a) $V_B = 1V_{pp}$, $V_T = 0V_{pp}$, (b) $V_B = 0.8V_{pp}$, $V_T = 0.3V_{pp}$, (c) $V_B = 0.5V_{pp}$, $V_T = 0.5V_{pp}$, and (d) $V_B = 0.3V_{pp}$, $V_T = 1V_{pp.}$

Fig. 4-12 shows the 2-D Lissajous scanning patterns obtained when various combinations of sinusoidal V_B and V_T were supplied by the two function generators and superimposed by the summing amplifier. In Fig. 4-12(a) and 4-12(b), straight horizontal laser trajectory lines, corresponding to ODAs of ±39° and ±7.2°, were obtained when 3 V_{pp} and 1 V_{pp} sinusoidal waveform were supplied by function generator 1, respectively. In Fig. 4-12(c) to 4-12(e), mixed mode occurs as both function generators were utilized, creating 2-D Lissajous scanning patterns on the screen. As the magnitude of V_B decreased from 1 V_{pp} in Fig. 4-12(b) to 0.3 V_{pp} in Fig. 4-12(e), the horizontal trajectory length or ODA along the horizontal axis dropped from ±7.2° to ±1.85°. Similarly, in the case for vertical scanning, as the magnitude of V_T increased from 0 V_{pp} in Fig. 4-12(b) to 1 V_{pp} in Fig. 4-12 (e), the vertical ODA increased from 0° to ±1.18°.

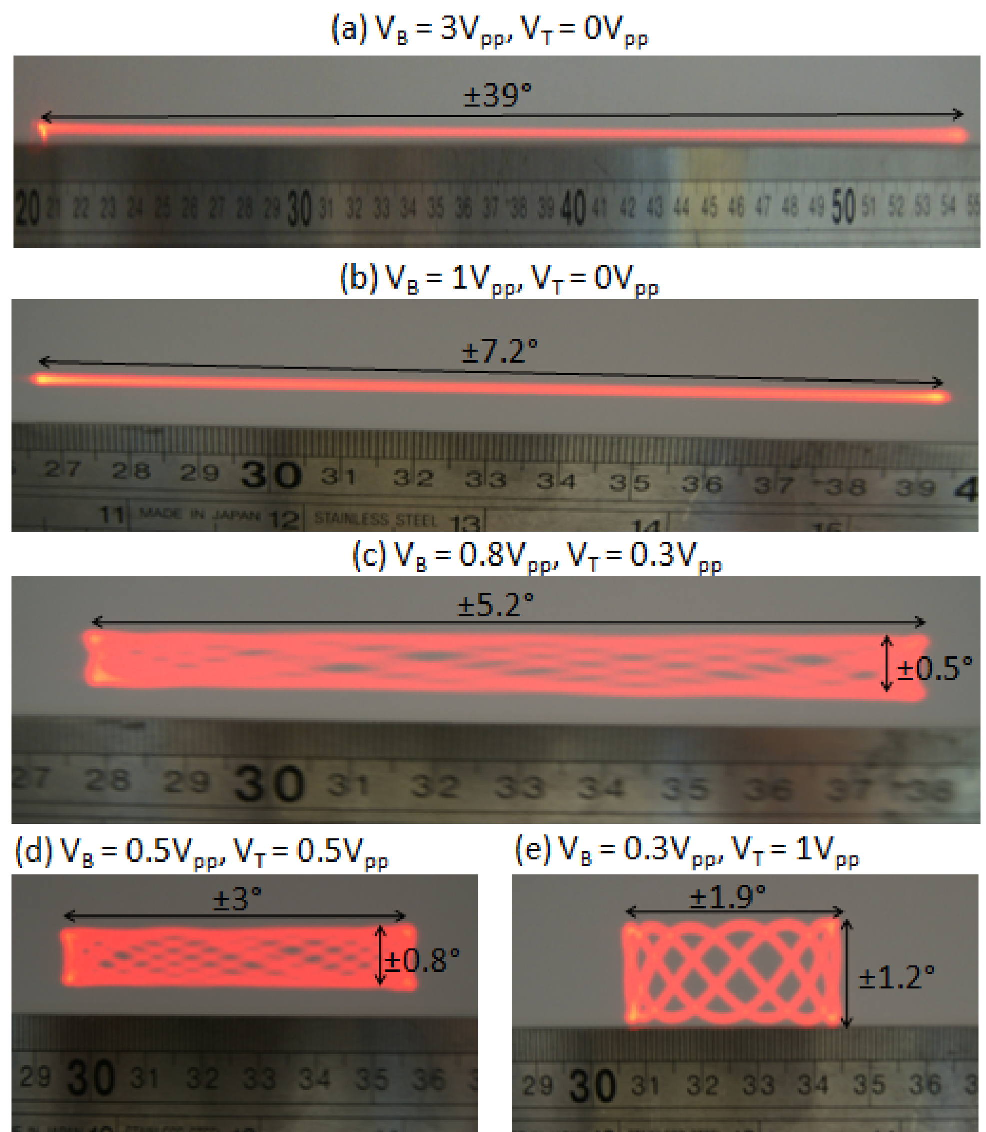

Fig. 4-12. 2-D Lissajous scanning patterns obtained when various combinations of sinusoidal V_B and V_T were supplied by the two function generators and superimposed by the summing amplifier, where (a) $V_B = 3V_{pp}$, $V_T = 0V_{pp}$, (b) $V_B = 1V_{pp}$, $V_T = 0V_{pp}$, (c)$V_B = 0.8V_{pp}$, $V_T = 0.3V_{pp}$, (d) $V_B = 0.5V_{pp}$, $V_T = 0.5V_{pp}$, and (e) $V_B = 0.3V_{pp}$, $V_T = 1V_{pp}$. The experimental setup of the scanning line obtained in (a) were slightly different from those obtained in (b)-(e) so that the entire scanning line can be accommodated onto the ruler scale.

In addition, the values of horizontal and vertical ODA obtained during mixed mode operation correspond closely to the results obtained independently during bending and torsional mode operations, as shown in Fig. 4-8. For example, from Fig. 4-10, ODAs of ±3.1° and ±0.8° were obtained at $0.5V_{pp}$ for bending and torsional modes respectively. These values are almost identical to those obtained during mixed mode in Fig. 4-12(d), where

horizontal and vertical ODA of ±3° and ±0.75° were obtained. These matching results implies that there was minimum coupling between the vertical and horizontal scanning axes during mixed mode operation and the summing amplifier only acts as an interface to superimpose the two ac signals from the function generators into one to excite the device. More importantly, the horizontal and vertical dimensions of the 2-D Lissajous pattern can be independently controlled by the ac biasing signals, hence offering flexibility and tunability.

4.5 Performance comparison of current designs with existing piezoelectric MEMS scanners

Table 4-2 compares the existing piezoelectric MEMS mirror performances according to the figure of merit (FOM), which is being used as a metric to compare the relative scanning efficiencies:

$$FOM = \frac{\theta_{opt} Df}{V}$$

where θ_{opt} is the total optical deflection angle (°), D is the mirror size along the scan axis (mm), f is the resonant frequency (kHz), V is the root-mean-square drive voltage (V). Regretfully, the piezoelectric MEMS scanners (designs A and B) investigated in chapter 1 fared poorly, while the S-shaped actuator driven MEMS scanner performed moderately when compared with other existing piezoelectric MEMS scanners that have been reported in the literature in the past decade. In the piezoelectric MEMS scanners deploying gimbal

Table 4-2. Comparison of FOM for different PZT MEMS scanner designs.

Ref	Unique feature	Frequency (Hz)	Mirror size (l × w × t)	FOM
Design A (Chapter 1)	2-D MEMS scanner driven by 1x10 actuator electrically connected in series	34	5mm × 5mm × 0.4mm	0.7
Design B (Chapter 2)	2-D MEMS scanner driven by 1x10 actuator electrically separated	30	5mm × 5mm × 0.4mm	0.3
Design C (Chapter 3)	2-D MEMS scanner driven by S-shaped actuator	27	1.65mm × 2mm × 0.4mm	1.6
Kobayashi *et al.* [136]	Low speed 1-D MEMS scanner	30	8mm × 2mm × 0.005mm	0.10
Gilchrist *et al.* [137]	1-D PZT cantilever MEMS scanner	650	0.6mm × 0.84mm × 0.03mm×	1.6
Chen *et al.* [87]	2-D MEMS scanner with inner and outer frame, gimbaled design	560	1mm × 1mm × 0.06mm	6.32
Yasuda *et al.* [69]	2-D MEMS scanner with inner and outer frame design, gimbaled design	4,300	1mm × 2mm × 0.02mm	6.6
Filhol et al. [138]	1-D MEMS gimbaled scanner	10,600	0.5mm diameter, 0.02mm thick	13.5
Baran *et al.* [71]	State-of-the-art 1-D gimbaled MEMS scanner	40,000	1.4mm diameter, × 0.3mm thick	146

designs demonstrated in refs. [69, 71, 87, 138], the torsion bar can be designed to reduce torsional stiffness without affecting the piezoelectric actuator

performance, and hence resulting in larger optical deflection angle. In addition, the small mirror plate used in these references reduces the mass inertia of the scanners, hence allow the resonant frequencies of these scanners to reach the kHz range. Both these factors, i.e. large optical angle and resonant frequency, explain why these existing MEMS scanners report high FOM. In the case of the 1-D high speed piezoelectric MEMS scanner demonstrated by Baran *et al.* in ref. [71], the exceptionally high FOM reported is due to a cascaded frame operating out-of-phase design, which allows the limited deflection of PZT actuator to be amplified to achieve large mirror rotation at resonance.

While such gimbaled, inner and outer frame piezoelectric MEMS scanners have been widely reported in the last decade which guarantee good performance, however, replicating such conventional designs is not the goal of this thesis. With one of the objectives targeting at developing proof-of-concept 2-D MEMS scanners driven by novel actuation mechanisms, gimbal-less designs making use of only a single set of piezoelectric actuator/s to elicit 2-D scanning, hence, becomes the goal as such designs have yet to be reported. Although the proposed piezoelectric MEMS scanner designs in chapter 1 and this chapter fared inferiorly, at this moment, compared to the conventional ones, there are still much room for improvement through the reduction of the mass inertia of the mirror plate. It is also noteworthy that the performances of the piezoelectric 2-D MEMS scanners have improved with each development cycle, starting from design A in chapter two to the S-shaped actuator driven design in this chapter.

4.6 Summary

In this chapter, development work on a novel piezoelectric driven MEMS scanner using a single S-shaped PZT actuator was explored and characterized. Instead of deploying a 1×10 array of PZT actuator design as demonstrated in chapter 2 or multiple meandering PZT actuators for inner and outer frames, our current unique proof-of-concept design of utilizing only one piezoelectric actuator has successfully demonstrated 2-D scanning by having two superimposed ac signals to drive the mirror simultaneously.

Both the DC and AC responses of the device were characterized. An ODA of 3.35° was achieved at 10 V_{dc}. Bending and torsional modes occur when ac electrical signals with resonant frequencies of 27 Hz and 70 Hz were used to excite the device, respectively. The maximum measured ODA obtained at 1 V_{pp} are ±7.26° and ±1.18°, respectively. For the same ac driving voltage, the ODA achieved by this S-shaped actuator design is significantly larger than that of the 1×10 PZT actuator design in chapter 2. In mixed mode operation, two ac electrical signals of 27Hz and 70Hz were applied simultaneously to the devices using a summing amplifier, hence enabling the mirror to achieve 2-D scanning capability. The device has performed successfully various Lissajous patterns, exhibiting flexibility and tunability through the adjustment of biasing voltages V_B and V_T. Further reduction of the driving voltage is possible by reducing the size and thickness of the mirror.

So far in this thesis, several piezoelectric actuated MEMS mirrors driven by novel actuation mechanisms have been investigated for 2-D scanner

and variable optical attenuator applications. However, the piezoelectric material (lead zirconate titanate) used is not CMOS compatible. Thus, attempts to explore CMOS compatible MEMS mirrors for 2-D scanner and variable optical attenuator will be made in chapters 5 and 6, respectively. The developed CMOS compatible MEMS mirror will allow for lower fabrication cost and monolithic integration with transistor circuits that enable electronic feedback to be made possible.

Chapter 5
A MEMS Scanner Using Hybrid Actuation Mechanisms With Low Operating Voltage

5.1 Introduction

Hybrid actuation mechanisms, i.e. combination of two or more of the four actuation schemes introduced in chapter 1, have already been demonstrated in various forms of MEMS devices such as RF switches [139], energy harvesters [140, 141] and mirrors [142, 143]. The combination of both electromagnetic and electrostatic actuation mechanisms in the RF MEMS switch design proposed in ref. [139] by Cho *et al.* allows them to achieve excellent switching characteristics at low power and voltage. Similarly, for both the cases of energy harvesters in ref. [140] and [141] where hybrid energy harvesting mechanisms were investigated, these devices demonstrated higher output power density when both the piezoelectric and electromagnetic elements were deployed.

In this chapter, the concept of mechanical amplification adopted in the design of the 1-D MEMS scanner in ref. [99] is leveraged while 2-D scanning using the single mirror approach is proposed. In addition, both electrothermal (ET) and electromagnetic (EM) actuation schemes will be integrated in our proof-of-concept MEMS scanner design. This approach differs greatly from most of the MEMS scanner designs already reported in the literature where the same actuation scheme is often used to drive both the orthogonal scanning

axes of the devices. Unlike the hybrid actuation approach taken on by Li *et al.* in ref. [142] and [143] where electrostatic comb drive actuators were used for the fast scanning actuation in their fabricated MEMS scanners, EM actuation has been chosen to drive the fast scanning axis in the mirror design proposed here. This is primarily due to the low actuation voltage and CMOS compatibility which EM actuation offers, hence allows for ease of monolithic integration with CMOS IC and lowers fabrication cost. The slow scanning axis will be driven by ET actuators as they have large static or dynamic displacement characteristic at low resonant condition. Such hybrid actuation mechanism proposed in this design allows for fast line scan driven by EM actuators operating at mechanical resonance condition to be produced on the horizontal axis, while a slower sweep, i.e. frame rate driven by ET actuators to be produced on the orthogonal vertical axis. As such, this unique design of using both ET and EM actuators, as well as mechanical amplification mechanism to excite 2-D raster scanning is the first demonstration of such hybrid-driven CMOS compatible MEMS mirror.

5.2 Design & Modeling

A schematic diagram of the proposed MEMS scanner incorporating hybrid actuation mechanisms is shown in Fig. 5-1. There are four sets of ET actuators responsible for the slow scanning about the horizontal axis, i.e. x-axis. The ET actuators are anchored to the substrate and are joined to the frame by C-shaped rigid hinges. EM coils are embedded in the frame, and in the presence of current flow and magnetic field will generate a mechanical torque, producing fast scanning about the horizontal axis, i.e. z-axis. The

mechanical energy from the EM actuation is coupled to the mirror plate through the T-shaped torsion bar. The details of the working principle and the modeling for both ET and EM actuations will ensue on in this section.

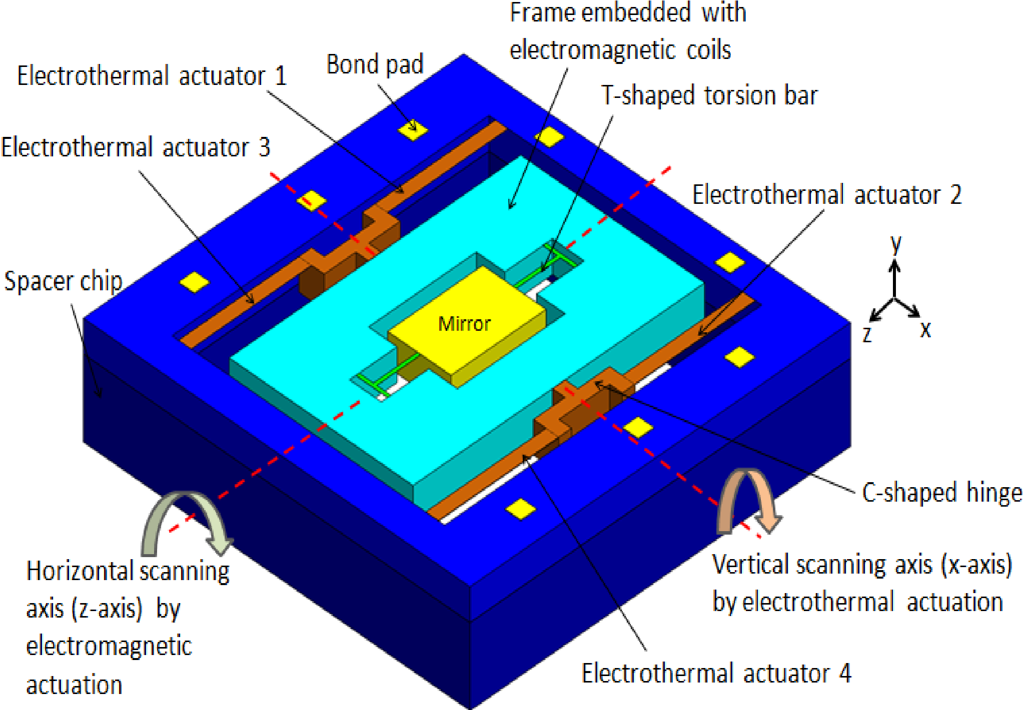

Fig. 5-1. Schematic diagram of the proposed MEMS scanner incorporated with hybrid actuation mechanisms. The vertical and horizontal scanning motions are driven by ET and EM actuation mechanisms, respectively.

5.2.1 Electrothermal Actuation

The design of the ET actuator is shown in Fig. 5-2(a). It consists of a silicon (Si) cantilever made from the device layer of a silicon-on-insulator (SOI) wafer and aluminum (Al) heater deposited and patterned on it. As shown in the inset of Fig. 2(a), the Al heater is patterned in a winding manner so as to increase the resistance and thermal reliability of the heater and actuator respectively. There are a total of 22 Al windings designed to have a resistance of 500Ω. Thin layer of SiO_2, which acts as thermal insulation, is deposited around Al to increase the actuation efficiency. Together with the Si

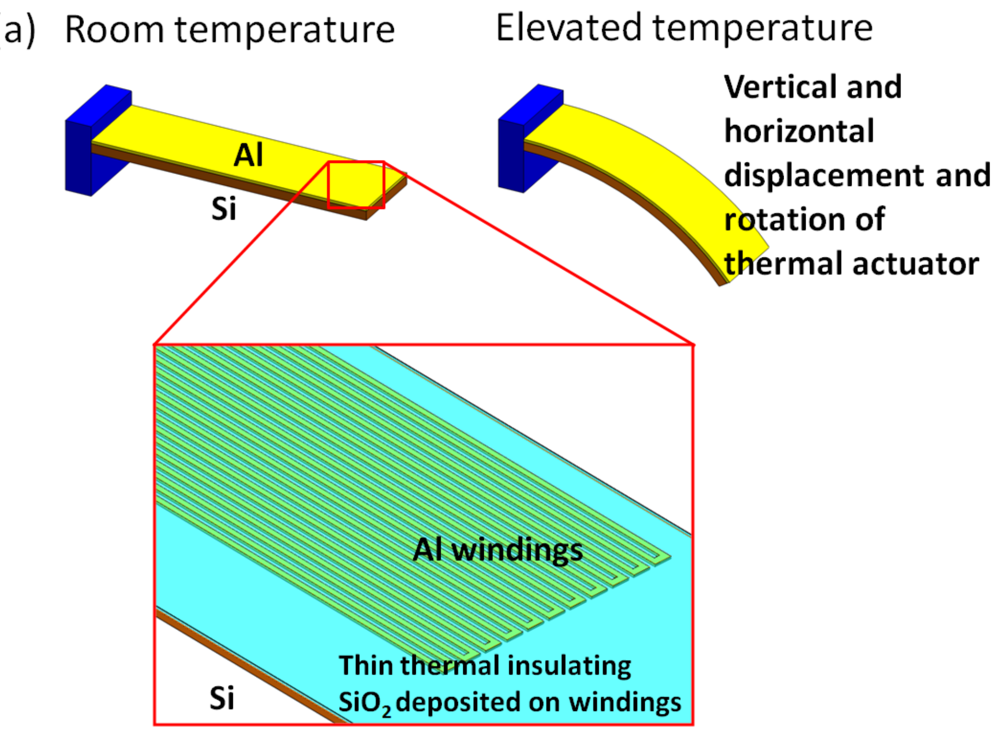

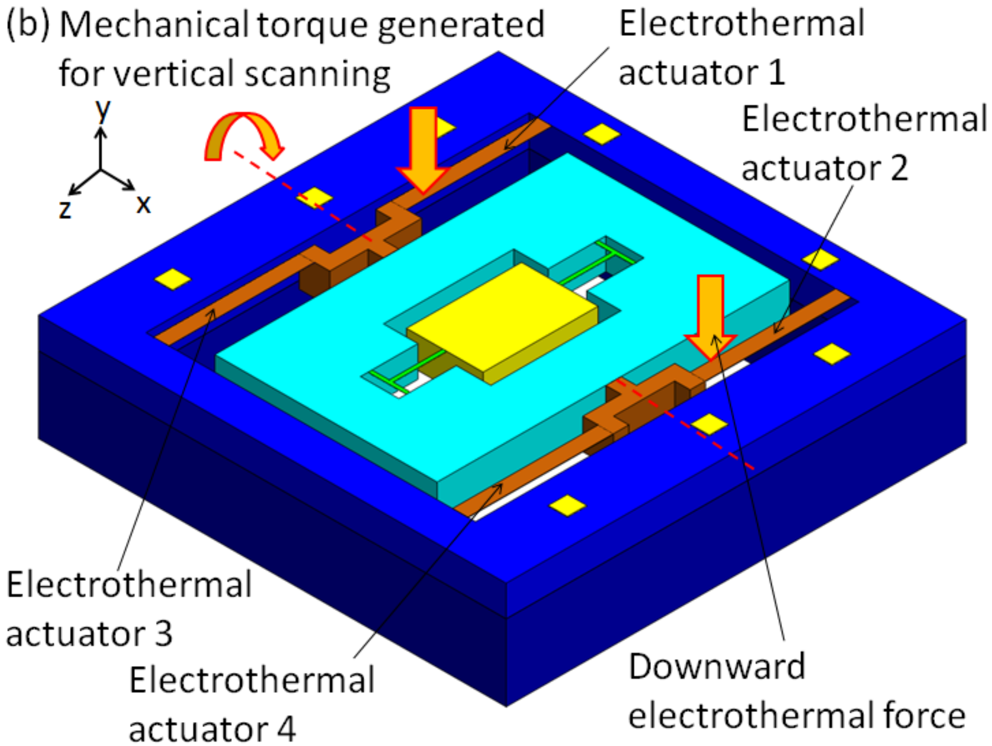

Fig. 5-2. Schematic diagram illustrating the (a) proposed ET bimorph actuator made of Al and Si, with the inset showing the winding design of the Al metal layer and thin thermal insulating SiO_2 deposited around the windings; (b) working principle of ET actuation and rotation about the vertical scanning axis i.e. x-axis when ET actuators 1 & 2 are biased serially to give a mechanical torque.

device layer used in the cantilever structure, the Al heater also functions as the other bimorph material for thermal actuation. When a current flows through the windings, the Al heats up and expands more than silicon, causing the actuator to bend downwards. To obtain the desired rotating orientation of the mirror, selective biasing and bending of the four sets of ET actuators can be made. For example, to achieve vertical scanning about x-axis as shown in Fig. 5-2(b), actuators 1 and 2 are biased serially so that both the actuators experience downward displacements simultaneously, hence introducing a mechanical torque about x-axis. Electronic control may be utilized to phase lock the biasing of the actuators such that there is a 180° phase delay between the voltage bias for actuators 1 and 2 with 3 and 4. This will enable bidirectional scanning capability, hence increasing the range of scanning.

Prior to fabrication, optimization based on mathematical modeling is done to determine the effect of the thickness of Si device layer of a SOI wafer and Al layer on the performance of the actuator. The tip displacement of a typical fixed-free bimorph beam of Al and Si under a strain mismatch has been readily derived in equation (5.1),

$$\delta = \frac{3w_{Si}w_{Al}E_{Si}E_{Al}t_{Si}t_{Al}(t_{Si}+t_{Al})(\alpha_{Al}-\alpha_{Si})\Delta TL^2}{(E_{Al}W_{Al}t_{Al}^2)^2+(E_{Si}W_{Si}t_{Si}^2)^2+2w_{Si}w_{Al}E_{Si}E_{Al}t_{Si}t_{Al}(2t_{Al}^2+3t_{Si}t_{Al}+2t_{Si}^2)} \quad (5.1)$$

where δ is the tip displacement of a bimorph beam, w_{Al} and w_{Si} are the width of the Al (200 µm) and Si (200 µm) layers, respectively, E_{Al} and E_{Si} are the Young's modulus of Al (65 GPa) and Si (167 GPa), respectively, α_{Al} and α_{Si} are the coefficient of thermal expansion of Al (2.6×10^{-6} K^{-1}) and Si (23.1×10^{-6} K^{-1}), respectively, L is the length of the beam (2.1 mm), ΔT is the

temperature change, t_{Al} and t_{Si} are the thickness of the Al and Si layers, respectively [144]. Using equation (5.1), the displacement change at tip of the bimorph beam actuator for different bimorph material thickness is analyzed and plotted in Fig. 5-3. As evident from Fig. 5-3, a thinner Si layer will give rise to better actuator performance. However, the tradeoff lies in the mechanical stability of the actuator as a thin Si cantilever breaks off from its anchor region easily. In view of these considerations, we started our fabrication using SOI wafers with 3 µm thick Si device layer for added mechanical stability as well as reasonable actuator performance. Besides investigating the influence of Si device layer thickness on the actuator performance, the impact of Al thickness on the actuator displacement is examined as well. For a Si device layer thickness of 3 µm, an optimal Al thickness of 2 µm yields maximum actuator performance. This leads us to use a thickness of 2 µm for our Al windings during the fabrication process.

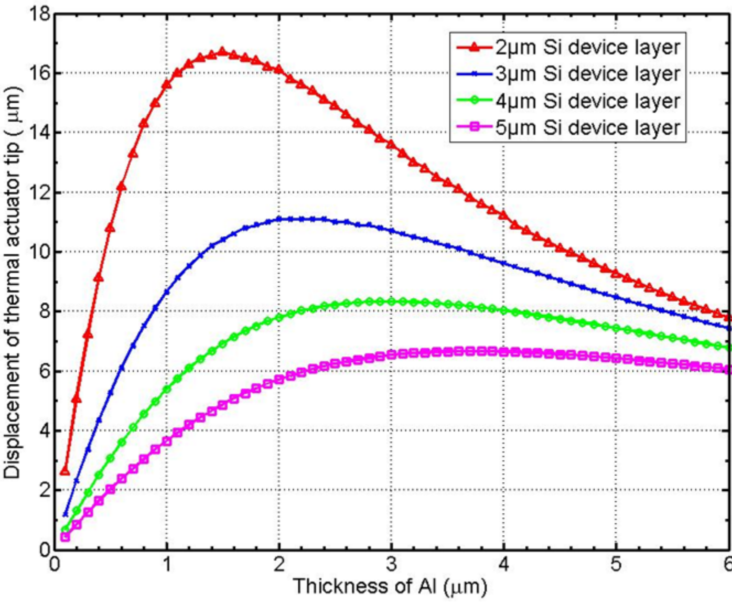

Fig. 5-3. Simulated plot illustrating the change in the tip displacement of a single clamped ETI actuator for a unit temperature change. The thickness of the Al metal layer is varied from 0.1µm to 6µm for different Si device layer thickness of a SOI wafer.

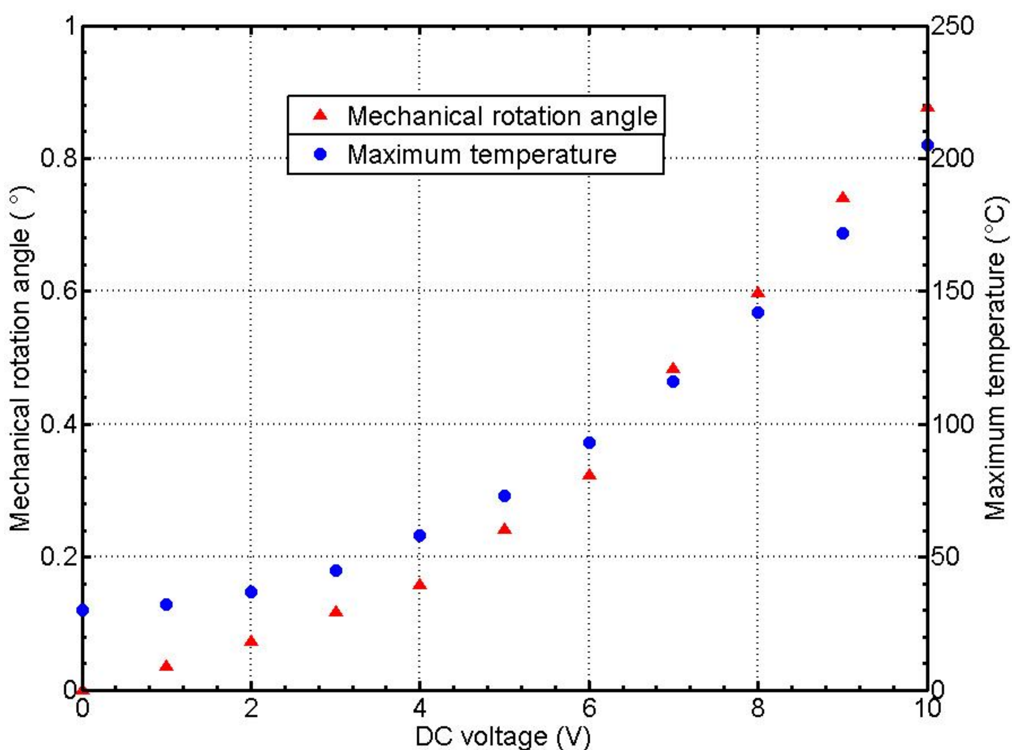

Fig. 5-4. Plots of mechanical rotation angle and maximum temperature of device versus total dc voltage applied to actuators 1 and 2. Results are obtained from FEM simulation using ANSYS.

Finite element method (FEM) based on the proposed ET actuator design is made using ANSYS simulation software. Fig. 5-4 shows the simulated plots of mechanical rotation angle and maximum temperature of device versus total dc voltage applied to actuators 1 and 2. As the dc voltage applied to actuators 1 and 2 increases, the mechanical rotation of the mirror and the maximum temperature of the actuator increases. These trends are expected as increase in current flow will result in greater actuator displacement and heating effect. More importantly, a maximum simulated temperature of 205 °C, which is well below the melting point of Al, is obtained at 10 V_{dc}. This signifies good device reliability within the bias range of 10 V_{dc}. The thermo-mechanical properties of the different material used in the ANSYS simulation are summarized in table 5-1.

Table 5-1. Thermo-mechanical properties of materials used for ET actuator simulation and modal analysis in ANSYS.

Thin film materials	Density (kgm^{-3})	Young's Modulus (10^9 Pa)	Poisson ratio	Thermal conductivity ($Wm^{-1}K^{-1}$)	Coefficient of thermal expansion (10^{-6} K^{-1})	Resistivity (10^{-3} Ωm)
Al	2700	65	0.33	237	23.1	2.82×10^{-5}
SiO_2	2200	74	0.17	1.04	0.4	1×10^{19}
Si	2330	167	0.28	150	2.6	100

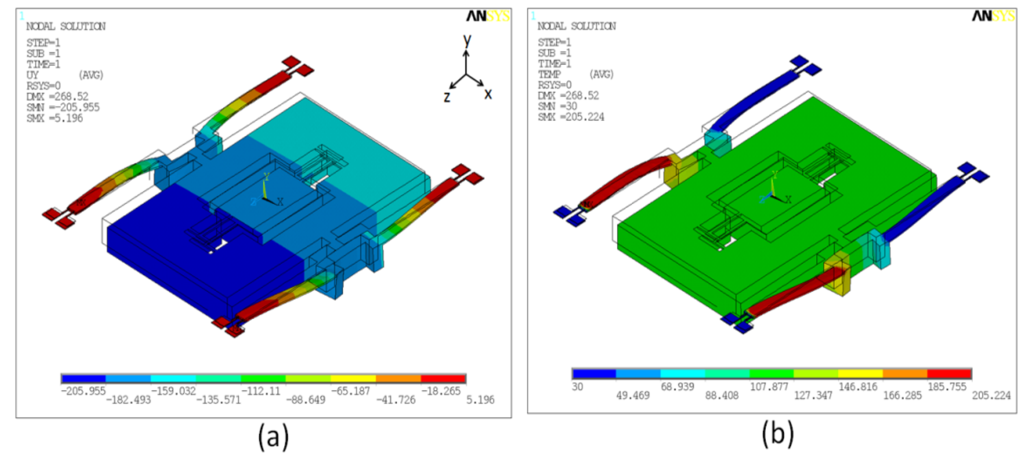

Fig. 5-5. Simulation result by ANSYS when ET actuators 3 and 4 are biased with a total DC voltage of 10V. (a) Y-displacement profile of the device where the mirror rotates about the x-axis. (b) Temperature distribution profile of the device.

The Y-displacement and temperature distribution profiles at 10 V_{dc} are shown in Fig. 5-5(a) and 5-5(b), respectively. In Fig. 5-5(a), a mechanical rotation angle of approximately 0.9° is obtained when a total voltage of 10 V_{dc} is applied to actuators 3 and 4. In addition, parasitic vertical out-of-plane displacement of approximately 170 µm can be noted at the center of the mirror. Such out-of-plane displacement may lead to off-center shift of laser spot. This is due to the limited capability of the four ET actuators to only actively actuate downwards, but not upwards as it would be needed for pure tilt motion without the off-center shift of laser spot. Fig. 5-5(b) shows the

temperature distribution profile of the device, where the greatest rise in temperature occurs at the biased ET actuators 3 and 4. The unbiased actuators 1 & 2 remains at room temperature while an uniform temperature of approximately 100°C is observed for the frame and mirror plate.

5.2.2 Electromagnetic Actuation

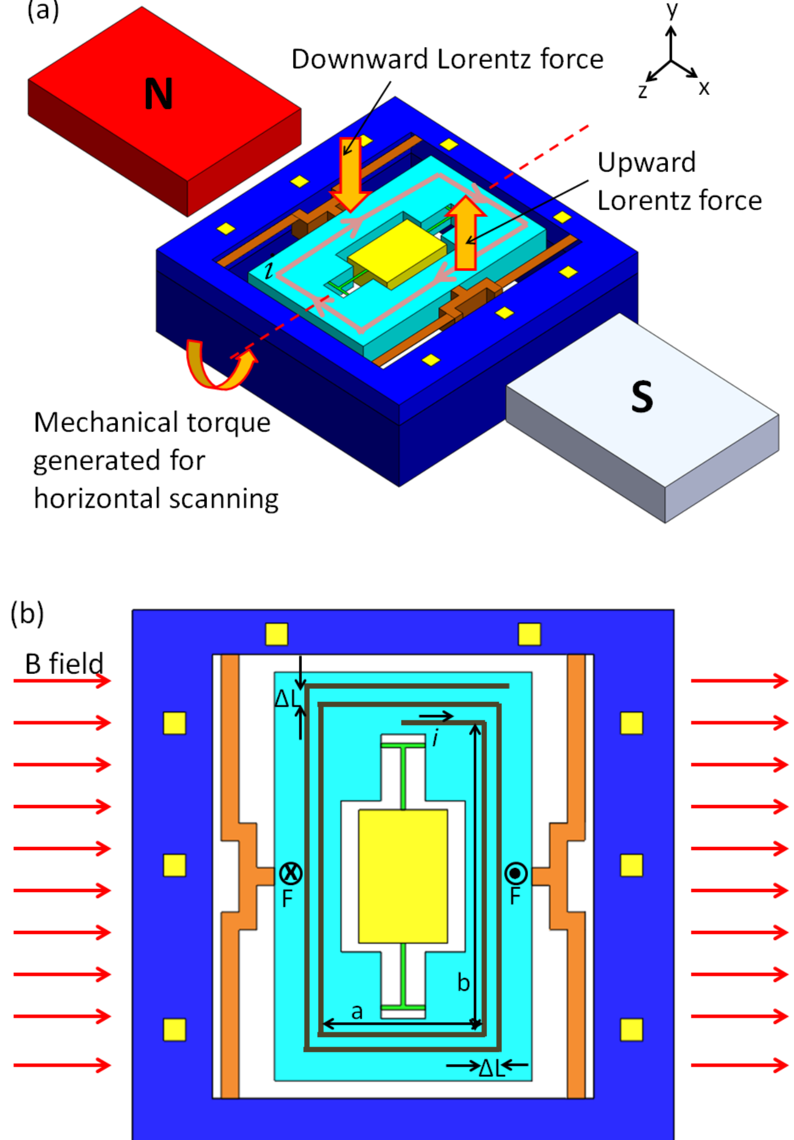

Fig. 5-6. Schematic drawing illustrating the working principle of EM actuation and rotation about the horizontal scanning axis i.e. z-axis when a mechanical torque, in the presence of external magnetic field, is generated due to the current flow in the coil embedded in the frame. (b) Top viewing drawing illustrating the dimensions of the coils. Two turns of the EM coil are shown for simplicity.

The horizontal scanning induced by EM actuation is based on the Lorentz force excitation of the MEMS mirror, which in turn is created by an external magnetic field and current carrying EM coils. Fig. 5-6(a) and 5-6(b) show the three-dimensional and top view schematic drawing of the mirror device in the presence of magnetic field. Two layers of EM coils, each having 54 turns, were deposited and patterned on the frame. Both layers of coils, which are made of Al, run in the same clockwise direction so that the Lorentz forces generated in both layers are the same. A pair of permanent magnets, as shown in Fig. 5-6(a), is arranged such that a magnetic field along the x-direction is formed across the device. The current direction is reversed across the scan axis due to the current forming a loop in the EM coils on the frame. This causes a change in direction of the Lorentz force across the scan axis, resulting in a torque normal to the external magnetic to be generated about the z-axis. To achieve continuous horizontal scanning operation, an AC current will be needed so that the Lorentz force and mechanical torque generated change direction according to the direction of current flow. As shown in Fig. 5-6(b), the out-of-plane Lorentz force acting on a DC current carrying conductor is given as:

$$\mathrm{F} = \oint_{\mathrm{L}} I\mathrm{dl} \times \mathrm{B} \qquad (5.2)$$

where I is the current flowing in a closed circuit of length L and B is the external magnetic field. The torque generated about z-axis is approximated as [74]:

$$\mathrm{T} = 2i\mathrm{B}\sum_{\mathrm{m}=0}^{\mathrm{N}-1}(\mathrm{b}+2\mathrm{m}\Delta\mathrm{l})(\mathrm{a}+2\mathrm{m}\Delta\mathrm{l}) \qquad (5.3)$$

where i is the current flowing in the EM coils, N is the number of coil turns, a and b are the side lengths of the most inner coil turn on the short and long sides of the frame respectively. The first term in the summation component of equation (5.3) arises from the Lorentz force generated due to the current carrying coils that are parallel to the z-axis while the second term arises from the torque induced from the Lorentz force generated in all the coils. Thus, from equation (5.3), it can be deduced that a greater torque is induced when stronger magnets, larger current are used and greater number of coil turns are fabricated on the device.

5.2.3 Modal Analysis

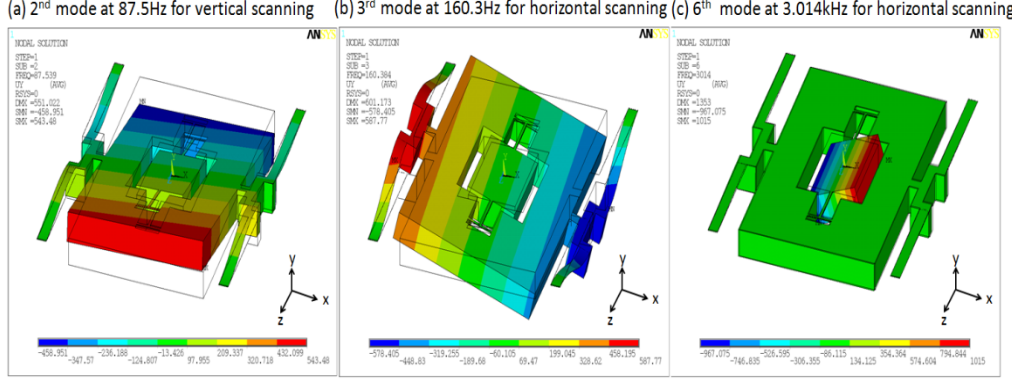

Fig. 5-7. Various mode shapes of the device derived from ANSYS simulation. (a) 2nd eigenmode at 87.5 Hz for vertical scanning. (b) 3rd eigenmode at 160.3 Hz for horizontal scanning. (c) 6th eigenmode at 3014 Hz for horizontal scanning.

Finite element modal analysis using ANSYS software is also made to investigate the frequency response and actuation behavior of our proposed MEMS scanner. To decrease the computational cost, the entire model was assumed to be made up of silicon. The values of the mechanical properties for silicon material required in the simulation are summarized in table 5-1. Fig. 5-7 shows the various mode shapes of the device derived from ANSYS simulation. The 2nd mode shape in Fig. 5-7(a), with a calculated

eigenfrequency of 87.5 Hz, corresponds to the intended purpose for vertical slow scanning by ET actuation. Fig. 5-7(b) shows the 3rd eigenmode at 160.3 Hz, in which the frame and the mirror move in phase and deflect by the same amount. Slight tilts about their respective scanning axes are observed from the mode shapes in both Fig. 5-7(a) and 5-7(b). However, at higher eigenfrequency of 3014 Hz shown in Fig. 5-7(c), there is negligible movement of the frame while the mirror plate oscillates along the z-axis. A thick Si substrate is intentionally left beneath the C-shaped hinge and frame so as to provide rigidity to these structures. This allows little energy to be lost due to structure deformation and more energy to be transferred through the T-shaped torsion bar to the mirror plate. Both of the derived mode shapes in Fig. 5-7(b) and 5-7(c) correspond to the intended purpose for horizontal fast scanning by EM actuation.

5.3 Device Microfabrication

Fig. 8 shows the CMOS compatible microfabrication process flow of the MEMS scanner investigated in this chapter. An 8 inch SOI wafer with 3-µm-thick Si device layer, 1.1-µm-thick buried oxide (BOX) layer and 725 µm Si handle layer was used as the starting material. First, a 0.2-µm-thick thermal insulating SiO_2 was deposited on the frontside of the wafer by plasma enhanced chemical vapour deposition (PECVD) [Fig. 5-8(a)]. This was followed by physical vapour deposition (PVD), patterning and reactive ion etching (RIE) of 2-µm-thick Al at the ET actuator winding, EM coil, bond pad and mirror regions using Cl_2 and Ar gases [Fig. 5-8(b)]. A 0.5-µm-thick SiO_2,

which serves as thermal and electrical insulation for the ET windings and EM coil regions respectively, was next deposited by PECVD. Bond pad openings

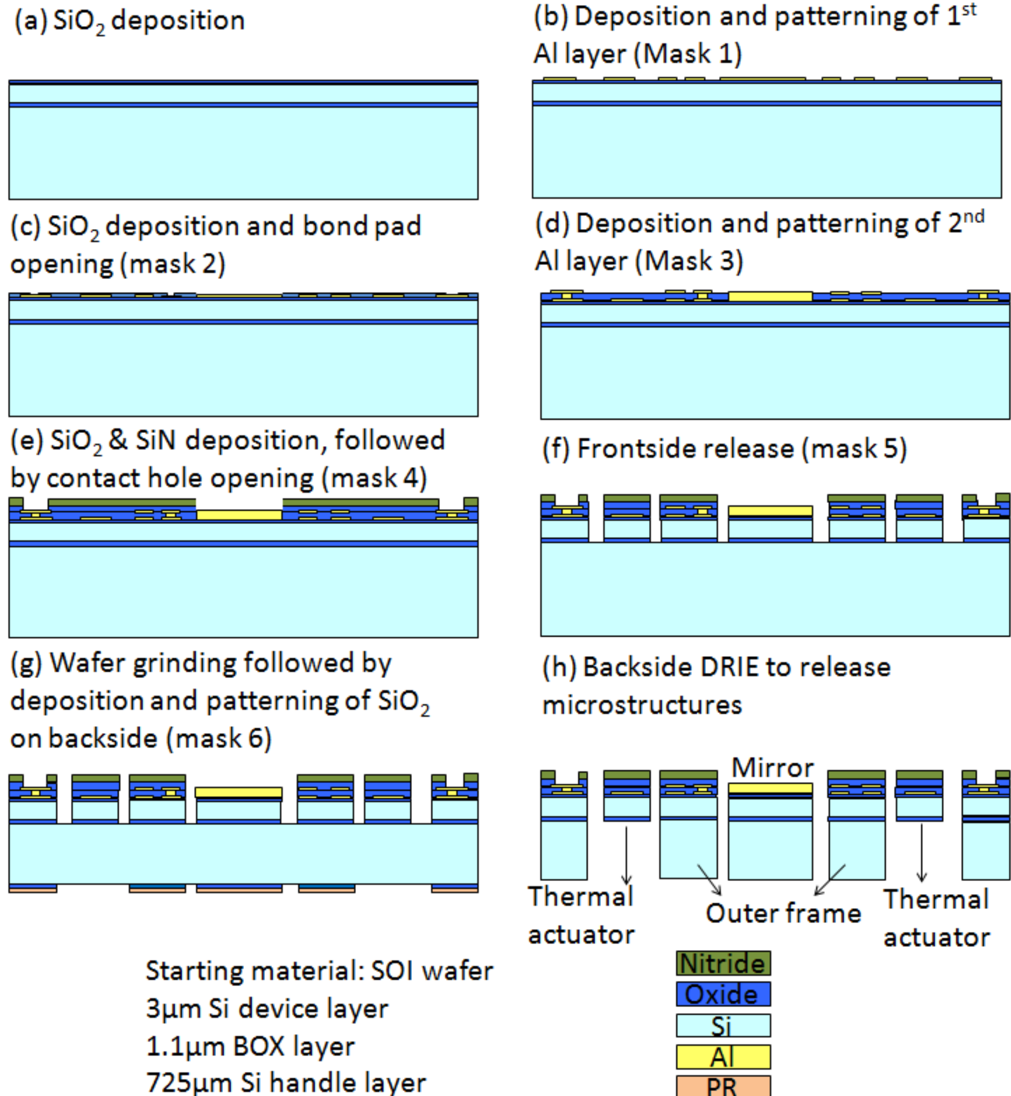

Fig. 5-8. Microfabrication process flow of the device

were then formed by RIE of SiO_2 using CHF_3 [Fig. 5-8(c)]. A second layer of Al was again deposited, patterned and etched, except that the processes happened only at the EM coil, mirror and bond pad regions [Fig. 5-8(d)]. PECVD SiO_2 and Si_3N_4, each of 0.5-µm-thick, were then deposited as passivating layers. Al remained as the top layer in the mirror region so as to enhance the reflectivity of the mirror surface. This was followed closely by

RIE of SiO_2 and Si_3N_4 for contact hole opening [Fig. 5-8(e)]. The frontside features of the microstructures such as the mirror, ET actuators, T-shaped torsion bar were then defined through RIE of Si_3N_4, SiO_2, Si device and BOX layers using CF_4 (for Si_3N_4), CHF_3 (for SiO_2) and SF_6 (for Si) respectively [Fig. 5-8(f)].

After all the frontside wafer processes were finished, the Si handle layer of the SOI wafer was reduced to approximately 450 µm by undergoing backside grinding and polishing. Next, a thin layer of 2 µm PECVD SiO_2 was deposited and patterned at the backside of the wafer. The photoresist used to pattern the oxide layer remained behind after the oxide etch so that both the photoresist and the oxide can function as hard mask for backside Si deep reactive ion etch (DRIE) during the subsequent step [Fig. 5-8(g)]. Prior to the DRIE process, the wafer was first diced to single mirror chip level (6mm × 6mm) as the mirror device would become very fragile when released and any impact either in a wet process or due to handling can break the microstructures easily. The diced mirror chips were then placed on a support wafer and immobilized using adhesive thermal tape. The DRIE process was conducted in a time controlled manner as the process does not stop effectively on the buried oxide (BOX) layer. 400 µm of silicon handle layer was first etched away, with the remaining 50 µm of silicon gradually etched in many etch steps, each of five minutes duration. After each etch steps, the wafer was taken out and the backside of the wafer was checked under the optical microscope so as to determine whether the entire Si handle layer had been fully etched away. A

450-µm-thick Si substrate was left beneath the mirror to maintain the rigidity and flexibility [Fig. 5-8(h)].

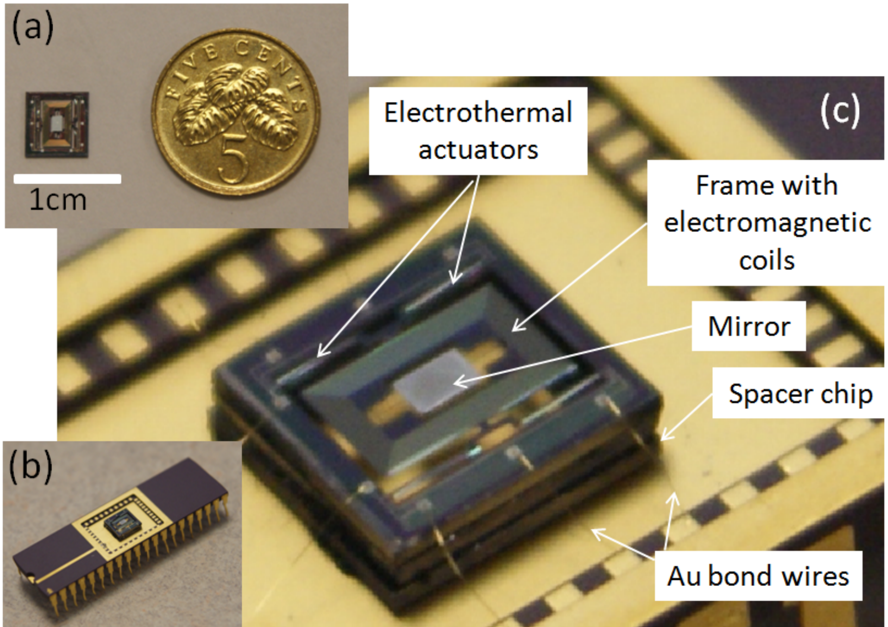

Fig. 5-9. Photos showing (a) an unpackaged 2-D MEMS scanner placed beside a Singapore five-cent coin, (b) the device packaged in a dual inline package, and (c) a close-up view showing the bond pads connected to the pins of the package via gold bond wires.

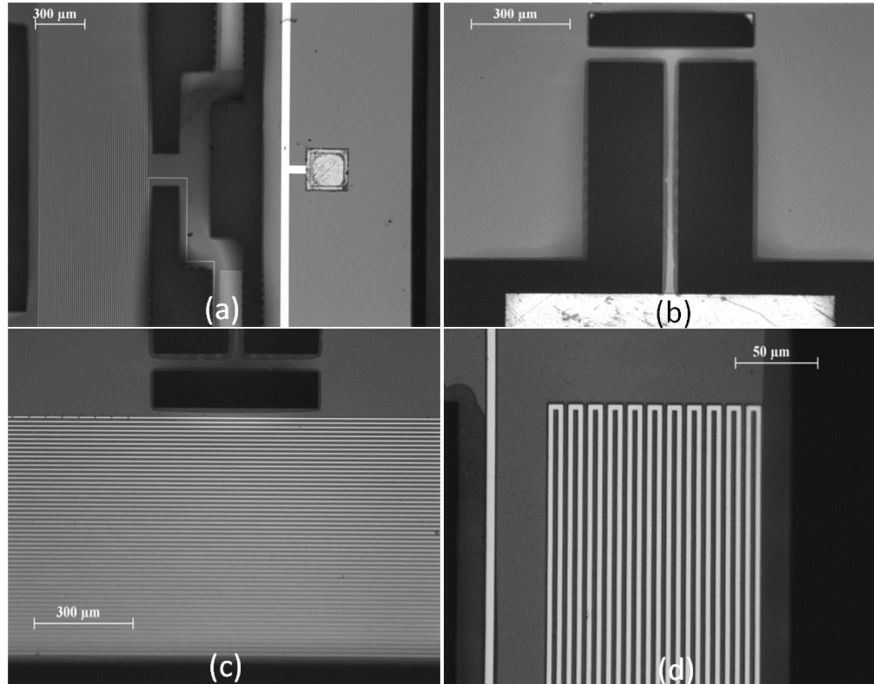

Fig. 5-10. Optical micrographs showing the (a) C-shaped hinge connecting the ETactuators to the frame, (b) T-shaped torsion bar, (c) Al EM coils embedded in the frame, and (d) Al windings of the ET actuator.

Fig. 5-9(a) shows a completed MEMS mirror device, placed beside a Singapore five-cent coin. As shown in Fig. 5-9(b), the device was bonded onto a dual inline package (DIP), with spacer chip placed beneath the device. The spacer chip elevates the device from the base of the DIP, hence avoiding hindrance to the mirror plate movement during actuation. The Al bond pads were connected by gold bond wires to the metal pins of the DIP. Fig. 5-10 shows the optical micrographs for various parts of the MEMS scanner. Fig. 5-10(a) shows the C-shaped hinge connecting the ET actuators to the frame, while Fig. 5-10(b) shows the T-shaped torsion bar of width 50 μm connecting the mirror plate to the frame. Fig. 5-10(c) and 5-10(d) show the EM Al coils embedded in the frame and Al windings of the ET actuator, respectively. There are two layers of Al EM coils, with each layer having 54 coils. Each ET actuator has 22 Al windings of width 3 μm. Table 5-2 summarizes the various dimensions of the structural parameters for the fabricated device.

Table 5-2. Structural parameters of the fabricated MEMS scanner shown in Fig. 5-10

Structural parameters	Values
Die size	6 mm × 6 mm
Mirror size (l × w × t)	1.5 mm × 1 mm × 0.45 mm
T-shaped torsion bar (w × t)	50 μm × 5 μm
Electrothermal actuator (l × w × t)	1850 μm × 200 μm × 7 μm
Electrothermal actuator winding (l × w × t)	1800 μm × 3 μm × 2 μm
No. of windings	22
Electromagnetic coil (w × t)	3 μm × 2 μm
No. of coils in each layer	54

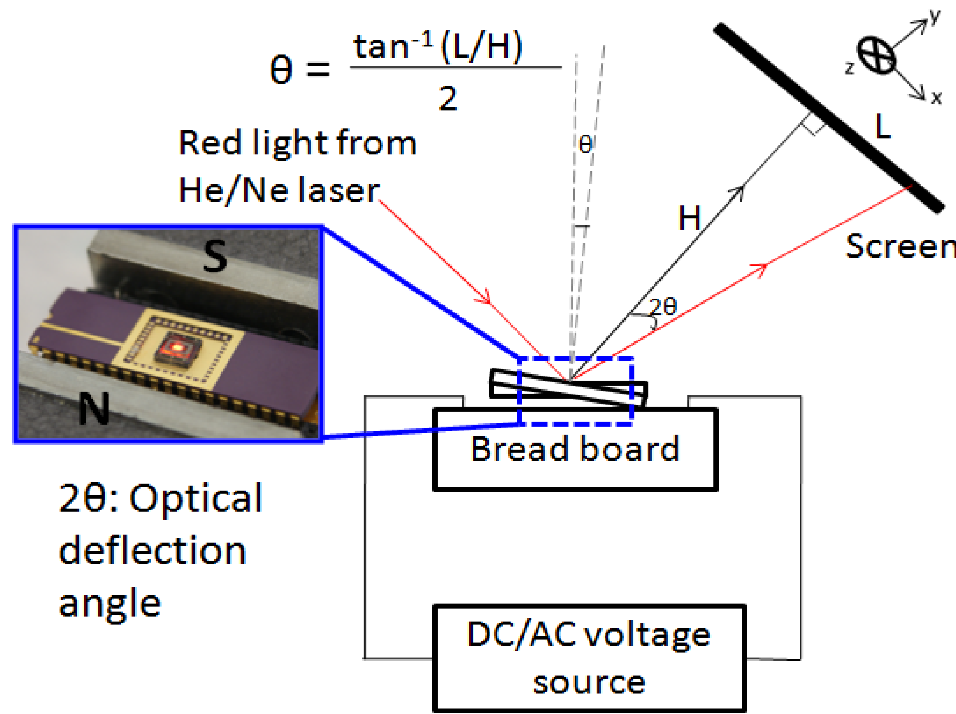

Fig. 5-11. Experimental setup for the optical characterization of device. Inset shows the packaged device placed in between the magnets, with red laser light impinging on the mirror surface

The schematic drawing of the experimental setup is illustrated in Fig. 5-11. The setup is largely identical to those used to characterize the MEMS scanners in the previous chapters. The inset of Fig. 11 shows the packaged device placed in between the magnetic field of a pair of Alcomax III magnets, with red laser light impinging on the mirror surface. The magnetic field strength at the center of the pair of magnets, which was measured by a Gauss meter, is approximately 0.15T.

5.4 Results & Discussion

Several experiments have been carried out to characterize both the ET and EM actuators in terms of static, dynamic responses and 2-D scanning patterns.

5.4.1 Static characterization

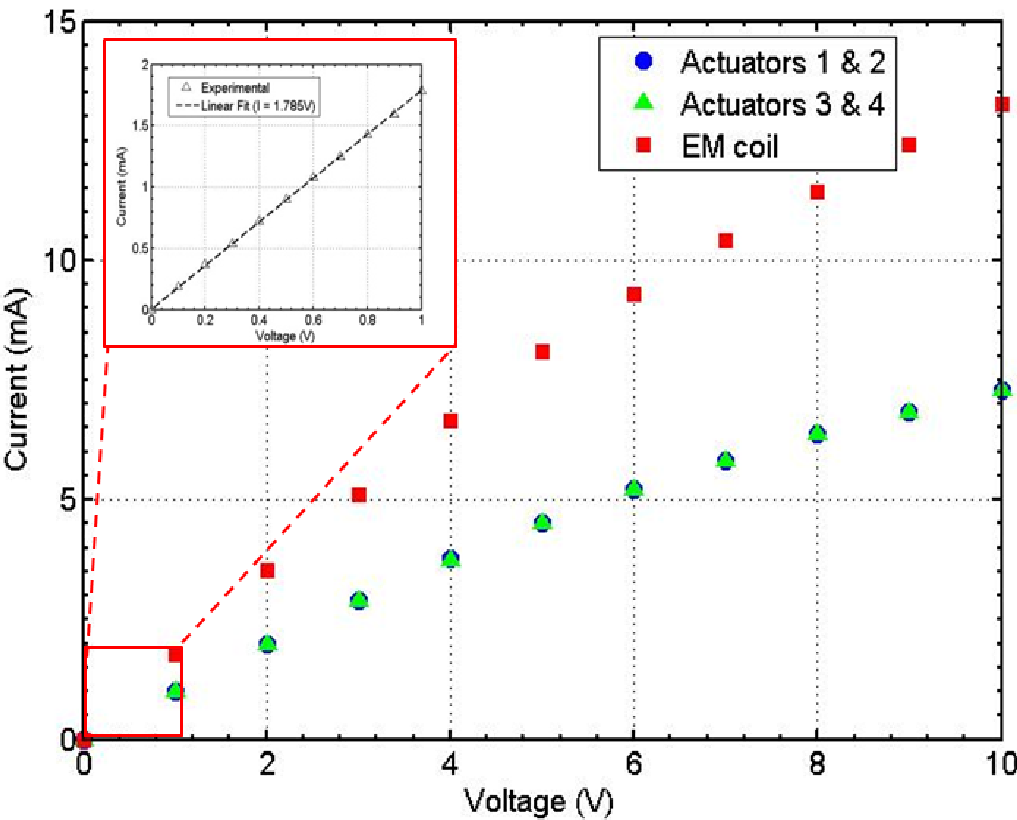

Fig. 5-12. I-V curves obtained for the EM coil, ET actuators 1 and 2 connected in series and ET actuators 3 and 4 connected in series. Inset shows a detailed sweep of the coil within the $1V_{dc}$ range, obeying a linear fit of I(mA) = 1.8V (V).

The I-V curves of the ET windings and the EM coils are shown in Fig. 5-12. An Agilent b1500a Semiconductor Device Analyzer was used to bias and obtain the I-V characteristic of the device. Both ET actuators 1 and 2 were connected electrically in serial for both static and dynamic characterizations. This also applies to ET actuators 3 and 4. As observed from Fig. 5-12, the I-V curves for the two sets of ET actuators are identical, with both having a thermal power consumption of approximately 73 mW at 10 V_{dc}. In the case of EM actuation, the magnitude of the current flow plays a more pivotal role in the actuation performance compared to thermal power consumption for ET actuation. A current of 13.3 mA was obtained when 10 V_{dc} was applied to the

EM coils. This is equivalent to a power consumption of 133 mW at $10V_{dc}$ for EM actuation. The inset of Fig. 5-12 shows a detailed sweep of the EM coil within the 1 V_{dc} range. In this bias range, the EM coil behaves like an ohmic conductor, obeying the linear fit I (mA) = 1.8V (V). The 1 V_{dc} bias range will be of interest during EM ac actuation, which will be discussed later in the section.

Fig. 5-13(a) and 5-13(b) show the static dc response for ET and EM actuations, respectively. The static rotation measurement was taken by applying a dc voltage to only one set of serially connected ET actuators, while leaving the other set unbiased. As shown in Fig. 5-13(a), when the ET actuators 1 and 2 were biased at 10 V_{dc}, the actuators bent down and caused the frame and mirror plate to rotate about the x-axis. This introduced a positive static ODA of 1.8°. Similarly, when ET actuators 3 and 4 were biased at 10 V_{dc}, the frame and mirror rotated in the opposite direction, introducing a negative static ODA of 1.5°. The dc static performance for actuators 1 and 2 is better compared to actuators 3 and 4. This small discrepancy may be due to lithographic and fabrication inaccuracies. Fig. 5-13(b) shows the dc response for the EM actuation, where positive and negative dc voltages were applied to the EM coils. When a positive dc bias was applied, the current flowed in a clockwise direction around the coils and the frame experienced a mechanical torque in the presence of a magnetic field. At 10 V_{dc}, the mirror rotated about the z-axis, causing an ODA of +3.1°. In the case where negative DC bias was applied, the current flowing in the coil changed direction, i.e. anti-clockwise

direction. The mirror rotated in the opposite direction about the same axis, introducing an ODA of -3.3°.

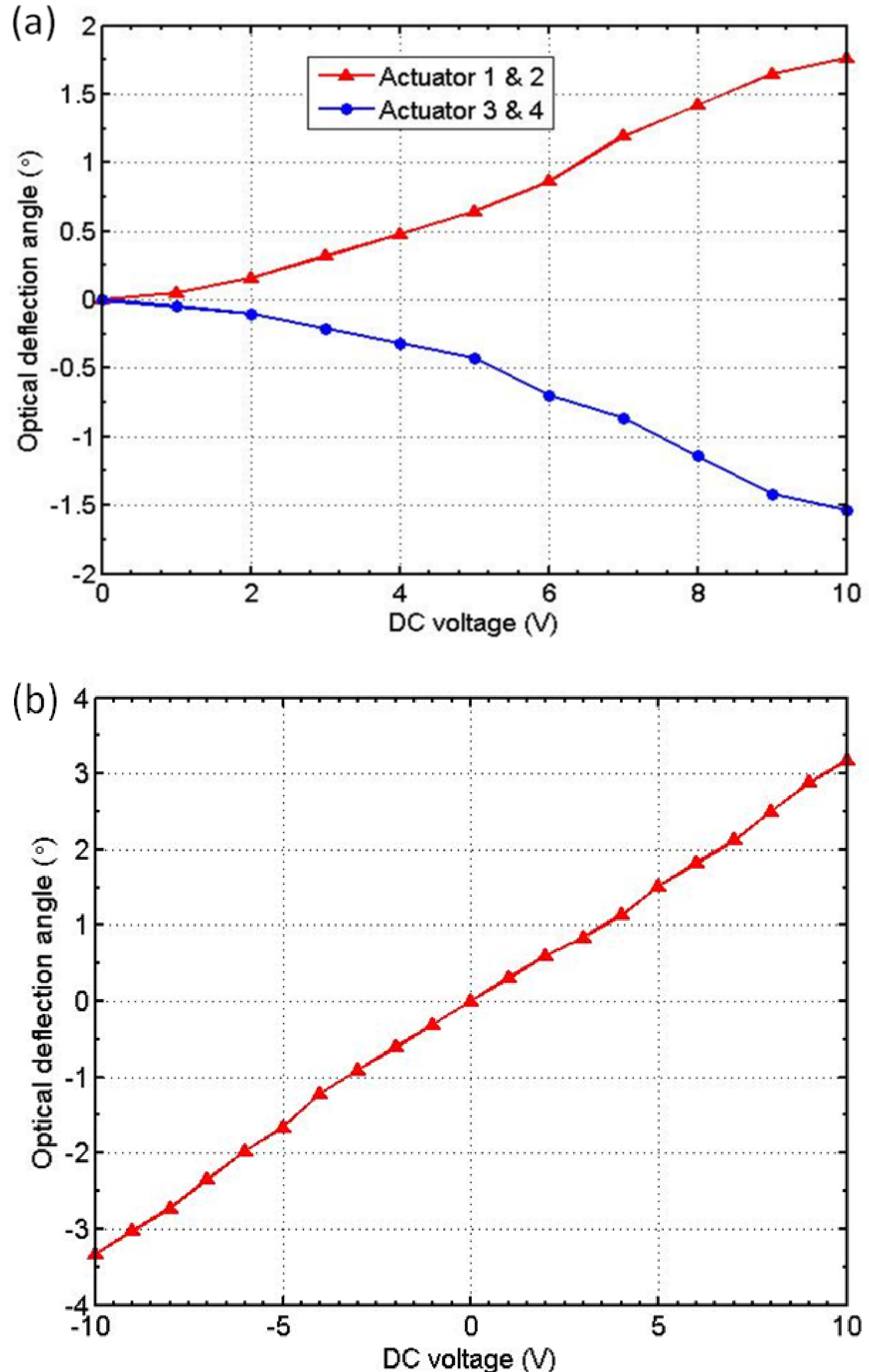

Fig. 5-13. DC response for (a) ET actuation, and (b) EM actuation.

5.4.2 Dynamic characterization

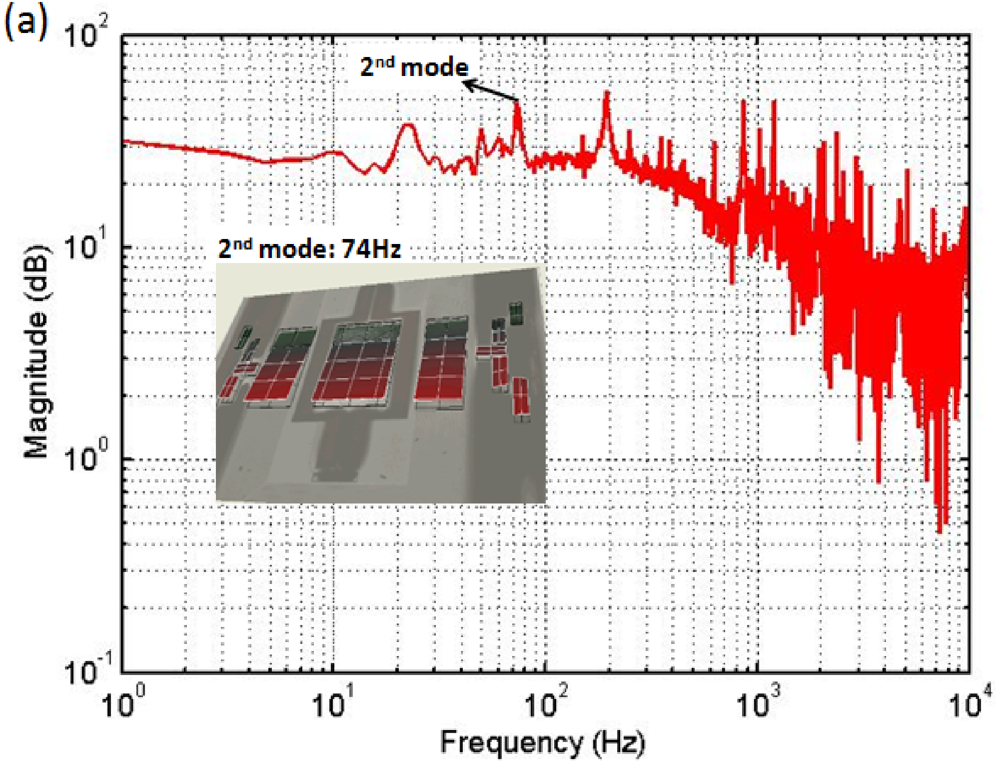

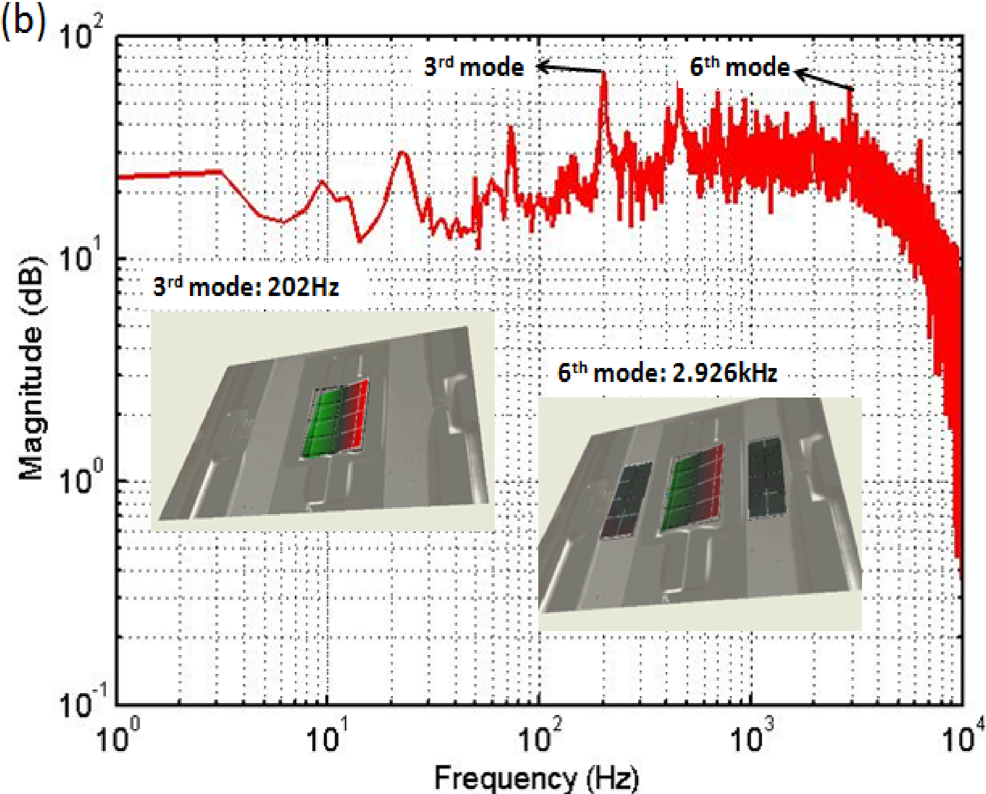

Fig. 5-14. Bode plots illustrating the frequency response for (a) ET actuation where actuators 1 and 2 are biased in series, and (b) EM actuation.

Fig. 5-14(a) and 5-14(b) show the Bode plots illustrating the frequency responses of ET and EM actuations respectively. A Polytec MSA-500 Laser Doppler Vibrometer (LDV) was used to obtain both the frequency responses of the device, with the measurement point being located at the top corner of the frame. A 1 V_{ac} sinusoidal excitation signal was used to bias the device while the LDV sent a laser beam to the point of interest and measures the Doppler shift of the returning beam. Fig. 5-14(a) shows the Bode plot obtained for ET actuation, where ET actuators 1 and 2 were biased with the excitation signal. The inset of Fig. 5-14(a) shows the second mode shape of the mirror obtained from the vibration analyzer in the LDV. This mode shape corresponds to that required for vertical scanning and it occurs at 74 Hz, which is pretty close to the modal frequency of 87.5Hz obtained from the FEM simulation. The mechanical q-factor obtained during ET actuation at 74 Hz is 50. The same procedure is made for EM actuation and a Bode plot, as shown in Fig. 5-14(b), is obtained. As shown in the inset of Fig. 5-14(b), the mode shapes of the mirror for third and sixth modes corresponds to that required for horizontal scanning. The third mode occurs at 202 Hz, while the modal frequency obtained from simulation is 160.3 Hz. Similarly, the sixth mode occurs at a higher frequency of 2926 Hz while the simulated modal frequency is 3014 Hz. The disparity between the experimental and simulated frequencies is due to the consideration of the entire model being made of silicon only during the ANSYS simulation while in reality, the device is made of several layers of thin film material in addition to single crystalline silicon. The mechanical quality factors obtained at 202 Hz and 2926 Hz is 40 and 488, respectively. The 3 dB cut-off frequency for ET actuation in Fig. 5-14(a) is

about 3 Hz. This slow thermal response is caused by the large thermal resistances introduced by the windings of the ET actuator.

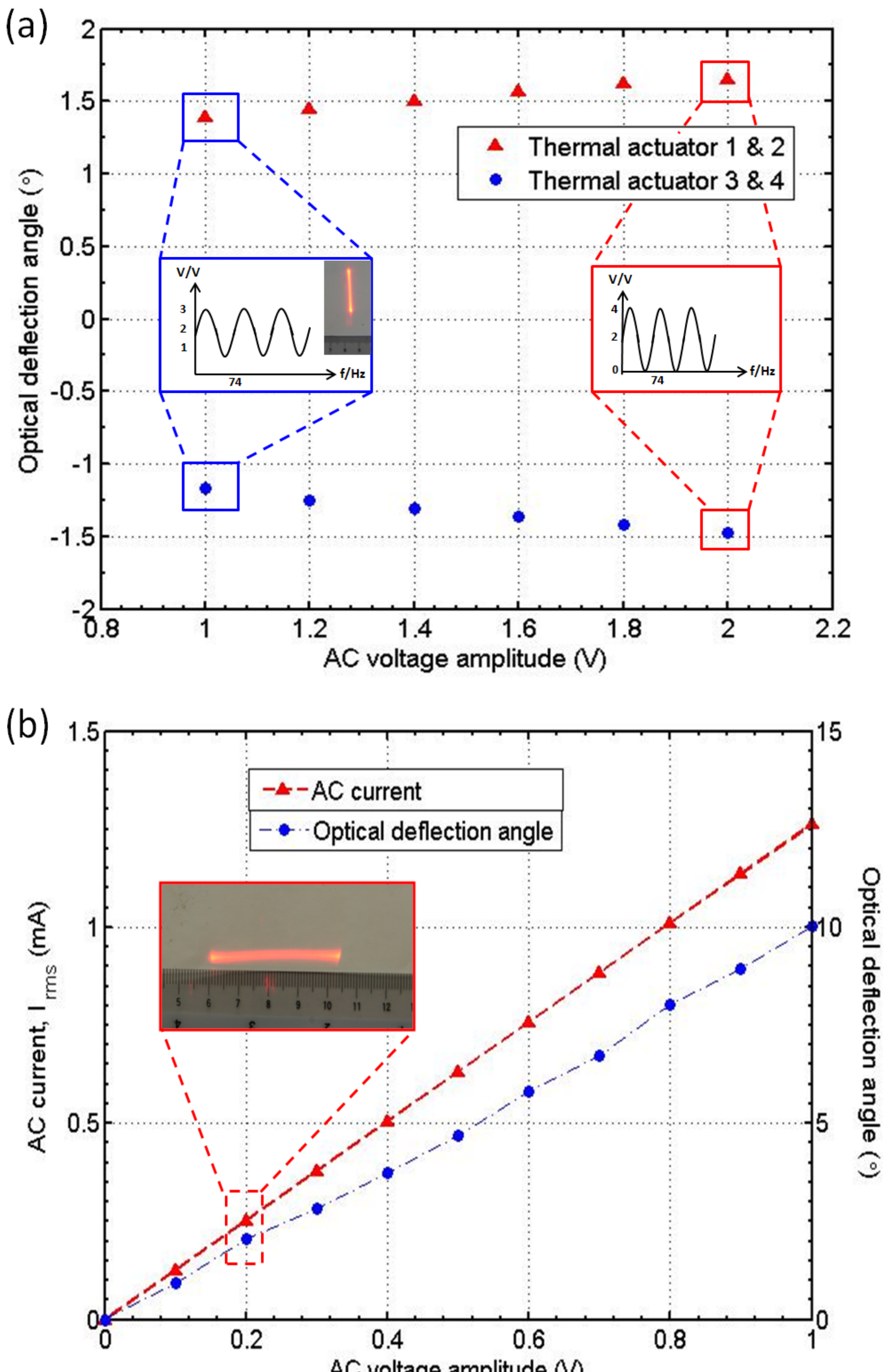

Fig. 5-15. AC response for (a) ET actuation at 74Hz for two different cases of biasing configurations; (b) EM actuation at 202Hz, with inset showing an example of a horizontal scanning trajectory line produced during EM actuation.

Fig. 5-15(a) and 5-15(b) depict the ac response of the device for ET and EM actuations, respectively. Both the ET and EM actuators were biased individually with a sinusoidal ac voltage at their respective resonant frequencies while observing the length of the scanning trajectories produced at varying ac voltage. Two Agilent 33120A Function Waveform Generators were used to bias and excite the device for ET and EM actuations, respectively. Fig. 5-15(a) shows the ac response for ET actuation at 74Hz for two different bias configurations. An ac voltage, on top of a 2 V_{dc} offset bias, was applied to the two sets of ET actuators separately. The insets of Fig. 5-15(a) show examples of the voltage bias waveforms at 1 V_{ac} and 2 V_{ac}. In the case where ET actuators 1 and 2 were biased, the ODA obtained at 2 V_{ac} with 2 V_{dc} offset is +1.6° compared to +1.4° at 1 V_{ac} with 2 V_{dc} offset. This is because of a larger peak-to-peak voltage difference for the former compared to the latter biasing condition, hence resulting in larger difference in the heating effect. In the case where ET actuators 3 and 4 are biased, the ODA obtained at 2 V_{ac} with 2 V_{dc} offset is -1.5°. Hence, from these results, we can potentially obtain an approximate optical scan range of ±1.5° at 2 V_{ac} with 2 V_{dc} offset when we bias the two sets of thermal actuators at 180° out of phase with each other. Such a biasing configuration would result in approximately 12 mW of thermal power being consumed by both sets of ET actuators. In addition, due to the electrical compliance of the function generator, the biasing condition for the ET actuators was limited to 2V_{ac} with 2V_{dc} offset. The red and blue curves in Fig. 5-15(b) show the root mean square values of the current flowing in the EM coil for various ac voltages and the ac response for EM actuation at 202 Hz, respectively. At 1 V_{ac} bias, a root-mean-square (rms) current value of 1.26

mA is derived, while a dynamic ODA of ±10° is obtained from the optical experiment. This dynamic ODA obtained is significantly larger when compared to the static ODA of 0.3° obtained at 1 V_{dc} during static actuation. This phenomenon is due to the mirror attaining mechanical resonance from the ac electrical excitation, resulting in maximum energy transfer from the ac electrical signal to the vibrating mechanical structures. In addition, straight vertical and horizontal scanning trajectories were observed, as shown in the insets of Fig. 5-15(a) and Fig. 5-15(b), respectively. Hence, the tilting mode shapes previously observed from the simulation in Fig. 5-7(a) and 5-7(b) contributes minimum effect to both the vertical and horizontal scanning trajectories respectively.

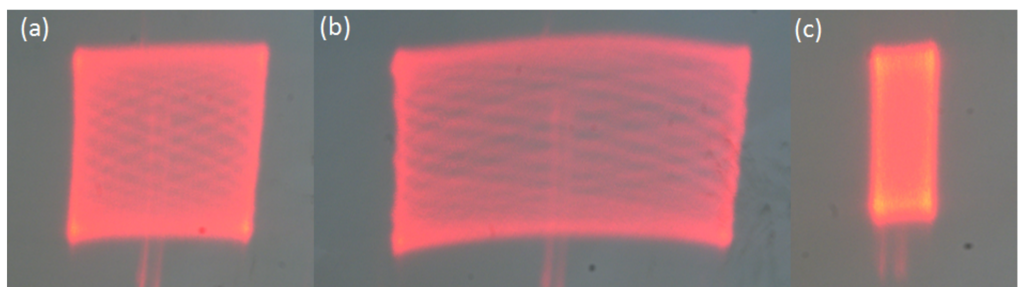

Fig. 5-16. Various Lissajous patterns generated from different combinations of ET and EM biasing configurations. ET actuators 1 and 2 at 2 V_{dc} and 2 V_{ac}, 74 Hz are responsible for the horizontal scanning in all 3 patterns while the biasing conditions for the vertical scanning are (a) 0.1 V_{ac} or 0.126 mA, 202 Hz; (b) 0.2 V_{ac} or 0.252 mA , 202Hz; (c) 2 V_{ac} or 2.5 mA, 2926 Hz respectively.

Various 2-D Lissajous patterns generated from different combinations of ET and EM biasing configurations are shown in Fig. 5-16. The vertical scanning in Fig. 5-16(a)-(c) was driven by biasing ET actuators 1 and 2 at 74 Hz, 2 V_{ac} with 2 V_{dc} offset. The horizontal scanning occurs by biasing the EM coils at the resonant frequencies of either 202 Hz or 2926 Hz. The horizontal trajectory length becomes longer as the bias applied to the EM coil increases. Minimum coupling was observed between the vertical and horizontal scanning

as the horizontal and vertical trajectories, shown in the insets of Fig. 15(a) and 15(b). respectively, forming straight lines instead of elliptical loops. The distortion of the scanning image seen in Fig. 5-16(b) is caused mainly by the inclined laser beam incidence on the mirror and the tilted screen against the optical axis. Such scanning image can be easily corrected using properly designed projection optics. Fig. 5-16(c) illustrates the raster scanning pattern obtained by biasing the EM coil at $2V_{ac}$, 2926 Hz. Unfortunately, no significant mechanical amplification experimental result is observed as the horizontal trajectory length obtained in Fig. 5-16(c) is relatively smaller (±1.1°, 2.5 mA) compared to Fig. 16(b) (±2°, 0.25 mA). This might be due to the thick bulk Si substrate underneath the mirror and the air damping force being larger at higher frequency, causing the actuation motion of the mirror plate to be heavily damped at 2926 Hz compared to 202Hz. Nevertheless, we are able to demonstrate the higher resonant mode (2.9 kHz) and its corresponding 2-D scanning pattern in Fig. 5-16(c). This illustrates the feasibility of using the hybrid actuated single mirror approach and leveraging the concept of mechanical amplification mechanism for 2-D scanning purposes.

5.5 Performance comparison of current design with existing EM MEMS scanners

Table 5-3 compares the published EM actuated MEMS mirror performances according to the figure of merit (FOM), which is being used as a metric to compare the relative scanning efficiencies:

$$FOM = \frac{\theta_{opt} Df}{I} \quad (5.4)$$

Table 5-3. Comparison of FOM for different EM scanner designs.

Ref	Unique feature	Frequency (Hz)	Current (mA)	FOM
This work	Hybrid actuated MEMS scanner	202	1.26	3.2
Yalcinkaya *et al.* [74]	State-of-the-art MEMS scanner	21,300	140	12.1
Ji *et al.* [77]	Cu plated MEMS scanner	19,100	130	1.9
Miyajima et al. [72]	MEMS scanner with polyimide hinges	2,700	177	1.3
Urey *et al.* [75]	Low cost FR4 based scanner	417	250	1.2
Yalcinkaya *et al.* [79]	Magnetostatic NiFe plated MEMS scanner	367	100	0.48
Yalcinkaya *et al.* [78]	Polymer based barcode scanner	56.5	16	0.43
Tang *et al.* [81]	Torque enhanced Ni plated scanner	11,149	400	0.38

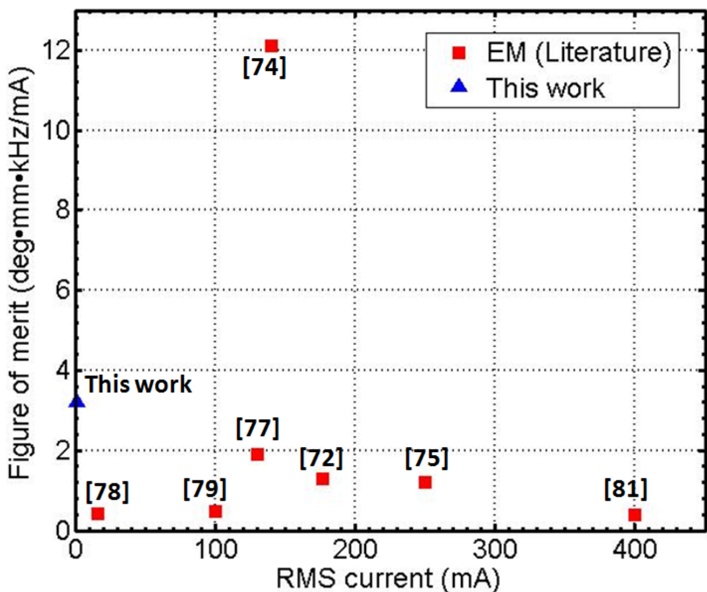

Fig. 5-17. Performance comparison of the various EM MEMS scanners reported in literature.

where θ_{opt} is the total optical deflection angle (°), D is the mirror size along the scan axis (mm), f is the resonant frequency (kHz), I is the rms drive current (mA). Fig. 5-17 shows the graphical representation for the performance comparison of the various EM MEMS scanners reported in literature. The FOM obtained during EM actuation for this work (θ_{opt} = 20°, D = 1mm, f = 0.202 kHz and I = 1.26mA) is better than most of the EM scanners reported in recent years. This may be attributed to the large number of EM coils fabricated, resulting in extremely low driving current. To the best of my knowledge, this proposed design has one of the lowest operation voltage and current among most of the MEMS scanners driven by EM actuation. For example, the MEMS scanners developed by Tang *et al.* and Yalcinkaya *et al.* in ref. [81] and [78], respectively, require approximately rms drive currents of 400mA and 16mA to reach a total optical deflection angle of 11° and 15° respectively. The performances of these scanners are less efficient than our obtained ODA of ±10° at 1 V_{ac}, 1.26 mA for EM actuation. However, this device's performance remains pale in comparison to the state-of-the-art EM MEMS scanner developed by Yalcinkaya *et al.* for high resolution retinal scanning display [74].

5.6 Summary

A novel proof-of-concept CMOS compatible MEMS scanner based on hybrid actuation mechanisms has been proposed in this chapter and verified for 2-D scanning application. Both ET and EM actuations have been integrated in the same device for slow and fast scanning purposes, respectively. This makes our design essentially different from most of the 2-D scanner

designs already reported in the literature where the same actuation scheme is often used to drive both the orthogonal scanning axes of the mirror devices. The added advantage of a CMOS compatible fabrication process allows for ease of monolithic integration, hence adding new functionality to integrated electronics. An optical deflection angle of ±1.5° for the 74 Hz vertical scan at 12 mW for ET actuation and ±10° for the horizontal scan frequency of 202 Hz at 1.26 mA, $1V_{ac}$ for EM actuation were reported. The outstanding optical performance in terms of low operating voltage and above-par FOM obtained by the device during EM actuation is among the best reported in literature. This unique design of using hybrid actuation mechanism is the first demonstration of such CMOS compatible 2-D MEMS scanner, with its low power consumption suitable for mobile applications powered by batteries with limited capacity.

In the next chapter, i.e. chapter 6, the developed hybrid actuated MEMS mirror will be examined further for VOA application.

Chapter 6
Study of a MEMS VOA Driven By Hybrid Electromagnetic and Electrothermal Actuation Mechanisms

6.1 Introduction

One of the key approaches of making MEMS VOA devices involves the integration of large reflective mirrors with optics typically realized in 3-D free space configuration. When such tilt reflective mirrors are deployed for 3-D optical attenuation in conjunction with large micro-optics such as dual fiber collimator, the resulting VOA device can gain excellent data in terms of return loss and wavelength dependent loss under reasonable driving voltage.

In recent years, 3-D reflective type MEMS VOA driven by piezoelectric $Pb(Zr,Ti)O_3$ (PZT) thin film actuators have been demonstrated in ref. [68] and in chapter 3 of this thesis, achieving 40 dB attenuation range at $1V_{dc}$. However, PZT is not a CMOS compatible material. Thus, in this chapter, a new CMOS compatible 3-D MEMS VOA that can be driven by either electrothermal (ET) or electromagnetic (EM) attenuation mechanism is explored. In addition, by addressing voltage biases to both the ET and EM actuators simultaneously, i.e. hybrid attenuation mechanism, better performance in terms of reduced electrical power consumption and obtaining an additional degree of freedom in attenuation control can be achieved. The

approach of using hybrid attenuation differs greatly from all of the planar and 3-D MEMS VOA designs that have already been reported in literature where only one type of actuation mechanism is used to drive the mirror/shutter in order to achieve attenuation. The attenuation efficiency for EM, ET and hybrid attenuation mechanism will be studied in detail in this chapter.

6.2 Design and modeling

A schematic diagram of the proposed hybrid MEMS VOA is shown in Fig. 6-1. The device investigated in this chapter for VOA application is similar to that in chapter 5. There are four sets of ET actuators along the longitudinal sides of the mirror which are responsible for the rotation of the mirror plate about the x-axis. The frame is embedded with numerous turns of aluminium (Al) EM coils, during which a Lorentz force and rotation of the mirror about z-axis will be generated when a current flows in the coils in the presence of a permanent magnetic field. The mirror surface is deposited with Al and is connected to the frame by the T-shaped torsion bars. The dual fiber collimator is arranged in a 3-D free space configuration where the infra-red (IR) laser beam focuses on the center of the Al mirror surface. With both the rotation axes being orthogonal to each other, the micromirror is able to move with six degree of freedom for enabling 3-D attenuation mechanism. The insets A and B in Fig. 6-1 show the top view drawing illustrating the dimensions and layouts of the EM coils and ET windings, respectively. The numbers of turns of EM coils and ET windings shown in the insets have been reduced for simplicity purposes. The details of the attenuation principle by the two modes of actuation, i.e. EM and ET will ensue on in this section.

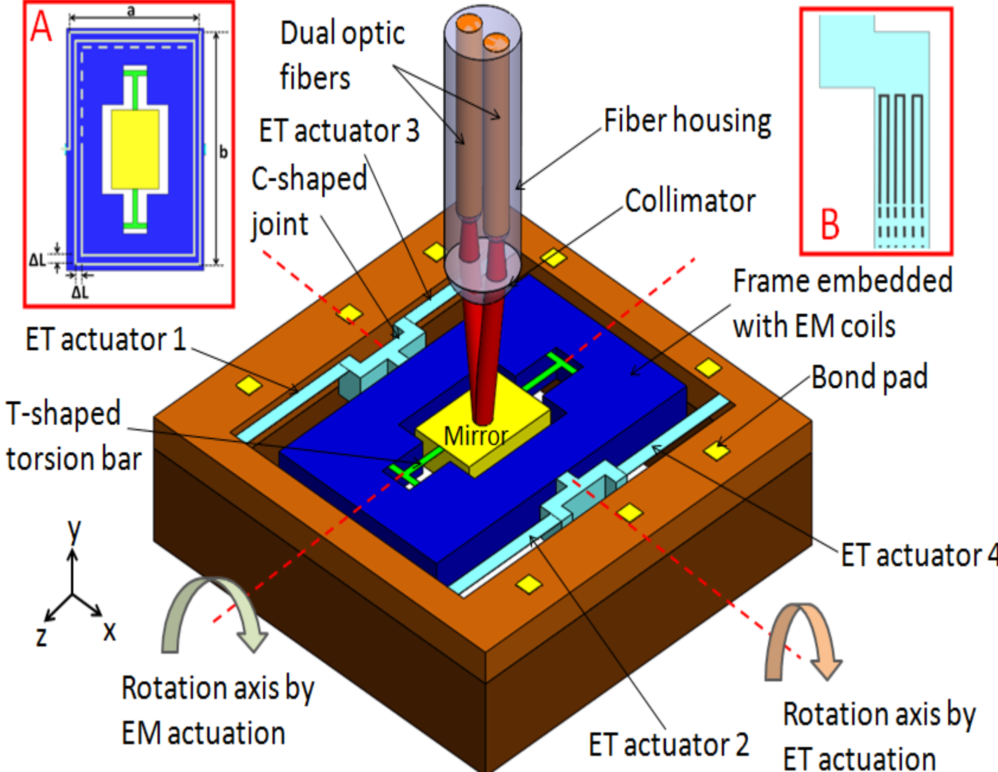

Fig. 6-1. Schematic diagram of the hybrid actuated MEMS VOA with dual-fiber collimator arranged in 3-D free space configuration such that the light beam focuses on the center of the aluminum mirror surface. Insets A and B show the top view drawings illustrating the dimensions and layout of the EM coils and ET windings, respectively. The number of EM coils and ET windings have been reduced for simplicity purposes.

6.2.1 EM actuation and attenuation principle

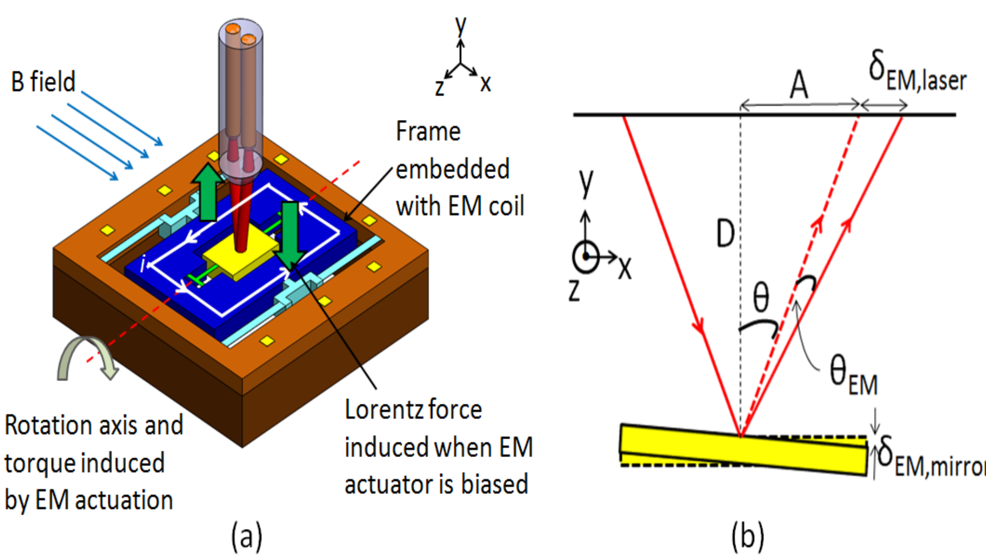

Fig. 6-2. Schematic diagrams showing the (a) EM actuation mechanism in the presence of an external permanent magnetic field and current flowing in the coils embedded in the frame, and (b) EM attenuation principle, where the laser beam is rotated and displaced by an angle θ_{EM} and distance $\delta_{EM,laser}$, respectively.

Fig. 6-2(a) shows the schematic diagram of the EM actuation mechanism in the presence of an external magnetic field and current flowing in the EM coils. Two layers of EM coils, made of Al, are deposited and patterned on the silicon (Si) frame. A pair of magnets may be arranged such that a uniform permanent magnetic field in the x-direction may be formed across the device. When the EM coils are biased and a current flows in an anti-clockwise direction as shown in Fig. 6-2(a), a pair of equal but opposite Lorentz force will be generated at the coils orthogonal to the magnetic field, i.e. those coils running along the z-direction. This pair of Lorentz force introduces a magnetic torque and cause the mirror to rotate about the z-axis. The torque generated may be approximated as:

$$\mathrm{T} = 2i\mathrm{B}\sum_{\mathrm{m}=0}^{\mathrm{N}-1}(\mathrm{b} - 2\mathrm{m}\Delta\mathrm{l})(\mathrm{a} - 2\mathrm{m}\Delta\mathrm{l}) \qquad (6.1)$$

where i is the current flowing in the EM coils, B is the magnetic field strength of the magnet (0.15 T), N is the number of coil turns in each layer (54), a and b are the side lengths of the most outer coil turn on the short (2.83 mm) and long sides (4.55 mm) of the frame, ΔL is the pitch of the EM coils (12 µm) as shown in the inset of Fig. 6-1. Thus, from equation (6.1), it can be deduced that a greater mechanical rotation angle of the mirror is obtained when a larger current, stronger magnet and greater number of coil turns are fabricated on the device.

Fig. 6-2(b) shows the schematic diagram illustrating the EM attenuation principle, where the laser beam is rotated and displaced by an angle θ_{EM} and distance $\delta_{EM,laser}$, respectively. When there is no current flowing

in the EM coils, the normal of the mirror surface is perfectly aligned with the IR laser beam, causing all the light to be coupled from the input fiber to the output fiber. When the mirror rotates about the z-axis due to the magnetic torque acting on the frame, the reflected laser beam is rotated and displaced by an angle θ_{EM} and distance $\delta_{EM,laser}$, respectively. A portion of the laser beam no longer couples into the output fiber, resulting in attenuation. An analytical model relating the optical deflection angle (θ_{EM}) to the displacement of the reflected laser beam from its original position can be derived from Fig. 6-2(b) and is represented by equations (6.2) and (6.3):

$$\theta = tan^{-1}\left(\frac{A}{D}\right) \qquad (6.2)$$

$$\delta_{EM,laser} = D\tan(\theta + \theta_{EM}) - A \qquad (6.3)$$

where θ_{EM} is the optical deflection angle of the laser beam when the EM coils are dc biased, A is the half distance between the input and output fiber in the dual fiber collimator (125 μm), D is the working distance (1 mm), θ is the angle between the incident laser beam and normal of the mirror before actuation, $\delta_{EM,laser}$ is the displacement of the reflected laser from its original position during electromagnetic actuation. With the above-mentioned equations (6.2) and (6.3), the theoretical displacement of the laser beam from its original position ($\delta_{EM,laser}$) can be calculated using the experimental optical deflection angle data (θ_{EM}) obtained by impinging a red visible laser light on the mirror surface.

6.2.2 ET actuation and attenuation principle

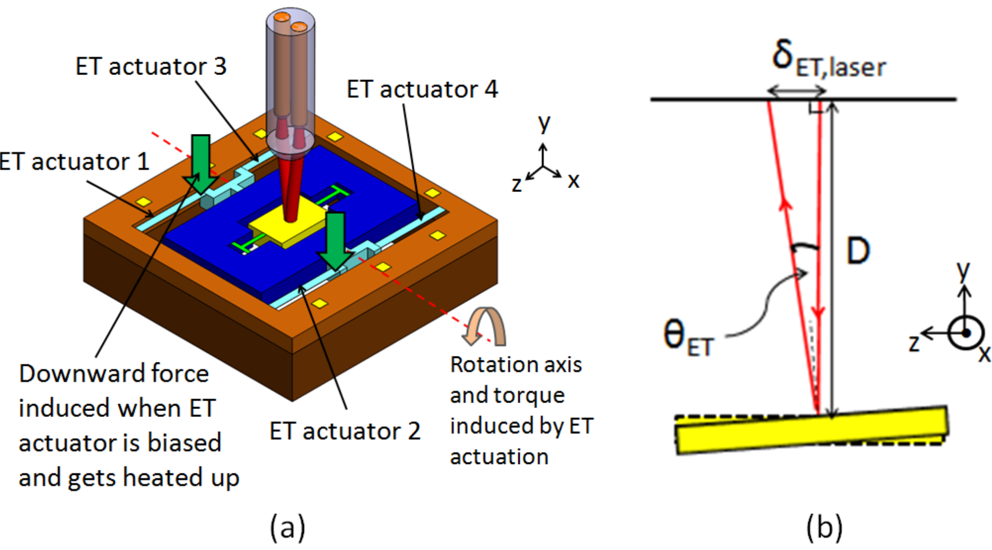

Fig. 6-3. Schematic diagram showing the (a) ET actuation mechanism where ET actuators 1 and 2 are biased and heated up, and (b) ET attenuation principle, where the laser beam is rotated and displaced by an angle θ_{ET} and distance $\delta_{ET,laser}$, respectively.

Fig. 6-3(a) shows the schematic diagram of the ET actuation mechanism when ET actuators 1 and 2 are biased. The ET actuator consists of a Si cantilever made from the device layer of a silicon-on-insulator (SOI) wafer and Al heater deposited and patterned on it. As shown in the inset B of Fig. 6-1, the Al heater is patterned in a winding manner so as to increase the resistance and thermal reliability of the heater and actuator, respectively. There are a total of 14 ET windings fabricated on each of the four actuators. When a current flows through the windings, the Al heats up and expands more than Si, causing the ET actuator to bend downwards. To introduce a mechanical torque about the x-axis, both actuators 1 and 2 or 3 and 4 are to be biased serially so that either set of actuators experiences downward displacements simultaneously. As shown in Fig. 6-3(b), when the mirror undergoes rotation about the x-axis, the reflected IR laser beam is displaced by an angle θ_{ET} and distance $\delta_{ET,laser}$, respectively. A portion of the laser beam no

longer couples into the output fiber, resulting in attenuation. Similar analytical model relating the optical deflection angle (θ_{ET}) to the displacement of the reflected laser beam from its original position ($\delta_{ET,laser}$) can be made from Fig. 6-3(b) and is represented by equation (6.5):

$$\delta_{ET,laser} = Dtan(\theta_{ET}) \qquad (6.4)$$

where θ_{ET} is the optical deflection angle of the laser beam when the ET actuators 1 and 2 are dc biased, D is the working distance (1 mm), $\delta_{ET,laser}$ is the displacement of reflected laser from its original position during ET actuation. With equation (6.4), the theoretical displacement of the laser beam from its original position can also be calculated using the experimental optical deflection angle data obtained during ET actuation.

6.3 Experimental setup

Fig. 6-4 shows the fabricated MEMS VOA device of size 6 mm × 6mm, wire-bonded to a dual inline package (DIP). The fabrication process for the device is identical to that described previously in section 3 of chapter 5. The rectangular mirror is 1.5 mm × 1mm in size, with its surface deposited with 4-μm-thick Al. Insets A and B show the optical micrographs of the windings on the ET actuator and EM coils on the frame respectively. Each ET actuator has 14 Al windings of width 5 μm, while a total of 108 turns, each of width 3 μm, are fabricated in the two layers of EM coils. Inset C shows a SEM micrograph of the device, which includes the ET actuator, C-shaped joint, frame, T-shaped torsion bar and micromirror. The detailed dimensions of the microstructures for the device are summarized in Table 6-1.

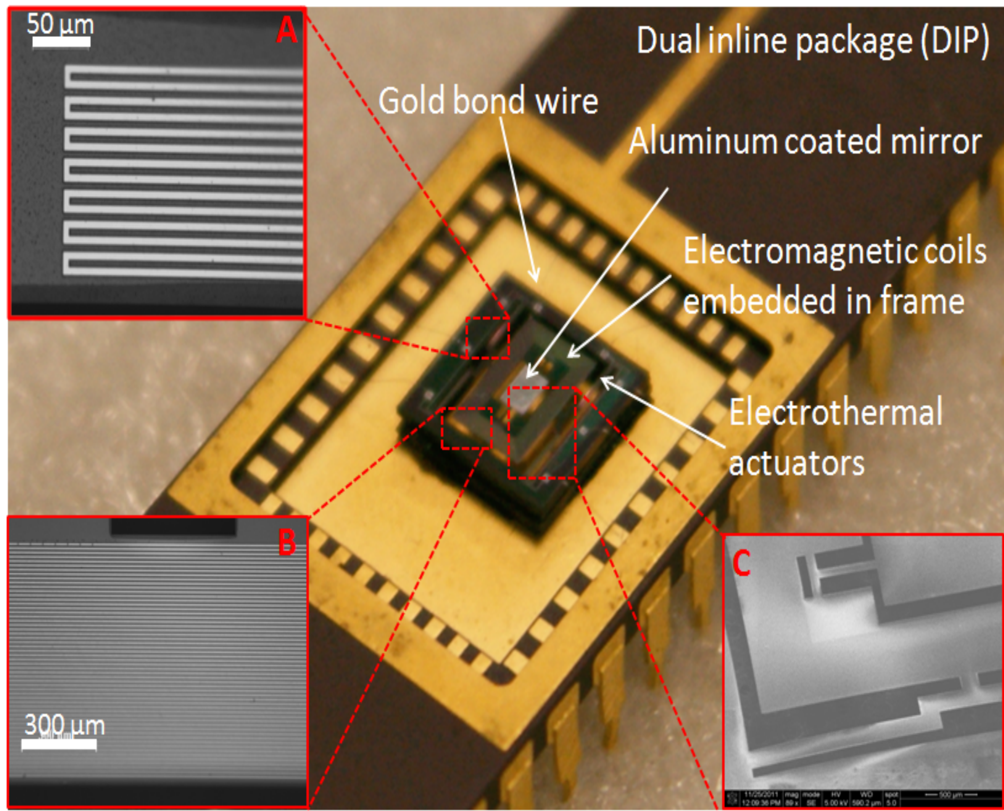

Fig. 6-4. A magnified photo showing the packaged MEMS VOA device. Insets A and B show the optical micrographs of the ET windings and EM coils respectively. Inset C shows a SEM micrograph of the ET actuator, C-shaped joint, frame, T-shaped torsion bar and mirror.

Table 6-1. Detailed dimension of the microstructures for the hybrid MEMS VOA device.

Structural parameters	Values
Size of the die	6 mm × 6 mm
Mirror size (l × w × t)	1.5 mm × 1 mm × 0.45 mm
T-shaped torsion bar (w × t)	150 µm × 5 µm
Electrothermal actuator (l × w × t)	1850 µm × 200 µm × 7 µm
Electrothermal actuator winding (l × w × t)	1800 µm × 5 µm × 2 µm
No. of windings	14
Electromagnetic coil (w × t)	3 µm × 2 µm
Total no. of electromagnetic coils	108

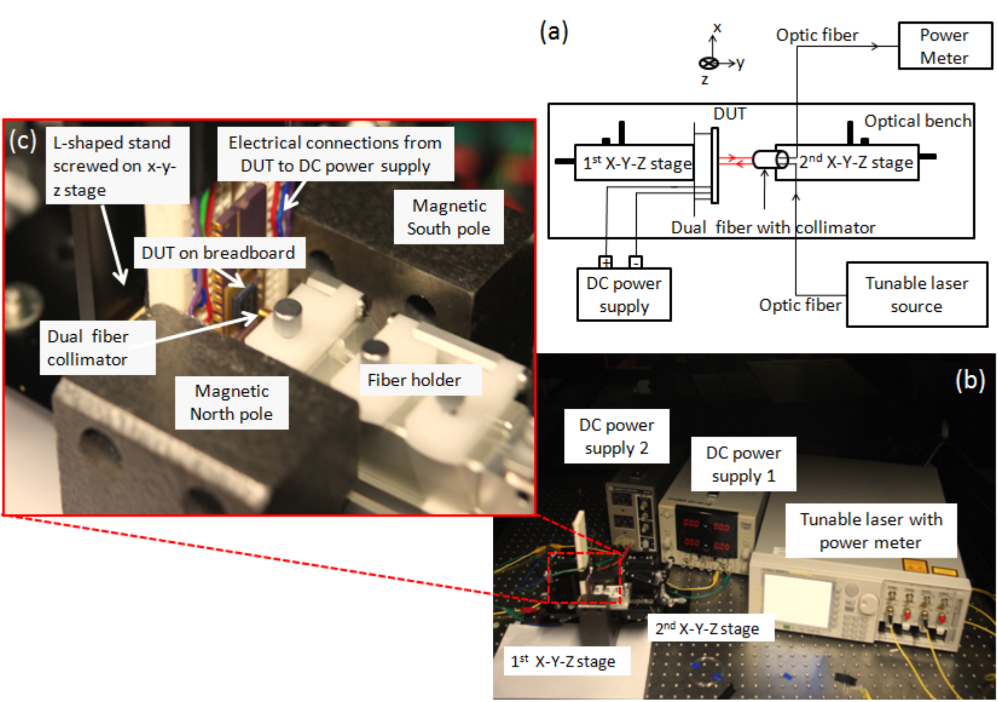

Fig. 6-5. (a) Schematic diagram of the measurement setup carried out on an anti-vibration optical bench. The stages are capable of moving in X-Y-Z directions and tilting along X-Y (θz) and Y-Z (θx) planes as well. (b) Photo illustrating the actual measurement setup which includes the tunable laser, power meter, two dc power supplies and stages. (c) A magnified photo at the DUT region, where the DUT is mounted upright in the presence of an external permanent magnetic field. The dual fiber collimator is adjusted to a working distance of 1mm away from the mirror surface.

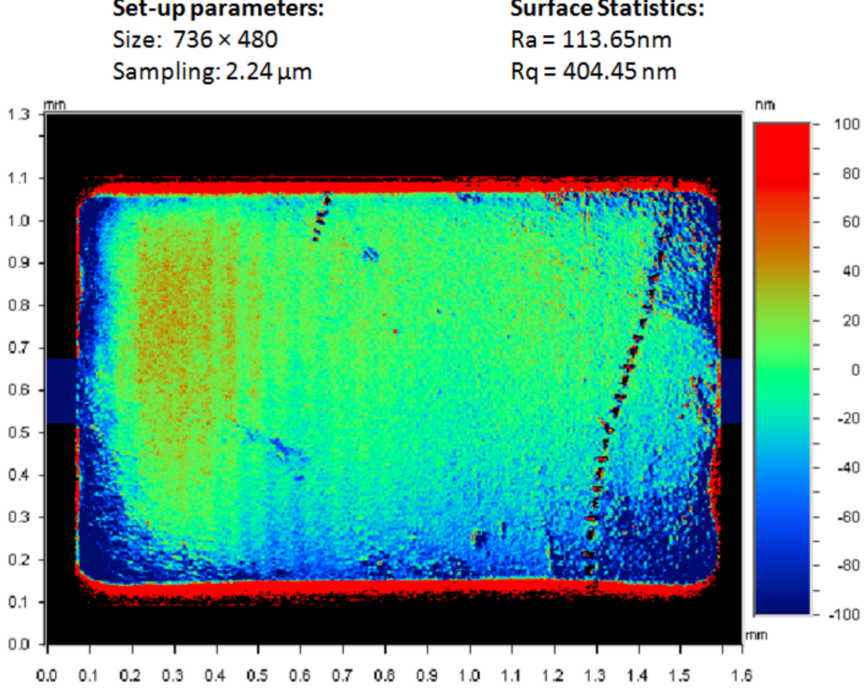

Fig. 6-6. White light interferometer measurement of the surface roughness for the aluminium coated mirror.

The schematic diagram of the measurement setup for the VOA characterization is illustrated in Fig. 6-5(a). The dual fiber with collimator used in this chapter is the same as that used in chapter 3. The optical measurement setup consists of a tunable infra-red (IR) laser source integrated with a power meter (Agilent 8164B Lightwave Measurement System), two multi-axis X-Y-Z-θx-θz adjustable stages, dual fiber with collimator and two dc power supplies. The device was mounted on the first adjustable stage via the breadboard while the dual fiber with collimator was mounted on the second adjustable stage via a fiber holder. The dual fiber collimator was placed at a working distance of 1 mm away from the mirror surface. The input IR light from the tunable laser was launched via one fiber, i.e. input fiber of the dual fiber through the collimator to the center of the mirror. The reflected light was collected by the same collimator to the power meter via the output fiber of the dual fiber. Two dc power supplies were used so that the ET actuators and the EM coils can be biased separately. The power of the IR laser source used in the experiment is 4 mW. The collimated beam diameter has been characterized to be 700 μm ± 25 μm, which is smaller than the mirror. The whole measurement setup was established on an anti-vibration optical table to reduce the effect of ambient shock to the characterization setup. Fig. 6-5(b) illustrates a photo of the actual measurement setup on an optical table while Fig. 6-5(c) shows a magnified photo of the device under test (DUT) region, where the DUT was mounted upright in the presence of a permanent magnetic field generated by a pair of Alcomax III magnets. The magnetic field strength at the center of the magnetic field was measured by a Gauss meter to be approximately 0.15 T. For the insertion loss measurement, the relative

position of the collimator and mirror was adjusted such that the coupling loss was minimized. In order to do so, red laser light of 632.8 nm was first shone through the collimator onto the center of the mirror. Both the stages were adjusted so that the red laser spot is centralized at the middle of the mirror. The IR tunable laser source was then fed into the input fiber after the coarse alignment step has been confirmed. During the fine alignment step, the relative position of the mirror to the collimator was adjusted by moving and tilting both the X-Y-Z-θx-θz stages such that minimum insertion loss was obtained. The measured insertion loss in this setup is about 1.8 dB, which is about a decibel higher than commercial VOA products. This is mainly caused by the surface warpage of the mirror and the inferior reflectivity of the Al coating compared to gold at 1550 nm.

The surface roughness of the fabricated Al-coated mirror was measured by a Veeco Wyko NT3300 white light interferometer and the mirror profile is shown in Fig. 6-6. The average surface roughness and root mean square roughness are 114nm and 404nm, respectively. The roughness of the mirror surface causes the measured insertion loss to be a decibel higher than commercial available VOA products. Further optimization of the VOA fabrication may improve the surface roughness of the mirror and reduce the insertion loss to less than 1 dB. For example, a very thin layer of sacrificial oxide may first be deposited on top of the aluminium reflective surface so that any physical damage sustained during the subsequent steps is on the sacrificial oxide layer only. This thin layer of sacrificial oxide can then be etched away using vapour hydrofluoric acid once the microstructures are released from the

backside. To further improve the surface quality of the mirror, atomic layer deposition (ALD) of aluminium on the mirror plate, instead of physical vapour deposition, may also be considered in order to improve the surface roughness and uniformity of the mirror.

6.4 Results and Discussion

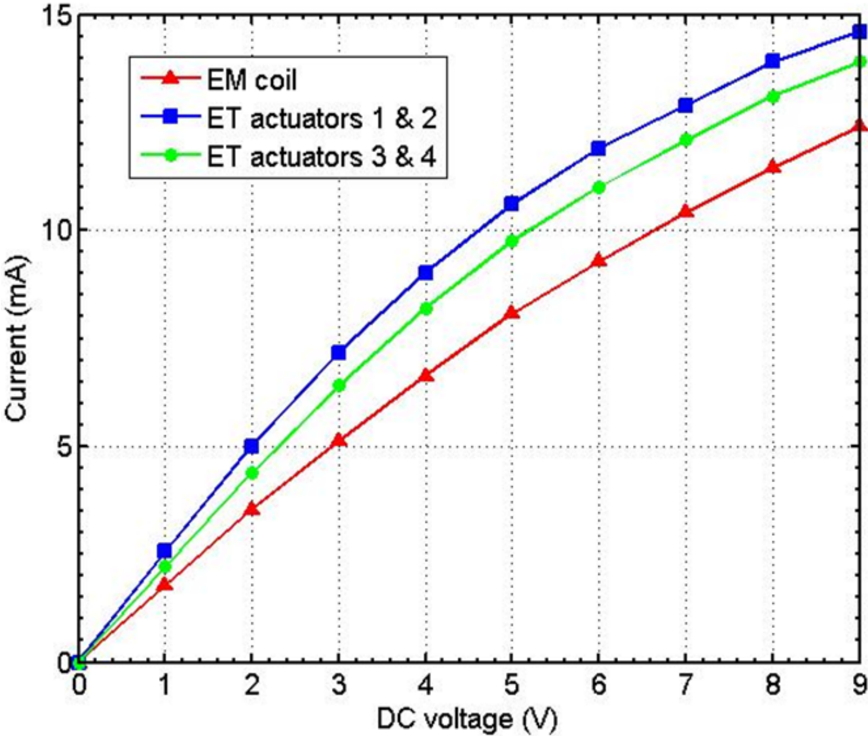

Fig. 6-7. Measured I-V curves for the EM coils and ET actuators, respectively.

The I-V curves of the EM coils and ET actuators are obtained from an Agilent b1500a Semiconductor Device Analyzer and shown in Fig. 6-7. A current of 6.6 mA was obtained when 4 V_{dc} was applied to the EM coils. This is equivalent to a power consumption of approximately 26 mW at 4 V_{dc}. In the case for ET actuation, the thermal power consumption plays a more pivotal role in the ET actuator performance compared to the magnitude of the current in EM actuation. Both ET actuators 1 and 2 were biased serially during the

characterization process, while the same was also applied to ET actuators 3 and 4. In addition, there is a slight discrepancy between the I-V curves for the two sets of ET actuators even though the layouts for both sets of actuators are the same. This may be due to the lithography inaccuracy and fabrication process variation. At 3 V_{dc}, the two sets of ET actuators 1 and 2, 3 and 4 have thermal power consumption of approximately 21 mW and 19 mW, respectively.

Besides the I-V characteristics of the EM coils and the ET actuators, several experiments were also carried out to study both the ET and EM attenuation in terms of static rotation angle and attenuation response under dc bias.

6.4.1 Optomechanical performance for EM attenuation mechanism

Fig. 6-8(a) shows both the optical deflection angle (ODA) obtained experimentally and the mathematically derived laser spot displacement for various dc driving voltages. In the case for the experimental ODA, it is obtained by shining a red He/Ne laser beam onto the mirror surface and measuring the displacements of the red laser spot on the screen when different dc voltages were applied to the EM coils. As evident from Fig. 6-8(a), an increase in dc voltage results in a larger ODA. This is expected as an increase in applied voltage will result in a larger current flowing in the EM coils, causing a larger Lorentz force to be acting on the frame, and hence rotating the mirror along the z-axis to a greater extent. An experimental optical rotation angle of 1.1° was obtained at 4 V_{dc}.

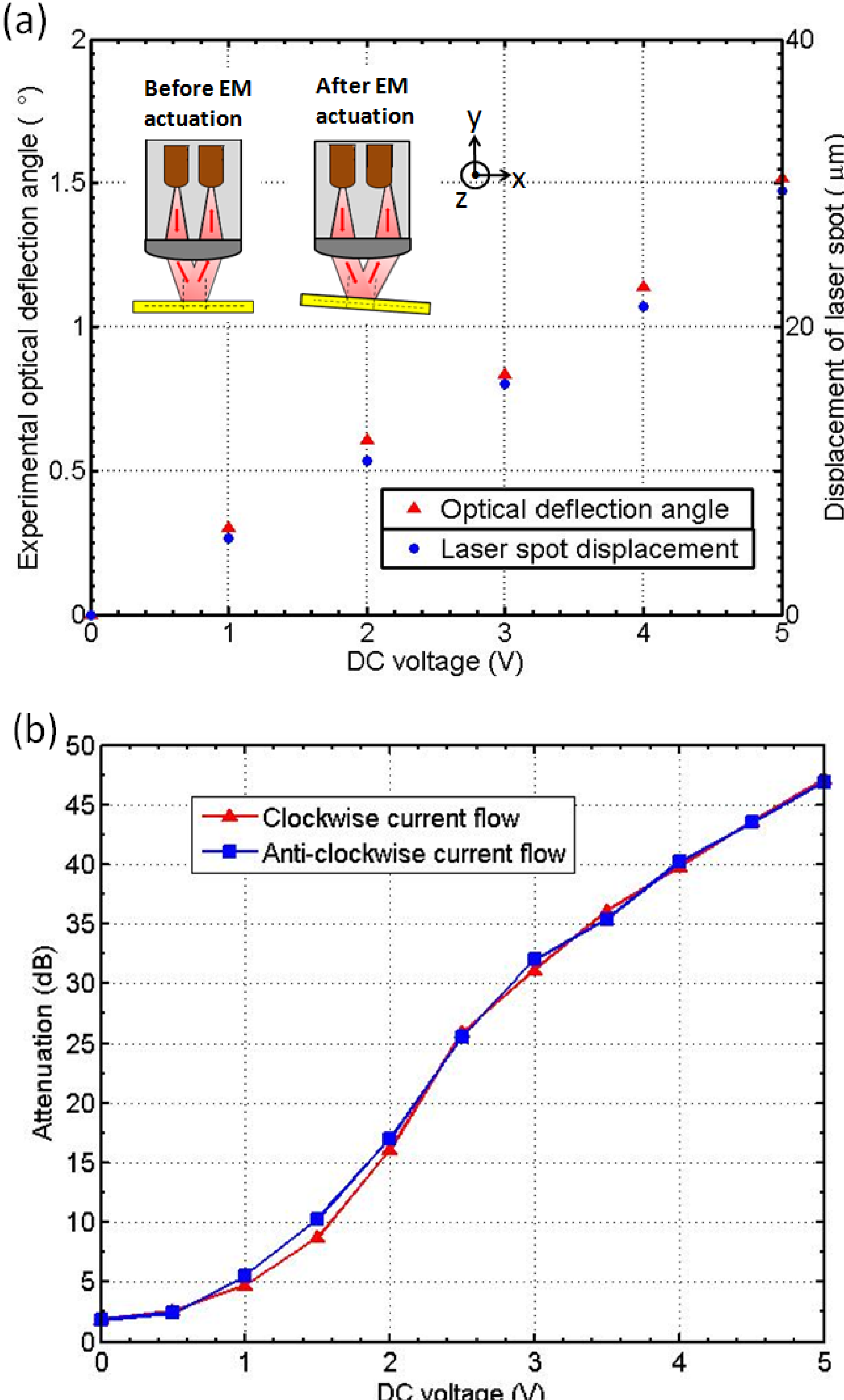

Fig. 6-8. (a) Experimental optical deflection angle and analytically calculated laser spot displacement versus dc voltage applied to the EM coil. The inset shows a schematic diagram of the EM attenuation mechanism, where the laser spot no longer couples perfectly from the input fiber into the output fiber after EM actuation. (b) Measured attenuation-bias curves for difference current direction in the EM coils.

Fig. 6-8(a) also shows the displacement of the IR laser spot from its original position ($\delta_{EM,laser}$) corresponding to minimum insertion loss at various dc voltages. Values for the laser spot displacements were derived using the experimental values of optical rotation angle (θ_{EM}) obtained in the same figure and substituting these values into equations (6.2) and (6.3). From Fig. 6-8(a), it is observed that the displacement of the laser spot, $\delta_{EM,laser}$, is approximately 21 μm at 4 V_{dc}. The inset shows the front profile of the mirror and the dual fiber collimator during EM attenuation. Before EM actuation when there is no current flowing in the coils, the normal of the mirror surface is perfectly aligned with the IR laser beam, hence coupling all the light from the input fiber to the output fiber, i.e., minimum insertion loss condition. When the mirror rotates due to a dc bias applied to the EM coils, the IR laser spot is displaced by $\delta_{EM,laser,}$ resulting in attenuation as a portion of the laser beam no longer couples into the output fiber.

Based on the VOA characterization setup shown in Fig. 6-5, the measured attenuation curves versus dc voltage applied to the EM coils for different current directions are shown in Fig. 6-8(b). The experiment was carried out at a fixed laser wavelength of 1550 nm as it is one of the three transmission windows where light attenuation and dispersion in the optical fiber are at the minimum during propagation. Both current directions in the EM coils yield almost identical attenuation characteristics, achieving a 40 dB dynamic attenuation at 4V_{dc} and electrical power consumption of 26 mW. A 40 dB dynamic attenuation range is sufficient with regards to most of the commercial applications. Correlating the experimental data obtained at 4 V_{dc}

in Fig. 6-8(a) and 6-8(b), it may be interpreted that 40 dB attenuation was achieved when the laser spot was displaced 21 μm away from its original position.

The wavelength dependent loss (WDL) of wavelengths ranging from 1510 nm - 1610 nm was also measured at various EM attenuation states and shown in Fig. 6-9. The WDL at driving voltages of 0 V_{dc} (1.8 dB), 1.5 V_{dc} (10 dB), 2.2 V_{dc} (20 dB) and 2.8 V_{dc} (30 dB) were less than 0.06 dB, 0.31 dB, 0.39 dB and 0.53 dB, respectively. These WDL data measured at the various attenuation states are of the same level with those data already reported in literature.

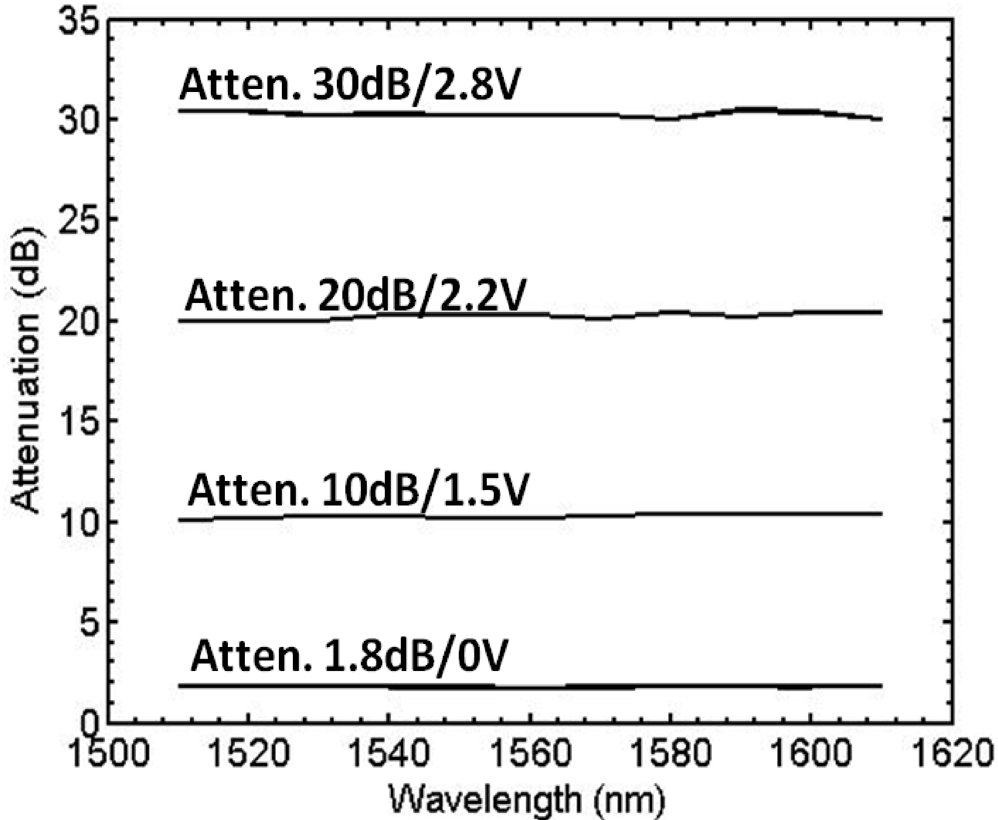

Fig. 6-9. Measured wavelength dependent loss at various attenuation states for EM attenuation.

6.4.2 Optomechanical performance for ET attenuation mechanism

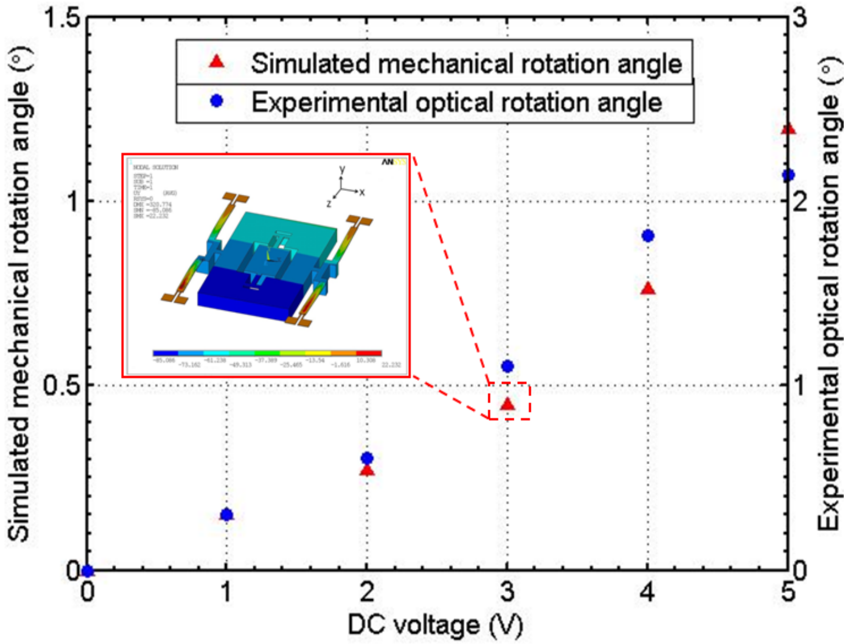

Fig. 6-10. Comparison of mechanical rotation angle (θ) obtained from simulation software ANSYS and optical rotation angle (2θ) obtained from He/Ne red laser experiment. Inset shows the simulated y-profile of the device obtained from ANSYS when ET actuators 1 and 2 were biased serially at $3V_{dc}$.

In the operation of the MEMS VOA based on ET attenuation mechanism, various dc voltages are applied to either one of the two sets of ET actuators 1 and 2 or 3 and 4. Fig. 6-10 compares the mechanical rotation angle (θ) obtained from finite element simulation software ANSYS and the optical rotation angle (2θ) obtained from the He/Ne red laser experiment, with ET actuators 1 and 2 biased at various dc voltages. The mechanical rotation angle derived from simulation matches closely with the optical rotation angle obtained from experiment as the experimental optical rotation angles (2θ) obtained at different DC voltages are almost twice larger than the simulated mechanical rotation angle (θ). The inset in Fig. 6-10 shows the simulated y-profile of the device obtained from ANSYS when ET actuators 1 and 2 are

biased serially at 3 V_{dc}, while an experimental optical rotation angle of 1.1° is obtained at $3V_{dc}$.

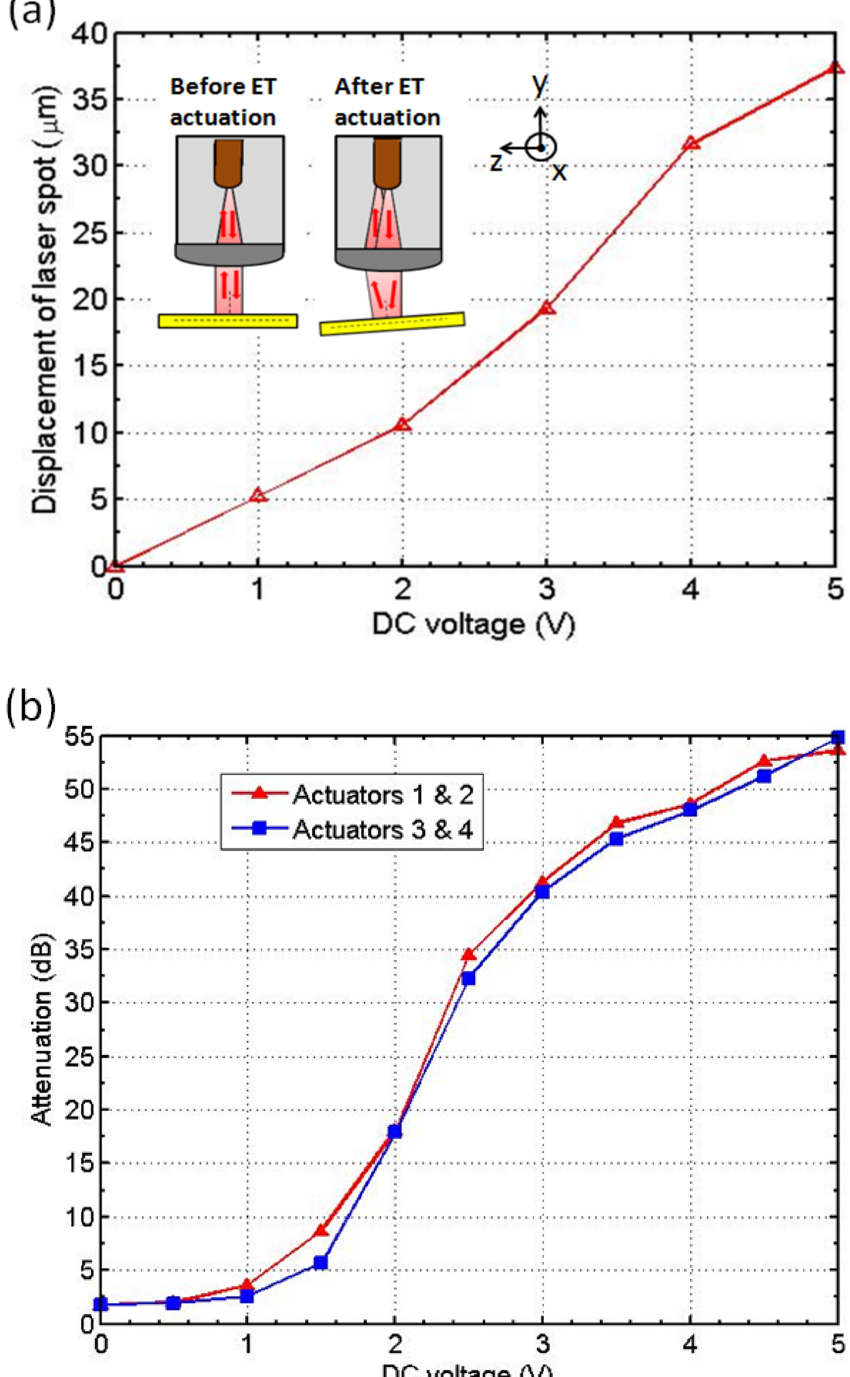

Fig. 6-11. Analytically calculated and experimental data obtained for ET attenuation mechanism. (a) Derived IR laser spot displacement versus dc driving voltage applied serially to ET actuators 1 and 2. The inset shows a schematic diagram of the ET attenuation mechanism, where the laser spot no longer couples perfectly from the input fiber into the output fiber after ET actuation. (b) Measured attenuation-bias curves for different sets of ET actuators.

The displacement of the laser spot for ET attenuation for different dc voltages, which is represented in Fig. 6-11(a), is also analytically calculated from equation (6-5) based on the experimental rotation angle derived in Fig. 6-10. The inset shows schematic diagram illustrating the side profile of the mirror and the dual fiber collimator during ET attenuation. When there is no bias applied to the ET actuators, all the light from the input fiber is coupled to the output fiber, i.e. minimum insertion loss condition. However, when ET actuators 1 and 2 are biased and heated up, they bend downwards and actuate the mirror during the process. As a result, the reflected light deviates from the optimized light path corresponding to minimum insertion loss. The coupled reflected light intensity towards the output fiber is reduced, resulting in increased attenuation with increasing DC voltages. As observed from Fig. 6-11(a), a laser spot displacement of 19 µm was obtained at 3 V_{dc}.

Fig. 6-11(b) shows the attenuation curve measured at 1550 nm when various dc voltages were applied to the two sets of ET actuators. ET actuators 1 and 2 had slightly better attenuation performance compared to ET actuators 3 and 4. This may be due to a greater amount of electrical power being converted to heating effect for ET actuators 1 and 2 compared to 3 and 4 at the same dc voltage, as evident from the I-V curves of the two sets of ET actuators in Fig. 6-7. Both sets of ET actuators, on average, achieved 40 dB attenuation range at 3V_{dc}, and electrical power consumption of 20 mW. Correlating the experimental data obtained at 3 V_{dc} in Fig 6-11(a) and 6-11(b), it may be interpreted that 40 dB attenuation was achieved when the laser spot was

displaced 19 μm away from its original position where minimum insertion loss is derived.

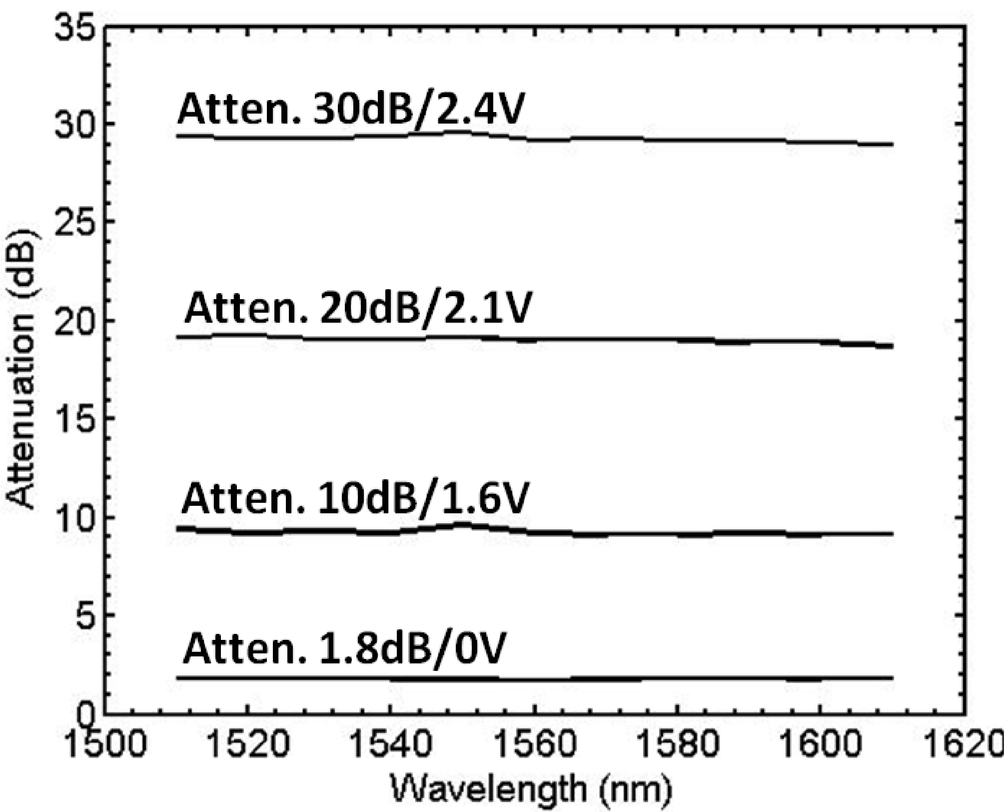

Fig. 6-12. Measured wavelength dependent loss at various attenuation states for ET attenuation.

The attenuation dependence on wavelength ranging from 1510 nm to 1610 nm was also measured at various ET attenuation states and shown in Fig. 6-12. The WDL at driving voltages of 0 V_{dc} (1.8 dB), 1.6 V_{dc} (10 dB), 2.1 V_{dc} (20 dB) and 2.4 V_{dc} (30 dB) were less than 0.06 dB, 0.50 dB, 0.59 dB and 0.63 dB, respectively.

Table 6-2 summarizes and compares the optomechanical performance obtained for both EM and ET attenuation schemes. To reach 40 dB dynamic attenuation range, voltages of 4 V_{dc} and 3 V_{dc} are needed, with 26 mW and 20 mW of electrical power being consumed by ET and EM attenuation schemes,

respectively. Analytical calculations have demonstrated that both attenuation schemes result in almost identical laser spot displacement, while the optical rotation angle (2θ) of the red laser derived experimentally are the same at 1.1° for both schemes. These results obtained are similar with the data derived in ref. [103] by Isamoto *et al.* where optical attenuation of 40 dB, corresponding to mechanical mirror angle (θ) of 0.3°, was obtained at 5 V_{dc} by their electrostatic microtorsion VOA device. WDL at the 30 dB attenuation state for both attenuation schemes are also at similar values with those VOAs already reported in literature.

Table 6-2. Comparison of the optomechanical performance for EM and ET attenuation

Attenuation state	40 dB				30 dB
Performance parameters	Voltage (V)	Electrical power consumption (mW)	Displacement of laser spot (µm)	Optical deflection angle (°)	WDL (dB)
EM	4	26	21	1.1	0.53
ET	3	20	19	1.1	0.63

In light of the above comparison, we may conclude that the analytical models used to derive the laser spot displacement are valid as both models require close to 20 µm of laser beam displacement in order to reach 40 dB attenuation range. The validity of the experimental attenuation results obtained are also verified separately through the red He/Ne red laser experiment where the optical rotation angle required to reach 40 dB attenuation range in both schemes are the same. In addition, based on the optomechanical performance matrix, ET attenuation mechanism is better than EM attenuation mechanism as

it consumes less electrical power for the same attenuation state. In terms of driving mechanisms, attenuation mechanism based on ET actuation is preferred over that of EM actuation as the former does not require an external magnetic source, hence offers better scaling viability and compact packaging. Despite the inherent capability of ET actuation being limited by the heat transfer into and out of the actuator, this is presently not a pressing issue in the operation of MEMS VOA as only dc operations are involved.

6.4.3 Optomechanical performance for hybrid attenuation mechanism

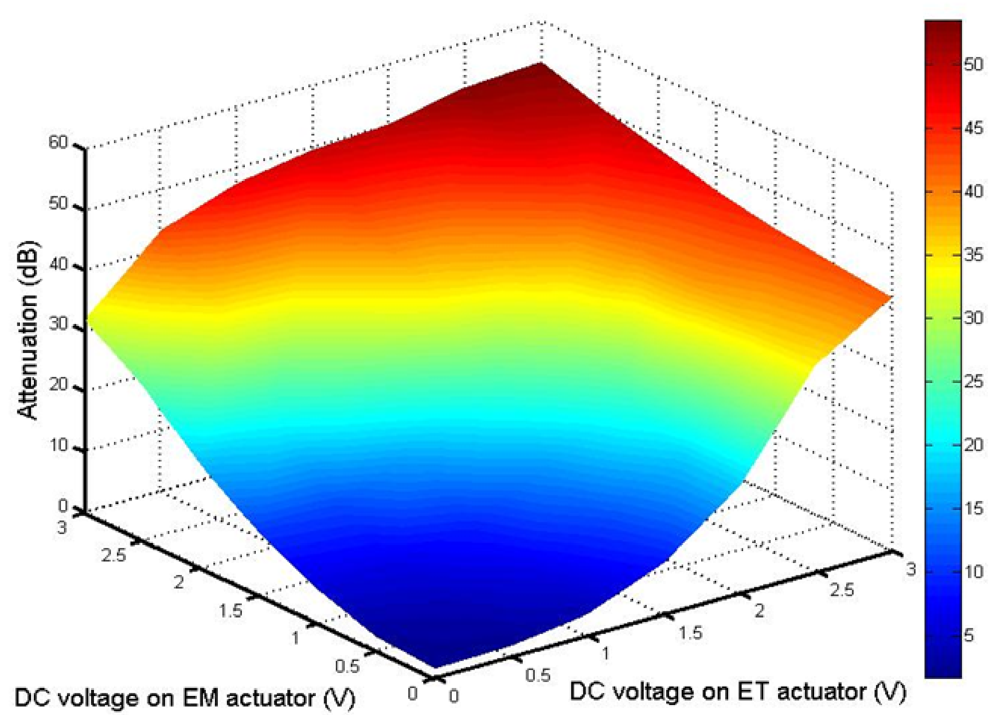

Fig. 6-13. Measured attenuation value as a function of dc driving voltages applied to EM and ET actuators during hybrid actuation.

In hybrid attenuation mechanism, dc voltages are applied simultaneously to the EM and ET actuators simultaneously. As shown in Fig. 6-13, various dc voltage combinations were applied to the two different actuators and an attenuation characteristic topography was derived. For

example, when a bias of 1.5 V_{dc} was applied serially to ET actuators 1 and 2, the attenuation changes from 8.6 dB to 49.4 dB as the voltage applied to the EM coils increased from 0 V_{dc} to 3 V_{dc}. For the reverse case, i.e. a voltage of 1.5 V_{dc} was applied to the EM coils, the attenuation changes from 10.3 dB to 45.8 dB as the voltage applied serially to the ET actuators 1 and 2 increased from 0 V_{dc} to 3 V_{dc}. Hence, from the attenuation topography, various voltage combinations could be made to the EM and ET actuators so as to obtain 40 dB attenuation range. For example, when 2 V_{dc} were applied to both the electromagetic and electrothermal actuators simultaneously, an attenuation of approximately 40 dB was obtained. This is equivalent to a total electrical power consumption of 17 mW, which is 3 mW lower than that achieved by electrothermal attenuation mechanism at 3 V_{dc}. As such, with the hybrid attenuation mechanism, lower electrical power consumption and an additional degree of freedom in attenuation control can be attained. More specifically, any deviation of attenuation-DC bias characteristics among the various VOA devices due to fabrication process and assembly steps can be compensated by changing the voltage combinations to the EM and ET actuators. By adopting ET actuation as the primary attenuation mechanism and EM attenuation for compensating any small deviations among the various VOA devices, smaller magnets of weaker magnetic field strength may be used, hence allowing room for miniature packaging.

6.5 Performance comparison of current designs with existing MEMS VOAs

Table 6-3. Comparison of FOM for different MEMS VOA designs

Actuation schemes	Ref	Unique feature	Attenuation range (dB)	DC voltage (V)	FOM
Piezoelectric (PZ)	VOA design in Chapter 3	3-D MEMS VOA driven by 1x10 piezoelectric actuators	47	2	23.5
	Lee *et al.* [68]	3-D reflective type MEMS VOA driven by piezoelectric actuators	50	1.2	41.7
Electrostatic (ES)	Hou *et al.* [110]	In-plane shutter-type VOA driven by rotary ES actuators	57	4.2	13.6
	Isamoto *et al.* [103]	3-D reflective type MEMS VOA driven by parallel plate ES actuators	40	5	8
	Kim *et al.* [109]	In-plane MEMS VOA based on dual 45 tilted vertical mirror driven by ES comb actuator	45	6	7.5
	Chen *et al.* [111]	In-plane retro-reflective type MEMS VOA driven by ES comb actuators	50	7	7.1
	Liu *et al.* [106]	In-plane shutter-type MEMS VOA using micromirror drawbridge driven by parallel plate ES actuator	45	8	5.6
	Cai *et al.* [108]	In-plane retro-reflective elliptical mirror driven by ES comb actuators	44	10.7	4.1
Electrothermal (ET)	VOA design in Chapter 6 (ET)	3-D MEMS VOA driven by hybrid actuators	55	5	11
	Lee *et al.* [129]	In-plane shutter type VOA driven by U-shaped ET actuator	37	3	12.3
	Lee *et al.* [112]	In-plane retro-reflective type MEMS VOA driven by H-shaped ET actuator	50	10	5
Electromagnetic (EM)	VOA design in Chapter 6 (EM)	3-D MEMS VOA driven by hybrid actuators	47	5	9.4

Table 6-3 compares the various existing MEMS VOA performances according to the figure of merit (FOM), which is being used as a metric to compare the relative attenuation efficiencies:

$$FOM = \frac{Attenuation}{V} \qquad (6.5)$$

where V is the voltage required to achieve the dynamic attenuation range. Voltage, instead of power consumption, has been considered for use as FOM due to the capacitive nature of electrostatic (ES) and piezoelectric (PZ) actuators, while for electrothermal (ET) and electromagnetic (EM) driven MEMS VOAs, voltage data are often reported in the literature. As evident from the table above, numerous MEMS VOAs based on in-plane reflective-type and shutter-type designs have been widely reported, with ES actuation especially favoured to drive the microshutter/micromirror.

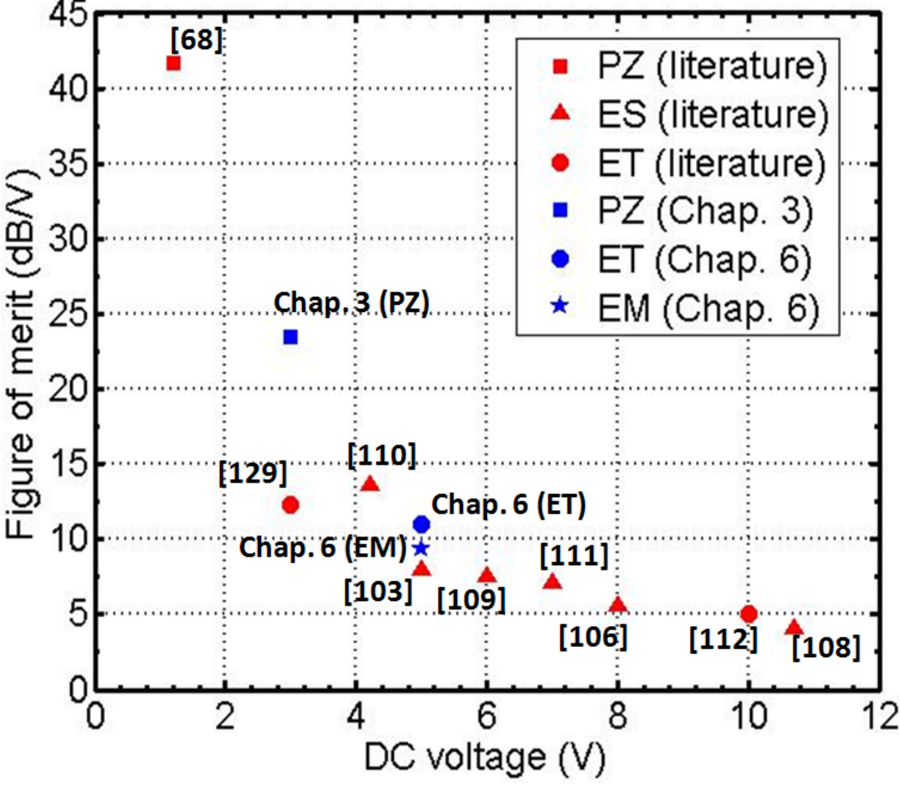

Fig. 6-14. Performance comparison of various MEMS VOAs reported in literature.

Fig. 6-14 summarizes the performance comparison of the various MEMS reported in literature (marked in red) and the 2 VOA designs (marked in blue) proposed in this thesis. Both the PZ and hybrid (EM & ET) VOA designs outperformed most of the reported electrostatic (ES) driven MEMS VOAs in the literature. This is generally expected as ES actuation often requires higher input voltage for the same actuator displacement compared with other actuation schemes. In the case of the MEMS VOAs proposed in this thesis, the piezoelectric driven MEMS VOA investigated in chapter 3 performs much better than the hybrid driven device proposed in this chapter. This is because in bending mode, both rotational and translational displacements were introduced to the mirror plate by the PZT actuators, whereas in both the cases of EM and ET attenuation mechanisms for the hybrid driven MEMS VOA, only rotational displacement was introduced to the micromirror. This causes less light to be coupled from the input fiber to the output fiber for the former, thus explaining why the piezoelectric MEMS VOA proposed in chapter 3 scores a much higher FOM compared to the hybrid MEMS VOA proposed in this chapter.

6.6 Summary

A novel MEMS mirror based on hybrid actuation mechanisms is proposed and verified for variable optical attenuation in a 3-D free space configuration. Both EM and ET actuations have been integrated in the same device for optical attenuation purposes. This makes our design essentially different from most of the shutter type, planar reflective and 3-D reflective VOAs that have already been reported in literature where only one form of

actuation mechanism is used to drive the shutter or mirror. Attenuation ranges of 40 dB have been achieved at 4 V_{dc}, 26mW and 3 $V_{dc,}$ 20mW by EM and ET attenuation schemes, respectively. Wavelength dependent loss has also been demonstrated to be less than 0.6 dB at all attenuation states for both attenuation mechanisms. ET attenuation mechanism has been concluded to perform better than EM attenuation as it consumes less electrical power for the same attenuation state and it removes the need for an external magnetic source. Hybrid attenuation mechanism has also been demonstrated successfully, allowing our device to consume even lesser electrical power and attain an additional degree of freedom in attenuation control. Last but not least, the use of CMOS compatible processes and material such as aluminium and silicon oxide for ET and EM actuation allow our design to be fully transferable to various foundry orientated CMOS-MEMS fabrication platforms. This allows for lower fabrication cost and monolithic integration with transistor circuits that enable a hybrid actuated MEMS VOA with electronic feedback to be developed.

Chapter 7
Conclusion and Future Work

7.1 Conclusion

This thesis presented various novel MEMS mirror designs and actuation mechanisms for 2-D scanning and VOA applications. With the focus on the development of novel actuation mechanisms to drive the MEMS mirror, characterization of the aforementioned designs have been made from the perspective of the aforementioned applications.

1. Two designs of piezoelectric driven MEMS mirror using mechanical supporting beam integrated with 1×10 individually biased PZT actuators were successfully designed, fabricated and characterized for 2-D scanning application. Although electrothermal bimorph beam actuators have been well characterized in terms of their capability to generate large deflection in bending mode, no design of torsional mirror driven by beam actuators has been reported for piezoelectric actuation mechanism yet. In the first design, i.e. design A, the array of PZT actuators were electrically connected in series, while in design B, the PZT actuators were electrically isolated. Through this design variation, the performance of these PZT MEMS scanners were investigated and compared by using different actuation mechanisms to elicit 2-D scanning for both the devices. Clear Lissajous patterns were obtained successfully for both designs, demonstrating the potential of both designs for low-frequency 2-D scanning applications.

In the case of dc operation for VOA application, design B was preferred due to the separated electrical connections to each of the actuators, which allowed the actuators to be individually biased. By addressing different bias voltages to the individual PZT actuators, different kind of actuation mechanisms such as translational motion (bending mode) and rotation motion (torsional mode) have been successfully demonstrated. An attenuation range of 40 dB was achieved at $1V_{dc}$ and $1.8V_{dc}$ during bending and torsional modes, respectively. This low operating voltage is among the smallest to be reported in the literature so far for MEMS-based VOA.

2. To further improve the scanning performance and reduce the number of PZT actuators and bonding pads, a S-shaped actuator design for MEMS scanner was developed as there are limited research effort being spent on a simple MEMS scanner design that makes use of only a single actuator to achieve 2-D scanning effect. For the same ac driving voltage, the ODA achieved by this S-shaped actuator design was demonstrated to be significantly larger than that of the 1×10 PZT actuator design. In addition, the superimposition of two ac excitation biases on a single piezoelectric actuator during dynamic mixed mode actuation is the first such actuation mechanism being demonstrated to drive a Si mirror plate. By addressing two excitation signals of different frequencies to the S-shaped PZT actuator, translational (bending mode) and rotational (torsional mode) motions operating at resonance condition were obtained. 2-D scanning was also successfully

demonstrated by superimposing the two ac signals into one combined signal to be used to excite the PZT actuator and drive the micromirror.

3. Although the proposed piezoelectric MEMS scanner designs in chapter 1 and chapter 3 fared inferiorly when compared to existing piezoelectric MEMS scanners in the literature, there are still much room for improvement through the reduction of the mass inertia of the mirror plate. In addition, while such gimbaled, piezoelectric MEMS scanners with inner and outer frame have been widely reported in the last decade which guarantees good performance, however, replicating such conventional designs is not the goal of this thesis. With one of the objectives of this thesis targeting at developing proof-of-concept 2-D MEMS scanners driven by novel actuation mechanisms, gimbal-less designs making use of only a single set of piezoelectric actuator/s to elicit 2-D scanning, hence, becomes the goal as such designs based on piezoelectric actuators have yet to be reported. It is also noteworthy that the performances of the proposed piezoelectric 2-D MEMS scanners have improved with each development cycle, starting from design A in chapter one to the S-shaped actuator driven design in chapter 3.
4. Besides piezoelectric-driven MEMS scanner, hybrid actuated MEMS scanner based on electrothermal and electromagnetic actuations were integrated in the same device for slow and scanning purposes, respectively. Such hybrid actuation mechanism proposed in this design allows for fast line scan driven by electromagnetic actuators operating at mechanical resonance condition to be produced on the horizontal

axis, while a slower sweep driven by electrothermal actuators to be produced on the orthogonal vertical axis. Optical deflection angles of ±1.5° for 74 Hz vertical scan at 12 mW by electrothermal actuation and ±10° for horizontal scan frequency of 202 Hz at 1.26 mA, 1 V_{ac} by electromagnetic actuation were reported. Various Lissajous patterns have been demonstrated at low power biasing condition, making the proposed hybrid actuation design approach suitable for mobile 2-D raster scanning applications powered by batteries with limited capacity.

For the case of VOA application, three types of attenuation mechanisms based on electromagnetic, electrothermal and hybrid, i.e. combination of electrothermal and electromagnetic, actuations were explored and studied. This approach of using hybrid attenuation differs greatly from all of the planar and 3-D MEMS VOA designs that have already been reported in literature where only one type of actuation mechanism is used to drive the mirror/shutter in order to achieve attenuation. An optical attenuation of 40 dB was obtained when 2 V_{dc} were applied to both the electromagnetic and electrothermal actuators simultaneously, while the electrical power consumption of the actuators was 17 mW in total. Our unique design of using both electrothermal and electromagnetic actuators simultaneously to achieve attenuation is the first demonstration of such hybrid driven CMOS compatible MEMS VOA device.

5. For the 2 designs of MEMS VOAs proposed in this thesis, the piezoelectric driven MEMS VOA investigated in chapter 3 performs

much better than the hybrid driven device proposed in chapter 6. This is because in bending mode, both rotational and translational displacements were introduced to the mirror plate by the PZT actuators, whereas in both the cases of EM and ET attenuation mechanisms for the hybrid driven MEMS VOA, only rotational displacement was introduced to the micromirror. This causes less light to be coupled from the input fiber to the output fiber for the former, thus explaining why the piezoelectric MEMS VOA proposed in chapter 3 scores a much higher FOM compared to the hybrid MEMS VOA proposed in chapter 6.

7.2 Future Work

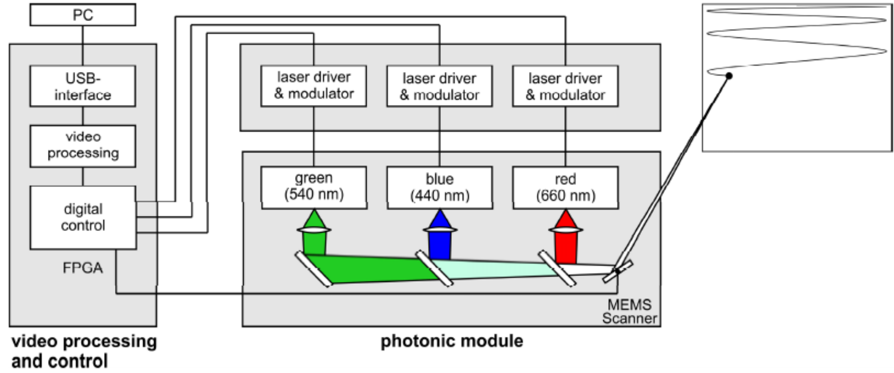

Fig. 7-1. Proposed system architecture to integrate proposed MEMS scanner for display applications.

Besides focusing on the development of new actuation mechanisms that has been undertaken in the thesis, further improvement from the standpoint of performance can still be done to improve the investigated MEMS mirror. One possible improvement is to reduce the mass inertia through the fabrication of a thinner mirror plate. This is important on many fronts. For example, with a smaller mass inertia, a smaller voltage will be

needed to drive the lighter mirror plate, while achieving the same optical performance. More importantly, high resolution display applications such as picoprojectors and heads-up display, which requires operating frequency in the range of 10 kHz – 20 kHz may now be deemed feasible since the resonant frequency of a mechanical system is inversely proportional to the square root of the mass of the system. To overcome the issue of dynamic deformation of a thinner mirror plate during high frequency scan, a reinforcement rib may be patterned and fabricated beneath the mirror surface to provide additional rigidity.

In order to make the developed MEMS scanner into a full-fledged product, the next step that can possibly be undertaken in the following phase is to develop the system architecture as shown in Fig. 7-1. A video processing and control unit based on USB-interface FPGA can be used to transmit the data from the computer to the electronic circuit. A computer is then used to read and decode the information streamed to it, while the information data in the form of image or video will be fed to the digital control which will produce signals that control the red, green and blue laser diodes for a full color display. The modulated light will then be passed to the already developed MEMS scanner and projected onto a screen. Vacuum packaging of the MEMS scanner can be considered to reduce the effect of air damping when the microstructures undergo high frequency oscillation. A housing, estimated to be of dimensions 5 cm × 5 cm × 2 cm, may be enough to package the whole system.

Besides using the MEMS mirror designs proposed in this thesis for VOA and 2-D scanning purposes, new application such as miniaturized free space optical laser communication among a swarm of nano-satellites is one of the possible direction that this research may be carried forward to as optical communication links offer many advantages over conventional microwave links. In particular, free space laser systems can provide narrow beam widths and high gains with much smaller hardware, unlike microwave communication where large antennas and high-power transmitters would have to be used at limited bandwidth. With MEMS mirror, high capacity laser beam steering can be enabled, allowing pointing within a swarm of nano-satellites in a dynamic constellation. On the other hand, by replacing the mirror plate with metamaterial or subwavelength structures such as photonic crystals, new application domain in the region of wavelength ranging from 10 µm – 3 mm, i.e. terahertz wave MEMS scanner for biological imaging or security screening can be conceptualized. The various actuator designs and microfabrication experience amassed from the works discussed in this thesis will be the cornerstones for the success of these proposed future works.

REFERENCES

[1] H. Schenk, P. Durr, T. Haase, D. Kunze, U. Sobe, H. Lakner, and H. Kuck, "Large deflection micromechanical scanning mirrors for linear scans and pattern generation," *IEEE J. Sel. Top. Quantum Electron.*, vol. 6, no. 5, pp. 715-722, 2000.

[2] T. Bifano, "Adaptive imaging: MEMS deformable mirrors," *Nature Photon.*, vol. 5, no. 1, pp. 21-23, 2011.

[3] L. Li, R. Li, W. Lubeigt, and D. Uttamchandani, "Design, Simulation, and Characterization of a Bimorph Varifocal Micromirror and Its Application in an Optical Imaging System," *J. Microelectromech. Syst.*, vol. 22, no. 2, pp. 285-294, 2013.

[4] R.R.A. Syms, H. Zou, J. Stagg, and H. Veladi, "Sliding-blade MEMS iris and variable optical attenuator," *J. Micromech. Microeng.*, vol. 14, no. 12, pp. 1700-1710, Dec 2004.

[5] L. Li, J. Zawadzka, and D. Uttamchandani, "Integrated self-assembling and holding technique applied to a 3-D MEMS variable optical attenuator," *J. Microelectromech. Syst.*, vol. 13, no. 1, pp. 83-90, 2004.

[6] Y. Du, G. Zhou, K.L. Cheo, Q. Zhang, H. Feng, and F.S. Chau, "Double-Layered Vibratory Grating Scanners for High-Speed High-Resolution Laser Scanning," *J. Microelectromech. Syst.*, vol. 19, no. 5, pp. 1186-1196, 2010.

[7] J. Yao, D. Leuenberger, M.C.M. Lee, and M.C. Wu, "Silicon Microtoroidal Resonators With Integrated MEMS Tunable Coupler," *IEEE J. Sel. Top. Quantum Electron.*, vol. 13, no. 2, pp. 202-208, 2007.

[8] K. Aljasem, L. Froehly, A. Seifert, and H. Zappe, "Scanning and Tunable Micro-Optics for Endoscopic Optical Coherence Tomography," *J. Microelectromech. Syst.*, vol. 20, no. 6, pp. 1462-1472, 2011.

[9] J.B. Chou, K. Yu, and M.C. Wu, "Electrothermally Actuated Lens Scanner and Latching Brake for Free-Space Board-to-Board Optical Interconnects," *J. Microelectromech. Syst.*, vol. 21, no. 5, pp. 1107-1116, 2012.

[10] M. Panicia and S. Koehl, "The silicon solution," *IEEE Spectr.*, vol. 42, no. 10, pp. 38-43, 2005.

[11] N. Savage, "Light at the end of the chip," *IEEE Spectr.*, vol. 47, no. 5, pp. 19-19, 2010.

[12] C.-D. Liao and J.-C. Tsai, "The Evolution of MEMS Displays," *IEEE Trans. Ind. Electon.*, vol. 56, no. 4, pp. 1057-1065, 2009.

[13] D. Graham-Rowe, "Projectors get personal," *Nature Photon.*, vol. 1, no. 12, pp. 677-679, Dec 2007.

[14] W. Noell, P.A. Clerc, L. Dellmann, B. Guldimann, H.P. Herzig, O. Manzardo, C.R. Marxer, K.J. Weible, R. Dandliker, and N. de Rooij, "Applications of SOI-based optical MEMS," *IEEE J. Sel. Top. Quantum Electron.*, vol. 8, no. 1, pp. 148-154, 2002.

[15] M.C. Wu, O. Solgaard, and J.E. Ford, "Optical MEMS for Lightwave Communication," *IEEE/OSA J. Lightw.Technol.*, vol. 24, no. 12, pp. 4433-4454, 2006.

[16] H. Toshiyoshi, "Lateral spread of MEMS WDM technologies," in *Proc. SPIE 7930*, MOEMS and Miniaturized Systems X, San Francisco, CA, 2011, pp. 793003.

[17] R.F. Wolffenbuttel, "MEMS-based optical mini- and microspectrometers for the visible and infrared spectral range," *J. Micromech. Microeng.*, vol. 15, no. 7, pp. S145-S152, Jul 2005.

[18] Y. Pan, H. Xie, and G.K. Fedder, "Endoscopic optical coherence tomography based on a microelectromechanical mirror," *Opt. Lett.*, vol. 26, no. 24, pp. 1966-1968, Dec 15 2001.

[19] W. Piyawattanametha and T.D. Wang, "MEMS-Based Dual-Axes Confocal Microendoscopy," *IEEE J. Sel. Top. Quantum Electron.*, vol. 16, no. 4, pp. 804-814, 2010.

[20] X. Mu, G. Zhou, H. Yu, Y. Du, H. Feng, J.M.L. Tsai, and F.S. Chau, "Compact MEMS-driven pyramidal polygon reflector for circumferential scanned endoscopic imaging probe," *Opt. Exp.*, vol. 20, no. 6, pp. 6325-6339, 2012.

[21] J.B. Sampsell, "Digital micromirror device and its application to projection displays," *J. Vac. Sci. Technol. B*, vol. 12, no. 6, pp. 3242-3246, 1994.

[22] L.J. Hornbeck, "Current status of the digital micromirror device (DMD) for projection television applications," in *Proc. IEEE Electron Devices Meeting*, Washington DC, USA, 1993, pp. 381-384.

[23] O. Solgaard, F.S.A. Sandejas, and D.M. Bloom, "Deformable grating optical modulator," *Opt. Lett.*, vol. 17, no. 9, pp. 688-690, May 1992.

[24] T.S. Perry, "Tomorrow's TV - the grating light valve," *IEEE Spectr.*, vol. 41, no. 4, pp. 38-41, 2004.

[25] J. Dolcourt 2012, "Samsung Galaxy Beam review," *http://reviews.cnet.com/smartphones/samsung-galaxy-beam-unlocked/4505-6452_7-35150645.html*.

[26] D. Murph 2010, "Microvision's PicoP-based SHOWWX+ projector: twice as bright, zero percent larger," *http://www.engadget.com/2010/11/23/microvisions-picop-based-showwx-projector-twice-as-bright-ze/*.

[27] C. Lee and J.A. Yeh, "Development and evolution of MOEMS technology in variable optical attenuators," *J. Micro/Nanolith. MEMS MOEMS*, vol. 7, no. 2, pp. 021003, 2008.

[28] T.-W. Yeow, K.L.E. Law, and A. Goldenberg, "MEMS optical switches," *IEEE Commun. Mag.*, vol. 39, no. 11, pp. 158-163, 2001.

[29] D.J. Bishop, C.R. Giles, and G.P. Austin, "The Lucent LambdaRouter: MEMS technology of the future here today," *IEEE Commun. Mag.*, vol. 40, no. 3, pp. 75-79, 2002.

[30] A. Neukermans and R. Ramaswami, "MEMS technology for optical networking applications," *IEEE Commun. Mag.*, vol. 39, no. 1, pp. 62-69, 2001.

[31] A.Q. Liu and X.M. Zhang, "A review of MEMS external-cavity tunable lasers," *J. Micromech. Microeng.*, vol. 17, no. 1, pp. R1-R13, 2007.

[32] D.J. Bell, T.J. Lu, N.A. Fleck, and S.M. Spearing, "MEMS actuators and sensors: observations on their performance and selection for purpose," *J. Micromech. Microeng.*, vol. 15, no. 7, pp. S153, 2005.

[33] A. Jain, H.W. Qu, S. Todd, and H. Xie, "A thermal bimorph micromirror with large bi-directional and vertical actuation," *Sens. Actuators A, Phys.*, vol. 122, no. 1, pp. 9-15, Jul 2005.

[34] S.T. Todd and H. Xie, "An Electrothermomechanical Lumped Element Model of an Electrothermal Bimorph Actuator," *J. Microelectromech. Syst.*, vol. 17, no. 1, pp. 213-225, 2008.

[35] J.J. Sun, S.G. Guo, L. Wu, L. Liu, S.W. Choe, B.S. Sorg, and H. Xie, "3D In Vivo optical coherence tomography based on a low-voltage, large-scan-range 2D MEMS mirror," *Opt. Exp.*, vol. 18, no. 12, pp. 12065-12075, Jun 7 2010.

[36] S. Pal and H. Xie, "Analysis and Fabrication of Curved Multimorph Transducers That Undergo Bending and Twisting," *J. Microelectromech. Syst.*, vol. 21, no. 5, pp. 1241-1251, 2012.

[37] J.H. Comtois and V.M. Bright, "Applications for surface-micromachined polysilicon thermal actuators and arrays," *Sens. Actuators A, Phys.*, vol. 58, no. 1, pp. 19-25, Jan 1997.

[38] L. Li and D. Uttamchandani, "Modified asymmetric micro-electrothermal actuator: analysis and experimentation," *J. Micromech. Microeng.*, vol. 14, no. 12, pp. 1734, 2004.

[39] H. Veladi, R.R.A. Syms, and H. Zou, "A single-sided process for differentially cooled electrothermal micro-actuators," *J. Micromech. Microeng.*, vol. 18, no. 5, pp. 055033, 2008.

[40] L. Li and D. Uttamchandani, "Dynamic response modelling and characterization of a vertical electrothermal actuator," *J. Micromech. Microeng.*, vol. 19, no. 7, pp. 075014, 2009.

[41] Y. Zhang, Y.-S. Choi, and D.-W. Lee, "Monolithic micro-electro-thermal actuator integrated with a lateral displacement sensor," *J. Micromech. Microeng.*, vol. 20, no. 8, pp. 085031, 2010.

[42] L. Que, J.S. Park, and Y.B. Gianchandani, "Bent-beam electrothermal actuators - Part I: Single beam and cascaded devices," *J. Microelectromech. Syst.*, vol. 10, no. 2, pp. 247-254, Jun 2001.

[43] C. Lee and C.-Y. Wu, "Study of electrothermal V-beam actuators and latched mechanism for optical switch," *J. Micromech. Microeng.*, vol. 15, no. 1, pp. 11, 2005.

[44] A.M.H. Kwan, S. Song, X. Lu, L. Lu, Y.-K. Teh, Y.-F. Teh, E.W.C. Chong, Y. Gao, W. Hau, F. Zeng, M. Wong, C. Huang, A. Taniyama, Y. Makino, S. Nishino, T. Tsuchiya, and O. Tabata, "Improved Designs for an Electrothermal In-Plane Microactuator," *J. Microelectromech. Syst.*, vol. 21, no. 3, pp. 586-595, 2012.

[45] R. Hokari and K. Hane, "A Varifocal Convex Micromirror Driven by a Bending Moment," *IEEE J. Sel. Top. Quantum Electron.*, vol. 15, no. 5, pp. 1310-1316, 2009.

[46] F. Zimmer, M. Lapisa, T. Bakke, M. Bring, G. Stemme, and F. Niklaus, "One-Megapixel Monocrystalline-Silicon Micromirror Array on CMOS Driving Electronics Manufactured With Very Large-Scale Heterogeneous Integration," *J. Microelectromech. Syst.*, vol. 20, no. 3, pp. 564-572, 2011.

[47] C. Lee, "Arrayed variable optical attenuator using retro-reflective MEMS mirrors," *IEEE Photon. Technol. Lett.*, vol. 17, no. 12, pp. 2640-2642, 2005.

[48] T.-S. Lim, C.-H. Ji, C.-H. Oh, H. Kwon, Y. Yee, and J.U. Bu, "Electrostatic MEMS variable optical attenuator with rotating folded micromirror," *IEEE J. Sel. Top. Quantum Electron.*, vol. 10, no. 3, pp. 558-562, 2004.

[49] J.A. Yeh, S.-S. Jiang, and C. Lee, "MOEMS variable optical attenuators using rotary comb drive actuators," *IEEE Photon. Technol. Lett.*, vol. 18, no. 10, pp. 1170-1172, 2006.

[50] U. Krishnamoorthy, D. Lee, and O. Solgaard, "Self-aligned vertical electrostatic combdrives for micromirror actuation," *J. Microelectromech. Syst.*, vol. 12, no. 4, pp. 458-464, 2003.

[51] R. Hyejun, W. Piyawattanametha, Y. Taguchi, D. Lee, M.J. Mandella, and O. Solgaard, "Two-Dimensional MEMS Scanner for Dual-Axes Confocal Microscopy," *J. Microelectromech. Syst.*, vol. 16, no. 4, pp. 969-976, 2007.

[52] J.-W. Jeong, S. Kim, and O. Solgaard, "Split-Frame Gimbaled Two-Dimensional MEMS Scanner for Miniature Dual-Axis Confocal Microendoscopes Fabricated by Front-Side Processing," *J. Microelectromech. Syst.*, vol. 21, no. 2, pp. 308-315, 2012.

[53] H. Dooyoung, S.T.Y. Huang, T. Jui-Che, H. Toshiyoshi, and M.C. Wu, "Low-voltage, large-scan angle MEMS analog micromirror arrays with hidden vertical comb-drive actuators," *J. Microelectromech. Syst.*, vol. 13, no. 2, pp. 279-289, 2004.

[54] K. Sunghoon, V. Milanovic, and L.P. Lee, "Vertical combdrive based 2-D gimbaled micromirrors with large static rotation by backside island isolation," *IEEE J. Sel. Top. Quantum Electron.*, vol. 10, no. 3, pp. 498-504, 2004.

[55] H.M. Chu and K. Hane, "Design, fabrication and vacuum operation characteristics of two-dimensional comb-drive micro-scanner," *Sens. Actuators A, Phys.*, vol. 165, no. 2, pp. 422-430, 2011.

[56] J. Kim and L. Lin, "Electrostatic scanning micromirrors using localized plastic deformation of silicon," *J. Micromech. Microeng.*, vol. 15, no. 9, pp. 1777-1785, 2005.

[57] J. Kim, D. Christensen, and L. Lin, "Monolithic 2-D scanning mirror using self-aligned angular vertical comb drives," *IEEE Photon. Technol. Lett.*, vol. 17, no. 11, pp. 2307-2309, 2005.

[58] H. Xie, Y. Pan, and G.K. Fedder, "A CMOS-MEMS mirror with curled-hinge comb drives," *J. Microelectromech. Syst.*, vol. 12, no. 4, pp. 450-457, 2003.

[59] H. Dooyoung, P.R. Patterson, H.D. Nguyen, H. Toshiyoshi, and M.C. Wu, "Theory and experiments of angular vertical comb-drive actuators for scanning micromirrors," *IEEE J. Sel. Top. Quantum Electron.*, vol. 10, no. 3, pp. 505-513, 2004.

[60] W. Piyawattanametha, P.R. Patterson, D. Hah, H. Toshiyoshi, and M.C. Wu, "Surface- and bulk- micromachined two-dimensional scanner driven by angular vertical comb actuators," *J. Microelectromech. Syst.*, vol. 14, no. 6, pp. 1329-1338, 2005.

[61] Y. Eun, H. Na, J. Choi, J.-i. Lee, and J. Kim, "Angular vertical comb actuators assembled on-chip using in-plane electrothermal actuators and latching mechanisms," *Sens. Actuators A, Phys.*, 2010.

[62] S. Trolier-McKinstry and P. Muralt, “Thin film piezoelectrics for MEMS,” *J. Electroceramics*, vol. 12, no. 1-2, pp. 7-17, Jan-Mar 2004.
[63] P. Muralt, R.G. Polcawich, and S. Trolier-McKinstry, “Piezoelectric Thin Films for Sensors, Actuators, and Energy Harvesting,” *MRS Bull.*, vol. 34, no. 9, pp. 658-664, Sep 2009.
[64] S. Tadigadapa and K. Mateti, “Piezoelectric MEMS sensors: state-of-the-art and perspectives,” *Meas. Sci. Technolo.*, vol. 20, no. 9, pp. 092001, 2009.
[65] Y. Hishinuma and E.-H. Yang, “Piezoelectric unimorph microactuator arrays for single-crystal silicon continuous-membrane deformable mirror,” *J. Microelectromech. Syst.*, vol. 15, no. 2, pp. 370-379, 2006.
[66] I. Kanno, T. Kunisawa, T. Suzuki, and H. Kotera, “Development of Deformable Mirror Composed of Piezoelectric Thin Films for Adaptive Optics,” *IEEE J. Sel. Top. Quantum Electron.*, vol. 13, no. 2, pp. 155-161, 2007.
[67] S.-J. Kim, Y.-H. Cho, H.-J. Nam, and J.U. Bu, “Piezoelectrically pushed rotational micromirrors using detached PZT actuators for wide-angle optical switch applications,” *J. Micromech. Microeng.*, vol. 18, no. 12, pp. 125022, 2008.
[68] C. Lee, F.-L. Hsiao, T. Kobayashi, K.H. Koh, P.V. Ramana, W. Xiang, B. Yang, C.W. Tan, and D. Pinjala, “A 1-V Operated MEMS Variable Optical Attenuator Using Piezoelectric PZT Thin-Film Actuators,” *IEEE J. Sel. Top. Quantum Electron.*, vol. 15, no. 5, pp. 1529-1536, 2009.
[69] Y. Yasuda, M. Akamatsu, M. Tani, T. Iijima, and H. Toshiyoshi, “Piezoelectric 2D Optical Micro Scanners with PZT Thick Films,” *Integr. Ferroelectr.*, vol. 76, no. 1, pp. 81-91, 2005.
[70] T. Kobayashi, R. Maeda, T. Itoh, and R. Sawada, “Smart optical microscanner with piezoelectric resonator, sensor, and tuner using $Pb(Zr,Ti)O_3$ thin film,” *Appl. Phys. Lett.*, vol. 90, no. 18, pp. 183514, 2007.
[71] U. Baran, D. Brown, S. Holmstrom, D. Balma, W.O. Davis, P. Muralt, and H. Urey, “Resonant PZT MEMS Scanner for High-Resolution Displays,” *J. Microelectromech. Syst.*, vol. 21, no. 6, pp. 1303-1310, 2012.
[72] H. Miyajima, N. Asaoka, M. Arima, Y. Minamoto, K. Murakami, K. Tokuda, and K. Matsumoto, “A durable, shock-resistant electromagnetic optical scanner with polyimide-based hinges,” *J. Microelectromech. Syst.*, vol. 10, no. 3, pp. 418-424, 2001.
[73] T. Mitsui, Y. Takahashi, and Y. Watanabe, “A 2-axis optical scanner driven nonresonantly by electromagnetic force for OCT imaging,” *J. Micromech. Microeng.*, vol. 16, no. 11, pp. 2482, 2006.
[74] A.D. Yalcinkaya, H. Urey, D. Brown, T. Montague, and R. Sprague, “Two-axis electromagnetic microscanner for high resolution displays,” *J. Microelectromech. Syst.*, vol. 15, no. 4, pp. 786-794, 2006.
[75] H. Urey, S. Holmstrom, and A.D. Yalcinkaya, “Electromagnetically Actuated FR4 Scanners,” *IEEE Photon. Technol. Lett.*, vol. 20, no. 1, pp. 30-32, 2008.

[76] I.-J. Cho and E. Yoon, "A low-voltage three-axis electromagnetically actuated micromirror for fine alignment among optical devices," *J. Micromech. Microeng.*, vol. 19, no. 8, pp. 085007, 2009.
[77] C.-H. Ji, M. Choi, S.-C. Kim, K.-C. Song, J.-U. Bu, and H.-J. Nam, "Electromagnetic Two-Dimensional Scanner Using Radial Magnetic Field," *J. Microelectromech. Syst.*, vol. 16, no. 4, pp. 989-996, 2007.
[78] A.D. Yalcinkaya, O. Ergeneman, and H. Urey, "Polymer magnetic scanners for bar code applications," *Sens. Actuators A, Phys.*, vol. 135, no. 1, pp. 236-243, 2007.
[79] A.D. Yalcinkaya, H. Urey, and S. Holmstrom, "NiFe Plated Biaxial MEMS Scanner for 2-D Imaging," *IEEE Photon. Technol. Lett.*, vol. 19, no. 5, pp. 330-332, 2007.
[80] C.P.B. Siu, H. Zeng, and M. Chiao, "Magnetically actuated MEMS microlens scanner for in vivo medical imaging," *Opt. Exp.*, vol. 15, no. 18, pp. 11154-11166, Sep 2007.
[81] T.-L. Tang, C.-P. Hsu, W.-C. Chen, and W. Fang, "Design and implementation of a torque-enhancement 2-axis magnetostatic SOI optical scanner," *J. Micromech. Microeng.*, vol. 20, no. 2, pp. 025020, 2010.
[82] N. Weber, D. Hertkorn, H. Zappe, and A. Seifert, "Polymer/Silicon Hard Magnetic Micromirrors," *J. Microelectromech. Syst.*, vol. 21, no. 5, pp. 1098-1106, 2012.
[83] A. Jain and H. Xie, "A single-crystal silicon micromirror for large bi-directional 2D scanning applications," *Sens. Actuators A, Phys.*, vol. 130-131, pp. 454-460, 2006.
[84] Y. Bai, J.T.W. Yeow, and B.C. Wilson, "Design, Fabrication, and Characteristics of a MEMS Micromirror With Sidewall Electrodes," *J. Microelectromech. Syst.*, vol. 19, no. 3, pp. 619-631, 2010.
[85] Y. Wang, M. Raj, H.S. McGuff, G. Bhave, B. Yang, T. Shen, and X. Zhang, "Portable oral cancer detection using a miniature confocal imaging probe with a large field of view," *J. Micromech. Microeng.*, vol. 22, no. 6, pp. 065001, 2012.
[86] H.-A. Yang, T.-L. Tang, S.T. Lee, and W. Fang, "A Novel Coilless Scanning Mirror Using Eddy Current Lorentz Force and Magnetostatic Force," *J. Microelectromech. Syst.*, vol. 16, no. 3, pp. 511-520, 2007.
[87] C.-D. Chen, Y.-J. Wang, and P. Chang, "A novel two-axis MEMS scanning mirror with a PZT actuator for laser scanning projection," *Opt. Exp.*, vol. 20, no. 24, pp. 27003-27017, 2012.
[88] M. Tani, M. Akamatsu, Y. Yasuda, and H. Toshiyoshi, "A two-axis piezoelectric tilting micromirror with a newly developed PZT-meandering actuator," *IEEE 20th International Conference on Micro Electro Mechanical Systems*, pp. 699-702, 21-25 Jan. 2007.
[89] M. Tani, M. Akamatsu, Y. Yasuda, H. Fujita, and H. Toshiyoshi, "A Combination of Fast Resonant Mode and Slow Static Deflection of SOI-PZT Actuators for MEMS Image Projection Display," *IEEE/LEOS International Conference on Optical MEMS and Their Applications*, pp. 25-26, 21-24 Aug. 2006 2006.
[90] Y. Xu, J. Singh, T. Selvaratnam, and N. Chen, "Two-Axis Gimbal-Less Electrothermal Micromirror for Large-Angle Circumferential

Scanning," *IEEE J. Sel. Top. Quantum Electron.*, vol. 15, (no. 5), pp. 1432-1438, 2009.

[91] L. Li, V. Stankovic, L. Stankovic, L. Li, S. Cheng, and D. Uttamchandani, "Single pixel optical imaging using a scanning MEMS mirror," *J. Micromech. Microeng.*, vol. 21, (no. 2), pp. 025022, 2011.

[92] K. Jia, S. Pal, and H. Xie, "An Electrothermal Tip-Tilt-Piston Micromirror Based on Folded Dual S-Shaped Bimorphs," *J. Microelectromech. Syst.*, vol. 18, (no. 5), pp. 1004-1015, 2009.

[93] S.R. Samuelson, L. Wu, J. Sun, S. Sun, B.S. Sorg, and H. Xie, "A 2.8-mm Imaging Probe Based On a High-Fill-Factor MEMS Mirror and Wire-Bonding-Free Packaging for Endoscopic Optical Coherence Tomography," *J. Microelectromech. Syst.*, vol. 21, (no. 6), pp. 1291-1302, 2012.

[94] V. Milanovic, G.A. Matus, and D.T. McCormick, "Gimbal-less monolithic silicon actuators for tip-tilt-piston micromirror applications," *IEEE J. Sel. Top. Quantum Electron.*, vol. 10, (no. 3), pp. 462-471, 2004.

[95] Y. Zhu, W. Liu, K. Jia, W. Liao, and H. Xie, "A piezoelectric unimorph actuator based tip-tilt-piston micromirror with high fill factor and small tilt and lateral shift," *Sens. Actuators A, Phys.*, vol. 167, (no. 2), pp. 495-501, 2011.

[96] M. Tani, M. Akamatsu, Y. Yasuda, and H. Toshiyoshi, "A two-axis piezoelectric tilting micromirror with a newly developed PZT-meandering actuator," in *IEEE 20th International Conference on Micro Electro Mechanical Systems*, 2007, pp. 699-702, 21-25 Jan. 2007.

[97] S. Schweizer, P. Cousseau, G. Lammel, S. Calmes, and P. Renaud, "Two-dimensional thermally actuated optical microprojector," *Sens. Actuators A, Phys.*, vol. 85, no. 1-3, pp. 424-429, Aug 2000.

[98] S.O. Isikman, O. Ergeneman, A.D. Yalcinkaya, and H. Urey, "Modeling and Characterization of Soft Magnetic Film Actuated 2-D Scanners," *IEEE J. Sel. Top. Quantum Electron.*, vol. 13, no. 2, pp. 283-289, 2007.

[99] A. Arslan, D. Brown, W.O. Davis, S. Holmstrom, S.K. Gokce, and H. Urey, "Comb-Actuated Resonant Torsional Microscanner With Mechanical Amplification," *J. Microelectromech. Syst.*, vol. 19, no. 4, pp. 936-943, 2010.

[100] K. Isamoto, K. Totsuka, T. Suzuki, T. Sakai, A. Morosawa, C. Chong, H. Fujita, and H. Toshiyoshi, "A high speed MEMS scanner for 140-kHz SS-OCT," in *Proc. IEEE Int. Conf. Opt. MEMS Nanophoton.*, Istanbul, Turkey, 2011, pp. 73-74.

[101] C.R. Giles, V. Aksyuk, B. Barber, R. Ruel, L. Stulz, and D. Bishop, "A silicon MEMS optical switch attenuator and its use in lightwave subsystems," *IEEE J. Sel. Top. Quantum Electron.*, vol. 5, no. 1, pp. 18-25, 1999.

[102] C. Lee, "Monolithic-integrated 8CH MEMS variable optical attenuators," *Sens. Actuators A, Phys.*, vol. 123–124, pp. 596-601, 2005.

[103] K. Isamoto, K. Kato, A. Morosawa, C. Changho, H. Fujita, and H. Toshiyoshi, "A 5-V operated MEMS variable optical attenuator by SOI

bulk micromachining," *IEEE J. Sel. Top. Quantum Electron.*, vol. 10, no. 3, pp. 570-578, 2004.

[104] J.E. Ford and J.A. Walker, "Dynamic spectral power equalization using micro-opto-mechanics," *IEEE Photon. Technol. Lett.*, vol. 10, no. 10, pp. 1440-1442, 1998.

[105] C. Marxer, P. Griss, and N.F. de Rooij, "A variable optical attenuator based on silicon micromechanics," *IEEE Photon. Technol. Lett.*, vol. 11, no. 2, pp. 233-235, 1999.

[106] A.Q. Liu, X.M. Zhang, C. Lu, F. Wang, C. Lu, and Z.S. Liu, "Optical and mechanical models for a variable optical attenuator using a micromirror drawbridge," *J. Micromech. Microeng.*, vol. 13, no. 3, pp. 400-411, May 2003.

[107] X.M. Zhang, A.Q. Liu, C. Lu, and D.Y. Tang, "MEMS variable optical attenuator using low driving voltage for DWDM systems," *Electron. Lett.*, vol. 38, no. 8, pp. 382-383, 2002.

[108] H. Cai, X.M. Zhang, C. Lu, A.Q. Liu, and E.H. Khoo, "Linear MEMS variable optical attenuator using reflective elliptical mirror," *IEEE Photon. Technol. Lett.*, vol. 17, no. 2, pp. 402-404, 2005.

[109] C.-H. Kim and Y.-K. Kim, "MEMS variable optical attenuator using a translation motion of 45° tilted vertical mirror," *J. Micromech. Microeng.*, vol. 15, no. 8, pp. 1466, 2005.

[110] M.T.-K. Hou, J.-Y. Huang, S.-S. Jiang, and J.A. Yeh, "In-plane rotary comb-drive actuator for a variable optical attenuator," *J. Micro/Nanolith. MEMS MOEMS*, vol. 7, no. 4, pp. 043015, 2008.

[111] C. Chen, C. Lee, and J.A. Yeh, "Retro-reflection type MOEMS VOA," *IEEE Photon. Technol. Lett.*, vol. 16, no. 10, pp. 2290-2292, 2004.

[112] C. Lee, "A MEMS VOA Using Electrothermal Actuators," *IEEE/OSA J. Lightw.Technol.*, vol. 25, no. 2, pp. 490-498, 2007.

[113] X.M. Zhang, A.Q. Liu, H. Cai, A.B. Yu, and C. Lu, "Retro-Axial VOA Using Parabolic Mirror Pair," *IEEE Photon. Technol. Lett.*, vol. 19, no. 9, pp. 692-694, 2007.

[114] N.A. Riza and F.N. Ghauri, "Hybrid analog-digital MEMS fiber-optic variable attenuator," *IEEE Photon. Technol. Lett.*, vol. 17, no. 1, pp. 124-126, 2005.

[115] W. Sun, W. Noell, M. Zickar, M.J. Mughal, F. Perez, N.A. Riza, and N.F. de Rooij, "Design, Simulation, Fabrication, and Characterization of a Digital Variable Optical Attenuator," *J. Microelectromech. Syst.*, vol. 15, no. 5, pp. 1190-1200, 2006.

[116] R.R.A. Syms, H. Zou, J. Yao, D. Uttamchandani, and J. Stagg, "Scalable electrothermal MEMS actuator for optical fibre alignment," *J. Micromech. Microeng.*, vol. 14, no. 12, pp. 1633, 2004.

[117] A. Unamuno, J. Yao, and D. Uttamchandani, "Alignment and fixing of fiber optics based on electrothermal MEMS actuators," *IEEE Photon. Technol. Lett.*, vol. 17, no. 4, pp. 816-818, 2005.

[118] A. Unamuno and D. Uttamchandani, "MEMS variable optical attenuator with vernier latching mechanism," *IEEE Photon. Technol. Lett.*, vol. 18, no. 1, pp. 88-90, 2006.

[119] G.K. Fedder, R.T. Howe, L. Tsu-Jae King, and E.P. Quevy, "Technologies for Cofabricating MEMS and Electronics," *Proc. IEEE*, vol. 96, no. 2, pp. 306-322, 2008.

[120] A. Jain, A. Kopa, Y. Pan, G.K. Fedder, and H. Xie, “A two-axis electrothermal micromirror for endoscopic optical coherence tomography,” *IEEE J. Sel. Top. Quantum Electron.*, vol. 10, no. 3, pp. 636-642, 2004.

[121] P.J. Gilgunn, J. Liu, N. Sarkar, and G.K. Fedder, “CMOS-MEMS Lateral Electrothermal Actuators,” *J. Microelectromech. Syst.*, vol. 17, no. 1, pp. 103-114, 2008.

[122] R. Maeda, J.J. Tsaur, S.H. Lee, and M. Ichiki, “Piezoelectric microactuator devices,” *J. Electroceramics*, vol. 12, no. 1-2, pp. 89-100, Jan-Mar 2004.

[123] J. Baborowski, “Microfabrication of piezoelectric MEMS,” *Integr. Ferroelectr.*, vol. 66, pp. 33-51, 2004.

[124] C. Lee, T. Itoh, and T. Suga, “Self-excited piezoelectric PZT microcantilevers for dynamic SFM - with inherent sensing and actuating capabilities,” *Sens. Actuators A, Phys.*, vol. 72, no. 2, pp. 179-188, Jan 1999.

[125] E.J. Boyd and D. Uttamchandani, “Measurement of the Anisotropy of Young's Modulus in Single-Crystal Silicon,” *J. Microelectromech. Syst.*, vol. 21, no. 1, pp. 243-249, 2012.

[126] B. Choubey, E.J. Boyd, I. Armstrong, and D. Uttamchandani, “Determination of the Anisotropy of Young's Modulus Using a Coupled Microcantilever Array,” *J. Microelectromech. Syst.*, vol. 21, no. 5, pp. 1252-1260, 2012.

[127] N. Sama, C. Soyer, D. Remiens, C. Verrue, and R. Bouregba, “Bottom and top electrodes nature and PZT film thickness influence on electrical properties,” *Sens. Actuators A, Phys.*, vol. 158, no. 1, pp. 99-105, Mar 2010.

[128] S.H. Hung, H.T. Hsieh, and G.D.J. Su, “An electro-magnetic micromachined actuator monolithically integrated with a vertical shutter for variable optical,” *J. Micromech. Microeng.*, vol. 18, no. 7, Jul 2008.

[129] C. Lee, Y.-S. Lin, Y.-J. Lai, M.H. Tasi, C. Chen, and C.-Y. Wu, “3-V driven pop-up micromirror for reflecting light toward out-of-plane direction for VOA applications,” *IEEE Photon. Technol. Lett.*, vol. 16, no. 4, pp. 1044-1046, 2004.

[130] J.G. Smits and W. Choi, “The constituent equations of piezoelectric heterogeneous bimorphs,” *IEEE Trans. Ultrason. Ferroelec. Freq. Contr.*, vol. 38, no. 3, pp. 256-270, 1991.

[131] X. Mu, Y. Xu, J. Singh, N. Chen, H. Feng, G. Zhou, A. Yu, C.W. Tan, K.W.S. Chen, and F.S. Chau, “A large rotational angle micromirror based on hypocycloidal electrothermal actuators for endoscopic imaging,” in *Proc. IEEE Int. Conf. Opt. MEMS Nanophoton.*, Sapporo, Japan, 2010, pp. 23-24.

[132] W.P. Robbins, D.L. Polla, and D.E. Glumac, “High-displacement piezoelectric actuator utilizing a meander-line geometry I. Experimental characterization,” *IEEE Trans. Ultrason. Ferroelec. Freq. Contr.*, vol. 38, no. 5, pp. 454-460, 1991.

[133] W.P. Robbins, “High-displacement piezoelectric actuator utilizing a meander-line geometry II. Theory,” *IEEE Trans. Ultrason. Ferroelec. Freq. Contr.*, vol. 38, no. 5, pp. 461-467, 1991.

[134] N.A. Riza, D.L. Polla, W.P. Robbins, and D.E. Glumac, "High resolution 50 nm linear displacement macroscale meander-line PZT actuator," *Electron. Lett.*, vol. 29, no. 18, pp. 1606-1608, 1993.

[135] G. Barillaro, A. Molfese, A. Nannini, and F. Pieri, "Analysis, simulation and relative performances of two kinds of serpentine springs," *J. Micromech. Microeng.*, vol. 15, no. 4, pp. 736, 2005.

[136] T. Kobayashi, R. Maeda, and T. Itoh, "Low speed piezoelectric optical microscanner actuated by piezoelectric microcantilevers using LaNiO3buffered Pb(Zr,Ti)O3thin film," *Smart Mater. Struct.*, vol. 18, no. 6, pp. 065008, 2009.

[137] K.H. Gilchrist, R.P. McNabb, J.A. Izatt, and S. Grego, "Piezoelectric scanning mirrors for endoscopic optical coherence tomography," *J. Micromech. Microeng.*, vol. 19, no. 9, pp. 095012, 2009.

[138] F. Filhol, E. Defay, C. Divoux, C. Zinck, and M.T. Delaye, "Resonant micro-mirror excited by a thin-film piezoelectric actuator for fast optical beam scanning," *Sens. Actuators A, Phys.*, vol. 123-24, pp. 483-489, Sep 23 2005.

[139] I.-J. Cho, T. Song, S.-H. Baek, and E. Yoon, "A low-voltage and low-power RF MEMS series and shunt switches actuated by combination of electromagnetic and electrostatic forces," *IEEE Trans. Microwave Theory Tech.*, vol. 53, no. 7, pp. 2450-2457, 2005.

[140] W. Xiaochun, A. Khaligh, and X. Yang, "Modeling, design and optimization of hybrid electromagnetic and piezoelectric MEMS energy scavengers," in *Proc. IEEE Cust. Integr. Circuits Conf.*, San Jose, CA, 2008, pp. 177-180.

[141] B. Yang, C. Lee, W.L. Kee, and S.P. Lim, "Hybrid energy harvester based on piezoelectric and electromagnetic mechanisms," *Journal of Micro/Nanolithography, MEMS and MOEMS*, vol. 9, no. 2, pp. 023002-10, 2010.

[142] G. Brown, L. Li, R. Bauer, J. Liu, and D. Uttamchandani, "A two-axis hybrid MEMS scanner incorporating electrothermal and electrostatic actuators," in *Proc. IEEE Int. Conf. Opt. MEMS Nanophoton.*, Sapporo, Japan, 2010, pp. 115-116.

[143] L. Li, R. Bauer, G. Brown, and D. Uttamchandani, "A symmetric hybrid MEMS scanner with electrothermal and electrostatic actuators," in *Proc. IEEE Int. Conf. Opt. MEMS Nanophoton.*, Istanbul, Turkey, 2011, pp. 163-164.

[144] C. Liu, "Foundations of MEMS," Englewood Cliffs, NJ: Prentice Hall, 2005.

APPENDIX

A. List of Awards

1. Best Paper Award for Photonics Global Conference (PGC) 2010.
2. Best Student Paper of Section Award for 16th Opto-Electronics and Communication Conference (OECC 2011).
3. Best Student Paper Award for 17th Opto-Electronics and Communication Conference (OECC 2012).
4. 1st prize for IEEE Region 10 Postgraduate Student Paper Contest 2012.

B. List of Publications

Book Chapter

1. C. Lee, and **K. H. Koh**, “Optical NEMS and MEMS,” *Chapter 14 of Optical Nano and Micro Actuator Technology*, Ed. G. K. Knopf and Y. Otani, CRC Press Inc., pp. 405-469, Dec. 2012, ISBN 9781439840535.

Journal Publications

1. C. Lee, F-L. Hsiao, T. Kobayashi, **K. H. Koh**, P. V. Ramana, W. Xiang, B. Yang, C. W. Tan, and D. Pinjala, “A 1-V operated MEMS variable optical attenuator using piezoelectric PZT thin film actuators,” *IEEE Journal of Selected Topics in Quantum Electronics*, vol. 15, no. 5, pp. 1529-1536, Sep/Oct 2009.
2. **K. H. Koh**, T. Kobayashi, F-L. Hsiao and C. Lee, “Characterization of piezoelectric PZT beam actuators for driving 2D scanning micromirrors,” *Sensors & Actuators A: Physical,* vol. 162, no. 2, pp. 336-347, 2010.
3. **K. H. Koh**, T. Kobayashi and C. Lee, “Low-voltage Driven MEMS VOA Using Torsional Attenuation Mechanism Based on Piezoelectric Beam Actuators,” *IEEE Photonics Technology Letters,* vol. 22, no. 18, pp. 1355-1357, Sep. 2010.
4. **K. H. Koh**, C. Lee, and T. Kobayashi, “A Piezoelectric-Driven Three-Dimensional MEMS VOA Using Attenuation Mechanism With Combination of Rotational and Translational Effects,” *Journal*

of Microelectromechanical Systems, vol. 19, no. 6, pp. 1370-1379, 2010.
5. **K. H. Koh**, J. Xie, T. Kobayashi, A. Yu and C. Lee, "Novel piezoelectric actuation mechanism for gimbal-less mirror in 2-D raster scanning applications," *Journal of Micromechanics and Microengineering,* vol. 21, no. 7, 075001, 2011.
6. **K. H. Koh**, T. Kobayashi and C. Lee, "A 2-D MEMS scanning mirror driven by a single S-shaped PZT piezoelectric thin film actuator," *Optics Express,* vol. 19, no 15, pp. 13812-13824, 2011.
7. **K. H. Koh**, T. Kobayashi and C. Lee, "Investigation of piezoelectric driven MEMS mirrors based on single and double S-shaped PZT actuator for 2D scanning applications," *Sensors & Actuators A: Physical,* vol. 184, pp. 149-159, 2012.
8. **K. H. Koh**, B. W. Soon, J. M.-L. Tsai, A. J. Danner and C. Lee, "Study of hybrid driven micromirrors for 3-D variable optical attenuator applications," *Optics Express,* vol. 20, no. 17, pp. 121598-121611, 2012.
9. **K. H. Koh**, Y. Qian and C. Lee, "Design and characterization of a 3-D MEMS VOA driven by hybrid electromagnetic and electrothermal actuation mechanisms," *Journal of Micromechanics and Microengineering,* vol. 22, no. 9, 095008, 2012.
10. **K. H. Koh** and C. Lee, "A two-dimensional MEMS scanning mirror using hybrid actuation mechanisms with low operation voltage," *Journal of Microelectromechanical Systems,* vol. 21, no. 15, pp. 1124-1135, 2012.
11. Y.-S. Lin, C. P. Ho, **K H. Koh** and C. Lee, "Fabry-Perot filter using grating structures," *Optics Letters,* vol. 38, no. 6, pp. 902-904, 2013.

Conference Proceedings

1. **K. H. Koh**, T. Kobayashi, F.-L. Hsiao and C. Lee, "A 2-D MEMS Scanning Mirror Using Piezoelectric PZT Beam Actuators," *Eurosensors 2009*, Lausanne, Switzerland, Sep. 6-9, 2009, pp.1303-1306. (Oral presentation)
2. **K. H. Koh**, T. Kobayashi and C. Lee, "Torsional mirror driven by a cantilever beam integrated with 1x10 individually biased PZT array actuator for VOA application," *IEEE International Conference on Optical MEMS and Nanophotonics 2010*, Sapporo, Japan, Aug. 9-12, 2010, pp. 119-120. (Poster presentation).
3. **K. H. Koh**, C. Lee, and T. Kobayashi, "A 3-D MEMS VOA using translational attenuation mechanism based on piezoelectric PZT thin film actuators," *Eurosensors 2010*, Linz, Austria, Sept. 5-8, 2010, pp. 613-616. (Poster presentation).

4. **K. H. Koh**, C. Lee, and T. Kobayashi, "MEMS VOA based on torsional and bending attenuation mechanisms using piezoelectric cantilever integrated with 1x10 PZT thin film actuators," *Photonics Global Conference 2010*, Singapore, Dec. 14-16, 2010. (Oral presentation, Best Student Paper Award).
5. **K. H. Koh**, T. Kobayashi and C. Lee, "Development of actuation mechanisms for MEMS mirror using PZT thin film cantilever actuators," *16th Opto-Electronics and Communication Conference*, Kaohsiung, Taiwan, Jul. 4-8, 2011, pp. 325-326. (Oral presentation, Best Student Paper of Section Award).
6. **K. H. Koh**, T. Kobayashi and C. Lee, "A 2-D raster scanning mirror driven by piezoelectric cantilever actuator array in combinational mode – bending and torsional," *IEEE International Conference on Optical MEMS and Nanophotonics 2011*, Istanbul, Turkey, Aug. 8-11, 2011, pp. 41-42. (Oral presentation)
7. **K. H. Koh**, C. Lee, J.-H. Lu, and C.-C. Chen, "Development of novel thermal actuator for driving scanning microlens," *IEEE International Conference on Optical MEMS and Nanophotonics 2011*, Istanbul, Turkey, Aug. 8-11, 2011, pp. 153-154. (Oral presentation)
8. **K. H. Koh**, T. Kobayashi, H. Liu, and C. Lee, "Investigation of a piezoelectric driven MEMS mirror based on single S-shaped PZT actuator," *Eurosensors 2011*, Athens, Greece, Sep. 4-7, 2011, pp. 701-704. (Oral presentation)
9. **K. H. Koh** and C. Lee, "3-D MEMS VOA using electromagnetic and electrothermal actuations," *17th Opto-Electronics and Communication Conference*, Busan, Republic of Korea, Jul. 2-6, 2012, pp. 255-256, (Oral presentation, Best Student Paper Award)
10. **K. H. Koh** and C. Lee, "A low power 2-D raster scanning MEMS mirror driven by hybrid electrothermal and electromagnetic actuation mechanisms," *IEEE International Conference on Optical MEMS and Nanophotonics 2012*, Banff, Canada, Aug. 6-9, 2012, pp. 236-237. (Oral presentation).